ASME
SETTING THE STANDARD

Transactions of the ASME, Journal of Heat Transfer (ISSN 0022-1481) is published monthly by The American Society of Mechanical Engineers, Three Park Avenue, New York, NY 10016. Periodicals postage paid at New York, NY and additional mailing offices. POSTMASTER: Send address changes to Transactions of the ASME, Journal of Heat Transfer, c/o THE AMERICAN SOCIETY OF MECHANICAL ENGINEERS, 22 Law Drive, Box 2300, Fairfield, NJ 07007-2300. **CHANGES OF ADDRESS** must be received at Society headquarters seven weeks before they are to be effective. Please send old label and new address.

Journal of Heat Transfer

Published Monthly by ASME

VOLUME 128 • NUMBER 5 • MAY 2006

RESEARCH PAPERS

TECHNICAL BRIEFS

(**Contents continued on inside back cover**)

This journal is printed on acid-free paper, which exceeds the ANSI Z39.48-1992 specification for permanence of paper and library materials. ♾™
♻ 85% recycled content, including 10% post-consumer fibers.

Journal of Heat Transfer **Volume 128, Number 5** **MAY 2006**

The ASME Journal of Heat Transfer is abstracted and indexed in the following:

Applied Science and Technology Index, Chemical Abstracts, Chemical Engineering and Biotechnology Abstracts (Electronic equivalent of Process and Chemical Engineering), Civil Engineering Abstracts, Compendex (The electronic equivalent of Engineering Index), Corrosion Abstracts, Current Contents, E & P Health, Safety, and Environment, Ei EncompassLit, Engineered Materials Abstracts, Engineering Index, Enviroline (The electronic equivalent of Environment Abstracts), Environment Abstracts, Environmental Engineering Abstracts, Environmental Science and Pollution Management, Fluidex, Fuel and Energy Abstracts, Index to Scientific Reviews, INSPEC, International Building Services Abstracts, Mechanical & Transportation Engineering Abstracts, Mechanical Engineering Abstracts, METADEX (The electronic equivalent of Metals Abstracts and Alloys Index), Petroleum Abstracts, Process and Chemical Engineering, Referativnyi Zhurnal, Science Citation Index, SciSearch (The electronic equivalent of Science Citation Index), Theoretical Chemical Engineering

Analysis of Enthalpy Approximation for Compressed Liquid Water

Milivoje M. Kostic
Northern Illinois University,
DeKalb, IL 60115-2854
e-mail: kostic@niu.edu

It is custom to approximate solid and liquid thermodynamic properties as being a function of temperature only, since they are virtually incompressible, and Pdv boundary work may be neglected. Furthermore, in classical literature, for isothermal compression processes, a general "improvement" and correction for liquid enthalpy approximation is given by adding the "pressure correction," vdP, to the corresponding saturation value. It is shown that such correction given for isothermal processes is generally valid for isentropic processes only. Analysis of water real properties, over the saturation temperature range and a wide pressure range up to 100 MPa, shows that the recommended corrections are only beneficial for higher pressures at smaller temperatures (below 200°C), insignificant for smaller pressures at most of the temperatures, about the same but opposite sign (thus unnecessary) for intermediate temperatures and pressures, and more erroneous (thus counterproductive and misleading) for higher temperatures and pressures, than the corresponding saturation values without any correction. The misconception in the literature is a result of the erroneous assumption, that due to incompressibility for liquids in general, the internal energy is less dependent on pressure than enthalpy. [DOI: 10.1115/1.2175090]

Keywords: enthalpy, water, thermodynamic properties, thermodynamic analysis, isothermal, isentropic

1 Introduction

Since solids and liquids are virtually (but not exactly) incompressible, then the compression work, Pdv, could be neglected and thus many properties virtually will not be a function of pressure but temperature only, such as specific internal energy, u, etc. Furthermore, any process is also at the same time an isochoric, constant-volume process. Namely, the isobaric, constant-pressure process will be a simultaneously constant-volume process for an incompressible substance, so that specific heat at constant pressure, c_p, and constant volume, c_v, are the same, or approximately the same for virtually incompressible real solids and liquids, particularly when compared to vapors and gases, i.e.:

$$u \approx u(T) \approx u_{\text{sat}}(T) \text{ and } c_p \approx c_v \approx c(T) \tag{1}$$

Even the specific enthalpy for a liquid (from here on word "specific" will be assumed and omitted for brevity), can be approximated to be independent from pressure and conveniently taken to be equal to the corresponding saturated liquid value at the given temperature:

$$h(P,T) \approx h(T) \approx h_{\text{sat}}(T) \tag{2}$$

However, enthalpy is unique, since it is explicitly defined as a function of pressure, namely:

$$h \equiv u + P \cdot v \quad \text{thus,} \quad h(T,P) = u(T,P) + P \cdot v \approx u_{\text{sat}}(T) + P \cdot v \tag{3}$$

Therefore, it is common in most engineering references, including classical and widely used thermodynamics textbooks [1,2], to evaluate the change of enthalpy, assuming incompressibility ($dv=0$), but taking correction for pressure increase as:

$$dh = d(u + P \cdot v) = \underbrace{du}_{dh_{du}} + \underbrace{P \cdot dv}_{dh_{dv}} + \underbrace{v \cdot dP}_{dh_{dP}}\Big|_{dv=0} \approx du + vdP \approx cdT + \underbrace{vdP}_{dh_{dP}=dh_{\text{corr}}} \tag{4}$$

Furthermore, for isothermal processes ($dT=0$ and $du \approx 0$, then $dh \approx vdP$), and finally, for finite pressure difference change from saturated pressure, P_{sat}, corresponding to the given temperature, T, the specific enthalpy with correction, $h_{\text{corr}}(T,P)$ at that temperature, T, and any pressure, P, will be [1,2]:

$$\Delta h_{\text{corr}} = h_{\text{corr}}(P,T) - h_{\text{sat}}(T) = v_{\text{sat}}(T) \cdot \overbrace{(P - P_{\text{sat}})}^{\Delta P_{\text{sat}}} \tag{5a}$$

$$h_{\text{corr}}(P,T) = h_{\text{sat}}(T) + \underbrace{v_{\text{sat}}(T) \cdot (P - P_{\text{sat}})}_{\Delta h_{\text{corr}}} \tag{5b}$$

where, $h_{\text{sat}}(T)$ and $v_{\text{sat}}(T)$ are liquid saturation enthalpy and liquid saturation specific volume at given temperature, T, respectively. It is stated in many references, including [1,2], that the above equations (5*a*) and (5*b*) are recommended as the correction for isothermal, liquid enthalpy dependence on pressure, and that it is more accurate than a simple, approximation without correction, h_{sat} (Eq. (2)).

It is the objective of this paper to point out the erroneous general recommendations in the literature. The correction (Eq. (5)), as recommended in many references, is only useful for higher pressures at smaller temperatures, but is actually more erroneous (thus counterproductive and misleading) for higher temperatures and pressures, and is about the same (but opposite sign, thus not necessary) for intermediate temperatures, than the simple approximation (Eq. (2)) without any correction. Corresponding analysis using real water data [3] and physical justification are presented below.

Contributed by the Heat Transfer Division of ASME for publication in the JOURNAL OF HEAT TRANSFER. Manuscript received December 13, 2004; final manuscript received November 1, 2005. Review conducted by John H. Lienhard V. Paper presented at the 2004 ASME International Mechanical Engineering Congress (IMECE2004), November 13–19, 2004, Anaheim, California, USA.

Table 1 Compressed liquid water property data at 260°C [3] and different enthalpy corrections

P (MPa)	v (m^3/kg)	u (kJ/kg)	h (kJ/kg)	s (kJ/kg K)	Cv (kJ/kg K)	Cp (kJ/kg K)	c_{sound} (m/s)	μ_{JT} (K/MPa)	$\Delta h_{\Delta u}$ (kJ/kg)	$\Delta h_{\Delta v}$ (kJ/kg)	$\Delta h_{\Delta P}$ (kJ/kg)	Δh_{corr} (kJ/kg)	Δh or $-\int \mu Cp dP$ (kJ/kg)	h_{sat}-h (kJ/kg)	h_{corr}-h (kJ/kg)
4.69sat	0.001276	1129.0	1135.0	2.8849	3.1301	4.9856	1105.3	0.03472	0.00	0.00	0.00	0.00	0.00	0.00	0.00
5	0.001276	1128.5	1134.9	2.8841	3.1299	4.9804	1107.2	0.03373	−0.50	0.00	0.39	0.39	−0.05	0.10	0.49
10	0.001265	1121.6	1134.3	2.8710	3.1257	4.9019	1135.8	0.01884	−7.40	−0.08	6.74	6.77	−0.70	0.70	7.47
15	0.001256	1115.1	1134.0	2.8586	3.1220	4.8336	1162.6	0.00582	−13.90	−0.20	13.05	13.15	−1.00	1.00	14.15
20	0.001247	1109.0	1134.0	2.8469	3.1187	4.7733	1187.8	−0.00568	−20.00	−0.35	19.31	19.53	−1.00	1.00	20.53
25	0.001239	1103.2	1134.2	2.8357	3.1158	4.7195	1211.7	−0.01595	−25.80	−0.53	25.52	25.91	−0.75	0.80	26.71
30	0.001231	1097.8	1134.7	2.8250	3.1131	4.6711	1234.3	−0.02519	−31.20	−0.74	31.70	32.30	−0.26	0.30	32.60
35	0.001224	1092.5	1135.4	2.8148	3.1107	4.6272	1256.0	−0.03355	−36.50	−0.98	37.84	38.68	0.42	−0.40	38.28
40	0.001217	1087.6	1136.3	2.8050	3.1084	4.5871	1276.7	−0.04117	−41.40	−1.24	43.94	45.06	1.28	−1.30	43.76
45	0.001211	1082.8	1137.3	2.7955	3.1063	4.5502	1296.6	−0.04816	−46.20	−1.52	50.01	51.44	2.30	−2.30	49.14
50	0.001204	1078.2	1138.4	2.7864	3.1043	4.5162	1315.8	−0.05458	−50.80	−1.82	56.05	57.82	3.46	−3.40	54.42
55	0.001199	1073.8	1139.7	2.7775	3.1024	4.4847	1334.3	−0.06051	−55.20	−2.12	62.05	64.20	4.76	−4.70	59.50
60	0.001193	1069.6	1141.1	2.7690	3.1006	4.4553	1352.2	−0.06601	−59.40	−2.45	68.03	70.58	6.17	−6.10	64.48
65	0.001187	1065.5	1142.7	2.7607	3.0989	4.4279	1369.5	−0.07113	−63.50	−2.80	73.98	76.96	7.70	−7.70	69.26
70	0.001182	1061.6	1144.3	2.7526	3.0973	4.4022	1386.3	−0.07590	−67.40	−3.15	79.91	83.34	9.32	−9.30	74.04
75	0.001177	1057.7	1146.0	2.7447	3.0957	4.3781	1402.6	−0.08037	−71.30	−3.52	85.80	89.72	11.03	−11.00	78.72
80	0.001172	1054.0	1147.8	2.7371	3.0943	4.3553	1418.5	−0.08456	−75.00	−3.90	91.68	96.10	12.83	−12.80	83.30
85	0.001167	1050.5	1149.7	2.7297	3.0928	4.3338	1433.9	−0.08850	−78.50	−4.29	97.53	102.48	14.71	−14.70	87.78
90	0.001163	1047.0	1151.6	2.7224	3.0914	4.3134	1449.0	−0.09220	−82.00	−4.69	103.35	108.86	16.67	−16.60	92.26
95	0.001158	1043.6	1153.7	2.7153	3.0901	4.2940	1463.7	−0.09570	−85.40	−5.09	109.15	115.24	18.69	−18.70	96.54
100	0.001154	1040.3	1155.8	2.7084	3.0888	4.2756	1478.1	−0.09901	−88.70	−5.51	114.93	121.62	20.77	−20.80	100.82

Table 2 Compressed liquid water property data at different temperatures and pressures [3]

	$T=4°C$			$T=20°C$			$T=50°C$			$T=100°C$			$T=150°C$		
P (MPa)	v (m^3/kg)	u (kJ/kg)	h (kJ/kg)	v (m^3/kg)	u (kJ/kg)	h (kJ/kg)	v (m^3/kg)	u (kJ/kg)	h (kJ/kg)	v (m^3/kg)	u (kJ/kg)	h (kJ/kg)	v (m^3/kg)	u (kJ/kg)	h (kJ/kg)
Sat	0.001000	16.81	16.81	0.001002	83.912	83.914	0.001012	209.33	209.34	0.001044	419.06	419.17	0.001091	631.66	632.18
5	0.000998	16.81	21.80	0.001000	83.609	88.607	0.001010	208.59	213.64	0.001041	417.64	422.85	0.001088	629.55	634.98
10	0.000995	16.79	26.75	0.000997	83.308	93.281	0.001008	207.86	217.94	0.001039	416.23	426.62	0.001084	627.27	638.11
15	0.000993	16.77	31.66	0.000995	83.007	97.934	0.001006	207.15	222.23	0.001036	414.85	430.39	0.001081	625.05	641.27
20	0.000990	16.74	36.55	0.000993	82.708	102.57	0.001004	206.44	226.51	0.001034	413.50	434.17	0.001078	622.89	644.45
25	0.000988	16.70	41.40	0.000991	82.409	107.18	0.001001	205.75	230.79	0.001031	412.17	437.95	0.001075	620.78	647.66
30	0.000986	16.65	46.23	0.000989	82.112	111.77	0.000999	205.07	235.05	0.001029	410.87	441.74	0.001072	618.73	650.89
35	0.000984	16.59	51.02	0.000987	81.815	116.34	0.000997	204.40	239.31	0.001027	409.60	445.54	0.001069	616.72	654.14
40	0.000981	16.53	55.79	0.000985	81.520	120.90	0.000995	203.75	243.56	0.001025	408.35	449.33	0.001066	614.77	657.42
45	0.000979	16.46	60.53	0.000982	81.225	125.44	0.000993	203.10	247.80	0.001022	407.13	453.14	0.001064	612.85	660.71
50	0.000977	16.38	65.24	0.000980	80.931	129.95	0.000991	202.46	252.03	0.001020	405.93	456.94	0.001061	610.98	664.02
55	0.000975	16.30	69.93	0.000978	80.637	134.45	0.000989	201.84	256.26	0.001018	404.76	460.75	0.001058	609.15	667.35
60	0.000973	16.21	74.59	0.000977	80.345	138.94	0.000988	201.22	260.47	0.001016	403.61	464.56	0.001056	607.36	670.69
65	0.000971	16.12	79.23	0.000975	80.053	143.40	0.000986	200.61	264.68	0.001014	402.47	468.37	0.001053	605.61	674.05
70	0.000969	16.01	83.84	0.000973	79.762	147.85	0.000984	200.01	268.88	0.001012	401.36	472.19	0.001051	603.89	677.43
75	0.000967	15.91	88.43	0.000971	79.471	152.29	0.000982	199.42	273.07	0.001010	400.27	476.00	0.001048	602.21	680.81
80	0.000965	15.80	93.00	0.000969	79.182	156.70	0.000980	198.84	277.26	0.001008	399.20	479.82	0.001046	600.56	684.21
85	0.000963	15.68	97.55	0.000967	78.893	161.10	0.000978	198.26	281.44	0.001006	398.14	483.64	0.001043	598.95	687.63
90	0.000961	15.56	102.07	0.000965	78.604	165.49	0.000977	197.70	285.61	0.001004	397.11	487.46	0.001041	597.36	691.05
95	0.000959	15.44	106.58	0.000964	78.317	169.86	0.000975	197.14	289.77	0.001002	396.09	491.29	0.001039	595.81	694.48
100	0.000958	15.31	111.06	0.000962	78.031	174.22	0.000973	196.59	293.92	0.001000	395.09	495.11	0.001036	594.29	697.93

	$T=200°C$			$T=250°C$			$T=300°C$			$T=350°C$		
P (MPa)	v (m^3/kg)	u (kJ/kg)	h (kJ/kg)	v (m^3/kg)	u (kJ/kg)	h (kJ/kg)	v (m^3/kg)	u (kJ/kg)	h (kJ/kg)	v (m^3/kg)	u (kJ/kg)	h (kJ/kg)
Sat	0.001157	850.47	852.27	0.001252	1080.8	1085.8	0.001404	1332.9	1345.0	0.00174	1642.1	1670.9
5	0.001153	847.91	853.68	0.00125	1079.5	1085.7	$P_{sat}=8.5879$ MPa			$P_{sat}=16.529$ MPa		
10	0.001148	844.31	855.80	0.001241	1073.4	1085.8	0.001398	1329.4	1343.3			
15	0.001144	840.84	857.99	0.001233	1067.6	1086.1	0.001378	1317.6	1338.3			
20	0.001139	837.49	860.27	0.001225	1062.2	1086.7	0.001361	1307.1	1334.4	0.001665	1612.7	1646.0
25	0.001135	834.24	862.61	0.001218	1057.0	1087.4	0.001346	1297.6	1331.3	0.001599	1583.9	1623.9
30	0.00113	831.10	865.02	0.001211	1052.0	1088.4	0.001332	1288.9	1328.9	0.001553	1562.2	1608.8
35	0.001126	828.06	867.48	0.001205	1047.3	1089.4	0.001320	1280.8	1327.0	0.001517	1544.5	1597.6
40	0.001122	825.10	870.00	0.001199	1042.7	1090.7	0.001308	1273.3	1325.6	0.001488	1529.3	1588.8
45	0.001119	822.23	872.57	0.001193	1038.4	1092.0	0.001298	1266.2	1324.6	0.001464	1515.9	1581.8
50	0.001115	819.45	875.19	0.001187	1034.2	1093.5	0.001288	1259.6	1324.0	0.001443	1503.9	1576.1
55	0.001111	816.73	877.85	0.001182	1030.1	1095.1	0.001279	1253.3	1323.6	0.001424	1493.1	1571.4
60	0.001108	814.09	880.55	0.001176	1026.2	1096.8	0.001270	1247.3	1323.5	0.001407	1483.1	1567.5
65	0.001104	811.51	883.29	0.001171	1022.5	1098.6	0.001262	1241.6	1323.6	0.001391	1473.8	1564.3
70	0.001101	809.00	886.07	0.001167	1018.8	1100.5	0.001254	1236.1	1323.9	0.001377	1465.2	1561.6
75	0.001098	806.56	888.89	0.001162	1015.3	1102.4	0.001247	1230.9	1324.4	0.001364	1457.1	1559.5
80	0.001095	804.17	891.73	0.001157	1011.8	1104.4	0.001240	1225.9	1325.1	0.001353	1449.5	1557.7
85	0.001091	801.83	894.61	0.001153	1008.5	1106.5	0.001233	1221.1	1325.9	0.001341	1442.3	1556.3
90	0.001088	799.55	897.51	0.001149	1005.3	1108.7	0.001227	1216.4	1326.8	0.001331	1435.5	1555.3
95	0.001086	797.32	900.44	0.001145	1002.1	1110.9	0.001221	1212.0	1327.9	0.001321	1429.0	1554.5
100	0.001083	795.14	903.40	0.001141	999.06	1113.1	0.001215	1207.6	1329.1	0.001312	1422.8	1554.0

Table 3 Compressed liquid water enthalpies, *h*, their approximation differences, $h_{sat}-h$ (Eq. (2)), and $h_{corr}-h$ (Eq. (5)), and related percentages (Note: More erroneous approximations are indicated in bold.)

T °C →	4°C		20°C		50°C		100°C		150°C		200°C		250°C		300°C		350°C	
	h (kJ/kg)		**h** (kJ/kg)		**h** (kJ/kg)		**h** (kJ/kg)		**h** (kJ/kg)		**h** (kJ/kg)		**h** (kJ/kg)		**h** (kJ/kg)		**h** (kJ/kg)	
P (MPa)	$h_{sat}-h$ (kJ/kg) %	$h_{corr}-h$ (kJ/kg) %	$h_{sat}-h$ (kJ/kg) %	$h_{corr}-h$ (kJ/kg) %	$h_{sat}-h$ (kJ/kg) %	$h_{corr}-h$ (kJ/kg) %	$h_{sat}-h$ (kJ/kg) %	$h_{corr}-h$ (kJ/kg) %	$h_{sat}-h$ (kJ/kg) %	$h_{corr}-h$ (kJ/kg) %	$h_{sat}-h$ (kJ/kg) %	$h_{corr}-h$ (kJ/kg) %	$h_{sat}-h$ (kJ/kg) %	$h_{corr}-h$ (kJ/kg) %	$h_{sat}-h$ (kJ/kg) %	$h_{corr}-h$ (kJ/kg) %	$h_{sat}-h$ (kJ/kg) %	$h_{corr}-h$ (kJ/kg) %
Sat.	**16.81**		**83.91**		**209.34**		**419.17**		**632.18**		**852.27**		**1085.80**		**1345.00**		**1670.90**	
	0	**0**	**0**	**0**	**0**	**0**	**0**	**0**	**0**	**0**	**0**	**0**	**0**	**0**	**0**	**0**	**0**	**0**
	0%	**0%**	**0%**	**0%**	**0%**	**0%**	**0%**	**0%**	**0%**	**0%**	**0%**	**0%**	**0%**	**0%**	**0%**	**0%**	**0%**	**0%**
5	21.80		88.61		213.64		422.85		634.98		853.68		1085.70		Vapor			
	−4.98	0.02	−4.69	0.31	−4.30	0.75	−3.68	1.43	−2.80	2.13	−1.41	2.57	0.10	1.38	P_{sat}=			
	−22.9%	0.1%	**−5.3**%	0.4%	**−2.0**%	0.4%	**−0.9**%	0.3%	**−0.4**%	0.3%	−0.2%	**0.3**%	0.0%	**0.1**%	8.5879 MPa			
10	26.75		93.28		217.94		426.62		638.11		855.80		1085.80		1343.30		Vapor	
	−9.93	0.07	−9.37	0.65	−8.60	1.51	−7.45	2.88	−5.93	4.46	−3.53	6.24	0.00	7.54	1.70	3.68	P_{sat}=	
	−37.1%	0.3%	**−10.0**%	0.7%	**−3.9**%	0.7%	**−1.7**%	0.7%	**−0.9**%	0.7%	−0.4%	**0.7**%	0.0%	**0.7**%	0.1%	**0.3**%	6.529 MPa	
15	31.66		97.93		222.23		430.39		641.27		857.99		1086.10		1338.30			
	−14.85	0.15	−14.02	1.00	−12.89	2.28	−11.22	4.33	−9.09	6.75	−5.72	9.83	−0.30	13.50	6.70	15.70		
	−46.9%	0.5%	**−14.3**%	1.0%	**−5.8**%	1.0%	**−2.6**%	1.0%	**−1.4**%	1.1%	−0.7%	**1.1**%	0.0%	**1.2**%	0.5%	**1.2**%		
20	36.55		102.57		226.51		434.17		644.45		860.27		1086.70		1334.40		1646.00	
	−19.74	0.27	−18.66	1.38	−17.17	3.06	−15.00	5.76	−12.27	9.02	−8.00	13.33	−0.90	19.16	10.60	26.62	24.90	30.94
	−54.0%	0.7%	**−18.2**%	1.3%	**−7.6**%	1.4%	**−3.5**%	1.3%	**−1.9**%	1.4%	−0.9%	**1.5**%	−0.1%	**1.8**%	0.8%	**2.0**%	1.5%	**1.9**%
30	46.23		111.77		235.05		441.74		650.89		865.02		1088.40		1328.90		1608.80	
	−29.41	0.59	−27.86	2.20	−25.71	4.64	−22.57	8.63	−18.71	13.49	−12.75	20.15	−2.60	29.97	16.10	46.17	62.10	85.54
	−63.6%	1.3%	**−24.9**%	2.0%	**−10.9**%	2.0%	**−5.1**%	2.0%	**−2.9**%	2.1%	−1.5%	**2.3**%	−0.2%	**2.8**%	1.2%	**3.5**%	3.9%	**5.3**%
40	55.79		120.90		243.56		449.33		657.42		870.00		1090.70		1325.60		1588.80	
	−38.98	1.03	−36.99	3.08	−34.22	6.25	−30.16	11.47	−25.24	17.86	−17.73	26.73	−4.90	40.19	19.40	63.51	82.10	122.94
	−69.9%	1.8%	**−30.6**%	2.6%	**−14.0**%	2.6%	**−6.7**%	2.6%	**−3.8**%	2.7%	−2.0%	**3.1**%	−0.4%	**3.7**%	1.5%	**4.8**%	5.2%	**7.7**%
50	65.24		129.95		252.03		456.94		664.02		875.19		1093.50		1324.00		1576.10	
	−48.43	1.58	−46.04	4.05	−42.69	7.90	−37.77	14.30	−31.84	22.17	−22.92	33.11	−7.70	49.91	21.00	79.15	94.80	153.04
	−74.2%	2.4%	**−35.4**%	3.1%	**−16.9**%	3.1%	**−8.3**%	3.1%	**−4.8**%	3.3%	−2.6%	**3.8**%	−0.7%	**4.6**%	1.6%	**6.0**%	6.0%	**9.7**%
60	74.59		138.94		260.47		464.56		670.69		880.55		1096.80		1323.50		1567.50	
	−57.78	2.23	−55.03	5.08	−51.13	9.58	−45.39	17.11	−38.51	26.40	−28.28	39.31	−11.00	59.12	21.50	93.69	103.40	179.04
	−77.5%	3.0%	**−39.6**%	3.7%	**−19.6**%	3.7%	**−9.8**%	3.7%	**−5.7**%	3.9%	−3.2%	**4.5**%	−1.0%	**5.4**%	1.6%	**7.1**%	6.6%	**11.4**%
80	93.00		156.70		277.26		479.82		684.21		891.73		1104.40		1325.10		1557.70	
	−76.19	3.82	−72.79	7.36	−67.92	13.04	−60.65	22.72	−52.03	34.69	−39.46	51.26	−18.60	76.56	19.90	120.18	113.20	223.64
	−81.9%	4.1%	**−46.4**%	4.7%	**−24.5**%	4.7%	**−12.6**%	4.7%	**−7.6**%	5.1%	−4.4%	**5.7**%	−1.7%	**6.9**%	1.5%	**9.1**%	7.3%	**14.4**%
100	111.06		174.22		293.92		495.11		697.93		903.40		1113.10		1329.10		1554.00	
	−94.25	5.76	−90.31	9.87	−84.58	16.62	−75.94	28.30	−65.75	42.78	−51.13	62.72	−27.30	92.89	15.90	144.26	116.90	262.14
	−84.9%	5.2%	**−51.8**%	5.7%	**−28.8**%	5.7%	**−15.3**%	5.7%	**−9.4**%	6.1%	−5.7%	**6.9**%	−2.5%	**8.3**%	1.2%	**10.9**%	7.5%	**16.9**%

2 Analysis

Compressed liquid water properties [3], for different pressure at 260°C, are presented in Table 1 and selected properties for different temperatures in Table 2. In addition, the corresponding corrections ($\Delta h_{\Delta u}$, $\Delta h_{\Delta v}$, and $\Delta h_{\Delta P}$, see Eqs. (4)–(8)) are tabulated along with differences of the approximated enthalpies, without ($h_{\text{sat}}-h$) and with correction ($h_{\text{corr}}-h$) from the real enthalpy values, h, in the last two columns in Table 1, respectively, for saturated liquid water and compressed liquid water up to 100 MPa. Cumulative water enthalpy data with the corresponding differences and related percentages are presented in Table 3 for a wide range of temperatures between triple and critical points, and, a wide range of pressures from saturation up to 100 MPa. Note that the tabulated enthalpy differences with correction is based on Eq. (5), i.e., using correction $\Delta h_{\text{corr}} \approx \Delta h_{\Delta P}$ only, as generally recommended in the literature, while corrections $\Delta h_{\Delta u}$, and $\Delta h_{\Delta v}$ are neglected [1,2].

The corrections in Tables 1 and 3 are calculated using the following equations:

$$\Delta h_{\Delta u} = \Delta u = u(P,T) - u_{\text{sat}}(T) \tag{6}$$

$$\Delta h_{\Delta v} = \int P \cdot dv \cong \sum_{i=1\text{sat}}^{N-1} \left[\frac{1}{2}(P_i + P_{i+1})\right] \cdot (v_{i+1} - v_i) \tag{7}$$

$$\Delta h_{\Delta P} = \int v \cdot dP \cong \sum_{i=1sat}^{N-1} \left[\frac{1}{2}(v_i + v_{i+1})\right] \cdot (P_{i+1} - P_i) \approx \Delta h_{\text{corr}} \tag{8}$$

Note that in Eq. (5) the fluid is assumed to be incompressible, while in Eqs. (6)–(8) variability in v, although small, is taken into account, thus the differences in Δh_{corr} and $\Delta h_{\Delta P}$ values in Table 1. Furthermore, for the isothermal compression, the correction $\Delta h_{\Delta v}$ is much smaller than the corrections $\Delta h_{\Delta u}$ and $\Delta h_{\Delta P}$, and thus it may be neglected. However, corrections $\Delta h_{\Delta u}$ (negative) and corrections $\Delta h_{\Delta P}$ (positive) are comparable in magnitude but opposite in sign, so it is better not to take the corrections, as in Eq. (2), than to take only the correction $\Delta h_{\text{corr}} \approx \Delta h_{\Delta P}$, as in Eq. (5). It will be shown below that the recommended enthalpy correction for the isothermal compression [1,2], is actually valid for isentropic compression.

It appears from real data values in Tables 1 and 2 that the magnitude of the negative correction $\Delta h_{\Delta u}$ (i.e., Δu) increases with both pressure and temperature, while positive correction $\Delta h_{\Delta P}$ (i.e., $\int v dP$) depends mostly on pressure since the specific volume, v, does not change significantly. As is evident from data in Table 3, the correction, Eq. (5) [1,2], as a general improvement for compressed liquid enthalpy calculation, is not justified in general, but for smaller temperatures only (less than 200°C). However, it is more erroneous (and thus counterproductive and misleading) for higher temperatures (above 200°C) and particularly at higher pressures, where a simple approximation (Eq. (2)), without any correction, is more accurate.

In Fig. 1, the compression of saturated liquid water, state (f_{sat}) at 260°C, is presented for isothermal compression to state (T50) at 50 MPa, and for isentropic compression to state (s50) to the same pressure of 50 MPa (see Table 1 for property data).

Since $du = \delta q - \delta w$ (where $\delta w = Pdv$), and real liquids (in this case water) are not exactly incompressible, then during isentropic compression ($\delta q = Tds = 0$) there will be some negative work (Pdv) and an increase of internal energy and temperature (in this case for 11.7°C, from 260°C to 271.7°C) [3]. However, during the isothermal compression, to cool and maintain constant water temperature, there must be some heat transfer out, q, and in the process the internal energy, u, will be decreased with pressure increase at constant temperature (see the corresponding data in Tables 1 and 2; note $\Delta h_{\Delta u} = \Delta u < 0$ if $\Delta P > 0$). At high temperatures, 300°C and above, even specific enthalpy is decreasing with pressure increase due to a strong decrease of internal energy, making the recommended positive correction, Δh_{corr}, to be erroneous and thus counterproductive and misleading, see Tables 2 and 3. The $\Delta h_{\Delta u}$ correction is not included in Eq. (5) even though its magnitude may be, and sometimes is, larger than the included $\Delta h_{\text{corr}} \approx \Delta h_{\Delta P}$ correction. Therefore, the recommended enthalpy correction for isothermal compression in the literature is appropriate for the isentropic processes (see additional justification below), but not appropriate for isothermal processes, although it may sometimes be beneficial, due to an erroneous assumption that internal energy is not, and enthalpy is, dependent on pressure. It is quite the opposite in Table 1, see how the corresponding values (u and h) change with pressure at constant temperature of 260°C.

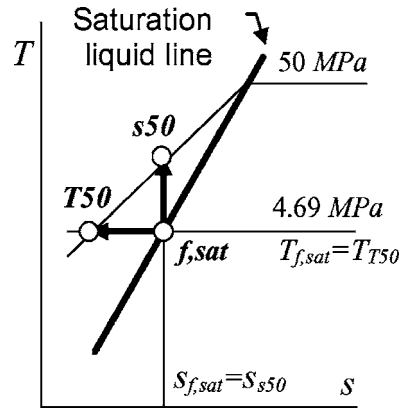

Fig. 1 Isothermal and isentropic compression of saturated liquid water

The above physical justifications could be confirmed using the corresponding differential property correlations obtained using the Maxwell's relations [1]:

$$du(T,v) = \underbrace{\left(\frac{\partial u}{\partial T}\right)_v}_{C_v = T\left(\frac{\partial s}{\partial T}\right)_v} dT + \underbrace{\left[T\left(\frac{\partial P}{\partial T}\right)_v - P\right]}_{\left(\frac{\partial u}{\partial v}\right)_T} dv$$

$$= \begin{cases} -Pdv, & \text{for } s = \text{const} \\ \left[T\left(\frac{\partial P}{\partial T}\right)_v - P\right] dv, & \text{for } T = \text{const} \end{cases} \tag{9}$$

$$dh(T,P) = \underbrace{\left(\frac{\partial h}{\partial T}\right)_P}_{C_P = T\left(\frac{\partial s}{\partial T}\right)_P} dT + \underbrace{\left[v - T\left(\frac{\partial v}{\partial T}\right)_P\right]}_{\left(\frac{\partial h}{\partial P}\right)_T} dP$$

$$= \begin{cases} v \cdot dP, & \text{for } s = const \\ \left[v - T\left(\frac{\partial v}{\partial T}\right)_P\right] dP, & \text{for } T = const \end{cases} \tag{10}$$

From Eq. (9) it is evident that change in internal energy for the isothermal process is zero ($du = 0$) only for ideal incompressible fluids ($dv = 0$), but for real liquids ($dv \neq 0$) the bracketed term with dv in Eq. (9) is not zero since real liquids are not exactly incompressible.

Equation (10) confirms that pressure correction (vdP) is always appropriate for isentropic processes ($dh = Tds + vdP = vdP$ for s = const), but not for isothermal processes as given in many refer-

ences [1,2]. For example, for an isentropic compression of liquid water from saturation at 260°C to 50 MPa, see Fig. 1 and data in Table 1 (P_{sat}=4.69 MPa, h_{sat}=1135.0 kJ/kg, s_{sat}=2.8849 kJ/kg K), the temperature and enthalpy will increase to 271.7°C and h_{s50}=1191.7 kJ/kg, respectively [3]. The isentropic enthalpy increase, $h_{s50}-h_{sat}$=(1191.7−1135.0) kJ/kg=56.7 kJ/kg is virtually identical to the corresponding enthalpy correction ($\Delta h_{\Delta P}=\int v dP$=56.05 KJ/kg)≈($\Delta h_{corr}$=57.82 kJ/kg), where the small differences in Table 1 are due to an integral approximation with discrete summation (Eq.(8)) or assuming $v=v_{sat}$=const in Eq. (5) during the process.

For the isothermal process the enthalpy pressure-correction could be evaluated using the three corrections, Eqs. (6)–(8), or integrating Eq. (9) or (10), or combined Eqs. (9) and (10), i.e.:

$$[\Delta h]_T=[h(P,T)-h_{sat}(T)]_T = \begin{cases} \Delta h_{\Delta u}(Eq.6)+\Delta h_{\Delta v}(Eq.7)+\Delta h_{\Delta P}(Eq.8) \\ \int_{P_{sat}}^{P}\left[v-T\left(\frac{\partial v}{\partial T}\right)_P\right]dP=\int_{P_{sat}}^{P}\left[-C_P\underbrace{\left(\frac{\partial T}{\partial P}\right)_h}_{\mu_{JT}}\right]dP \\ \int_{P_{sat}}^{P} v dP+\int_{v_{sat}}^{v}\left[T\left(\frac{\partial P}{\partial T}\right)_v\right]dv \end{cases} \tag{11}$$

Since the Joule-Thomson coefficient is defined as $\mu_{JT}=(\partial T/\partial P)_h$, then Eq. (11) could be expressed as:

$$[\Delta h]_T=[h(P,T)-h_{sat}(T)]_T=\Delta h_{\Delta u}+\Delta h_{\Delta v}+\Delta h_{\Delta P}$$
$$=\int_{P_{sat}}^{P}[-C_P\mu_{JT}]dP$$
$$\cong\sum_{i=1sat}^{N-1}\left[\frac{1}{2}(C_P\mu_{JT,i}+C_P\mu_{JT,i+1})\right](P_{i+1}-P_i) \tag{12}$$

Note that real data values for both, the μ_{JT} and C_p are available [3], and for the isothermal enthalpy correction, Δh, Eq. (12) was used instead of Eqs. (6)–(8), see Table 1.

Compressed liquid water enthalpies (h), different corrections, their approximation differences ($h_{sat}-h$, and $h_{corr}-h$) and the corresponding error percentages, with regard to the saturation value, are presented in Table 3, without any correction (Eq. (2)) and the correction recommended in the literature ($\Delta h_{corr}\approx\Delta h_{\Delta P}$, Eq. (5)), for a wide range of temperatures and pressures. The corrections, as recommended in [1,2] (Eq. (5)), are only beneficial for higher pressures at smaller temperatures, insignificant for smaller pressures at most of the temperatures, about the same but opposite sign (thus unnecessary) for intermediate temperatures and pressures, and more erroneous (thus counterproductive and misleading) for higher temperatures and pressures, than the simple approximation without any correction (Eq. (2)), as seen from Tables 1 and 3.

3 Conclusion

An analysis with physical justification, supported by water real enthalpy data, regarding liquid enthalpy approximation, is presented here. The analysis shows, and a conclusion is drawn, that the recommendation in the classical reference textbooks for improvement of enthalpy calculation of compressed liquids, by accounting for pressure dependence, is not generally valid for isothermal processes. The misconception in the literature is a result of the erroneous assumption that, due to incompressibility for liquids in general, the internal energy is less dependent on pressure than enthalpy. The literature recommendations may be erroneous and thus counterproductive and misleading, as is the case for liquid water at higher temperatures and pressures. For intermediate pressures and temperatures, the enthalpy corrections recommended in the literature are unnecessary, since the errors are about the same in magnitude (but opposite in sign) as if the corresponding saturated enthalpy values without any corrections were used. The isothermal corrections are only beneficial for very high pressures at smaller temperatures (below 200°C for liquid water).

In summary, the recommended pressure corrections in the classical reference textbooks for isothermal, liquid enthalpy approximation are not appropriate and often insignificant, unnecessary or more erroneous than the simple approximation using the corresponding saturated values. Furthermore, it is shown here that the recommended pressure correction for isothermal processes are actually valid in general for enthalpy correction for isentropic processes.

Nomenclature

- c, c_p, c_v = specific heat, at constant pressure, or constant volume
- c_{sound} = speed of sound
- Δh = enthalpy correction including all relevant corrections, Eq. (12)
- Δh_{corr} = enthalpy correction due to the change of $\Delta P_{sat}=P-P_{sat}$, Eq. (5*a*)
- Δh_{Δ_u} = enthalpy correction due to the change of Δu, Eq. (6)
- Δh_{Δ_v} = enthalpy correction due to the change of Δv, Eq. (7)
- Δh_{Δ_P} = enthalpy correction due to the change of ΔP, Eq. (8)
- h = liquid enthalpy at any P and T
- h_{corr} = liquid enthalpy approximation with $v_{sat}\Delta P_{sat}$ correction as recommended in the literature
- h_{sat} = saturation liquid enthalpy
- P = pressure
- q = heat transfer per unit of mass
- s = entropy
- T = temperature
- u = internal thermal energy
- v = specific volume
- w = boundary work per unit of mass
- μ_{JT} = The Joule-Thomson coefficient

Subscripts

- s50 = isentropic compression from saturated to 50 MPa
- sat = for saturated liquid
- T50 = isothermal compression from saturated to 50 MPa

References

[1] Cengel, Y. A., and Boles, M. A., 2002, *Thermodynamics, An Engineering Approach*, 4th ed., McGraw-Hill, New York, Sec. 2.5.3, p. 84 and Chap. 11, pp. 603–626.

[2] Moran, M. J., and Shapiro, H. N., 2000, *Fundamentals of Engineering Thermodynamics*, 4th ed., Wiley, New York, Sec. 3.3.6, p. 109.

[3] Lemmon, E. W., McLinden, M. O., and Friend, D. G., 2005, "Thermophysical Properties of Fluid Systems," *NIST Chemistry WebBook*, NIST Standard Reference Database No. 69, P. J. Linstrom, and W. G. Mallard, eds., National Institute of Standards and Technology, Gaithersburg, MD (http://webbook.nist.gov/chemistry/fluid).

A Model for Condensate Retention on Plain-Fin Heat Exchangers[1]

A. I. ElSherbini[2]
e-mail: asherbini@kisr.edu.kw
Building and Energy Technologies Department,
Kuwait Institute for Scientific Research,
P.O. Box 24885 Safat, 13109, Kuwait

A. M. Jacobi
e-mail: a-jacobi@uiuc.edu
Department of Mechanical and Industrial Engineering,
University of Illinois at Urbana-Champaign,
1206 W. Green St., Urbana, IL 61801

A model has been developed for predicting the amount of condensate retained as drops on the air-side of heat exchangers operating under dehumidifying conditions. For a coil with a given surface wettability, characterized by the advancing contact angle, the maximum diameter for a retained drop is obtained from a balance between gravitational and surface tension forces. A logarithmic function is used to describe the size-distribution of drops on fins, based on the fraction of fin-area covered by liquid. The volumes of individual drops are calculated by a geometric method for approximating the three-dimensional shapes of drops on vertical and inclined surfaces. The total volume of condensate accumulated on a coil is then found by multiplying the size-distribution and volume functions and integrating over all drop diameters. The model is successful in predicting measurements by other researchers of the mass of condensate retained on plain-fin heat exchangers. The critical fin spacing to avoid the formation of condensate bridges is also predicted. [DOI: 10.1115/1.2175091]

Keywords: condensation, retention, heat exchangers

Introduction

In air conditioning and refrigeration systems, evaporators usually operate below the dewpoint of conditioned air. Thus, under normal air-cooling and dehumidification conditions, water condenses and accumulates on the air-side surfaces of heat exchangers. Condensate retained on an evaporator affects the indoor air quality by providing a medium for biological activity. In addition, condensate retention can have a significant impact on the performance of the heat exchanger.

The effects of condensate retention on the thermal and hydraulic performance of heat exchangers have been studied by many researchers. Retained condensate generally causes the friction factor to increase. For example, Yin and Jacobi [1] found the friction factor for a plain-fin coil under wet conditions to be 70% higher than that for a dry coil. The degradation in hydraulic performance is less pronounced at a large fin spacing and high Reynolds numbers, Re [1–6]. Water drops are believed to roughen the heat exchanger surfaces and increase friction factors. Also, condensate removal from the surface is harder at smaller fin spacing and lower Re, especially when condensate "bridges" form. The increased retention results in more blockage of the air flow path and higher friction. Condensation may increase or decrease heat transfer, depending on the heat exchanger geometry and operating conditions. For plain-fin coils, condensate decreases sensible heat transfer at low Re, but it increases heat transfer at high Re. Wang et al. [5] reported such a behavior with the transition occurring at Re=2000 based on tube diameter. Wet conditions enhance heat transfer at larger fin spacing, f_s, and degrade it at smaller f_s. Yin and Jacobi [1] observed a 55% decrease in heat transfer under wet conditions for a plain-fin coil with a fin spacing of 1.3 mm. The roughness caused by droplets is thought to result in the heat transfer enhancement, while bridging at low Re and narrow fin spacing can be responsible for the degradation. Heat exchangers with other geometries have also been tested under dehumidifying conditions (see for example [7–9]). The data in the literature suggest that the quantity of retained condensate and its mode play significant roles in characterizing the thermal and hydraulic performance of heat exchangers under wet conditions. Therefore, developing a model that can predict condensate retention on heat exchangers will provide a useful tool for designing heat exchangers for wet operation.

Some researchers [10,11] presented models to calculate the amount of condensate retained on finned-tubes, in order to determine the condensation heat transfer coefficient for pure vapors. Jacobi and Goldschmidt [7] studied moisture condensation on finned-tubes and proposed a model for condensate bridging that helped explain coil performance at different airflow rates. These simple models, however, were restricted to annular geometry and the filmwise mode of the condensation.

Korte and Jacobi [6] developed a model for predicting the amount of condensate retained on plain-fin heat exchangers with wide fin spacings. The volume of retained condensate was obtained by integrating a size distribution function, multiplied by the volumes of individual drops, over all drop sizes, as will be explained later. A balance of forces was used to find the maximum drop diameter, D_{max}, to set the integration limit. The model showed reasonable success in predicting condensate retention on a heat exchanger tested by Korte and Jacobi. However, simplifications in calculating the shapes and size distributions of drops have limited the accuracy and applicability of the model.

The objective of this article is to develop a model for predicting the steady-state mass of condensate retained as drops on heat exchangers. To achieve this goal, the volumes of drops held on the fins of a heat exchanger need to be reliably determined under various surface conditions. Then, the steady-state distribution of drop sizes on a fin surface is considered. Finally, the total mass of condensate is found to close the model.

Retention Model

Consider a plain-fin heat exchanger operating under dehumidification conditions. At steady state, the mass of condensate removed from the coil by drainage or fly-out is equal to the mass added by condensation. Thus, the amount of water retained on the heat exchanger is constant. Measurements of retained condensate

[1]Presented at the 2004 ASME Heat Transfer/Fluids Engineering Summer Conference (HT-FED2004), July 11, 2004–July 15, 2004, Charlotte, NC.

[2]Corresponding author.

Contributed by the Heat Transfer Division of ASME for publication in the JOURNAL OF HEAT TRANSFER. Manuscript received January 23, 2005; final manuscript received October 19, 2005. Review conducted by A. Haji-Sheikh.

[1,6] show that the mass reaches steady-state values. For wide fin spacing, where inter-fin bridges cannot form, the total mass of retained condensate can be expressed as

$$M = \rho_w \int_{A_T} \int_D V(D) n(D) dD dA \tag{1}$$

where ρ_w is the density of water, $V(D)$ is the volume of a droplet with diameter D, and $n(D)$ is the number of droplets with diameter D per unit area and per droplet diameter. The integration is performed for all drop sizes over the entire surface area of the heat exchanger, A_T. This formulation of the condensate retention model, reduces the problem into finding the volume function, V, and the size-distribution function, n, for drops. These functions are written in terms of D to emphasize the dependence on diameter; however, they also depend on other variables, such as the wettability (contact angles) and inclination angle of the heat transfer surfaces. The maximum diameter, $D_{\max}$, is also needed as a limit for the integration in Eq. (1), and will prove useful when calculating $n(D)$. In the next sections, we discuss the volume and size-distribution functions.

Volume Function

Finding the volume of a drop requires knowledge of its shape. For a small drop on a horizontal fin, the shape can be defined by a spherical cap. However, a large drop on a vertical surface cannot be described by a simple function. The shapes of liquid drops on vertical and inclined surfaces have been studied by many investigators, as in [12–15]. These studies disagreed on key parameters affecting drop shapes, such as contact angles and contact lines, as explained in [16]. Moreover, they did not provide a reliable function relating the volume of a drop to its diameter and to surface conditions. In a related paper [17], we developed a method for approximating the shapes of liquid drops on vertical and inclined surfaces. The method is briefly explained below.

Two-Circle Model. Consider a liquid drop on a fin surface that is inclined an angle α from the horizontal. For an arbitrary cross section taken at an azimuthal angle, ϕ, the profile displays two contact angles, θ_1 and θ_2, as in Fig. 1. The two-circle method approximates the profile at the given cross section by parts of two circles sharing a common tangent, as shown in the figure. The drop volume is found by integrating all profiles along the circumference of the drop base. The total volume is divided into two parts,

$$V = V_{\mathrm{I}} + V_{\mathrm{II}} \tag{2}$$

The integrals can be expressed as

$$V_{\mathrm{I}} = \int_0^{\pi/2} \left[\frac{(y_b - Y_0)^3}{3}(2 - 3\cos\theta_1 + \cos^3\theta_1) + X_0(y_b - Y_0)^2\theta_1 - X_0(y_a - Y_0)(y_b - Y_0)\sin\theta_1 + X_0^2(y_b - y_a) - \frac{2}{3}y_b^3 + \frac{2}{3}y_b^2 y_c - X_0^2 y_b + \frac{X_0^2}{3}y_c + X_0 y_b^2\left(\frac{\pi}{2} - \sin^{-1}\left(\frac{y_c}{y_b}\right)\right)\right] d\phi \tag{3a}$$

and

$$V_{\mathrm{II}} = \int_{\pi}^{3\pi/2} \left[y_c\left(\frac{2}{3}y_b^2 + \frac{X_0^2}{3}\right) - y_b^2 y_a + \frac{y_a^3}{3} - X_0^2 y_a + X_0 y_a y_b \sin\theta_2 - X_0 y_b^2\left(\sin^{-1}\left(\frac{y_c}{y_b}\right) - \frac{\pi}{2} + \theta_2\right)\right] d\phi \tag{3b}$$

where the variables y_a, y_b, y_c, X_0, and Y_0 are as shown in Fig. 1. Expressions for these variables have been developed in [17] in terms of the radius of the drop base, ζ, and the contact angles, θ_1 and θ_2. Thus, the two-circle method provides an approximation for the volume of a drop in the form

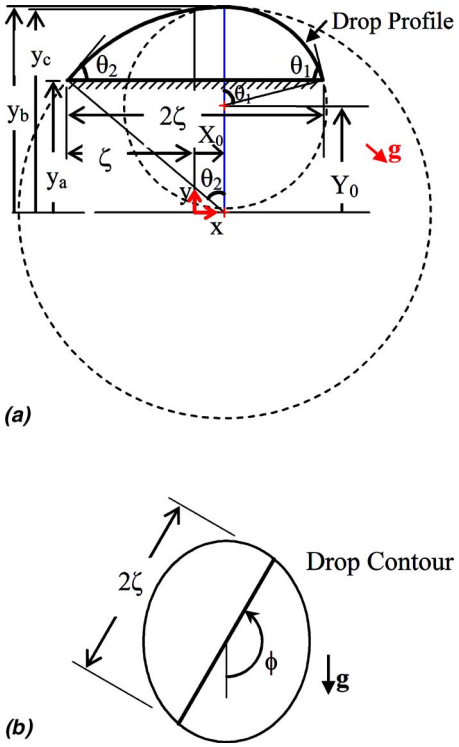

Fig. 1 (*a*) Profile of a liquid drop fit by parts of two circles. (*b*) Contact line at the base of the drop. The two-circle method approximates the profiles and volumes of drops on vertical or inclined fins.

$$V = \int F(\zeta(\phi), \theta(\phi)) d\phi \tag{4}$$

where $\zeta(\phi)$ is a function describing the contact line (contour) of the drop, and $\theta(\phi)$ describes the contact-angle variation along the drop circumference. The method was validated against experimental measurements.

Contact Angle and Contour Functions. Investigators have predicted different forms for the function $\theta(\phi)$, which describes the contact angle, θ, as it varies with the azimuthal angle, ϕ, for a drop on an inclined surface (see for example [11,12,15]). Also, several shapes have been reported for the contour, $\zeta(\phi)$, at the base of the drop [16]. We have conducted experiments, reported in [18], to investigate the general shapes of these two functions. Based on observations and analysis, it was concluded that the contact-angle variation is best fit by a third-degree function that takes the form

$$\cos\theta(\phi) = 2\frac{\cos\theta_{\max} - \cos\theta_{\min}}{\pi^3}\phi^3 - 3\frac{\cos\theta_{\max} - \cos\theta_{\min}}{\pi^2}\phi^2 + \cos\theta_{\max} \tag{5}$$

where $\theta_{\max}$ and $\theta_{\min}$ are the maximum and minimum contact angles in a drop, respectively. Such angles are observed in the symmetry plane ($\phi = 0$ in Fig. 1) of the drop.

The drop contour was found to be best fit by an ellipse. Let L and w denote the major and minor axes of the ellipse, respectively. The radius of the ellipse is described as

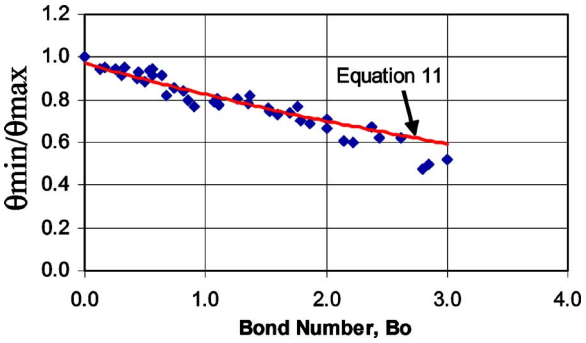

Fig. 2 Minimum contact angle, normalized by the maximum angle, as it varies with the Bond number for different liquids and surfaces. A single relation fits the data with a coefficient of determination $r^2=0.90$.

$$\zeta(\phi) = \frac{L}{\sqrt{\cos^2\phi + \beta^2 \sin^2\phi}} \tag{6}$$

where β is the aspect ratio ($\beta = L/w$). The ellipse can also be described by an equivalent diameter, D, which yields the same contour area, and its aspect ratio. Using the equivalent diameter, the contour equation becomes

$$\zeta(\phi) = \frac{D}{2}\sqrt{\frac{\beta}{\cos^2\phi + \beta^2 \sin^2\phi}} \tag{7}$$

Equations (5) and (7) define the inputs needed for the volume function in Eq. (4). Thus, the volume of a drop can be found, given its diameter, contour aspect ratio, and maximum and minimum contact angles,

$$V = \int H(D, \beta, \theta_{\max}, \theta_{\min}) d\phi \tag{8}$$

Contact Angle and Contour Values. In order to predict the volumes of all drops, the variables β, $\theta_{\max}$, and $\theta_{\min}$ need to be determined at different conditions. These variables were measured and reported [18] for a range of drop sizes on surfaces with various inclination angles and contact angles. Two liquids were tested on eight surfaces to cover a wide range of advancing and receding contact angles. Notice that $\theta_{\max}$ and $\theta_{\min}$ refer to the contact angles in a drop, while the advancing and receding contact angles refer to those angles characteristic of the liquid-surface combination. The results were presented in terms of the Bond number, Bo, which is a measure of gravitational to surface tension forces,

$$\mathrm{Bo} = \frac{\rho_w g D^2 \sin\alpha}{\gamma} \tag{9}$$

where ρ_w is the liquid density, g is the acceleration of gravity, D is the equivalent drop diameter, α is the surface inclination angle, and γ is surface tension of the liquid-vapor interface. For a given liquid drop at constant temperature, an increase in Bo indicates an increase in drop diameter and/or surface inclination. The maximum contact angle in a drop, $\theta_{\max}$, was found to be almost equal to the advancing contact angle, θ_A, for all tested conditions

$$\theta_{\max} = \theta_A \tag{10}$$

The minimum contact angle of a drop was found to decrease as the Bond number is increased for various drop sizes and surface-inclination angles. In addition, the ratio ($\theta_{\min}/\theta_A$) followed a single curve for all tested surfaces, as shown in Fig. 2. This behavior allowed describing the minimum contact angle by the general relation

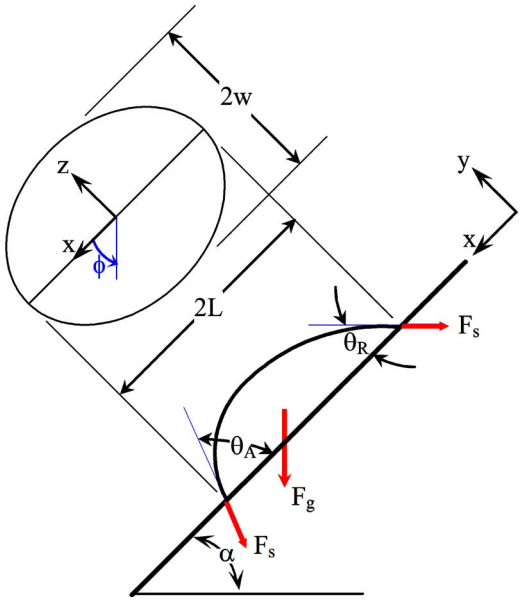

Fig. 3 A force balance on a drop on an inclined fin, used to find the maximum drop diameter

$$\frac{\theta_{\min}}{\theta_A} = 0.01\,\mathrm{Bo}^2 - 0.155\,\mathrm{Bo} + 0.97 \tag{11}$$

Similarly, an empirical relation was obtained for the aspect ratio of the contour,

$$\beta = 1 + 0.096\,\mathrm{Bo} \tag{12}$$

This relation compares well to measurements from the literature. More details can be found in [18]. Equations (10)–(12) can now be used to find the volume of any droplet on the heat exchanger. Consider a plain-fin evaporator with surface wettability characterized by the advancing contact angle θ_A. For any droplet of diameter D, the Bond number can be calculated from Eq. (9), and the values of $\theta_{\max}$, $\theta_{\min}$, and β can be found from Eqs. (10)–(12). The volume of the drop is obtained by a numerical integration of Eq. (8), which is based on the two-circle approximation. Thus, the $V(D)$ function in Eq. (1) is determined. The next step in the retention model is to find the maximum drop diameter that can be held on the heat-exchanger surface.

Maximum Drop Diameter

In order to set the limits of the integration in Eq. (1), the minimum and maximum drop diameters, $D_{\min}$ and $D_{\max}$, are required. Typical values measured for $D_{\max}$ are in the order of millimeters. The lower limit, $D_{\min}$, is several orders of magnitude smaller, and is conveniently taken as 10 μm. Smaller sizes do not add significant value to the area covered by drops or their total volume. The maximum diameter is obtained from a balance of forces acting on a drop on a fin surface, as in Fig. 3. Earlier experiments show air-flow forces to have small effects on condensate retention over flow rates typical to the current conditions [6]. Therefore, drag forces will be neglected and the balance is performed between gravitational and surface-tension forces acting in the x-z plane.

The surface tension force acting on the drop of Fig. 3 is found by integrating the differential forces over the contour of the drop. Due to symmetry, the components of the surface-tension force in the z direction will cancel; the resulting surface-tension force acts in the x direction and can be calculated from

$$F_{sx} = -2\gamma \int_0^{\pi} \zeta \cos\theta \cos\phi d\phi \tag{13}$$

where γ is the liquid surface tension, and θ and ϕ are as defined earlier. The surface tension is assumed to be constant, and changes associated with the temperature distribution of the fin are neglected. By substituting for $\cos\theta$ from Eq. (5) and using the equivalent diameter of the drop, D, instead of 2ζ, the integration leads to (see [19])

$$F_{sx} = \frac{24}{\pi^3}\gamma D(\cos\theta_{\min} - \cos\theta_A) \tag{14}$$

where $\theta_{\max} = \theta_A$.

The gravitational force acting on the drop of Fig. 3 in the x-direction can be written as

$$F_{gx} = -\rho_w g V \sin\alpha \tag{15}$$

which can be rearranged, using an equivalent diameter, to be

$$F_{gx} = -\gamma D \,\mathrm{Bo}\frac{V}{D^3} \tag{16}$$

A force balance on the drop in the x direction is obtained by setting

$$F_{gx} + F_{sx} = 0 \tag{17}$$

ElSherbini [16] showed that the force balance leads to a relation that takes the form

$$\theta_{\min} = G(\theta_A, \mathrm{Bo}). \tag{18}$$

If the volume of the drop is calculated based on approximating its shape as a spherical cap, Eq. (18) can be expressed as

$$\cos\theta_{\min} = \cos\theta_A + \frac{\pi^4}{576}\left(\frac{2 - 3\cos\theta_{\mathrm{av}} + \cos^3\theta_{\mathrm{av}}}{\sin^3\theta_{\mathrm{av}}}\right)\mathrm{Bo} \tag{19}$$

where $\theta_{\mathrm{av}} = (\theta_{\min} + \theta_A)/2$. A more reliable version of Eq. (18) uses the two-circle method to find the drop volume. Equations (18) and (11) can be solved simultaneously to obtain the critical values for Bo and $\theta_{\min}$. The maximum Bond number, $\mathrm{Bo}_{\max}$, is then used to find $D_{\max}$ from Eq. (9). The critical drop sizes found by this analysis agreed well with measurements reported in the literature, as shown in [19].

Size-Distribution for Drops

Drops condensing on a vertical or inclined surface grow by condensation and coalescence until they reach the maximum diameter, if they are not swept by other sliding drops. At maximum size, the force due to gravity overcomes surface-tension forces and the drop starts sliding. The work of early researchers [20–23] showed that the distribution of drop sizes can be described by a steady-state function which has a logarithmic nature. The logarithmic function changes its slope when drop sizes become large and the drop growth mechanism changes. The growth of small drops is dominated by condensation, while the growth of large drops is more influenced by coalescence. Other distribution functions were also proposed [24–26]. They agreed with measurements for small drops, but did not capture the change in distribution for large drops. Graham [20] noticed that the change in slope for the size-distribution function occurred at $(D/D_{\max})$ of 0.2. Yin and Jacobi [1] confirmed that finding. The measurements of Tanasawa and Ochiai [22] indicate that the change occurs when $(D/D_{\max})$ is in the vicinity of that number (0.18–0.26). Therefore, the size distribution function can be written as

$$n_s = Q_s D^{B_s} \quad \text{for } D_{\min} \leqslant D \leqslant 0.2D_{\max} \tag{20a}$$

and

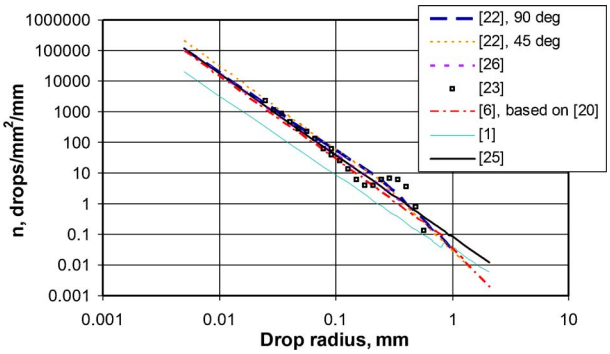

Fig. 4 Size-distribution functions for drops condensing on plane surfaces, obtained by different researchers

$$n_b = Q_b D^{B_b} \quad \text{for } 0.2D_{\max} \leqslant D \leqslant D_{\max} \tag{20b}$$

where n_s and n_b denote distributions for small and big drops, respectively, and Q_s, B_s, Q_b, and B_b are constants. Previous investigators have associated different values to these constants. We will present a simple approach for finding the best values for such constants. Our model will follow prior work and neglect edge effects in describing droplet distributions. Although the fin edges can be expected to influence droplet sizes, the number of droplets near the edges is small in comparison to the total number of droplets on the fin.

Figure 4 compares the size-distribution functions obtained by different researchers. The figure shows that earlier studies of n_s agreed on the slope, B_s, of the distribution function for small drops. In fact, the distribution of Graham [20] and one of the distributions of Tanasawa and Ochiai [22] resulted in the same B_s value of −2.73. Adopting this value, three other constants (Q_s, Q_b, B_b) still need to be determined. In the present analysis, these constants will be considered as parameters depending on the maximum diameter and the surface area covered by drops. The fraction of area covered by small drops can be found from

$$A_{\mathrm{cov},s} = \int_{D_{\min}}^{0.2D_{\max}} n_s\left(\frac{\pi D^2}{4}\right)dD \tag{21a}$$

and the fraction of area covered by large drops is

$$A_{\mathrm{cov},b} = \int_{0.2D_{\max}}^{D_{\max}} n_b\left(\frac{\pi D^2}{4}\right)dD \tag{21b}$$

It is important to use consistent units in Eq. (21). The fraction of area covered by drops is the total area of drops per unit area, which is dimensionless. The size distribution function is a number per unit area per diameter, with dimensions of $(\mathrm{length})^{-3}$. It is common to describe n as the number of drops per cm^2 per μm and D in μm. Using these units, Eq. (21) can be integrated to become

$$A_{\mathrm{cov},s} = \frac{\pi}{4(10)^8}\frac{Q_s}{B_s + 3}[(0.2D_{\max})^{B_s+3} - D_{\min}^{B_s+3}] \tag{22a}$$

and

$$A_{\mathrm{cov},b} = \frac{\pi}{4(10)^8}\frac{Q_b}{B_b + 3}[D_{\max}^{B_b+3} - (0.2D_{\max})^{B_b+3}] \tag{22b}$$

The continuity of the size-distribution function requires that $n_s = n_b$ at $D = 0.2D_{\max}$. Therefore,

$$Q_b = Q_s(0.2D_{\max})^{(B_s - B_b)} \tag{22c}$$

Using the maximum drop diameter, $D_{\max}$, and the fractions of area covered by small and large drops, $A_{\mathrm{cov},s}$ and $A_{\mathrm{cov},b}$, as inputs, Eq. (22) can be solved for the three unknowns: Q_s, Q_b, and B_b. The maximum diameter is determined from a force balance as de-

scribed in the previous section. The area covered by drops is an important parameter for n that needs to be found.

The fraction of area covered by small and large drops calculated from [20–23] ranged between 0.75 and 0.85, with maximum drop diameters of 2–2.9 mm. However, the test surfaces used were circular with diameters of only 2–4 cm. Fin-and-tube heat exchangers typically have much larger lengths, where falling drops sweep greater areas of the fin surfaces. Therefore, the fractional area covered by drops, A_{cov}, should be smaller for such heat exchangers. Yin and Jacobi [1] measured the area covered by drops at three locations on a heat-exchanger fin with a length of 20 cm. The average fractional area covered by drops was 0.34, with a maximum diameter of 4.2 mm. The average A_{cov} for the small and large portions of the size distribution function were 0.16 and 0.18, respectively. These values are considered representative of the geometry and conditions of fin-and-tube heat exchangers, and will be used to compare the predicted condensate retention to measurements for coils with fin lengths of 15 and 27 cm.

The analysis presented in this section generalizes the size-distribution function by allowing the constants of its two portions to vary for different conditions. The fractional areas covered by small and large drops, along with the calculated value of D_{max}, can be used in Eq. (22) for obtaining the constants defining n_s and n_b. Defining these size-distribution functions completes the model for predicting the mass of retained condensate.

Mass of Retained Condensate

The mass of condensate retained as drops on a heat exchanger is calculated from Eq. (1), which can be divided into two parts in order to represent small and large drops,

$$M_s = \rho_w \int_{A_T} \int_{D_{min}}^{0.2D_{max}} V(D) n_s(D) dD dA \tag{23a}$$

and

$$M_b = \rho_w \int_{A_T} \int_{0.2D_{max}}^{D_{max}} V(D) n_b(D) dD dA \tag{23b}$$

where

$$M = M_s + M_b \tag{23c}$$

The procedure for calculating the mass of condensate retained on a heat exchanger can now be summarized. The inputs to the model are the inclination angle of the coil, α, measured from the horizontal, and the advancing contact angle, θ_A.[3] The fractional areas covered by small and large drops, $A_{cov,s}$, and $A_{cov,b}$, are considered known for the given wettability and dimensions of the coil surfaces. The maximum Bond number is obtained by numerically searching for the solution to Eqs. (11) and (18). The maximum diameter is then calculated from Eq. (9). The minimum diameter, D_{min}, is taken as 10 μm, and $B_s = -2.73$. The values of D_{max}, $A_{cov,s}$ and $A_{cov,b}$ are used in Eq. (22) to obtain the constants defining the size-distribution functions. The integrations in Eqs. (23*a*) and (23*b*) are performed for diameters between the lower and upper limits. For each increment in diameter, Eqs. (9) and (12) are used to find the contact angles and aspect ratio, which are substituted into Eq.(8) and integrated to calculate the volume corresponding to that diameter. The volume is multiplied by the size distribution for that diameter and the integration continues. The mass of condensate retained per unit area is finally found from Eq. (23*c*).

The model developed in this work is used to compare predictions of condensate retention to experimental data. Notice that changing the fin spacing may change the total area of the heat exchanger and total mass of retained condensate, but the retention per unit area should remain constant as long as bridging does not take place. Korte and Jacobi [6] presented condensate retention measurements for a fin-and-tube heat exchanger with a fin spacing of 6.4 mm. The coil had vertical aluminum fins, as shown in Fig. 5, with an advancing angle, θ_A, of about 90 deg. At very low air velocity, the condensate per unit area becomes 129 g/m^2. Shin and Ha [27] also tested an aluminum heat exchanger with the same advancing contact angle and a fin spacing of 5.4 mm at a low face velocity of 0.6 m/s. Figure 6 compares the measurements of Korte and Jacobi [6] and Shin and Ha [27] to the predictions of the present retention model and the model of Korte and Jacobi. The new model succeeds in predicting the two independent measurements of condensate retention. The simplified model of Korte and Jacobi overpredicts the mass of the retained condensate.

The success of the current model confirms the validity of its components. The predictions of drop volumes, contact angles, maximum diameters, and retentive forces had been validated separately in earlier works. When considered together, the model predicts the mass of condensate with excellent accuracy.

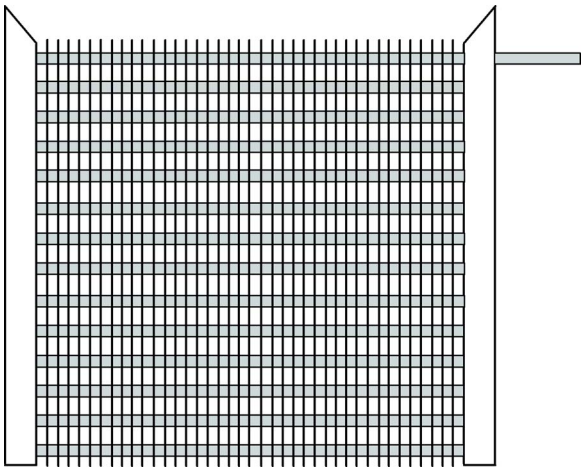

Fig. 5 Heat-exchanger geometry used for comparing the model to measurements of retained condensate

Predicting Condensate Bridges

The proposed retention model is applicable for heat exchangers with small fin densities. As the fin density increases, drops from adjacent fins coalesce together to form bridges and significantly change the distribution of condensate on the coil. Drop-shape analysis can be used to develop an equation for the critical fin spacing for condensate bridging to occur. The height-to-diameter ratio for a drop is expressed as (see [16]),

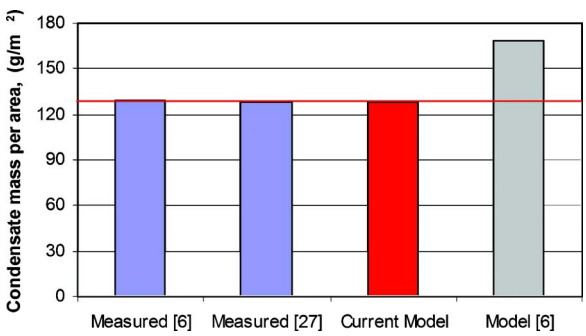

Fig. 6 Predicted mass of condensate retained on heat exchangers compared to measurements reported by Shin and Ha [27] and Korte and Jacobi [6], and to an earlier model

[3]The receding contact angle, θ_R, is not required, but can be incorporated—if know—into calculating D_{max}.

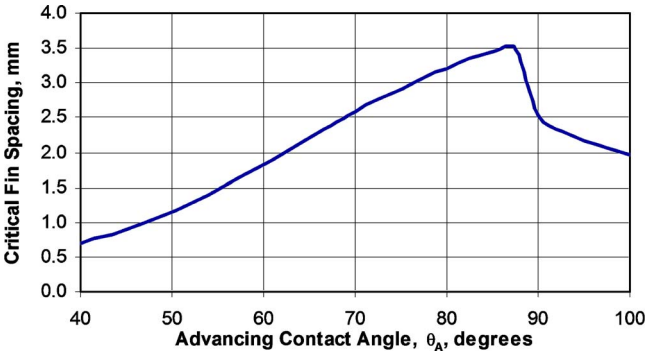

Fig. 7 Critical fin spacing, beyond which condensate bridges cannot occur, as a function of the advancing contact angle

$$\frac{h}{D} = \frac{\sqrt{\beta}}{\left(\frac{\sin\theta_{\max}}{1-\cos\theta_{\max}}\right)+\left(\frac{\sin\theta_{\min}}{1-\cos\theta_{\min}}\right)} \tag{24}$$

where β is the aspect ratio of the drop contour, and $\theta_{\max}$ and $\theta_{\min}$ are the maximum and minimum contact angles, respectively. For drops on two fins to coalesce into a bridge, the fin spacing cannot exceed the value of $2h_{\max}$, where $h_{\max}$ is the height of the largest drop that can be retained on a fin. Thus, the critical fin spacing is

$$f_{s,\mathrm{cr}} = \frac{2D_{\max}\sqrt{\beta}}{\left(\frac{\sin\theta_A}{1-\cos\theta_A}\right)+\left(\frac{\sin\theta_R}{1-\cos\theta_R}\right)} \tag{25}$$

where θ_A and θ_R are the advancing and receding contact angles, respectively, that are characteristic of the fin surface. Heat exchangers with fin spacings greater than $f_{s,\mathrm{cr}}$ will not have condensate bridges.

The critical fin spacing, $f_{s,\mathrm{cr}}$, sets the limit for the applicability of the current condensate retention model. It also provides a tool for designing heat exchangers for wet conditions of operation. In order to avoid condensate bridging, which degrades coil performance, a fin spacing larger than $f_{s,\mathrm{cr}}$ should be used. Figure 7 shows the variation of $f_{s,\mathrm{cr}}$ with advancing contact angle, where the variables θ_R, $D_{\max}$, and β are calculated based on analysis of critical-size drops. The critical fin spacing increases with the advancing angle to a maximum, and then it decreases. This behavior of $f_{s,\mathrm{cr}}$ follows the pattern of the maximum drop size, since $f_{s,\mathrm{cr}}$ is proportional to $D_{\max}$ (Eq. (25)). Critical drop sizes are discussed in more detail in another work [19]. It is interesting to note that both hydrophilic and hydrophobic coatings can be used to reduce $f_{s,\mathrm{cr}}$ and prevent the formation of bridges. Retention measurements by Korte and Jacobi [28] support the predicted critical fin spacing. A coil with a fin spacing of 3.2 mm showed bridging behavior. After extended operation, the advancing contact angle decreased, causing $f_{s,\mathrm{cr}}$ to fall below 3.2 mm and the bridging behavior disappeared.

Conclusions

In this article, we developed a model for predicting the steady-state mass of the condensate retained on plain-fin heat exchangers. Coils are assumed to have wide fin spacing so that condensate bridges cannot form. The model takes the inclination angle and the advancing contact angle of the coil surfaces as inputs. The fractional areas covered by small and large drops are also known from observations of coils with similar wettability and surface dimensions. Application of the model should be constrained to surfaces with roughness and materials that manifest advancing contact angles from 45 deg to 120 deg, because the empirical basis for the model is restricted to that range. The maximum diameter is obtained from a balance of forces acting on a drop. The volumes of individual drops are found using the two-circle approximation. The maximum diameter and fractional areas covered by drops are used to define the logarithmic functions describing the distribution sizes for drops. The total amount of retained condensate is found by integrating the volume and size-distribution functions over drop diameters. The model successfully predicts the condensate retention measurements by other researchers. The critical fin spacing to avoid bridges is also calculated from drop geometry.

Nomenclature

A_{cov} = fraction of area covered by drops
A_T = total surface area of a heat exchanger
B = constant in Eq. (20)
Bo = Bond number
D = equivalent diameter of drop
F, G, H = functions
f_s = fin spacing
F_s = surface tension force
F_g = gravitational force
g = acceleration of gravity
h = drop height
L = major axis of ellipse
M = total mass
n = size distribution of drops (number per unit area, per diameter)
Q = constant in Eq. (20)
r^2 = coefficient of determination
Re = Reynolds number
V = volume
w = minor axis of ellipse
X_0, Y_0 = variables in Fig. 1
y_a, y_b, y_c = variables in Fig. 1

Greek Symbols

ϕ = azimuthal angle
α = inclination angle of a surface
β = aspect ratio of contour
γ = surface tension of the liquid-vapor interface
ζ = radius of contour
θ = contact-angle
θ_1, θ_2 = contact angles, see Fig. 1
ρ_w = mass density of water

Subscripts

A = advancing
b = for big drops
cr = critical
max = maximum
min = minimum
R = receding
s = for small drops
x = in the x direction

Acknowledgment

The authors would like to acknowledge the support of the Air Conditioning and Refrigeration Center (ACRC) of the University of Illinois at Urbana-Champaign.

References

[1] Yin, J., and Jacobi, A. M., 2000, "Condensate Retention Effects on the Air-Side Heat Transfer Performance of Plain and Wavy-Louvered Heat Exchangers," Report No. TR-158, ACRC, University of Illinois at Urbana-Champaign, IL.
[2] McQuiston, F. C., 1978, "Heat, Mass, and Momentum Transfer Data for Five Plate-Fin-Tube Heat Transfer Surfaces," ASHRAE Trans., **84**, pp. 266–293.
[3] McQuiston, F. C., 1978, "Correlation of Heat, Mass, and Momentum Transport Coefficients for Plate-Fin-Tube Heat Transfer Surfaces with Staggered Tubes," ASHRAE Trans., **84**, pp. 294–308.
[4] Eckels, P. W., and Rabas, T. J., 1987, "Dehumidification: On the Correlation of

Wet and Dry Transport Processes in Plate Finned-Tube Heat Exchangers," ASME J. Heat Transfer, **109**, pp. 575–582.
[5] Wang, C. C., Hsieh, Y. C., and Lin, Y. T., 1997, "Performance of Plate Finned Tube Heat Exchangers Under Dehumidifying Conditions," ASME J. Heat Transfer, **119**, pp. 109–117.
[6] Korte, C. M., and Jacobi, A. M., 2001, "Condensate Retention Effects on the Performance of Plain-Fin-and-Tube Heat Exchangers: Retention Data and Modeling," ASME J. Heat Transfer, **123**, pp. 926–936.
[7] Jacobi, A. M., and Goldschmidt, V. W., 1990, "Low Reynolds Number Heat and Mass Transfer Measurements of an Overall Counterflow, Baffled, Finned-Tube, Condensing Heat Exchanger," Int. J. Heat Mass Transfer, **33**, pp. 755–765.
[8] Wang, C. C., Du, Y. J., Chang, Y. J., and Tao, W. H., 1999, "Airside Performance of Herringbone Fin-and-Tube Heat Exchangers in Wet Conditions," Can. J. Chem. Eng., **77**, pp. 1225–1230.
[9] Kim, G. J., and Jacobi, A. M., 2000, "Condensate Accumulation Effects on the Air-Side Thermal Performance of Slit-Fin Surfaces," Report No. CR-26, ACRC, University of Illinois, Urbana.
[10] Beatty, K. O., Jr., and Katz, D. L., 1948, "Condensation of Vapors on Outside of Finned Tubes," Chem. Eng. Prog., **44**, pp. 55–70.
[11] Rudy, T. M., and Webb, R. L., 1985, "An Analytical Model to Predict Condensate Retention on Horizontal Integral-Fin Tubes," ASME J. Heat Transfer, **107**, pp. 361–368.
[12] Brown, R. A., Orr, F. M., Jr., and Scriven, L. E., 1980, "Static Drop on an Inclined Plate: Analysis by the Finite Element Method," J. Colloid Interface Sci., **73**, pp. 76–87.
[13] Milinazzo, F., and Shinbrot, M., 1988, "A Numerical Study of a Drop on a Vertical Wall," J. Colloid Interface Sci., **121**, pp. 254–264.
[14] Rotenberg, Y., Boruvka, L., and Neumann, A. W., 1984, "The Shape of Nonaxisymmetric Drops on Inclined Planar Surfaces," J. Colloid Interface Sci., **102**, pp. 424–434.
[15] Dimitrakopoulos, P., and Higdon, J. J. L., 1999, "On the Gravitational Displacement of Three-Dimensional Fluid Droplets from Inclined Solid Surfaces," J. Fluid Mech., **395**, pp. 181–209.
[16] ElSherbini, A. I., 2003, "Modeling Condensate Drops Retained on the Air-Side of Heat Exchangers," Ph.D. thesis, University of Illinois at Urbana-Champaign, IL.
[17] ElSherbini, A. I., and Jacobi, A. M., 2004, "Liquid Drops on Vertical and Inclined Surfaces: Part II—A Method for Approximating Drop Shapes," J. Colloid Interface Sci., **273**, pp. 566–575.
[18] ElSherbini, A. I., and Jacobi, A. M., 2004, "Liquid Drops on Vertical and Inclined Surfaces: Part I—An Experimental Study of Drop Geometry," J. Colloid Interface Sci., **273**, pp. 556–565.
[19] ElSherbini, A. I., and Jacobi, A. M., 2005, "Retention Forces and Contact Angles for Critical Liquid Drops on Non-Horizontal Surfaces," J. Colloid Interface Sci. (in press).
[20] Graham, C., 1969, "The Limiting Heat Transfer Mechanisms of Dropwise Condensation," Ph.D. thesis, Massachusetts Institute of Technology, MA.
[21] Graham, C., and Griffith, P., 1973, "Drop Size Distributions and Heat Transfer in Dropwise Condensation," Int. J. Heat Mass Transfer, **16**, pp. 337–346.
[22] Tanasawa, I., and Ochiai, J., 1973, "Experimental Study on Dropwise Condensation," Bull. JSME, **16**, pp. 1184–1197.
[23] Tanaka, H., 1975, "Measurements of Drop-Size Distributions During Transient Dropwise Condensation," ASME J. Heat Transfer, **97**, pp. 341–346.
[24] Sugawara, S., and Michiyoshi, I., 1956, "Dropwise Condensation," Mem. Fac. Eng., Kyoto Univ., Kyoto University, **18**, pp. 84–111.
[25] Wu, Y. T., Yang, C. X., and Yuan, X. G., 2001, "Drop Distributions and Numerical Simulation of Dropwise Condensation Heat Transfer," Int. J. Heat Mass Transfer, **44**, pp. 4455–4464.
[26] Rose, J. W., and Glicksman, L. R., 1973, "Dropwise Condensation–The Distribution of Drop Sizes," Int. J. Heat Mass Transfer, **16**, pp. 411–425.
[27] Shin, J., and Ha, S., 2002, "The Effect of Hydrophilicity on Condensation Over Various Types of Fin-And-Tube Heat Exchangers," Int. J. Refrig., **25**, pp. 688–694.
[28] Korte, C. M., and Jacobi, A. M., 1997, "Condensate Retention and Shedding Effects on Air-Side Heat Exchanger Performance," Report No. TR-132, ACRC, University of Illinois, Urbana.

Heat Transfer in a Porous Electrode of Fuel Cells

J. J. Hwang
Professor, Dean of Graduate School
e-mail: azaijj@mdu.edu.tw
Research Center for Advanced Science and Technology,
Mingdao University,
Changhua, 52345 Taiwan

The thermal-fluid behaviors in a porous electrode of a proton exchange membrane fuel cell (PEMFC) in contact with an interdigitated gas distributor are investigated numerically. The porous electrode consists of a catalyst layer and a diffusion layer. The heat transfer in the catalyst layer is coupled with species transports via a macroscopic electrochemical model. In the diffusion layer, the energy equations based on the local thermal nonequilibrium (LTNE) are derived to resolve the temperature difference between the solid phase and the fluid phase. Parametric studies include the Reynolds number and the Stanton number (St). Results show that the wall temperature decreases with increasing Stanton number. The maximum wall temperatures occur at the downstream end of the module, while the locations of local minimum wall temperature depend on the Stanton numbers. Moreover, the solid phase and the fluid phase in the diffusion layer are thermally insulated as $\mathrm{St} \ll 1$. *The diffusion layer becomes local thermal nonequilibrium as the Stanton number around unity. The porous electrode is local thermal equilibrium for* $\mathrm{St} \gg 1$. *Finally, the species concentrations inside the catalyst and diffusion layers are also provided.* [DOI: 10.1115/1.2175092]

Keywords: porous electrode, proton exchange membrane fuel cell (PEMFC), catalyst layer, diffusion layer, local thermal nonequilibrium (LTNE)

1 Introduction

Study of fluid flow and heat transfer in a porous medium is a subject of continuous interest for decades because of the wide range of engineering applications such as solar receivers, building thermal insulation materials, packed bed heat exchangers, and energy storage units. Recently, the emerging field of fuel cell thermal management has received particular attention due to the rise of the importance of new energy technology. The gas diffusion electrode of a fuel cell is a typical porous medium. The heat dissipation by the electrochemical reaction in the active layer of a fuel cell should be removed thoroughly to keep proper operation. It not only optimizes an operating temperature range but also keeps a high uniformity of temperature distribution in the porous electrode. Therefore, a superior thermal management becomes critical for safely operating and prolonging a fuel cell.

A variety of analytical and/or numerical studies based on the assumption of local thermal equilibrium (LTE) have been conducted [1,2] to investigate the transport phenomena in the porous medium. Under the LTE assumption, the so-called one-equation model is employed to obtain the phase-mixing temperatures in the porous medium. It is simple and straightforward, but is applicable only if the temperature difference between the solid and the fluid phases is very small. When the temperature difference is significant, it becomes a local thermal nonequilibrium (LTNE). The one-equation model is not more valid, and should be modified with the two-equation model, which treats the solid-phase temperature and the fluid-phase temperature separately. An analysis of heat transfer in a porous medium based on the two-equation model is more involved because it requires interstitial information inside the porous medium such as heat transfer coefficient between the fluid and solid phases and the interfacial surface area [3–7]. Due to this difficulty, most investigations about the porous electrode of a fuel cell either used the one-equation model to obtain the phase-mixing temperatures [8–11] or did not consider thermal transports at all [12–16]. Up to the present time, quite a few efforts have ever been devoted to simultaneously predict the fluid and solid temperatures inside the porous electrode of a fuel cell in the open literature [17].

In the present study, an LTNE model is proposed to simulate the thermal-fluid transports in the porous electrode of a fuel cell. A multiphysics model coupling heat/mass transfer with electrochemical kinetics is developed. This model is capable of predicting the thermal-fluid and electrochemical behaviors, such as flow velocities, fluid/solid phase temperatures, reactant concentrations, and current densities in the porous electrode of fuel cells. Moreover, the heat/mass transfer mechanisms together with the thermal pathways in a fuel cell can be clearly identified. It would be beneficial for further accurate analyses of the fuel-cell thermal performance by considering the temperature-dependent physical properties inside a fuel cell. The present research along with [17] is the first attempt to develop an LTNE model to simultaneously predict the fluid and solid temperatures inside a porous electrode of a fuel cell.

2 Mathematical Numerical Model

The sectional view of a typical porous electrode in contact with an interdigitated flow field of a PEMFC is shown schematically in Fig. 1. Figure 2 shows the dimensions of the present computational module. The anodic reaction is neglected due to its fast kinetics [18]. Therefore, only the oxygen reduction reaction (ORR) on the cathode is considered [19] in the present model.

$$O_2 + 4H^+ + 4e^- \leftrightarrow 2H_2O \tag{1}$$

The oxygen-water vapor mixture enters the porous cathode form the module inlet (inlet channel), then transverses the diffusion layer to the catalyst layer. The electrochemical reaction occurring in the catalyst layer consumes the oxygen (C_{O_2}) and, meanwhile, produces the water vapor (C_{H_2O}). In addition, the heat generation (Q) due to the overpotential and irreversibility heating during the electrochemical reaction is removed by either the fluid or the solid.

The assumptions in this model include (i) mixtures are ideal gas, (ii) flow is steady, laminar, and incompressible (iii) thermal physical properties are constant, (iv) porous electrode is homoge-

Contributed by the Heat Transfer Division of ASME for publication in the JOURNAL OF HEAT TRANSFER. Manuscript received February 6, 2005; final manuscript received October 21, 2005. Review conducted by N. K. Anand.

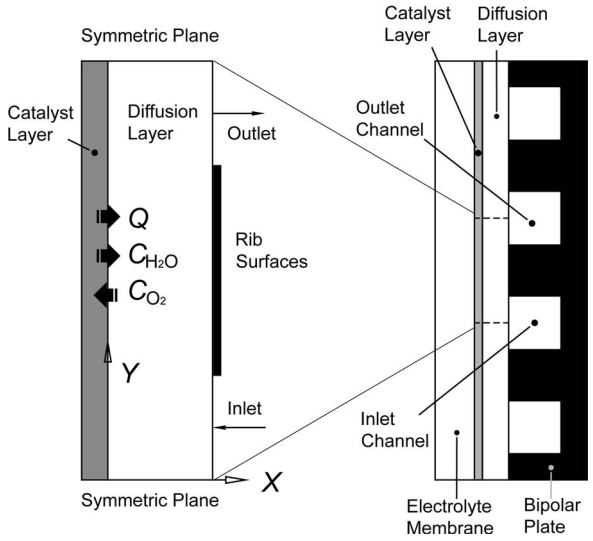

Fig. 1 Schematic drawing of porous electrode of the interdigitated flow field

neous and isotropic, (v) water exits as vapor only, and (vi) both inlet-fluid temperature and rib-surface temperature are uniform.

2.1 Governing Equations. In both diffusion and catalyst layers, the steady volume-averaged continuity and momentum equations that govern fluid flow are given by

$$\frac{\partial(\rho_f u)}{\partial x} + \frac{\partial(\rho_f v)}{\partial y} = S_\phi \tag{2}$$

$$\rho_f u\frac{\partial u}{\partial x} + \rho_f v\frac{\partial u}{\partial y} = -\frac{\partial p}{\partial x} + \mu\left(\frac{\partial^2 u}{\partial x^2} + \frac{\partial^2 u}{\partial y^2}\right) - \frac{\mu}{\kappa}\varepsilon u \tag{3}$$

Geometric parameters	Dimension
Module length	L=160μm
Catalyst layer thickness	δ_c =10μm
Diffusion layer thickness	δ=40μm
Channel width	$2W$=80μm
Shoulder width	Ws= 80μm

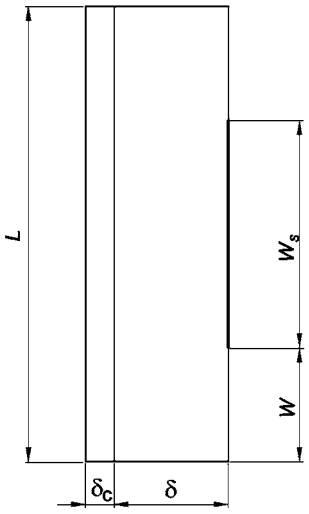

Fig. 2 Configuration of the computational domain

$$\rho_f u\frac{\partial v}{\partial x} + \rho_f v\frac{\partial v}{\partial y} = -\frac{\partial p}{\partial y} + \mu\left(\frac{\partial^2 v}{\partial x^2} + \frac{\partial^2 v}{\partial y^2}\right) - \frac{\mu}{\kappa}\varepsilon v \tag{4}$$

The last terms on the RHS of Eqs. (3) and (4) are the traditional Darcy dissipation which is used to account for the pressure drop due to viscous friction at the surfaces of carbon fibers.

As for the energy equations, the LTNE model is used to describe the thermal behavior in the diffusion layer. The energy equations for solid and fluid phases, respectively, are [5]

$$0 = k_{s,\text{eff}}\left(\frac{\partial^2 T_s}{\partial x^2} + \frac{\partial^2 T_s}{\partial y^2}\right) - h_s S_V(T_s - T_f) \tag{5}$$

$$(\rho c_p)_f u\frac{\partial T_f}{\partial x} + (\rho c_p)_f v\frac{\partial T_f}{\partial y} = k_{f,\text{eff}}\left(\frac{\partial^2 T_f}{\partial x^2} + \frac{\partial^2 T_f}{\partial y^2}\right) + h_s S_V(T_s - T_f) \tag{6}$$

The source term on the RHS of Eq. (6), $h_s S_V(T_s - T_f)$, means the convective heat transfer from the carbon fiber to the fluid, and vice versa for the source term in Eq. (5). The effective thermal conductivities of both phases are respectively defined as

$$k_{s,\text{eff}} = (1-\varepsilon)k_s \tag{7}$$

$$k_{f,\text{eff}} = \varepsilon k_f \tag{8}$$

In the catalyst layer, physically, the electrochemical reaction occurs at the interface of reactant (fluid) and catalyst (solid) under a fixed temperature. Therefore, the fluid and solid phases in the catalyst layer have the same local temperatures, i.e.,

$$T_f = T_s \tag{9}$$

$$(\rho c_p)_f u\frac{\partial T_f}{\partial x} + (\rho c_p)_f v\frac{\partial T_f}{\partial y} = k_{c,\text{eff}}\left(\frac{\partial^2 T_f}{\partial x^2} + \frac{\partial^2 T_f}{\partial y^2}\right) + j_T\eta \tag{10}$$

The source term $j_T\eta$ represents the overpotential heating by the electrochemical reaction. According to the Butler-Volmer correlation [20], the relationship between the local transfer current density and the reactant concentrations can be described as the following equation;

$$j_T = \alpha_1\left(\frac{c_{O_2}}{c_{O_2,\text{ref}}}\right) - \alpha_2\left(\frac{c_{H_2O}}{c_{H_2O,\text{ref}}}\right)^2 \tag{11}$$

α_1 and α_2 are electrochemical coefficients depending on the exchange current density and the overpotential on the electrode surfaces. They are regarded as constants in the present model. The effective thermal conductivity of the catalyst layer can be determined by the following equation [21]

$$k_{c,\text{eff}} = -2k_c + \frac{1}{\dfrac{\varepsilon_C}{2k_c + k_f} + \dfrac{1-\varepsilon_C}{3k_c}} \tag{12}$$

where k_c is the weight-averaged conductivity between the ionic conductor (such as Nafion™) and the electric conductor (such as Pt/C). ε_C is the porosity of the catalyst layer.

In the catalyst layer, the energy equation is coupled with the species concentration (Eqs. (10) and (11)). Therefore, prior to solving the temperature distribution it is necessary to determine the species concentration distribution in the porous electrode. The species transports of the oxygen and water vapor in the porous cathode can be governed by the following equations

$$u\frac{\partial c_{O_2}}{\partial x} + v\frac{\partial c_{O_2}}{\partial y} = D_{O_2,\text{eff}}\left(\frac{\partial^2 c_{O_2}}{\partial x^2} + \frac{\partial^2 c_{O_2}}{\partial y^2}\right) + S_{O_2} \tag{13}$$

Table 1 Governing equations of the present model

	Equations	S_Φ: Diffusion layer	S_Φ: Catalyst layer	Eq.
Mass	$\frac{\partial U}{\partial X}+\frac{\partial V}{\partial Y}=S_\Phi$	0	S_Φ	(17)
Momentum	$U\frac{\partial U}{\partial X}+V\frac{\partial U}{\partial Y}=-\frac{\partial P}{\partial X}+\frac{1}{\mathrm{Re}}\left(\frac{\partial^2 U}{\partial X^2}+\frac{\partial^2 U}{\partial Y^2}\right)+S_\Phi$	$-\frac{1}{\mathrm{Re\,Da}}\varepsilon U$	$-\frac{1}{\mathrm{Re\,Da}}\varepsilon_C U$	(18)
	$U\frac{\partial V}{\partial X}+V\frac{\partial V}{\partial Y}=-\frac{\partial P}{\partial Y}+\frac{1}{\mathrm{Re}}\left(\frac{\partial^2 V}{\partial X^2}+\frac{\partial^2 V}{\partial Y^2}\right)+S_\Phi$	$-\frac{1}{\mathrm{Re\,Da}}\varepsilon V$	$-\frac{1}{\mathrm{Re\,Da}}\varepsilon_C V$	(19)
Energy, diffusion layer	$0=\frac{\partial^2\theta_s}{\partial X^2}+\frac{\partial^2\theta_s}{\partial Y^2}+S_\Phi$	$\mathrm{Bi}(\theta_f-\theta_s)$	⋯	(20)
	$U\frac{\partial\theta_f}{\partial X}+V\frac{\partial\theta_f}{\partial Y}=\frac{1}{\mathrm{Re\,Pr_{eff}}}\left(\frac{\partial^2\theta_f}{\partial X^2}+\frac{\partial^2\theta_f}{\partial Y^2}\right)+S_\Phi$	$\mathrm{St}(\theta_s-\theta_f)$	⋯	(21)
Energy, catalyst layer	$\theta_s=\theta_f$	⋯	⋯	(22)
	$U\frac{\partial\theta_f}{\partial X}+V\frac{\partial\theta_f}{\partial Y}=\frac{1}{\mathrm{Re\,Pr_{eff}}}\left(\frac{\partial^2\theta_f}{\partial X^2}+\frac{\partial^2\theta_f}{\partial Y^2}\right)+S_\Phi$	⋯	$\frac{1}{\mathrm{Re\,Pr_{eff}}}[Ec_1 C_{\mathrm{O_2}}-Ec_2(C_{\mathrm{H_2O}})^2]$	(23)
Species	$U\frac{\partial C_{\mathrm{O_2}}}{\partial X}+V\frac{\partial C_{\mathrm{O_2}}}{\partial Y}=\frac{1}{\mathrm{Re\,Sc_{O_2}}}\left(\frac{\partial^2 C_{\mathrm{O_2}}}{\partial X^2}+\frac{\partial^2 C_{\mathrm{O_2}}}{\partial Y^2}\right)+S_\Phi$	0	$\frac{1}{\mathrm{Re\,Sc_{O_2}}}[R_{\mathrm{M1}}C_{\mathrm{O_2}}-R_{\mathrm{M2}}(C_{\mathrm{H_2O}})^2]$	(24)
	$U\frac{\partial C_{\mathrm{H_2O}}}{\partial X}+V\frac{\partial C_{\mathrm{H_2O}}}{\partial Y}=\frac{1}{\mathrm{Re\,Sc_{H_2O}}}\left(\frac{\partial^2 C_{\mathrm{H_2O}}}{\partial X^2}+\frac{\partial^2 C_{\mathrm{H_2O}}}{\partial Y^2}\right)+S_\Phi$	0	$\frac{1}{\mathrm{Re\,Sc_{H_2O}}}[R_{\mathrm{N1}}C_{\mathrm{O_2}}-R_{\mathrm{N2}}(C_{\mathrm{H_2O}})^2]$	(25)

$$u\frac{\partial c_{\mathrm{H_2O}}}{\partial x}+v\frac{\partial c_{\mathrm{H_2O}}}{\partial y}=D_{\mathrm{H_2O,eff}}\left(\frac{\partial^2 c_{\mathrm{H_2O}}}{\partial x^2}+\frac{\partial^2 c_{\mathrm{H_2O}}}{\partial y^2}\right)+S_{\mathrm{H_2O}} \quad (14)$$

In the catalyst layer, the source terms for oxygen transport and water-vapor transport are $S_{\mathrm{O_2}}=j_T/4F$ and $S_{\mathrm{H_2O}}=-(j_T/2F)$, respectively. In the diffusion layer they are nothing. The effective diffusivities of the oxygen and water vapor in the porous electrode, $D_{\mathrm{O_2,eff}}$ and $D_{\mathrm{H_2,eff}}$, follows the Bruggemann model [18], i.e.,

$$D_{\mathrm{O_2,eff}}=\varepsilon^\tau D_{\mathrm{O_2}} \quad (15)$$

$$D_{\mathrm{H_2O,eff}}=\varepsilon^\tau D_{\mathrm{H_2O}} \quad (16)$$

Using the nondimensional parameters of

$$X=\frac{x}{\delta},\quad Y=\frac{y}{\delta},\quad u_d=\frac{\dot m}{\rho_f A\varepsilon},\quad U=\frac{u}{u_d},\quad V=\frac{v}{u_d}$$

$$P=\frac{p}{\rho_f u_d^2},\quad C_{\mathrm{O_2}}=\frac{c_{\mathrm{O_2}}}{c_{\mathrm{tot}}},\quad C_{\mathrm{O_2,ref}}=\frac{c_{\mathrm{O_2,ref}}}{c_{\mathrm{tot}}}$$

$$C_{\mathrm{H_2O}}=\frac{c_{\mathrm{H_2O}}}{c_{\mathrm{tot}}},\quad C_{\mathrm{H_2O,ref}}=\frac{c_{\mathrm{H_2O,ref}}}{c_{\mathrm{tot}}},\quad \theta=\frac{T-T_r}{T_{f,\mathrm{in}}-T_r}$$

$$\mathrm{Re}=\frac{u_d\delta}{\nu},\quad \mathrm{Da}=\frac{\kappa}{\delta^2},\quad \mathrm{Pr_{eff}}=\frac{\mu(c_p)_f}{k_{f,\mathrm{eff}}},\quad \mathrm{Bi}=\frac{h_s S_V\delta^2}{k_{s,\mathrm{eff}}}$$

$$\mathrm{St}=\frac{h_s S_V\delta}{(\rho c_p)_f u_d},\quad \mathrm{Sc_{O_2}}=\frac{\nu}{D_{\mathrm{O_2,eff}}}$$

$$\mathrm{Sc_{H_2O}}=\frac{\nu}{D_{\mathrm{H_2O,eff}}},\quad R_{M1}=\frac{\alpha_1\delta^2}{4Fc_{\mathrm{tot}}D_{\mathrm{O_2,eff}}}$$

$$R_{M2}=\frac{\alpha_2\delta^2}{4Fc_{\mathrm{tot}}D_{\mathrm{O_2,eff}}},\quad R_{N1}=\frac{\alpha_1\delta^2}{2Fc_{\mathrm{tot}}D_{\mathrm{H_2O,eff}}}$$

$$R_{N2}=\frac{\alpha_2\delta^2}{2Fc_{\mathrm{tot}}D_{\mathrm{H_2O,eff}}},\quad R_k=\frac{k_{f,\mathrm{eff}}}{k_{s,\mathrm{eff}}},\quad Ec_1=\frac{\alpha_1\eta\delta^2}{k_{s,\mathrm{eff}}(T_{f,\mathrm{in}}-T_r)C_{\mathrm{O_2,ref}}}$$

and

$$Ec_2=\frac{\alpha_2\eta\delta^2}{k_{s,\mathrm{eff}}(T_{f,\mathrm{in}}-T_r)C^2_{\mathrm{H_2O,ref}}},$$

the above governing equations can be deduced to dimensionless forms of Table 1.

2.2 Boundary Conditions. Conditions for the boundaries of the present computational domain can be summarized as follows.

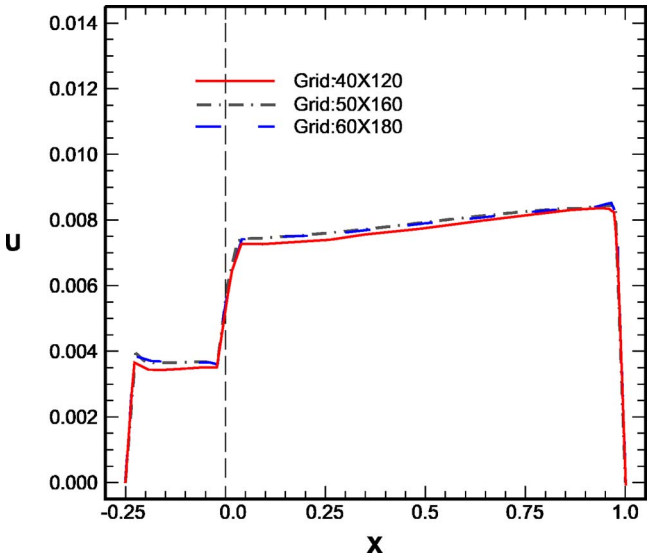

Fig. 3 Grid test by comparing the axial velocity at $Y=2.0$

1. At the module inlet,

$$P = P_{\text{in}}, \quad \theta_f = \theta_{f,\text{in}}, \quad \frac{\partial \theta_s}{\partial X} = \text{Bi}(\theta_s - \theta_f)$$

$$C_{O_2} = C_{O_2,\text{in}}, \quad C_{H_2O} = C_{H_2O,\text{in}} \tag{26}$$

2. At the rib (current collector) surfaces,

$$\frac{\partial P}{\partial X} = 0, \quad U = V = 0, \quad \theta_s = 1$$

$$\frac{\partial \theta_f}{\partial X} = \text{St}(\theta_s - \theta_f), \quad \frac{\partial C_{O_2}}{\partial X} = \frac{\partial C_{H_2O}}{\partial X} = 0 \tag{27}$$

3. At the interface of the membrane and the catalyst layer ($X=-0.1$),

$$U = V = 0, \quad \frac{\partial P}{\partial X} = \frac{\partial \theta_s}{\partial X} = \frac{\partial \theta_f}{\partial X} = \frac{\partial C_{O_2}}{\partial X} = \frac{\partial C_{H_2O}}{\partial X} = 0 \tag{28}$$

4. At the symmetric planes

$$\frac{\partial P}{\partial Y} = \frac{\partial U}{\partial Y} = \frac{\partial V}{\partial Y} = \frac{\partial \theta_s}{\partial Y} = \frac{\partial \theta_f}{\partial Y} = \frac{\partial C_{O_2}}{\partial Y} = \frac{\partial C_{H_2O}}{\partial Y} = 0 \tag{29}$$

5. At the module outlet,

$$P = P_{\text{out}}, \quad \frac{\partial \theta_f}{\partial X} = 0, \quad \frac{\partial \theta_s}{\partial X} = \text{Bi}(\theta_s - \theta_f), \quad \frac{\partial C_{O_2}}{\partial X} = \frac{\partial C_{H_2O}}{\partial X} = 0 \tag{30}$$

2.3 Numerical Methods. The governing equations are numerically solved by the control-volume-based finite element method. The discretization procedure as well as the numerical scheme has been described in detailed elsewhere [22], and is not elaborated on here. In the present work, all computations are performed on 503,160 (X by Y) structured, orthogonal meshes. Additional runs for the coarser meshes, 403,120, and the finer meshes, 603,180, are taken for a check of grid independence. As shown in Fig. 3, the maximum discrepancy in the axial velocity at $Y=2.0$ between the grid sizes of 503,160 and 603,180 is only 0.6%. In addition, results indicate a maximum change of 0.6% in wall temperature distribution between the solutions of 503,160 and 603,180 grids. All of the above discrepancies are so small that the accuracy of the solutions on a 503,160 grid is deemed satisfactory. A typical simulation requires about 200 min of central processing unit time on a Pentium IV 2.8 GHz PC.

3 Results and Discussion

3.1 Prior to Predictions. Two important issues should be clarified before the subsequent presentation and discussion of the predicted results, i.e., variation (or typical values) of the parameters and validation of the model.

To perform a practical simulation of thermal behaviors in a fuel cell, a realistic operation condition of fuel cells should be known. Table 2 summarizes the physical, geometric, and flow prosperities of a typical porous electrode of a PEMFC. Most data in the table are from the manufacturer and the textbook. Some of them are assumed, such as the flow properties of interstitial heat transfer coefficient (h_s) and surface-to-volume ratio (S_V). In addition, from the data listed in Table 2, typical values or ranges of the nondimensional parameters can be calculated. For example, the Reynolds number based on the pore velocity and the diffusion layer thickness becomes

$$\text{Re} = \frac{u_d \delta}{\nu} = \frac{0.239 \cdot 400 \times 10^{-6}}{1.586 \times 10^{-5}} = 6$$

which is typical in the following predictions.

Up to the present time, it is hard to measure the local temperature inside the porous electrode of a fuel cell. Strictly speaking, no data about the local thermal-fluid characteristics such as local temperatures and heat transfer coefficients inside the porous electrode of a fuel cell are available in the open literature. Therefore, a macroscopic comparison of polarization curve is made between the present predictions and previous experiments [23], which have been widely used to verify a fuel cell simulation model. Figure 4 compared the predicted polarization curves with the measured ones. The cell potential in the experiment is measured directly, while in the present prediction the cell potential, neglecting the overpotential on the anode side, is calculated as

$$V_{\text{cell}} = V_{\text{OC}} - \eta - I \cdot R_\Omega \tag{31}$$

where the Ohmic resistance, R_Ω, is set to a constant value of $0.2\ \Omega \cdot \text{cm}^2$ through the electrode, which is a typical value measured in the experiment [24]. Generally speaking, the agreement for the comparison above is satisfactory, indicating that the results obtained by the present computation are reliable.

3.2 Velocity Distributions. Figure 5 shows the distribution of flow velocity magnitude, $(U^2+V^2)^{1/2}$, at several Y stations in the porous electrode. The Reynolds number and Darcy number are fixed at $\text{Re}=6$ and $\text{Da}=9.83\times10^{-6}$, respectively. It is seen that the velocities are higher in the diffusion layer than in the catalyst layer. This is because a higher porosity and a higher permeability are accompanied by the diffusion layer (Table 2). In addition, the velocities near the shoulder surface ($X=0.4$) are higher than those adjacent to the catalyst layer. It is reasonable because the flow paths from the inlet channel to the outlet channel are shorter for the flow closer to the shoulder surface. A shorter flow path has a lower pressure-drop penalty, which allows more fluids to pass through. The effect of Reynolds number on the velocity distributions at module middle ($Y=2.0$) is shown in Fig. 6. It is seen that the velocity increases with increasing Reynolds number in both catalyst and diffusion layers.

3.3 Porous Matrix Temperatures. Figures 7–9 compare the distributions of the fluid-phase temperature (θ_f) and the solid-phase temperature (θ_s) along the X direction at several Y stations ($Y=0.5$, 2.0, 2.8, and 3.6) in the porous electrode under various Stanton numbers. The Reynolds number and Darcy number are fixed at $\text{Re}=6$, and $\text{Da}=9.83\times10^{-6}$, respectively.

In Fig. 7, clearly, both solid and fluid phases have the same temperatures in the catalyst layer ($-0.25<X<0$). It starts with a

Table 2 Porous electrode data sheet

Property name		Solid phase	Fluid phase
Physical properties[a]	Material	Carbon fiber	Oxygen
	Bulk density, ρ	1100 kg/m^3	1.13 kg/m^3
	Specific resistance, σ^{-1}	115 $\mu\Omega$ m	···
	Thermal conductivity, k	1.71 W/m K[c]	0.0268 W/m K
	Coeff. of thermal expansion, β	9.03×10^{-7}/K	3.333×10^{-3}/K
	Viscosity, ν	···	1.5863×10^{-5} m^2/s
	Thermal diffusivity, α_f	···	2.2353×10^{-5} m^2/s
Geometric properties	Diffusion layer porosity, ε	48%	
	Catalyst layer porosity, ε_C	42%	
	Diffusion layer thickness, δ	400 μm	
	Catalyst layer thickness, δ_C	100 μm	
	Diffusion layer tortuosity, τ	1.5	
	Catalyst layer tortuosity, τ	1.5	
	Average pore diameter, d	33 μm	
	Diffusion layer permeability, κ[b]	1.573×10^{-12} m^2	
	Catalyst layer permeability, κ_C[b]	1.023×10^{-12} m^2	
Flow properties	Interstitial heat transfer coefficient, h_s	100–1000 W m^{-2} (assumed)	
	Surface-to-volume ratio, S_V	1.03×10^3–1.03×10^6 m^{-1} (assumed)	
	Pore velocity, u_d for I=1.0–3.0 A at stoichiometric flow ratio 5	0.239–0.717 m/s	
Nondimensional parameters	Conductivity ratio, R_k	0.01447	
	Prandtl number, Pr	0.709	
	Reynolds number, Re$_d$	6	
	Stanton number, St	1.39 (h_s=100 W m^{-2} and S$_V$=10,000 m^{-1})	

[a]Data from manufacture (Toray).
[b]ASTM E1530.
[c]Oxygen at 25°C with 15% RH, p=0.15 atm, plate thickness: 2.5 cm, 51 l/m^2 s.

local maximum value at the interface of the catalyst layer and the electrolyte membrane ($X=-0.25$), decreases slightly and then drops sharply as it approaches the diffusion layer ($X=0$). In the diffusion layer, the fluid-phase and solid-phase temperatures separate from $X=0$ due to the LTNE effect. At the station of $Y=0.5$, a low fluid-phase temperature from the module inlet ($X=1.0$) increases linearly as the flow approaches the catalyst layer ($X=0$). Meanwhile, the solid-phase temperature decreases along the X direction from the interface of the catalyst layer and the diffusion layer ($X=0$) to the module inlet ($X=1.0$). During this stage, the hot solid-matrix transfers a part of heat to the cold fluid via convection (h_s). At the middle of the module, i.e., $Y=2.0$, the solid-phase temperatures decrease sharply and linearly from $X=0$ to $X=1.0$, meaning that a large amount of heat passes through the solid matrix and then is removed out from the rib surface by conduction. It is interesting to note that this is the shortest conductive (solid-phase) pathway form the catalyst layer to the rib shoulder. At this station, the fluid-phase temperatures are higher

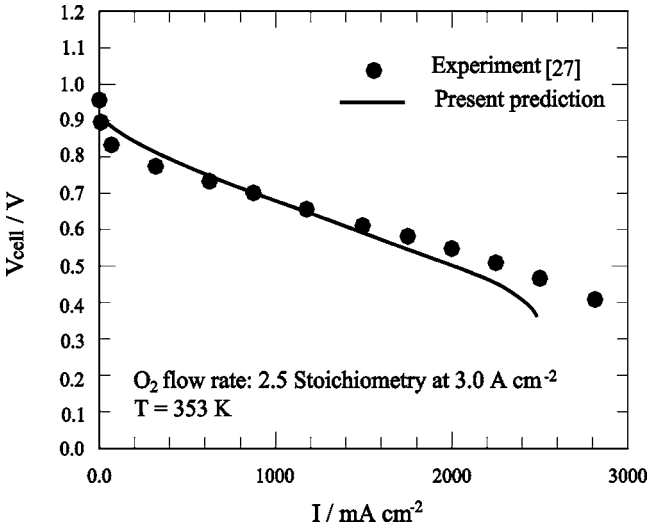

Fig. 4 Comparison of the present predictions with the experimental results

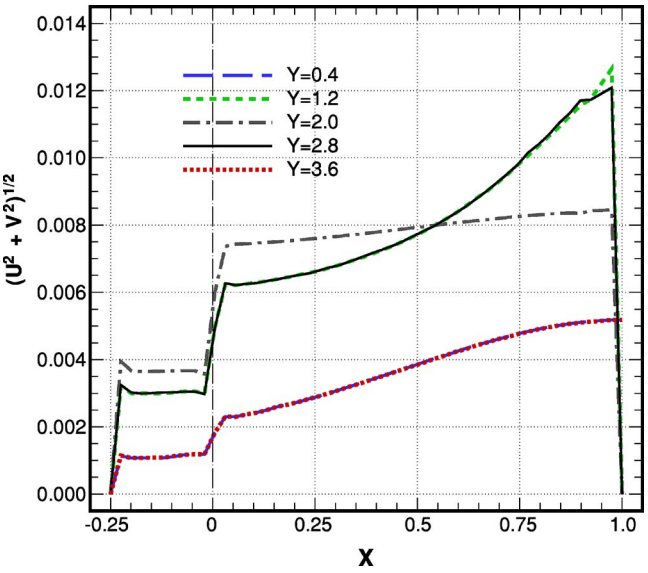

Fig. 5 Velocity magnitudes in the porous electrode at several Y stations, Da=9.83×10^{-6}, Re=10

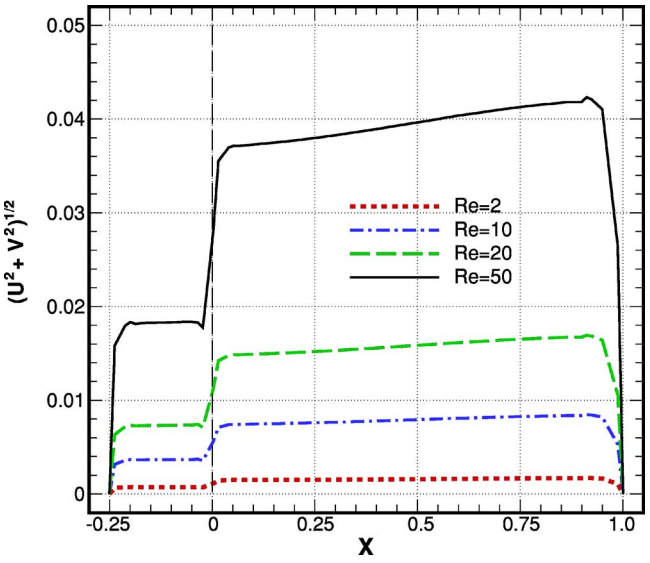

Fig. 6 Effect of Reynolds number on the velocity magnitude in the porous electrode, Da=9.83×10^{-6}

than the solid-phase ones. This indicates that the heat possessed with the high-temperature fluid not only is carried downstream by bulk motion but also is convected to the solid matrix, which is then conducted out through the rib surfaces. At the station of $Y=2.8$, the fluid-phase temperature is further elevated, while the solid-phase temperature distribution is puffed up a little in the middle region since the RHS boundary ($X=1.0$) is confided by a fixed temperature $\theta_s=1$. As for the cross-section cutting across the module outlet, i.e., $Y=3.6$, both the fluid-phase and solid-phase temperatures are significantly lifted up.

When the Stanton number increases to St=14.73, as shown in Fig. 8, the temperature difference between the solid and fluid phases has been narrowed down. This trend is more significant as the flow moves downstream. It means that the porous electrode approaches the local thermal equilibrium. As the Stanton number further increases to St=1.473×10^3, as shown in Fig. 9, the curves of the fluid-phase and solid-phase temperatures merge together, except for the region near the module inlet ($Y=0.5$, $0.8<X<1.0$). A large similarity in the temperature distribution between the solid phase and the fluid phase gives an indication that the thermal-fluid field in the porous electrode has become local thermal equilibrium.

3.4 Wall Temperature Distributions. Figures 10–12 show the temperature distributions along the interface of the electrolyte membrane and catalyst layer ($X=-0.25$), which is referred to as the wall temperature θ_w hereafter. Note that the wall temperature is always a local maximum temperature with respect to the X direction (see Figs. 7–9), As far as the fuel cell thermal management concern, to keep the maximum wall temperature within a reasonable range has a benefit of prolonging fuel cells, which requires a cooling scheme to ensure the removal of the heat dissipation by electrochemical reaction.

Figure 10 shows the effect of Stanton number on the wall temperature distribution along the Y direction. The Darcy number and Reynolds number are fixed at Da=9.83×10^{-6} and Re=6, respectively. It is clearly observed from this figure that the wall temperature decreases with increasing Stanton number. In addition, the maximum wall temperatures occur at the downstream end of the

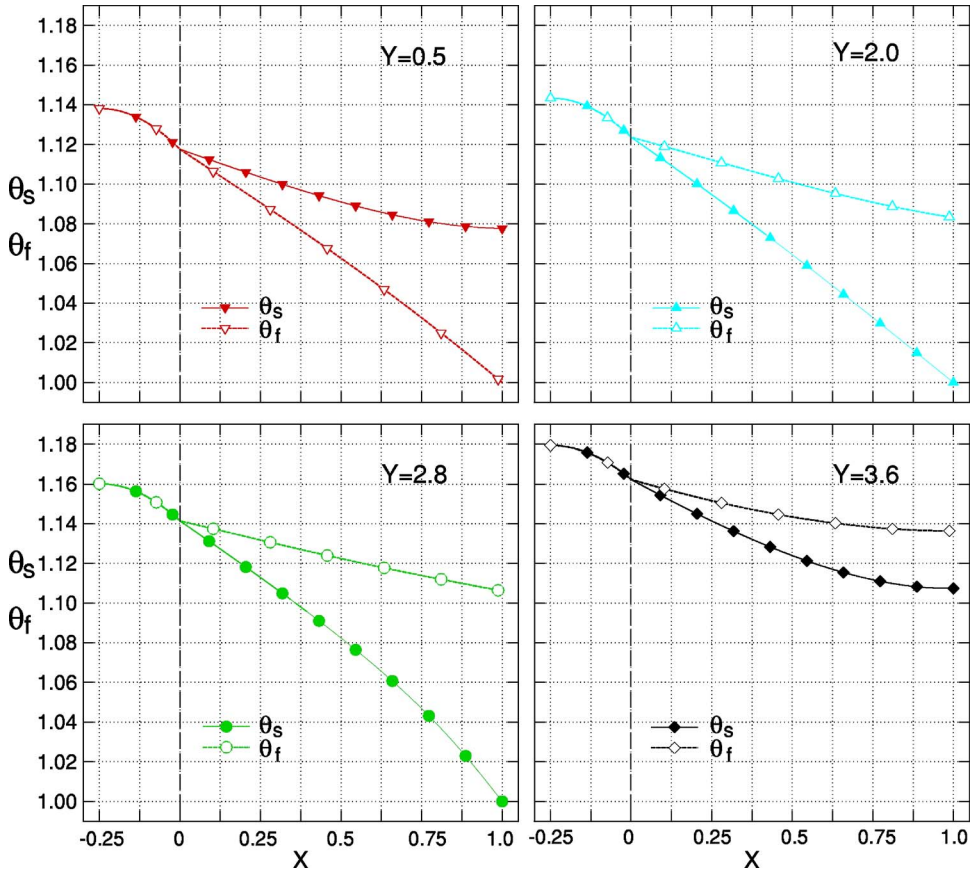

Fig. 7 Comparison of fluid-phase and solid-phase temperature distributions inside the porous electrode for Re=6, Da=9.83×10^{-6}, and St=0.74

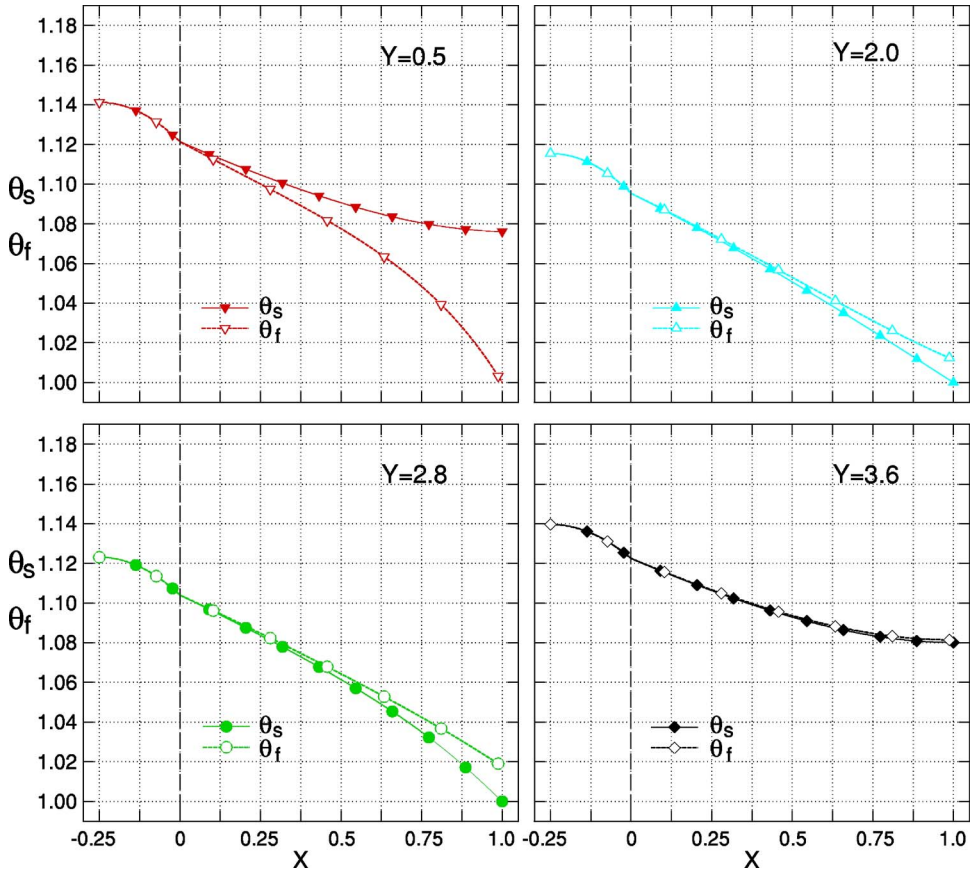

Fig. 8 Comparison of fluid-phase and solid-phase temperature distributions inside the porous electrode for Re=6, Da=9.83×10^{-6}, and St=14.73

module ($Y=1.6$). However, the locations of local minimum wall temperature depend on the Stanton numbers, which will be discussed later. In general, the wall temperature distributions can be sorted by three groups, depending on the magnetite of the Stanton number. The first group is collected under small Stanton numbers, $St \ll 1$ (St=0.0074, 0.0118, and 0.0147, open symbol lines). It is seen that the wall temperatures increase downstream monotonously and fall into a single curve almost. This trend is largely similar to a developing flow over a thermal flat plate. At a small value of Stanton number, the source terms of Eqs. (20) and (21) are neglected. Therefore, the thermal pathways of convection and conduction in the diffusion layer are independent. In other words, there is no heat transfer between the solid phase and the fluid phase due to drastically small interfacial heat transfer coefficients and/or surface area. The second group goes with the Stanton number around unity ($0.88 \leqslant St \leqslant 1.47$, broken lines). It starts with a little drop of wall temperature and then sharply increases downstream. As for the third group of curves ($1.473\times10^3 \leqslant St \leqslant 1.473\times10^4$, solid symbol lines), the wall temperature decreases first and then increases to a local maximum at the downstream end. A significant local minimum occurs at the module middle ($Y=0.8$). The effect of Reynolds number on the local wall temperature distributions at the Stanton number of $St=1.473\times10^3$ is further shown in Fig. 11. It is seen from this figure that the wall temperature at the upstream half module decreases with increasing Reynolds number, but is not affected by the Reynolds number at the downstream half module. The wall temperature distributions are roughly symmetrical about the local minimum at the module middle ($Y=0.8$) where it faces the cold shoulder (rib) surface. A valley distribution of wall temperature gives an indication that the conduction dominates the thermal transport in the porous medium.

Under LTNE conditions (St=1.03), as shown in Fig. 12, the wall temperature distribution separates from $Y=0.2$ as the Reynolds number varies. The wall temperature decreases with increasing Reynolds number. It is clear from this figure that the wall temperature distribution neither has a large valley in the module middle nor increases downstream monotonously. This trend shows a mixed thermal-transport mode in combination of convection and conduction in the porous electrodes of fuel cells.

3.5 Species Concentration Distributions. The oxygen and water-vapor concentration distributions along the X direction at several Y stations in the porous electrode are shown in Figs. 13 and 14, respectively. The composition of the oxygen-water vapor mixture at the module inlet is $C_{O_2}=0.9$ and $C_{H_2O}=0.1$. The Reynolds number and Stanton number are fixed Re=6 and St=0.74, respectively. It is seen from Fig. 13 that at the station cutting across the module inlet, i.e., $Y=0.4$, high-concentrated oxygen from the module entrance ($X=1.0$) decreases as the flow moves closely to the catalyst layer. The inclination of C_{O_2} curves decreases as the flow moves downstream. It is further seen from Figs. 13 and 14 that the oxygen/water vapor concentration decreases/increases along the Y direction due to the ORR on the reaction surface. The lowest values of C_{O_2} are found at the interface between the catalyst layer and the electrolyte membrane ($X=-0.25$). The C_{H_2O} distributions shown in Fig. 14 just compensate for those of C_{O_2}. It increases along the flow direction due to the convective accumulation downstream of the water vapor generated in the catalyst layer.

4 Conclusions

Detailed heat transfer characteristics inside a fuel cell porous electrode in contact with a typical interdigitated flow field have

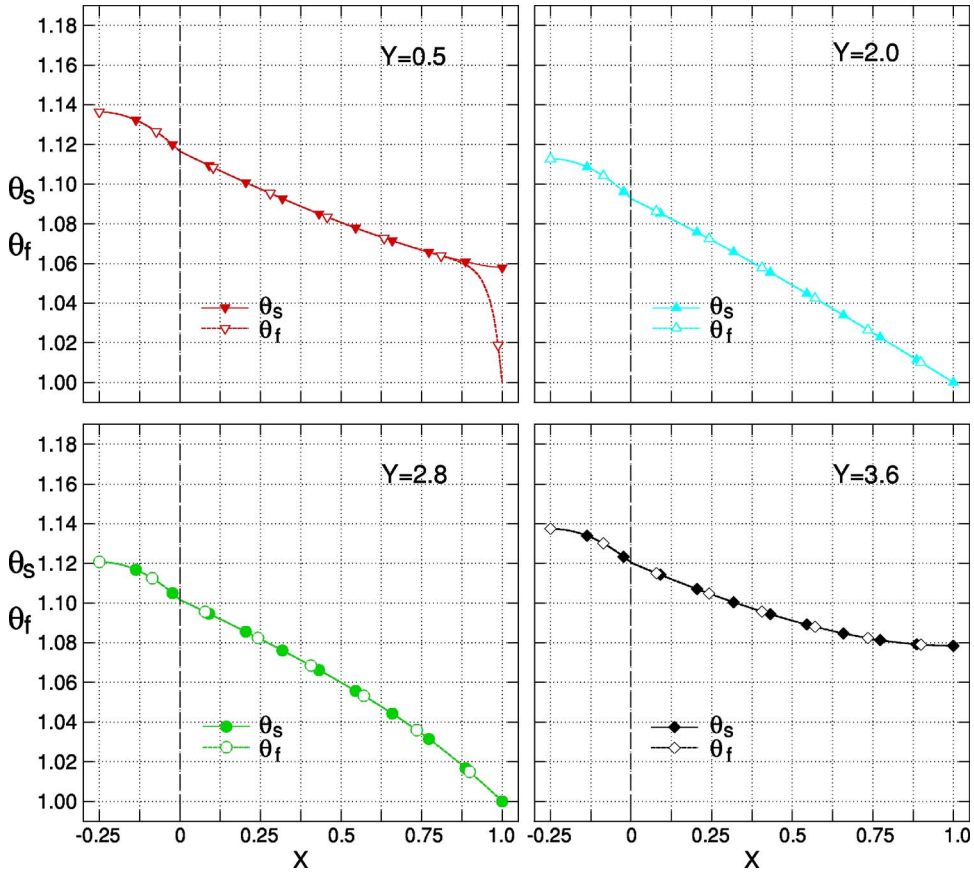

Fig. 9 Comparison of fluid-phase and solid-phase temperature distributions inside the porous electrode for Re=6, Da=9.83×10^{-6}, and St=1.473×10^{3}

been studied numerically. A two-dimensional multiphysics model coupling heat/mass transfer with electrochemical kinetics has been performed to simulate thermal-fluid/species transports inside a porous electrode of a fuel cell. In thermal analysis, the local thermal nonequilibrium (LTNE) model is first implemented to investigate the heat transfer in the fuel cell porous electrode. In species transports, the Bruggemann model is employed to describe the effective diffusivities of the oxygen and water vapor in the porous electrode of a fuel cell. Results show that the wall temperature decreases with increasing Stanton number. The local maximum wall temperature always occurs at the downstream end of the module, while the location of the local minimum depends on the Stanton number. Three categories of thermal-fluid behaviors in the porous electrode have been characterized according to

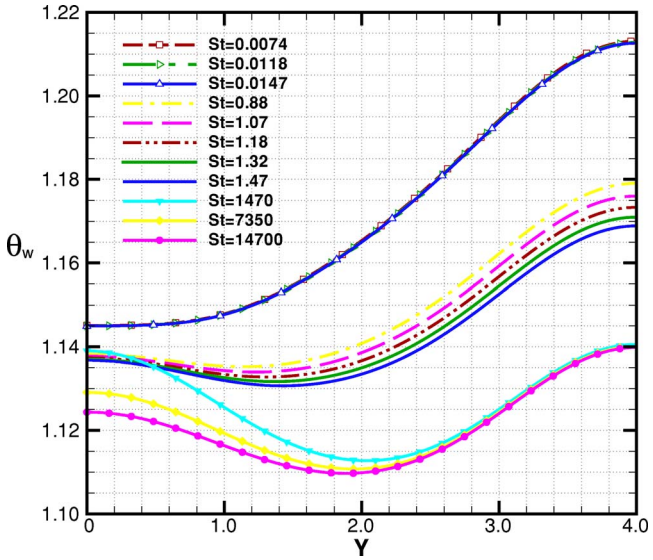

Fig. 10 Effect of Stanton number on the wall temperature distributions for Da=9.83×10^{-6}, and Re=6

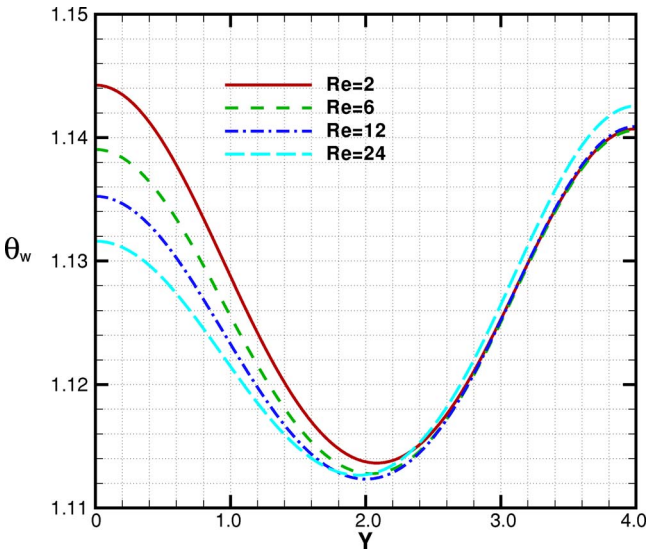

Fig. 11 Effect of Reynolds number on the wall temperature distributions for Da=9.83×10^{-6} and St=1.473×10^{3}

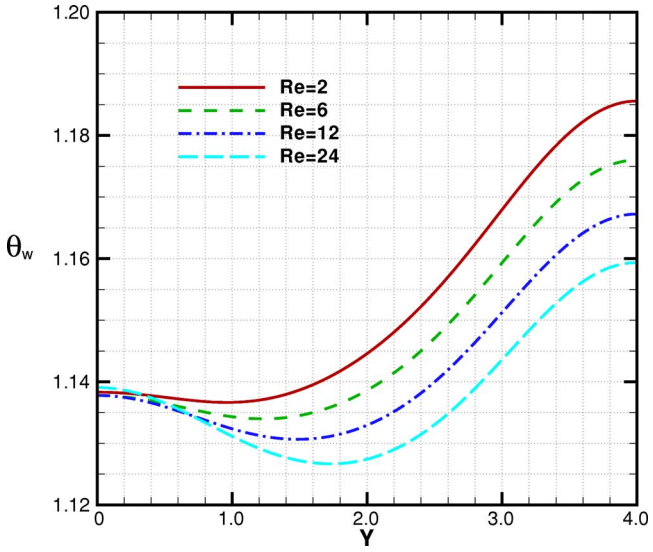

Fig. 12 Effect of Reynolds number on the wall temperature distributions for Da=9.83×10^{-6} and St=1.03

the numerical results. The solid phase and fluid phase in the diffusion layer are thermally independent for a small value of Stanton number (St≪1). As the Stanton number approaches unity, the porous electrode becomes local thermal nonequilibrium (LTNE) with a strong thermal interaction (heat transfer) between the solid and fluid phases. Under the conditions of St≫1, the porous electrode is local thermal equilibrium.

Acknowledgment

This work was partly sponsored by the National Science Council of the Taiwan, ROC under Contract No. NSC 92-2212-E-451-002.

Nomenclature

Bi = Biot number
d = pore diameter of the porous medium, m
c_{H_2O} = water vapor mole concentration, mol m^{-3}
$c_{H_2O,ref}$ = water vapor mole concentration at inlet, mol m^{-3}
C_{H_2O} = normalized water vapor concentration, c_{H_2O}/c_{tot}
$C_{H_2O,ref}$ = normalized water vapor mole concentration at inlet, $c_{H_2O,ref}/c_{tot}$
c_{O_2} = oxygen concentration, mol m^{-3}
$c_{O_2,ref}$ = oxygen mole concentration at inlet, mol m^{-3}
C_{O_2} = normalized oxygen concentration, c_{O_2}/c_{tot}
$C_{O_2,ref}$ = normalized oxygen mole concentration at inlet, $c_{O_2,ref}/c_{tot}$
c_p = specific heat at constant temperature, J kg^{-1} K^{-1}
c_{tot} = total mole concentration of the reacting fluid, mol m^{-3}
D_{H_2O} = binary diffusivity of water vapor in the oxygen, m^2 s^{-1}
$D_{H_2O,eff}$ = effective diffusivity of water vapor in the gas diffusion layer, m^2 s^{-1}
D_{O_2} = binary diffusivity of oxygen in the water vapor, m^2 s^{-1}
$D_{O_2,eff}$ = effective diffusivity of oxygen in the gas diffusion layer, m^2 s^{-1}
Da = Darcy number
Ec_1, Ec_2 = coefficients in Eq. (23)
F = Faraday's constant, 96,487 C mol^{-1}
I = current, A
h_s = interstitial heat transfer coefficient in the porous medium, W m^{-2} K^{-1}
k = thermal conductivity, W m^{-1} K^{-1}
L = length of the computational domain, m
$\dot{m}$ = mass flux, kg m^{-2} s^{-1}
p = pressure, Pa
P = nondimensional pressure
Pr = Prandtl number
Q = heat dissipation by the electrochemical reaction, W
Re = Reynolds number
R_{M1}, R_{M2} = coefficients in Eq. (24)
R_{N1}, R_{N2} = coefficients in Eq. (25)

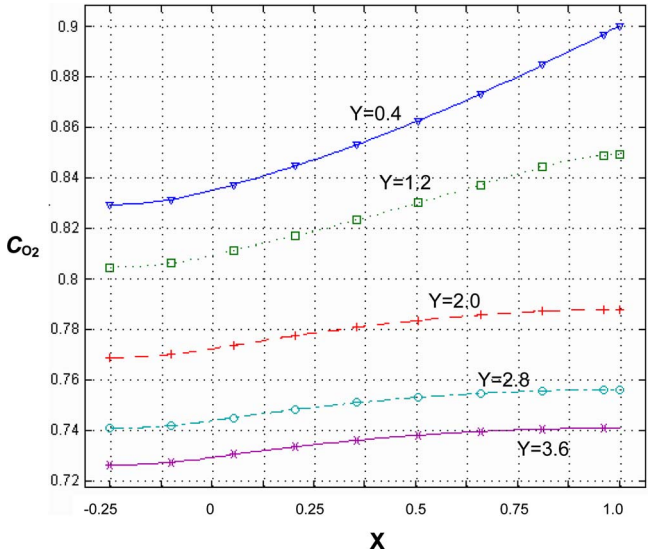

Fig. 13 Oxygen concentration distributions of along the reaction surfaces, Re=6, Da=9.83×10^{-6}, and St=0.74

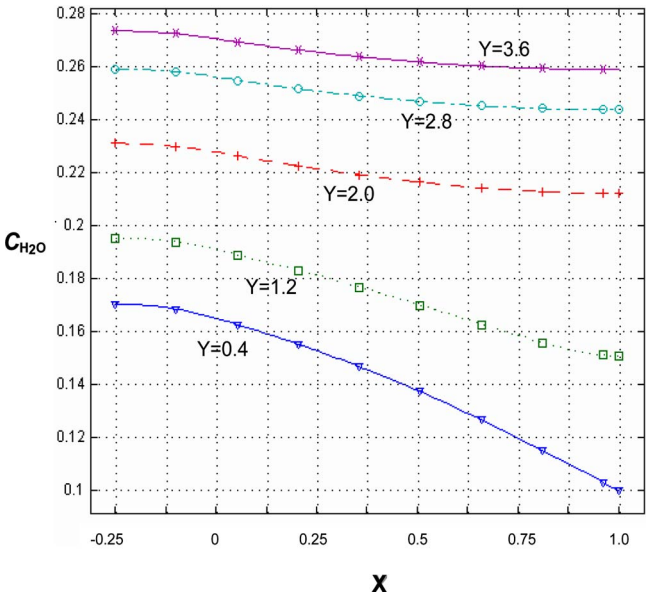

Fig. 14 Water vapor concentration distributions of along the reaction surfaces, Re=6, Da=9.83×10^{-6}, and St=0.74

R_ς = Ohmic resistance, ς
S_V = surface area-to-volume ratio, m^{-1}
Sc = Schmidt number
St = Stanton number
S_Φ = nondimensional source term
S_ϕ = source term
T = temperature, K
u,v = velocity components in the x and y directions, respectively, m s^{-1}
U,V = nondimensional velocity components in the x and y direction
V_{cell} = cell voltage, V
V_{oc} = open circuit voltage, V
x,y = coordinate system, m
X,Y = nondimensional x and y coordinate

Greek Symbols

α_1, α_2 = coefficients in Eq. (11)
δ = thickness of the diffusion layer, m
δ_C = thickness of the catalyst layer, m
ε = porosity of the diffusion layer
ε_C = porosity of the catalyst layer
κ = permeability, m^2
ρ = density, kg m^3
η = cathodic overpotential, V
θ = nondimensional temperature
τ = tortuosity

Subscript

C = catalyst layer
D = diffusion layer
eff = effective
f = fluid phase
in = inlet
loc = local
o = oxygen
out = outlet
r or ref = reference
s = solid phase
tot = total

References

[1] Quintard, M., and Whitaker, S., 1995, "Local Thermal Equilibrium for Transient Heat Conduction: Theory and Comparison With Numerical Experiments," Int. J. Heat Mass Transfer, **38**, pp. 2779–2796.
[2] Sahraoui, M., and Kaviany, M., 1994, "Slip and No-Slip Temperature Boundary Condition at the Interface of Porous, Plain Media: Convection," Int. J. Heat Mass Transfer, **37**, pp. 1029–1044.
[3] Quintard, M., and Whitaker, S., 2000, "Theoretical Modeling of Transport in Porous Media," *Handbook of Heat Transfer in Porous Media*, 1st ed., K. Vafai, ed., Decker, New York.
[4] Kaviany, M., 1995, *Principles of Heat Transfer in Porous Media*, 2nd ed., Springer, Berlin.
[5] Hwang, J. J., Hwang, G. J., Yeh, R. H., and Chao, C. H., 2002, "Measurement of Interstitial Convective Heat Transfer and Fictional Drag for Flow Across Metal Foams," ASME J. Heat Transfer, **124**, pp. 120–129.
[6] Alazmi, B., and Vafai, K., 2002, "Constant Wall Heat Flux Boundary Conditions in Porous Media Under Local Thermal Non-Equilibrium Conditions," Int. J. Heat Mass Transfer, **45**, pp. 3071–3087.
[7] Alazmi, B., and Vafai, K., 2004, "Analysis of Variable Porosity, Thermal Dispersion, and Local Thermal Non-equilibrium on Free Surface Flows Through Porous Media," ASME J. Heat Transfer, **126**, pp. 389–399.
[8] Bernardi, D. M., and Verbrugge, M. W., 1991, "Mathematical Model of a Gas Diffusion Electrode Bonded to a Polymer Electrolyte," Am. Inst. Chem. Eng. Symp. Ser., **37**, pp. 1151–1163.
[9] Springer, T. E., Zawodzinski, T. A., and Gottesfeld, S., 1991, "Polymer Electrolyte Fuel Cell Model," J. Electrochem. Soc., **138**(8), pp. 2334–2342.
[10] Nguyen, T. V., and White, R. E., 1993, "A Water and Heat Management Model for Proton-Exchange-Membrane Fuel Cells," J. Electrochem. Soc., **140**(8), pp. 2178–2186.
[11] Ackmann, T., de Haart, L. G. J., Lehnert, W., and Stolten, D., 2003, "Modeling of Mass and Heat Transport in Planar Substrate Type SOFCs," J. Electrochem. Soc., **150**, pp. A783–A789.
[12] Yuan, J., Rokni, M., and Sunden, B., 2003, "Three-Dimensional Computational Analysis of Gas and Heat Transport Phenomena in Ducts Relevant for Anode-Supported Solid Oxide Fuel Cells," Int. J. Heat Mass Transfer, **46**, pp. 809–821.
[13] Yi, J. S., and Nguyen, T. V., 1998, "An Along the Channel Model for Proton Exchange Membrane Fuel Cells," J. Electrochem. Soc., **145**, pp. 1149–1159.
[14] Dutta, S., Shimpalee, S., and Van Zee, J. W., 2001, "Numerical Prediction of Mass-Exchange Between Cathode and Anode Channels in a PEM Fuel Cell," Int. J. Heat Mass Transfer, **44**, pp. 2029–2042.
[15] Ju, H., and Wang, C. Y., 2004, "Experimental Validation of a PEM Fuel Cell Model by Current Distribution Data," J. Electrochem. Soc., **151**, pp. A1954–A1960.
[16] Um, S., and Wang, C. Y., 2004, "Three-Dimensional Analysis of Transport and Electrochemical Reactions in Polymer Electrolyte Fuel Cells," J. Power Sources, **125**, pp. 40–51.
[17] Hwang, J. J., 2006, "Thermal-Electrochemical Modeling of a PEM Fuel Cell," J. Electrochem. Soc., **153**, pp. A216–A224.
[18] Meredith, R. E., and Tobias, C. W., 1962, in *Advances in Electrochemistry and Electrochemical Engineering*, *2*, C. W. Tobias, ed., Interscience, New York.
[19] Hwang, J. J., Chen, C. K., Savinell, R. F., Liu, C. C., and Wainright, J., 2004, "A Three-Dimensional Numerical Simulation of the Transport Phenomena in the Cathodic Side of a PEMFC," J. Appl. Electrochem., **34**, pp. 217–224.
[20] Oldham, H., and Myland, J., 1994, *Fundamentals of Electrochemical Science*, Academic, New York.
[21] Hwang, J. J., Chen, C. K., and Lai, D. Y., 2005, "Detailed Characteristic Comparison Between Planar and MOLB-Type Sofcs," J. Power Sources, **143**, pp. 75–83.
[22] Hwang, J. J., Chao, C. H., Ho, W. Y., Chang, C. L., and Wang, D. Y., 2005, "Effect of Flow Orientation on the Thermal-Electrochemical Transports in a PEM Fuel Cell," J. Power Sources (in press).
[23] Hwang, J. J., Lo, K. H., Wang, S. H., and Tsay, K. C., 2001, The 25th Conference on Theoretical and Applied Mechanics, Taichung, Taiwan, ROC.
[24] Hwang, J. J., and Hwang, H. S., 2002, "Parametric Studies of a Double-Cell Stack of PEMFC Using Grafoil Flow-Field Plates," J. Power Sources, **104**, pp. 24–32.

A Correlation for Interfacial Heat Transfer Coefficient for Turbulent Flow Over an Array of Square Rods

Marcelo B. Saito

Marcelo J. S. de Lemos[1]
Mem. ASME
e-mail: delemos@ita.br

Departamento de Energia - IEME,
Instituto Tecnológico de Aeronáutica - ITA,
12228-900 - São José dos Campos - SP, Brazil

Interfacial heat transfer coefficients in a porous medium modeled as a staggered array of square rods are numerically determined. High and low Reynolds k-ϵ turbulence models are used in conjunction of a two-energy equation model, which includes distinct transport equations for the fluid and the solid phases. The literature has documented proposals for macroscopic energy equation modeling for porous media considering the local thermal equilibrium hypothesis and laminar flow. In addition, two-energy equation models have been proposed for conduction and laminar convection in packed beds. With the aim of contributing to new developments, this work treats turbulent heat transport modeling in porous media under the local thermal nonequilibrium assumption. Macroscopic time-average equations for continuity, momentum, and energy are presented based on the recently established double decomposition concept (spatial deviations and temporal fluctuations of flow properties). The numerical technique employed for discretizing the governing equations is the control volume method. Turbulent flow results for the macroscopic heat transfer coefficient, between the fluid and solid phase in a periodic cell, are presented. [DOI: 10.1115/1.2175150]

Keywords: turbulence modeling, porous media, heat transfer coefficient

1 Introduction

Convection heat transfer in porous media has been extensively investigated due to its many important engineering applications. The wide applications available have led to numerous investigations in this area. Such applications can be found in solar receiver devices, building thermal insulation, heat exchangers, energy storage units, etc. From the point of view of the energy equation there are two different models, local thermal equilibrium model and the two energy approach. The first model assumes that the solid temperature is equal to the fluid temperature, thus local thermal equilibrium between the fluid and the solid-phases is achieved at any location in the porous media. This model simplifies theoretical and numerical research, but the assumption of local thermal equilibrium between the fluid and the solid is inadequate for a number of problems [1–4]. In recent years more attention has been paid to the local thermal nonequilibrium model and its use has increased in theoretical and numerical research for convection heat transfer processes in porous media [5,6].

Kuwahara et al. [7] proposed a numerical procedure to determine macroscopic transport coefficients from a theoretical basis without any empiricism. They used a single unit cell and determined the interfacial heat transfer coefficient for the asymptotic case of infinite conductivity of the solid phase. Nakayama et al. [8] extended the conduction model of Hsu [9] for treating also convection in porous media and the monographs of [3,10,11] fully document forced convection in porous media. Having established the macroscopic energy equations for both phases, useful exact solutions were obtained for two fundamental heat transfer processes associated with porous media, namely, steady conduction in a porous slab with internal heat generation within the solid, and also, thermally developing flow through a semi-infinite porous medium. Sahraouri and Kaviany [12] performed direct numerical simulations of premixed combustion in a two-dimensional porous medium made of in-line and staggered arrangements of square cylinders. Results therein were limited to the laminar flow regime.

Saito and de Lemos [13] considered local thermal nonequilibrium and obtained the interfacial heat transfer coefficient for laminar flow using a single unit cell with local instantaneous transport equations.

In all of the above, only laminar flow has been considered. When treating turbulent flow in porous media, however, difficulties arise due to the fact that the flow fluctuates with time and a volumetric average is applied [14]. For handling such situations, a new concept called *double decomposition* has been proposed for developing macroscopic models for turbulent transport in porous media [15–19]. This methodology has been extended to nonbuoyant heat transfer [20], buoyant flows [21–24], mass transfer [25], and double diffusion [26]. In addition, a general classification of models has been published [27]. Recently, the problem of treating interfaces between a porous medium and a clear region, considering a diffusion-jump condition for laminar [28] and turbulence fields [29–31], have also been investigated under the concept first proposed by [15–19]. Following this same concept, de Lemos and Rocamora [32] have developed a macroscopic turbulent energy equation for a homogeneous, rigid, and saturated porous medium, considering local thermal equilibrium between the fluid and solid matrix.

Motivated by the foregoing, this work focuses on turbulent flow through a packed bed, which represents an important configuration for efficient heat and mass transfer and suggests the use of equations governing thermal nonequilibrium involving distinct energy balances for both the solid and fluid phases. Accordingly, the use of such two-energy equation model requires an extra parameter to be determined, namely, the heat transfer coefficient between the fluid and the solid. The contribution herein consists in proposing a new correlation for obtaining the interfacial heat transfer coefficient for turbulent flow in a packed bed. The bed is

[1]Corresponding author.

Contributed by the Heat Transfer Division of ASME for publication in the JOURNAL OF HEAT TRANSFER. Manuscript received April 15, 2005; final manuscript received October 28, 2005. Review conducted by N.K. Anand.

modeled as an infinite staggered array of square rods and the range of Reynolds number, based on the size of the rod, is extended up to 10^7. In-line rod arrangement is not considered here as the objective of this work to first consolidate results for staggered arrays. Future investigations shall consider different array arrangements as well as distinct rod shapes, such as elliptical and circular rods.

The next sections detail the basic mathematical model, including the mean and turbulent fields for turbulent flows. Although the discussion of turbulent motion in porous media is not presented in this work, the definitions and concepts to calculate the interfacial heat transfer coefficient for macroscopic flows are presented.

2 Governing Equations

2.1 Microscopic Transport Equations. Microscopic transport equations or local time-averaged transport equations for incompressible fluid flow in a rigid homogeneous porous medium have already been presented in the literature and for that they are just presented here [32]. The governing equations for the flow and energy for an incompressible fluid are given by:

Continuity:

$$\nabla \cdot \mathbf{u} = 0 \tag{1}$$

Momentum:

$$\rho\left[\frac{\partial \mathbf{u}}{\partial t} + \nabla \cdot (\mathbf{uu})\right] = -\nabla p + \mu \nabla^2 \mathbf{u} \tag{2}$$

Energy-fluid phase:

$$(\rho c_p)_f \left\{\frac{\partial T_f}{\partial t} + \nabla \cdot (\mathbf{u} T_f)\right\} = \nabla \cdot (k_f \nabla T_f) + S_f \tag{3}$$

Energy-solid phase (porous matrix):

$$(\rho c_p)_s \frac{\partial T_s}{\partial t} = \nabla \cdot (k_s \nabla T_s) + S_s \tag{4}$$

where the subscripts f and s refer to fluid and solid phases, respectively. Here, T is the temperature, k_f is the fluid thermal conductivity, k_s is the solid thermal conductivity, c_p is the specific heat, and S is the heat generation term. If there is no heat generation either in the solid or in the fluid, one has further $S_f = S_s = 0$.

For turbulent flows the time averaged transport equations can be written as:

Continuity:

$$\nabla \cdot \overline{\mathbf{u}} = 0 \tag{5}$$

Momentum:

$$\rho_f[\nabla \cdot (\overline{\mathbf{u}}\overline{\mathbf{u}})] = -\nabla \overline{p} + \nabla \cdot \{\mu[\nabla \overline{\mathbf{u}} + (\nabla \overline{\mathbf{u}})^T] - \rho \overline{\mathbf{u}'\mathbf{u}'}\} \tag{6}$$

where the low and high Reynolds k-ϵ model is used to obtain the eddy viscosity, μ_t, whose equations for the turbulent kinetic energy per unit mass and for its dissipation rate read:

Turbulent kinetic energy per unit mass:

$$\rho_f[\nabla \cdot (\overline{\mathbf{u}} k)] = \nabla \cdot \left[\left(\mu + \frac{\mu_t}{\sigma_k}\right) \nabla k\right] - \rho \overline{\mathbf{u}'\mathbf{u}'} : \nabla \overline{\mathbf{u}} - \rho \epsilon \tag{7}$$

Turbulent kinetic energy per unit mass dissipation rate:

$$\rho_f[\nabla \cdot (\overline{\mathbf{u}} \epsilon)] = \nabla \cdot \left[\left(\mu + \frac{\mu_t}{\sigma_\epsilon}\right) \nabla \epsilon\right] + [c_1(-\rho \overline{\mathbf{u}'\mathbf{u}'} : \nabla \overline{\mathbf{u}}) - c_2 f_2 \rho \epsilon] \frac{\epsilon}{k} \tag{8}$$

Reynolds stresses and the eddy viscosity is given by, respectively,

$$-\rho \overline{\mathbf{u}'\mathbf{u}'} = \mu_t[\nabla \overline{\mathbf{u}} + (\nabla \overline{\mathbf{u}})^T] - \frac{2}{3}\rho k \mathbf{I} \tag{9}$$

$$\mu_t = \rho c_\mu f_\mu \frac{k^2}{\epsilon} \tag{10}$$

where, ρ is the fluid density, p is the pressure, μ represents the fluid viscosity.

In the above equation set σ_k, σ_ϵ, c_1, c_2, and c_μ are dimensionless constants, whereas f_2 and f_μ are damping functions. The turbulence model constants are

$$c_\mu = 0.09, \quad c_1 = 1.5, \quad c_2 = 1.9, \quad \sigma_k = 1.4, \quad \sigma_\epsilon = 1.3$$

For the high Re model the standard constants of Launder and Spalding [33] were employed.

Also, the time averaged energy equations become:

Energy-fluid phase:

$$(\rho c_p)_f[\nabla \cdot (\overline{\mathbf{u}} \overline{T_f})] = \nabla \cdot (k_f \nabla \overline{T_f}) - (\rho c_p)_f \nabla \cdot (\overline{\mathbf{u}' T_f'}) \tag{11}$$

Energy-solid phase (porous matrix):

$$\nabla \cdot (k_s \nabla \overline{T_s}) + S_s = 0 \tag{12}$$

2.2 Decomposition of Flow Variables in Space and Time. Macroscopic transport modeling of incompressible flows in porous media has been based on the volume-average methodology for either heat [34] or mass transfer [35,36]. If time fluctuations of the flow properties are also considered, in addition to spatial deviations, there are two possible methodologies to follow in order to obtain macroscopic equations: (a) application of time-average operator followed by volume-averaging [37–42], or (b) use of volume-averaging before time-averaging is applied [43–45]. However, both sets of macroscopic mass transport equations are equivalent when examined under the recently established double decomposition concept [15–19]. As mentioned, the double decomposition concept has been published in a number of worldwide available journal articles [15–32] and does not need to be repeated here.

2.3 Macroscopic Flow and Energy Equations. When the average operators are simultaneously applied over Eqs. (1) and (2), macroscopic equations for turbulent flow are obtained. Volume integration is performed over a REV Refs. [14,46], resulting in

Continuity:

$$\nabla \cdot \overline{\mathbf{u}}_D = 0 \tag{13}$$

where, $\overline{\mathbf{u}}_D = \phi \langle \overline{\mathbf{u}} \rangle^i$ and $\langle \overline{\mathbf{u}} \rangle^i$ identifies the intrinsic (liquid) average of the time-averaged velocity vector $\overline{\mathbf{u}}$.

Momentum:

$$\rho\left[\frac{\partial \overline{\mathbf{u}}_D}{\partial t} + \nabla \cdot \left(\frac{\overline{\mathbf{u}}_D \overline{\mathbf{u}}_D}{\phi}\right)\right] = -\nabla(\phi \langle \overline{p} \rangle^i) + \mu \nabla^2 \overline{\mathbf{u}}_D - \nabla \cdot (\rho \phi \langle \overline{\mathbf{u}'\mathbf{u}'} \rangle^i) - \left[\frac{\mu \phi}{K} \overline{\mathbf{u}}_D + \frac{c_F \phi \rho |\overline{\mathbf{u}}_D| \overline{\mathbf{u}}_D}{\sqrt{K}}\right] \tag{14}$$

where the last two terms in Eq. (14) represent the Darcy and Forchheimer contributions by [47]. The symbol K is the porous medium permeability, c_F is the form drag or Forchheimer coefficient, $\langle \overline{p} \rangle^i$ is the intrinsic average pressure of the fluid, and ϕ is the porosity of the porous medium.

The macroscopic Reynolds stress, $-\rho \phi \langle \overline{\mathbf{u}'\mathbf{u}'} \rangle^i$, appearing in Eq. (14) is given as

$$-\rho \phi \langle \overline{\mathbf{u}'\mathbf{u}'} \rangle^i = \mu_{t_\phi} 2 \langle \overline{D} \rangle^\nu - \frac{2}{3} \phi \rho \langle k \rangle^i \mathbf{I} \tag{15}$$

where

$$\langle \overline{D} \rangle^{\nu} = \tfrac{1}{2}[\nabla(\phi\langle \overline{\mathbf{u}} \rangle^i) + [\nabla(\phi\langle \overline{\mathbf{u}} \rangle^i)]^T] \tag{16}$$

is the macroscopic deformation tensor, $\langle k \rangle^i = \langle \overline{\mathbf{u}'\mathbf{u}'} \rangle^i / 2$ is the intrinsic turbulent kinetic energy, and μ_{t_ϕ}, is the turbulent viscosity, which is modeled in [27] similarly to the case of clear flow, in the form,

$$\mu_{t_\phi} = \rho c_\mu \frac{\langle k \rangle^{i^2}}{\langle \epsilon \rangle^i} \tag{17}$$

The intrinsic turbulent kinetic energy per unit mass and its dissipation rate are governed by the following equations:

$$\rho\left[\frac{\partial}{\partial t}(\phi\langle k \rangle^i) + \nabla \cdot (\overline{\mathbf{u}}_D \langle k \rangle^i)\right] = \nabla \cdot \left[\left(\mu + \frac{\mu_{t_\phi}}{\sigma_k}\right) \nabla (\phi\langle k \rangle^i)\right] - \rho\langle \overline{\mathbf{u}'\mathbf{u}'} \rangle^i : \nabla \overline{\mathbf{u}}_D + c_k \rho \frac{\phi\langle k \rangle^i |\overline{\mathbf{u}}_D|}{\sqrt{K}} - \rho\phi\langle \epsilon \rangle^i \tag{18}$$

$$\rho\left[\frac{\partial}{\partial t}(\phi\langle \epsilon \rangle^i) + \nabla \cdot (\overline{\mathbf{u}}_D \langle \epsilon \rangle^i)\right] = \nabla \cdot \left[\left(\mu + \frac{\mu_{t_\phi}}{\sigma_\epsilon}\right) \nabla (\phi\langle \epsilon \rangle^i)\right] + c_1(-\rho\langle \overline{\mathbf{u}'\mathbf{u}'} \rangle^i : \nabla \overline{\mathbf{u}}_D) \frac{\langle \epsilon \rangle^i}{\langle k \rangle^i} + c_2 c_k \rho \frac{\phi\langle \epsilon \rangle^i |\overline{\mathbf{u}}_D|}{\sqrt{K}} - c_2 \rho\phi \frac{\langle \epsilon \rangle^{i^2}}{\langle k \rangle^i} \tag{19}$$

where, c_k, c_1, c_2, and c_μ are nondimensional constants. The second terms on the left-hand side of Eqs. (18) and (19) represent the generation rate of $\langle k \rangle^i$ and $\langle \epsilon \rangle^i$, respectively, due to the mean gradient of $\overline{\mathbf{u}}_D$. The third terms in the same equations are the generation rates due to the action of the porous matrix (see [16]).

Similarly, macroscopic energy equations are obtained for both fluid and solid phases by applying time and volume average operators to Eqs. (3) and (4). As in the flow case, volume integration is performed over a REV, resulting in

$$(\rho c_p)_f \left[\frac{\partial \phi \langle \overline{T}_f \rangle^i}{\partial t} + \nabla \cdot \{\phi(\langle \overline{\mathbf{u}} \rangle^i \langle \overline{T}_f \rangle^i + \langle {}^i\overline{\mathbf{u}}^i \overline{T}_f \rangle^i + \overline{\langle \mathbf{u}' \rangle^i \langle T_f' \rangle^i} + \langle \overline{{}^i\mathbf{u}'^i T'_f} \rangle^i)\}\right] = \nabla \cdot \left[k_f \nabla (\phi \langle \overline{T}_f \rangle^i) + \frac{1}{\Delta V} \int_{A_i} \mathbf{n}_i k_f \overline{T}_f \, dA\right] + h_i a_i (\langle \overline{T}_s \rangle^i - \langle \overline{T}_f \rangle^i) \tag{20}$$

$$(\rho c_p)^s \left\{\frac{\partial (1-\phi) \langle \overline{T}_s \rangle^i}{\partial t}\right\} = \nabla \cdot \left\{k_s \nabla [(1-\phi) \langle \overline{T}_s \rangle^i] - \frac{1}{\Delta V} \int_{A_i} \mathbf{n}_i k_s \overline{T}_s \, dA\right\} - h_i a_i (\langle \overline{T}_s \rangle^i - \langle \overline{T}_f \rangle^i) \tag{21}$$

where, h_i and a_i are the interfacial convective heat transfer coefficient and surface area per unit volume, respectively.

2.4 Macroscopic Two-Energy Equation Modeling. In order to apply Eqs. (20) and (21) to obtain the temperature field for turbulent flow in porous media, the underscored terms have to be modeled in some way as a function of the intrinsically averaged temperature of solid phase and fluid, $\langle \overline{T}_s \rangle^i$ and $\langle \overline{T}_f \rangle^i$. To accomplish this, a gradient-type diffusion model is used for all the terms, i.e., thermal dispersion due to spatial deviations, turbulent heat flux due to temporal fluctuations, turbulent thermal dispersion due to temporal fluctuations, and spatial deviations and local conduction.

Using these gradient type diffusion models, we can write:

Turbulent heat flux:

$$-(\rho c_p)_f (\phi \overline{\langle \mathbf{u}' \rangle^i \langle T_f' \rangle^i}) = \mathbf{K}_t \cdot \nabla \langle \overline{T}_f \rangle^i \tag{22}$$

Thermal dispersion:

$$-(\rho c_p)_f (\phi \langle {}^i\overline{\mathbf{u}}^i \overline{T}_f \rangle^i) = \mathbf{K}_{\text{disp}} \cdot \nabla \langle \overline{T}_f \rangle^i \tag{23}$$

Turbulent thermal dispersion:

$$-(\rho c_p)_f (\phi \langle \overline{{}^i\mathbf{u}'^i T'_f} \rangle^i) = \mathbf{K}_{\text{disp},t} \cdot \nabla \langle \overline{T}_f \rangle^i \tag{24}$$

Local conduction:

$$\nabla \cdot \left[\frac{1}{\Delta V} \int_{A_i} \mathbf{n}_i k_f \overline{T}_f \, dA\right] = \mathbf{K}_{f,s} \cdot \nabla \langle \overline{T}_s \rangle^i$$

$$\nabla \cdot \left[\frac{1}{\Delta V} \int_{A_i} \mathbf{n}_i k_f \overline{T}_s \, dA\right] = \mathbf{K}_{s,f} \cdot \nabla \langle \overline{T}_f \rangle^i \tag{25}$$

For the above shown expressions, Eqs. (20) and (21) can be written as:

$$\{(\rho c_p)_f \phi\} \frac{\partial \langle \overline{T} \rangle^i}{\partial t} + (\rho c_p)_f \nabla \cdot (\mathbf{u}_D \langle \overline{T}_f \rangle^i) = \nabla \cdot \{\mathbf{K}_{\text{eff},f} \cdot \nabla \langle \overline{T}_f \rangle^i\} + h_i a_i (\langle \overline{T}_s \rangle^i - \langle \overline{T}_f \rangle^i) \tag{26}$$

$$\{(1-\phi)(\rho c_p)_s\} \frac{\partial \langle \overline{T} \rangle^i}{\partial t} = \nabla \cdot \{\mathbf{K}_{\text{eff},s} \cdot \nabla \langle \overline{T}_s \rangle^i\} + h_i a_i (\langle \overline{T}_s \rangle^i - \langle \overline{T}_f \rangle^i) \tag{27}$$

where, $\mathbf{K}_{\text{eff},f}$ and $\mathbf{K}_{\text{eff},s}$ are the effective conductivity tensor for fluid and solid, respectively, given by:

$$\mathbf{K}_{\text{eff},f} = \lfloor \phi k_f \rfloor \mathbf{I} + \mathbf{K}_{f,s} + \mathbf{K}_t + \mathbf{K}_{\text{disp}} + \mathbf{K}_{\text{disp},t} \tag{28}$$

$$\mathbf{K}_{\text{eff},s} = [(1-\phi) k_s] \mathbf{I} + \mathbf{K}_{s,f} \tag{29}$$

and $\mathbf{I}$ is the unit tensor. Details of interfacial convective heat transfer coefficient are presented next section.

In order to be able to apply Eq. (26), it is necessary to determine the dispersion and conductivity tensors in Eq. (28), i.e., $\mathbf{K}_{f,s}$, $\mathbf{K}_t$, $\mathbf{K}_{\text{disp}}$, and $\mathbf{K}_{\text{disp},t}$. Following Kuwahara and Nakayama [38] and Quintard et al. [5], this can be accomplished for the thermal dispersion and conductivity tensors, $\mathbf{K}_{f,s}$ and $\mathbf{K}_{\text{disp}}$, by making use of a unit cell subjected to periodic boundary conditions for the flow and a linear temperature gradient, to represent the porous medium. The dispersion and conductivity tensors are then obtained directly from the microscopic results for the unit cell, using Eqs. (23) and (25). Besides, it can be used for the following correlations for the transverse and longitudinal components of the thermal dispersion tensor, which are valid for $\text{Pe}_D \geqslant 10$:

$$\frac{(k_{\text{dis}})_{xx}}{k_f} = 2.1 \frac{\text{Pe}_D}{(1-\phi)^{0.1}}, \text{ for longitudinal dispersion} \tag{30}$$

$$\frac{(k_{\text{dis}})_{yy}}{k_f} = 0.052(1-\phi)^{0.5} \text{Pe}_D, \text{ for transverse dispersion} \tag{31}$$

The turbulent heat flux and turbulent thermal dispersion terms, $\mathbf{K}_t$ and $\mathbf{K}_{\text{disp},t}$, which can not be determined from such a microscopic calculation, are modeled through the eddy diffusivity concept, similarly to Nakayama and Kuwahara [42]. It should be noticed that these terms arise only if the flow in the porous medium is turbulent, whereas the thermal dispersion terms exist for

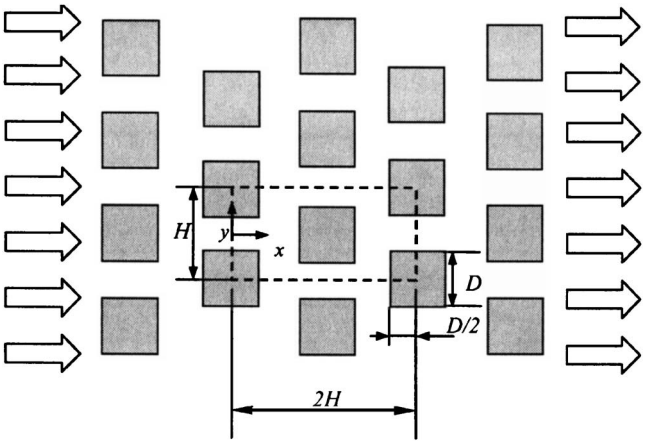

Fig. 1 Physical model and coordinate system

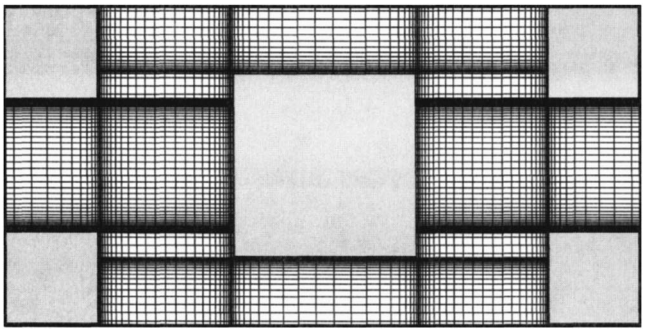

Fig. 2 Nonuniform computational grid

both laminar and turbulent flow regimes. Starting out from the time averaged energy equation coupled with the microscopic modeling for the "turbulent thermal stress tensor" through the microscopic eddy diffusivity, $\Gamma_T = \mu_t/\sigma_T$, one can write:

$$-(\rho c_p)_f \overline{\mathbf{u}' T_f'} = (\rho c_p)_f \frac{\nu_t}{\sigma_T} \nabla \overline{T}_f \tag{32}$$

where σ_T is the turbulent Prandtl number which is taken here as a constant.

Applying the volume average to the resulting equation, one obtains the macroscopic version of the "turbulent thermal stress tensor," given by:

$$-(\rho c_p)_f \langle \overline{\mathbf{u}' T_f'} \rangle^i = (\rho c_p)_f \frac{\nu_{t_\phi}}{\sigma_T} \nabla \langle \overline{T}_f \rangle^i \tag{33}$$

where we have adopted the symbol ν_{t_ϕ} to express the macroscopic version of the eddy viscosity, $\mu_{t_\phi} = \rho_f \nu_{t_\phi}$.

Equation (33) is the sum of the turbulent heat flux and the turbulent thermal dispersion found by Rocamora and de Lemos [20]. In view of the arguments given above, the turbulent heat flux and turbulent thermal dispersion components of the conductivity tensor, $\mathbf{K}_t$ and $\mathbf{K}_{\text{disp},t}$, respectively, will be expressed as:

$$\mathbf{K}_t + \mathbf{K}_{\text{disp},t} = \phi (\rho c_p)_f \frac{\nu_{t_\phi}}{\sigma_T} \mathbf{I} \tag{34}$$

2.5 Interfacial Heat Transfer Coefficient. In Eqs. (20) and (21) the heat transferred between the two phases can be modeled by means of a film coefficient h_i such that,

$$h_i a_i (\langle \overline{T}_s \rangle^i - \langle \overline{T}_f \rangle^i) = \frac{1}{\Delta V} \int_{\Lambda_i} \mathbf{n}_i \cdot k_f \nabla \overline{T}_f \, dA = \frac{1}{\Delta V} \int_{\Lambda_i} \mathbf{n}_i \cdot k_s \nabla \overline{T}_s \, dA \tag{35}$$

where, $a_i = A_i/\Delta V$.

Wakao et al. [48] obtained a heuristic correlation for closely packed bed, of particle diameter D and compared their with experimental data. This correlation for the interfacial heat transfer coefficient is given by,

$$\frac{h_i D}{k_f} = 2 + 1.1 \, \mathrm{Re}_D^{0.6} \, \mathrm{Pr}^{1/3} \tag{36}$$

For numerically determining h_i, Kuwahara et al. [7] modeled a porous medium by considering an infinite number of solid square rods of size D, arranged in a regular triangular pattern (see Fig. 1). They numerically solved the governing equations in the void region, exploiting to advantage the fact that for an infinite and geometrically ordered medium a repetitive cell can be identified. Periodic boundary conditions were then applied for obtaining the temperature distribution under fully developed flow conditions. A numerical correlation for the interfacial convective heat transfer coefficient was proposed by Kuwahara et al. [7] for laminar flow as,

$$\frac{h_i D}{k_f} = \left(1 + \frac{4(1-\phi)}{\phi}\right) + \frac{1}{2}(1-\phi)^{1/2} \, \mathrm{Re}_D^{0.6} \, \mathrm{Pr}^{1/3}, \text{ valid for } 0.2 < \phi < 0.9 \tag{37}$$

Equation (37) is based on porosity dependency and is valid for packed beds of particle diameter D.

Saito and de Lemos [13] obtained the interfacial heat transfer coefficient for laminar flows though an infinite square rod; this same physical model will be used here for obtaining the interfacial heat transfer coefficient h_i for turbulent flows.

The flow through an infinite square rod can be associated with flow across a bundle of tubes. Furthermore the heat transfer coefficient related to a tube is determined by its position in the package. The tube rows of a bundle are either aligned or staggered in the direction of the fluid velocity. In this work the geometric arrangement is staggered (see Fig. 1). For the staggered configuration Zhukauskas [27] has proposed a correlation of the form,

$$\frac{h_i D}{k_f} = 0.022 \, \mathrm{Re}_D^{0.84} \, \mathrm{Pr}^{0.36} \tag{38}$$

where the values 0.022 and 0.84 are constants for tube bank in cross flow and for this particular case $2 \times 10^5 < \mathrm{Re}_D < 2 \times 10^6$.

3 Periodic Cell and Boundary Conditions

The macroscopic hydrodynamic and thermodynamic behavior of practical interest can be obtained from the direct application of the first principles to viscous flow and heat transfer at a pore scale. In reality, however, it is impossible to resolve the details of the flow and heat transfer fields within a real porous medium. Nakayama et al. [8] and Kuwahara et al. [7] modeled a porous medium in terms of obstacles arranged in a regular pattern, and solved the set of the microscopic governing equations, exploiting periodic boundary conditions.

In order to evaluate the numerical tool to be used in the determination of the film coefficient given by Eq. (35), a test case was run for obtaining the flow field in a periodic cell, which is here assumed to represent the porous medium. Consider a macroscopically uniform flow through an infinite number of square rods of lateral size D, placed in a staggered arrangement and maintained at constant temperature T_w. The periodic cell or representative elementary volume, ΔV is schematically showed in Fig. 1 and has dimensions $2H \times H$. Computations within this cell were carried out using a nonuniform grid, as shown in Fig. 2, to ensure that the

results were grid independent. The Reynolds number $\mathrm{Re}_D = \rho \overline{\mathbf{u}}_D D/\mu$ was varied from 10^4 to 10^7 and the porosity, $\phi = 1 - (D/H)^2$.

The numerical method utilized to discretize the flow and energy equations in the unit cell is the finite control volume approach. The SIMPLE method of Patankar [49] was used for handling Eqs. (1)–(4) the velocity-pressure coupling. Convergence was monitored in terms of the normalized residue for each variable. The maximum residue allowed for convergence check was set to 10^{-9}, being the variables normalized by appropriate reference values.

For fully developed flow in the cell of Fig. 1, the velocity at exit ($x/H=2$) must be identical to that at the inlet ($x/H=0$). Temperature profiles, however, are only identical at both the cell exit and inlet if presented in terms of an appropriate nondimensional variable. The situation is analogous to the case of forced convection in a channel with isothermal walls. Due to the periodicity of the model and a single structural unit as indicated in Fig. 1 may be taken as a calculation domain. The equations used for turbulent flow in the unit cell are Eqs. (5), (6), and (11).

Thus, boundary conditions and periodic constraints are given by:

On the solid walls (Low Re Model):

$$\overline{u} = 0, \quad k = 0, \quad \epsilon = \nu \frac{\partial^2 k}{\partial y^2}, \quad \overline{T} = \overline{T}_w \tag{39}$$

On the solid walls (High Re Model):

$$\frac{\overline{u}}{u_\tau} = \frac{1}{\kappa} \ln(y^+ E), \quad k = \frac{u_\tau^2}{c_\mu^{1/2}}, \quad \epsilon = \frac{c_\mu^{3/4} k_w^{3/2}}{\kappa y_w},$$

$$q_w = \frac{(\rho c_p)_f c_\mu^{1/4} k_w^{1/2} (\overline{T} - \overline{T}_w)}{\left(\frac{\mathrm{Pr}_t}{\kappa} \ln(y_w^+) + c_Q(\mathrm{Pr}) \right)} \tag{40}$$

where,

$$u_\tau = \left(\frac{\tau_w}{\rho} \right)^{1/2}, \quad y_w^+ = \frac{y_w u_\tau}{\nu},$$

$$c_Q = 12.5\, \mathrm{Pr}^{2/3} + 2.12 \ln(\mathrm{Pr}) - 5.3 \text{ for } \mathrm{Pr} > 0.5$$

where, Pr and Pr_t are Prandtl and turbulent Prandtl number, respectively, q_w is wall heat flux, u_τ is wall-friction velocity, y_w is the coordinate normal to wall, κ is a constant for turbulent flow past smooth impermeable walls or von Kármán's constant, and E is an integration constant that depends on the roughness of the wall. For smooth walls with constant shear stress $E=9$.

On the symmetry planes:

$$\frac{\partial \overline{u}}{\partial y} = \frac{\partial \overline{v}}{\partial y} = \frac{\partial k}{\partial y} = \frac{\partial \epsilon}{\partial y} = 0 \tag{41}$$

where $\overline{u}$ and $\overline{v}$ are components of $\mathbf{u}$.

On the periodic boundaries:

$$\overline{u}|_{\mathrm{inlet}} = \overline{u}|_{\mathrm{outlet}}, \quad \overline{v}|_{\mathrm{inlet}} = \overline{v}|_{\mathrm{outlet}}, \quad k|_{\mathrm{inlet}} = k|_{\mathrm{outlet}}, \quad \epsilon|_{\mathrm{inlet}} = \epsilon|_{\mathrm{outlet}} \tag{42}$$

$$\theta|_{\mathrm{inlet}} = \theta|_{\mathrm{outlet}} \Leftrightarrow \left. \frac{\overline{T} - \overline{T}_w}{\overline{T}_B(x) - \overline{T}_w} \right|_{\mathrm{inlet}} = \left. \frac{\overline{T} - \overline{T}_w}{\overline{T}_B(x) - \overline{T}_w} \right|_{\mathrm{outlet}} \tag{43}$$

The bulk mean temperature of the fluid is given by:

$$\overline{T}_B(x) = \frac{\int \overline{u}\,\overline{T}\, dy}{\int \overline{u}\, dy} \tag{44}$$

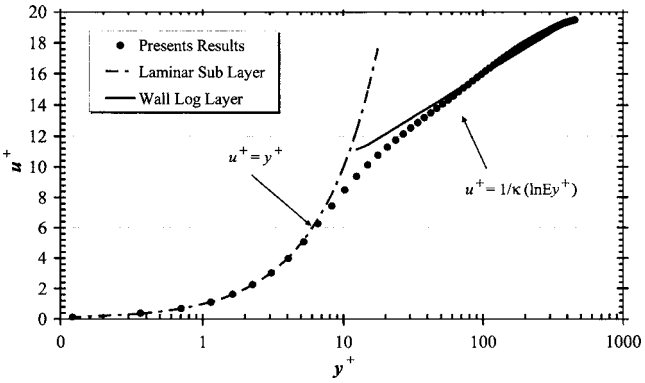

Fig. 3 Velocity profile in fully developed pipe flow

Computations are based on the Darcy velocity, the length of structural unit H, and the temperature difference $(\overline{T}_B(x) - \overline{T}_w)$, as references scales.

3.1 Film Coefficient h_i. Determination of h_i is here obtained by calculating, for the unit cell of Fig. 1, an expression given as,

$$h_i = \frac{Q_{\mathrm{total}}}{A_i \Delta T_{\mathrm{ml}}} \tag{45}$$

where $A_i = 8Dx1$. The overall heat transferred in the cell, Q_{total}, is giving by,

$$Q_{\mathrm{total}} = (H - D)\rho \overline{u}_B c_p (\overline{T}_B|_{\mathrm{outlet}} - \overline{T}_B|_{\mathrm{inlet}}) \tag{46}$$

The bulk mean velocity of the fluid is given by:

$$\overline{u}_B(x) \frac{\int \overline{u}\, dy}{\int dy} \tag{47}$$

and the logarithm mean temperature difference, ΔT_{ml} is,

$$\Delta T_{\mathrm{ml}} = \frac{(\overline{T}_w - \overline{T}_B|_{\mathrm{outlet}}) - (\overline{T}_w - \overline{T}_B|_{\mathrm{inlet}})}{\ln[(\overline{T}_w - \overline{T}_B|_{\mathrm{outlet}})(\overline{w} - \overline{T}_B|_{\mathrm{inlet}})]} \tag{48}$$

Equation (46) represents an overall heat balance on the entire cell and associates the heat transferred to the fluid to a suitable temperature difference ΔT_{ml}. As mentioned earlier, Eqs. (1)–(4) were numerically solved in the unit cell until conditions (42) and (43) were satisfied.

4 Results and Discussion

4.1 Periodic Flow. Results for velocity and temperature fields were obtained for different Reynolds numbers. In order to assure that the flow was hydrodynamically and thermally developed in the periodic cell of Fig. 1, the governing equations were solved repetitively in the cell, taking the outlet profiles for $\overline{\mathbf{u}}$ and θ at the exit and plugging them back at the inlet. In the first run, uniform velocity and temperature profiles were set at the cell entrance for $\mathrm{Pr}=1$ giving $\theta=1$ at $x/H=0$. Then, after convergence of the flow and temperature fields, $\overline{\mathbf{u}}$ and θ at $x/H=2$ were used as inlet profiles for a second run, corresponding to solving again the flow for a similar cell beginning in $x/H=2$. Similarly, a third run was carried out and again outlet results, this time corresponding to an axial position $x/H=4$, were recorded. This procedure was repeated several times until $\overline{\mathbf{u}}$ and θ did not differ substantially at both inlet and outlet positions. Figure 3 further shows that the velocity profile here obtained in with a low Re model has a good

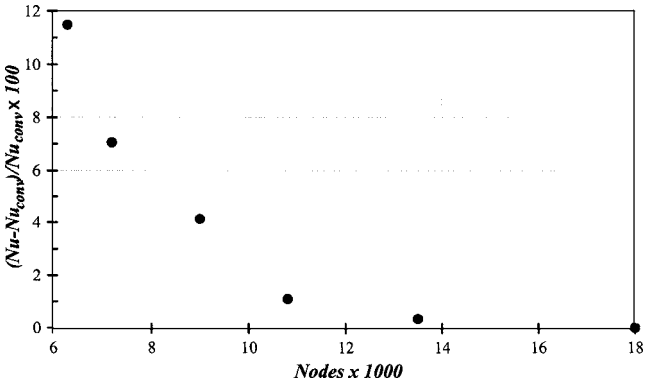

Fig. 4 Grid independence study

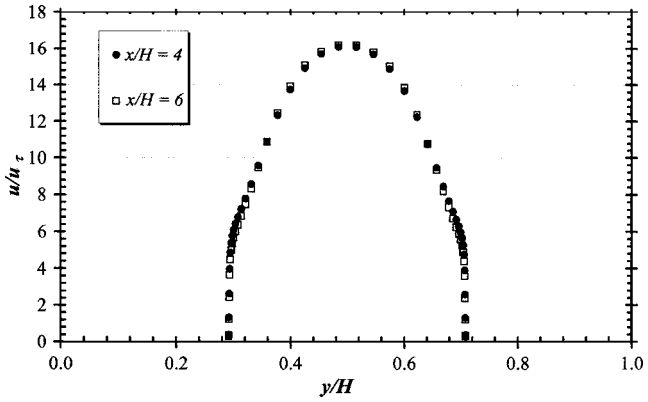

Fig. 5 Dimensionless velocity profile for Pr=1 and $Re_D=5\times10^4$

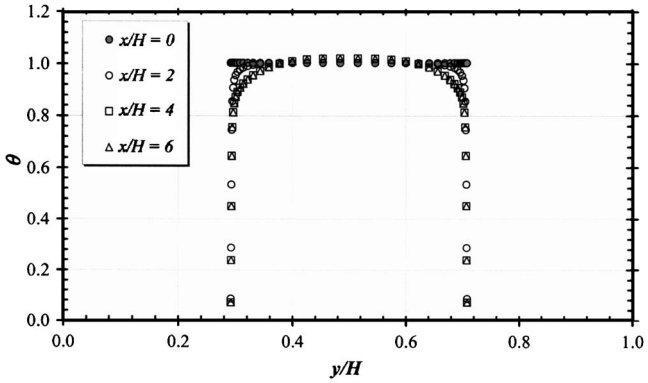

Fig. 6 Dimensionless temperature profile for Pr=1 and $Re_D=5\times10^4$

agreement within the laminar and the wall log layers.

Grid independence studies are summarized in Fig. 4, which presents results for Nu as a function of the number of grid points. The subscript conv refers to the asymptotic value as the grid increases. The figure indicates that for grids greater than 12,000, errors in Nu are less that 1%. For that, all results presented below considered this grid size.

Nondimensional velocity and temperature profiles are shown in Figs. 5 and 6, respectively, showing that the periodicity constraints imposed by Eqs. (42) and (43) was satisfied for $x/H>4$. For the entrance region ($0<x/H<4$), θ profiles change with length x/H being essentially invariable after this distance. Under this condition of constant θ profile, the flow was considered to be macroscopically developed for Re_D up to 10^7.

For the low Re model, the first node adjacent to the wall requires that the nondimensional wall distance be such that $y^+=u_\tau y\rho/\mu\leqslant1$. To accomplish this requirement, the grid needs a greater number of points close to the wall leading to computational meshes of large sizes. As a further code validation for turbulent flow calculation, which uses the $k-\epsilon$ model, a developing turbulent channel flow has been solved for $Re=5\times10^4$, where Re is based on the duct hydraulic diameter.

4.2 Developed Flow and Temperature Fields. Macroscopically developed flow field for Pr=1 and $Re_D=5\times10^4$ is presented in Fig. 5, corresponding to $x/D=6$ at the cell inlet. The expression "macroscopically developed" is used herein to account for the fact that periodic flow has been achieved at that axial position. Figures 7–9 show distributions of pressure, isotherms, and turbulence kinetic energy in a microscopic porous structure, obtained at $Re_D=10^5$ for cases of $\phi=0.65$. Pressure increases at the front face of the square rod and drastically decreases around the corner, as can be seen from the pressure contours shown in Fig. 7.

Temperature distribution is shown in Fig. 8. Colder fluid impinges on the left-hand side of the rod yielding strong temperature gradients on that face. Downstream the obstacles, fluid recirculation smooths temperature gradients and deforms isotherms within the mixing region. When the Reynolds number is sufficiently high (not shown here), thermal boundary layers cover the rod surfaces indicating that convective heat transfer overwhelms thermal diffusion. Figure 9 presents levels of turbulence kinetic energy, which are higher around the rod corners where a strong shear layer is formed. Further downstream the rods in the weak region, steep velocity gradients appear due to flow deceleration, also increasing the local level of k.

Once fully developed flow and temperature fields are achieved, for the fully developed condition ($x>6H$), bulk temperatures were calculated according to Eq. (44), at both inlet and outlet positions. They were then used to calculate h_i using Eqs. (45)–(48). Results for h_i are plotted in Fig. 10 for Re_D up to 10^7. Also plotted in this figure are results computed with correlation (37) by Kuwahara et al. [7] using $\phi=0.65$. The figure seems to

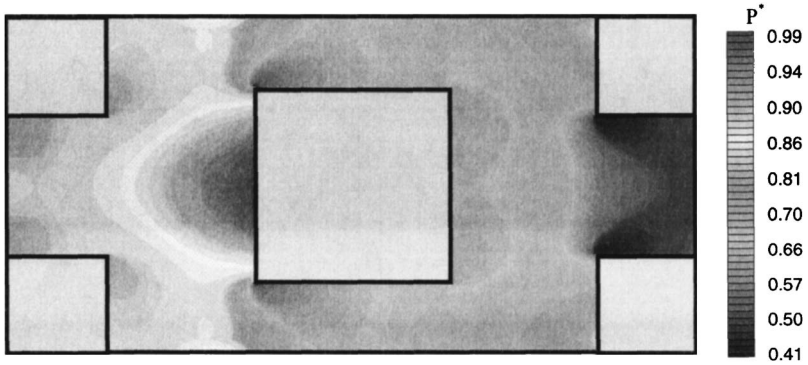

Fig. 7 Nondimensional pressure field for $Re_D=10^5$ and $\phi=0.65$

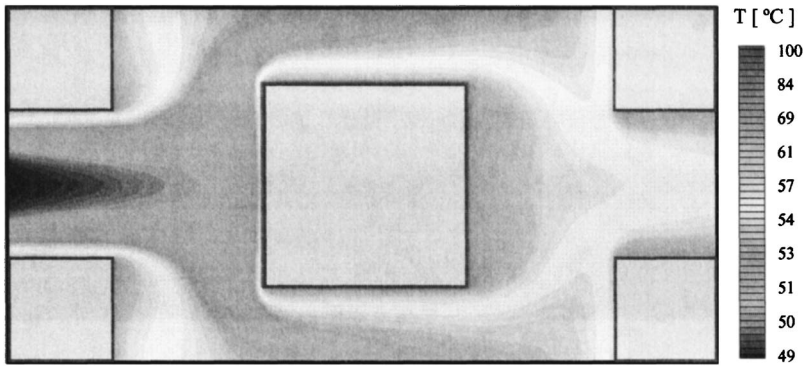

Fig. 8 Isotherms for Pr=1, $Re_D=10^5$, and $\phi=0.65$

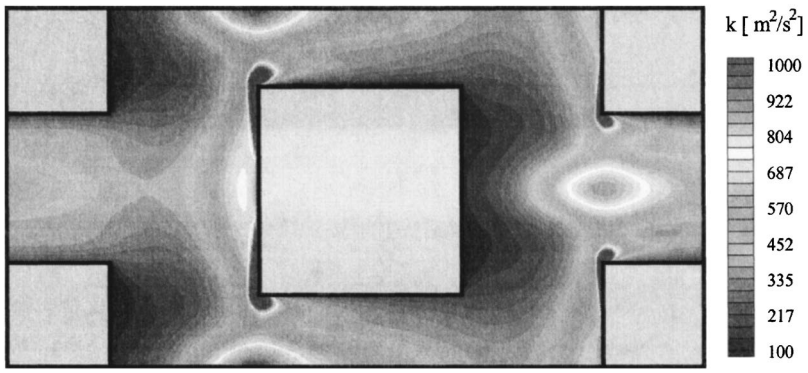

Fig. 9 Turbulence kinetic energy for $Re_D=10^5$ and $\phi=0.65$

indicate that both computations show a reasonable agreement for laminar results. In addition, numerical results for turbulent flow using low and High Re models are also presented in this figure.

Figure 11 shows numerical results for the interfacial convective heat transfer coefficient for various porosities ($\phi=0.44$, $\phi=0.65$, and $\phi=0.90$). Results for h_i are plotted for Re_D up to 10^7. In order to obtain a correlation for h_i in the turbulent regime, all curves were first collapsed after plotting them in terms of Re_D/ϕ, as shown in Fig. 12. Furthermore, the least squares technique was applied in order to determine the best correlation, which lead to a minimum overall error. Thus, the following expression is here proposed:

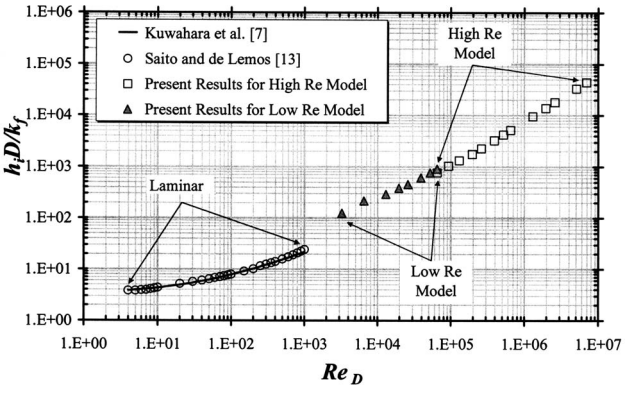

Fig. 10 Effect of Re_D on h_i for Pr=1 and $\phi=0.65$

$$\frac{h_i D}{k_f} = 0.08\left(\frac{Re_D}{\phi}\right)^{0.8} Pr^{1/3} \quad \text{for}$$

$$1.0\times 10^4 < \frac{Re_D}{\phi} < 2.0\times 10^7 \quad \text{valid for}$$

$$0.2 < \phi < 0.9 \tag{49}$$

Equation (49), which gives the heat transfer coefficient for turbulent flow, is compared with numerical results obtained with low and high Re models. Such comparison is presented in Fig. 13, which also shows computations using correlations given by Eqs. (36) and (37) by Wakao et al. [48] and Zhukauskas [50], respectively. The agreement between the present correlation, other correlations in the literature, and the numerical simulations stimulates further investigation on this subject, contributing towards the building of a more general expression for the interfacial heat transfer coefficient for porous media.

5 Concluding Remarks

A computational procedure for determining the convective coefficient of heat exchange between the porous substrate and the working fluid for a porous medium was detailed. As a preliminary result, macroscopically uniform laminar and turbulent flow through a periodic cell of isothermal square rods was computed, considering periodical velocity and temperature fields. Quantitative agreement was obtained when comparing laminar results herein with simulations by Kuwahara et al. [7]. For turbulent flows, low and high Reynolds turbulence models were employed in order to obtain the interfacial heat transfer coefficient. A correlation was then proposed for such coefficients. Further work will be carried out in order to simulate fully turbulent flow and heat transfer in a porous medium formed by arrays of elliptic, cylin-

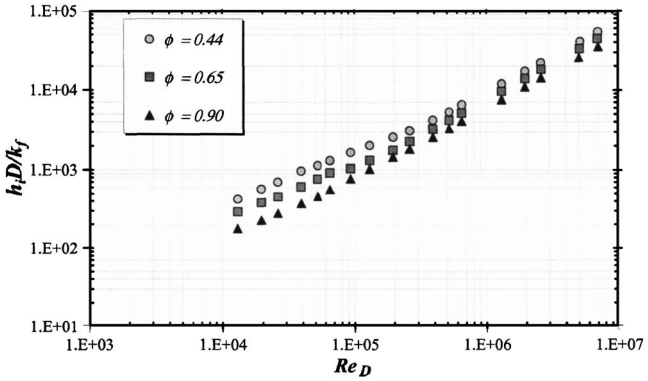

Fig. 11 Effect of porosity on h_i for Pr=1

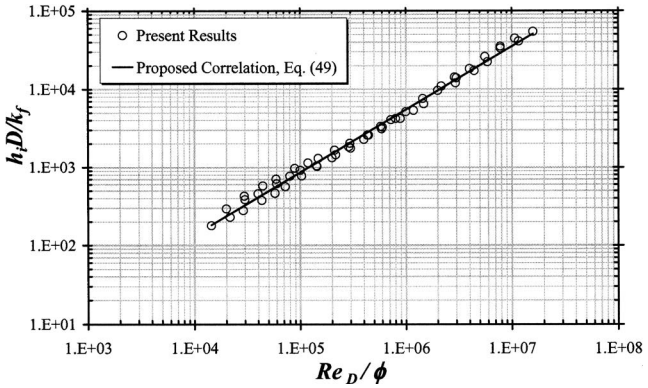

Fig. 12 Comparison of the numerical results and proposed correlation

drical and transverse elliptic rods, displaced in in-line as well as staggered arrangements. Ultimately, it is expected that a more general correlation for h_i be obtained to be used in conjunction with macroscopic two-energy equation models.

Nomenclature

A_i = interface total area between the fluid and solid
c_F = Forchheimer coefficient
c_p = fluid specific heat
D = square rods of lateral size
h_i = interfacial convective heat transfer coefficient
H = periodic cell height
$\mathbf{I}$ = unit tensor
K = permeability
k = turbulence kinetic energy per unit mass
k_f = fluid thermal conductivity
k_s = solid thermal conductivity
$\mathbf{K}_{\text{disp}}$ = dispersion conductivity tensor
$\mathbf{K}_{f,s}$ = two-equation model effective thermal conductivity tensor in fluid phase
$\mathbf{K}_{s,f}$ = two-equation model effective thermal conductivity tensor in solid phase
$\mathbf{K}_t$ = turbulence conductivity tensor
$\mathbf{K}_{\text{disp},t}$ = turbulent dispersion tensor
Nu = Interfacial Nusselt number; $\text{Nu}=h_i D/k_f$
P = pressure
P^* = $P^*(P-P_{\min})/(P_{\max}-P_{\min})$, nondimensional Pressure
Pr = $\text{Pr}=\nu/\alpha$, Prandtl number
Pe_D = Peclet number based on D and the macroscopically uniform velocity

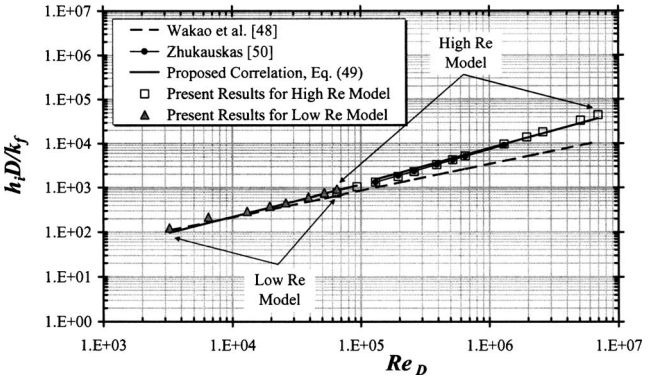

Fig. 13 Comparison of the numerical results and various correlations for $\phi=0.65$

Re_D = Reynolds number based on D and the macroscopically uniform velocity
T = temperature
$\overline{T}$ = time averaged temperature
$\mathbf{u}$ = microscopic velocity
$\mathbf{u}_D$ = Darcy or superficial velocity (volume average of $\mathbf{u}$)

Greek Symbols

α = fluid thermal diffusivity
ΔV = representative elementary volume
ΔV_f = fluid volume inside ΔV
μ = fluid dynamic viscosity
μ_t = eddy viscosity
μ_{t_ϕ} = macroscopic eddy viscosity
ν = fluid kinematic viscosity
ρ = fluid density
θ = dimensionless temperature
ϕ = $\phi=\Delta V_f/\Delta V$, porosity
σ_T = turbulent Prandtl number
φ = general variable
$\langle\varphi\rangle^i$ = intrinsic average
$\langle\varphi\rangle^v$ = volume average
$^i\varphi$ = spatial deviation

Acknowledgment

The authors are thankful to CNPq and FAPESP, Brazil, for their financial support during the course of this research.

References

[1] Schumann, T. E. W., 1929, "Heat Transfer: Liquid Flowing Through a Porous Prism," J. Franklin Inst., **208**, pp. 405–416.
[2] Quintard, M., 1998, "Modeling Local Non-Equilibrium Heat Transfer in Porous Media," in *Proc. 11th Int. Heat Transfer Conf.*, Kyongyu, Korea, Vol. 1, pp. 279–285.
[3] Kuznetsov, A. V., 1998, "Thermal Nonequilibrium Forced Convection in Porous Media," Chap. 5 in *Transport Phenomena in Porous Media*, D. B. Ingham and I. Pop, eds., Elsevier, Oxford, pp. 103–129.
[4] Kaviany, M., 1995, *Principles of Heat Transfer in Porous Media*, 2nd ed., Springer, New York.
[5] Quintard, M., Kaviany, M., and Whitaker, S., 1997, "Two-Medium Treatment of Heat Transfer in Porous Media: Numerical Results for Effective Properties," Adv. Water Resour., **20**, pp. 77–94.
[6] Ochoa-Tapia, J. A., and Whitaker, S., 1997, "Heat Transfer at the Boundary Between a Porous Medium and a Homogeneous Fluid," Int. J. Heat Mass Transfer, **40**, pp. 2691–2707.
[7] Kuwahara, F., Shirota, M., and Nakayama, A., 2001, "A Numerical Study of Interfacial Convective Heat Transfer Coefficient in Two-Energy Equation Model for Convection in Porous Media," Int. J. Heat Mass Transfer, **44**, pp. 1153–1159.
[8] Nakayama, A., Kuwahara, F., Sugiyama, M., and Xu, G., 2001, "A Two-Energy Equation Model for Conduction and Convection in Porous Media," Int. J. Heat Mass Transfer, **44**, pp. 4375–4379.
[9] Hsu, C. T., 1999, "A Closure Model for Transient Heat Conduction in Porous

Media," ASME J. Heat Transfer, **121**, pp. 733–739.
[10] Nield, D. A., and Bejan, A., 1992, *Convection in Porous Media*, Springer, New York.
[11] Bear, J., 1972, *Dynamics of Fluids in Porous Media*, American Elsevier, New York.
[12] Sahraouri, M., and Kaviany, M., 1994, "Direct Simulation Versus Volume-Averaged Treatment of Adiabatic, Premixed Flame in a Porous Medium," Int. J. Heat Mass Transfer, **37**(18), pp. 2817–2834.
[13] Saito, M. B., and de Lemos, M. J. S., 2005, "Interfacial Heat Transfer Coefficient for NonEquilibrium Convective Transport in Porous Media," Int. Commun. Heat Mass Transfer, **32**(5), pp. 667–677.
[14] Gray, W. G., and Lee, P. C. Y., 1977, "On the Theorems for Local Volume Averaging of Multiphase System," Int. J. Multiphase Flow, **3**, pp. 333–340.
[15] Pedras, M. H. J., and de Lemos, M. J. S., 2000, "On the Definition of Turbulent Kinetic Energy for Flow in Porous Media," Int. Commun. Heat Mass Transfer, **27**(2), pp. 211–220.
[16] Pedras, M. H. J., and de Lemos, M. J. S., 2001, "Macroscopic Turbulence Modeling for Incompressible Flow Through Undeformable Porous Media," Int. J. Heat Mass Transfer, **44**(6), pp. 1081–1093.
[17] Pedras, M. H. J., and de Lemos, M. J. S., 2001, "Simulation of Turbulent Flow in Porous Media Using a Spatially Periodic Array and a Low-Re Two-Equation Closure," Numer. Heat Transfer, Part A, **39**(1), pp. 35–59.
[18] Pedras, M. H. J., and de Lemos, M. J. S., 2001, "On the Mathematical Description and Simulation of Turbulent Flow in a Porous Medium Formed by an Array of Elliptic Rods," J. Fluids Eng., **123**(4), pp. 941–947.
[19] Pedras, M. H. J., and de Lemos, M. J. S., 2003, "Computation of Turbulent Flow in Porous Media Using a Low Reynolds k-ϵ Model and an Infinite Array of Transversally-Displaced Elliptic Rods," Numer. Heat Transfer, Part A, **43**(6), pp. 585–602.
[20] Rocamora, F. D. Jr., and de Lemos, M. J. S., 2000, "Analysis of Convective Heat Transfer of Turbulent Flow in Saturated Porous Media," Int. Commun. Heat Mass Transfer, **27**(6), pp. 825–834.
[21] de Lemos, M. J. S., and Braga, E. J., 2003, "Modeling of Turbulent Natural Convection in Saturated Rigid Porous Media," Int. Commun. Heat Mass Transfer, **30**(5), pp. 615–624.
[22] Braga, E. J., and de Lemos, M. J. S., 2004, "Turbulent Natural Convection in a Porous Square Cavity Computed with a Macroscopic k-ϵ Model," Int. J. Heat Mass Transfer, **47**(26), pp. 5639–5650.
[23] Braga, E. J., and de Lemos, M. J. S., 2005, "Heat Transfer in Enclosures Having a Fixed Amount of Solid Material Simulated with Heterogeneous and Homogeneous Models," Int. J. Heat Mass Transfer, **48**(23-24), pp. 4748–4765.
[24] Braga, E. J., and de Lemos, M. J. S., 2000, "Laminar Natural Convection in Cavities Filled with Circular and Square Rods," Int. Commun. Heat Mass Transfer, **32**(10), pp. 1289–1297.
[25] de Lemos, M. J. S., and Mesquita, M. S., 2003, "Turbulent Mass Transport in Saturated Rigid Porous Media," Int. Commun. Heat Mass Transfer, **30**(1), pp. 105–113.
[26] de Lemos, M. J. S., and Tofaneli, L. A., 2004, "Modeling of Double-Diffusive Turbulent Natural Convection in Porous Media," Int. J. Heat Mass Transfer, **47**(19-20), pp. 4221–4231.
[27] de Lemos, M. J. S., and Pedras, M. H. J., 2001, "Recent Mathematical Models for Turbulent Flow for Saturated Rigid Porous Media," J. Fluids Eng., **123**(4), pp. 935–940.
[28] Silva, R. A., and de Lemos, M. J. S., 2003, "Numerical Analysis of the Stress Jump Interface Condition for Laminar Flow over a Porous Layer," Numer. Heat Transfer, Part A, **43**(6), pp. 603–617.
[29] Silva, R. A., and de Lemos, M. J. S., 2003, "Turbulent Flow in a Channel Occupied by a Porous Layer Considering the Stress Jump at the Interface," Int. J. Heat Mass Transfer, **46**(26), pp. 5113–5121.
[30] de Lemos, M. J. S., 2005, "Turbulent Kinetic Energy Distribution Across the Interface Between a Porous Medium and a Clear Region," Int. Commun. Heat Mass Transfer, **32**(1-2), pp. 107–115.
[31] de Lemos, M. J. S., and Silva, R. A., 2006, "Turbulent Flow Over A Layer Of A Highly Permeable Medium Simulated With A Diffusion-Jump Model For The Interface," Int. J. Heat Mass Transfer, **49**(3-4), pp. 546–556.
[32] de Lemos, M. J. S., and Rocamora, F. D., 2002, "Turbulent Transport Modeling for Heated Flow in Rigid Porous Media, in *Proceedings of the Twelfth International Heat Transfer Conference*, Grenoble, France, August 18–23, pp. 791–795.
[33] Launder, B. E., and Spalding, D. B., 1974, "The Numerical Computation of Turbulent Flows," Comput. Methods Appl. Mech. Eng., **3**, pp. 269–289.
[34] Hsu, C. T., and Cheng, P., 1990, "Thermal Dispersion in a Porous Medium," Int. J. Heat Mass Transfer, **33**, pp. 1587–1597.
[35] Whitaker, S., 1966, "Equations of Motion in Porous Media," Chem. Eng. Sci., **21**, pp. 291–300.
[36] Whitaker, S., 1967, "Diffusion and Dispersion in Porous Media," AIChE J., **13**(3), pp. 420–427.
[37] Masuoka, T., and Takatsu, Y., 1996, "Turbulence Model for Flow Through Porous Media," Int. J. Heat Mass Transfer, **39**(13), pp. 2803–2809.
[38] Kuwahara, F., Nakayama, A., and Koyama, H., 1996, "A Numerical Study of Thermal Dispersion in Porous Media," ASME J. Heat Transfer, **118**, pp. 756–761.
[39] Kuwahara, F., and Nakayama, A., 1998, "Numerical Modeling of Non-Darcy Convective Flow in a Porous Medium, *Heat Transfer 1998, Proceedings of the 11th Int. Heat Transf. Conf.*, Kyongyu, Korea, Taylor and Francis, Washington, D.C., Vol. 4, pp. 411–416.
[40] Kuwahara, F., Kameyama, Y. Yamashita, S. and Nakayama, A., 1998, "Numerical Modeling of Turbulent Flow in Porous Media Using a Spatially Periodic Array," J. Porous Media, **1**(1), pp. 47–55.
[41] Ergun, S., 1952, "Fluid Flow Through Packed Columns," Chem. Eng. Prog., **48**, pp. 89–94.
[42] Nakayama, A., and Kuwahara, F., 1999, "A Macroscopic Turbulence Model for Flow in a Porous Medium," J. Fluids Eng., **121**, pp. 427–433.
[43] Lee, K., and Howell, J. R., 1987, "Forced Convective and Radiative Transfer Within a Highly Porous Layer Exposed to a Turbulent External Flow Field," in *Proceedings of the 1987 ASME-JSME Thermal Engineering Joint Conf.*, Honolulu, Hawaii, ASME, New York, Vol. 2, pp. 377–386.
[44] Antohe, B. V., and Lage, J. L., 1997, "A General Two-Equation Macroscopic Turbulence Model for Incompressible Flow in Porous Media," Int. J. Heat Mass Transfer, **40**(13), pp. 3013–3024.
[45] Getachewa, D., Minkowycz, W. J., and Lage, J. L., 2000, "A Modified Form of the k-ϵ Model for Turbulent Flow of a Incompressible Fluid in Porous Media," Int. J. Heat Mass Transfer, **43**, pp. 2909–2915.
[46] Slattery, J. C., 1967, "Flow of Viscoelastic Fluids Through Porous Media," AIChE J., **13**, pp. 1066–1071.
[47] Forchheimer, P., 1901, "Wasserbewegung durch Boden," Z. Ver. Deutsch. Ing., **45**, pp. 1782–1788.
[48] Wakao, N., Kaguei, S., and Funazkri, T., 1979, "Effect of Fluid Dispersion Coefficients on Particle-to-Fluid Heat Transfer Coefficients in Packed Bed," Chem. Eng. Sci., **34**, pp. 325–336.
[49] Patankar, S. V., 1980, *Numerical Heat Transfer and Fluid Flow*, Hemisphere, Washington, D.C.
[50] Zhukauskas, A., 1972, "Heat Transfer from Tubes in Cross Flow," Adv. Heat Transfer, **8**, pp. 93–160.

Convective Heat Transfer in a Rectangular Channel Filled With Sintered Bronze Beads and Periodically Spaced Heated Blocks

Sheng Chung Tzeng
Associate Professor
Department of Mechanical Engineering,
Chienkuo Technology University,
Changhua 500, Taiwan, R.O.C.
e-mail: tsc@ctu.edu.tw; tsc33@ms32.hinet.net

This work numerically investigated the steady state fluid flow and heat transfer behaviors associated with a sintered porous channel that contains periodically spaced heated blocks. Some typical cases are experimentally examined in this study. The relevant varied parameters were the average bead diameter (d)*, the relative block height* (h/H)*, the relative block width* (w/H)*, the relative block spacing* (s/H)*, and the Reynolds number (Re). The numerical results revealed a lack of global recirculation in regions between the blocks, where the forced convective heat transfer was low, but the heat in those regions was transferred to the metallic block by conduction through porous media, before being dissipated into the fluid that passed over the zone above the heated block. Additionally, the relevant parameters considerably affect the local Nusselt number distribution along the periphery of the block surface. The average Nusselt number for each block decreased along the direction of the flow until it reached its fully developed value. The Nusselt number increased with* h/H *or Re in the fully developed region. The effect of* h/H *on the fully developed Nusselt number became stronger as Re increased and* w/H *decreased. The effects of* s/H *and d on the fully developed Nusselt number were insignificant over the ranges of parameters considered herein (*$d=0.7$ *and* 1.16 mm, $h/H=0.12-0.59$, $w/H=0.24-0.47$, $s/H=0.24-0.7$, *and* $\mathrm{Re}=1019-5059$*). Finally, this study summarized the average Nusselt number for different configurations of the heated blocks with various d,* h/H, w/H, s/H, *and Re.* [DOI: 10.1115/1.2175151]

Keywords: sintered porous channel, periodically spaced heated blocks, convective heat transfer

1 Introduction

The electronics industry is manufacturing denser and more powerful products, and so requires better cooling technology. Typically, the power density values at the chip level of plastic DIPs and PGA ceramic packages are around 10 and 25 $\mathrm{W/cm^2}$, respectively [1,2]. The cooling technology by conventional air-handling methods is insufficient in most cases. Therefore, more effective cooling is required. Investigating the convective cooling of heated blocks mounted on a channel wall is valuable because such blocks are used to simulate heated electronic components. Some investigations of channels with heated block or filled with various porous materials were reported.

Kang et al. [3] experimentally studied mixed convective heat transfer from a heated module on a horizontal plate. Their data revealed that the heat transfer and fluid flow characteristics varied strongly with the mixed convection parameter, $\mathrm{Gr/Re^{5/2}}$. A transition range for their system in the external flow was observed to be $\mathrm{Gr/Re^{5/2}}=0.9-1.1$. The average Nusselt number was found to drop as $\mathrm{Gr/Re^{5/2}}$ increased. Kang et al. also determined that the Nusselt number at the left face of the heated module was the largest of any of the three faces because of the impact of the external flow. Kim et al. [4] numerically examined mixed convective flow around three blocks in both horizontal and vertical channels. Details of the flow and thermal fields for various Reynolds numbers and Grashof numbers were provided. They reported the largest heat transfer in the first block, declining progressively downstream. They also demonstrated that the cooling efficiency of the vertical channel was slightly higher than that of the horizontal channel because of the buoyancy effect. Young and Vafai [5,6] numerically studied in a comprehensive manner the fluid and thermal transport in a two-dimensional channel that contained a heated block or multiple heated blocks. The effects of the number of blocks and their width, height, and spacing as well as the heating method, solid thermal conductivity, and flow rate were considered. Their results indicated that smaller, more widely spaced blocks were associated with better heat transfer performance. Narrow gaps between blocks were found to allow upstream thermal transport, which, in some cases, actually heated the upstream blocks.

Hunt and Tien [7] experimentally measured forced convection in channels filled with various porous foam materials. Forced convection in horizontal square channels through packed spheres was investigated by Chou et al. [8]. Hwang and Chao [9] and Hwang et al. [10] measured heat transfer through channels filled with a porous media made of sintered beads, and numerically solved the two-equation model to make accurate predictions. Peterson and Chang [11] experimentally investigated two-phase dissipation in porous channels of various sizes filled with sintered copper beads. Calmidi and Mahajan [12] experimentally and numerically examined the forced convection in highly porous aluminum foams, using air as the cooling fluid. Angirasa [13,14] studied the forced

Contributed by the Heat Transfer Division of ASME for publication in the JOURNAL OF HEAT TRANSFER. Manuscript received May 16, 2005; final manuscript received October 31, 2005. Review conducted by Jose L. Lage.

convective heat transfer in metallic fibrous materials with various porosities and fiber thicknesses. Jiang et al. [15,16] investigated heat transfer by forced convection in sintered porous channels. The studies cited herein provide insights into the transfer of heat by porous metallic materials. The results of these investigations reveal that a porous material can be used as an extremely effective heat sink, possibly providing an effective means of cooling circuit boards on which heat-generating electronic components are mounted.

Recently, porous materials are employed to promote heat transfer in a channel with discrete heated sources. Rizk and Kleinstreuer [17] analyzed laminar forced convection on discrete heated blocks in a porous channel. They presented empirical correlations between Reynolds number and heat transfer coefficient associated with the porous material and the solid blocks. By comparing the traditional open channel with their results indicated that the heat transfer enhancement of the porous channel was about 50%. Hadim [18] numerically studied forced convection in a partially porous channel that contained discrete heat sources on the bottom wall. He reported that heat transfer increased as the Darcy number declined, especially at the leading edge of each heat source. Hadim and Bethancourt [19] extended the work of Hadim [18]. They numerically examined the effects of the spacing between heat sources and the width of the heat source on heat transfer. Their results indicated that increasing the spacing between heat sources insignificantly increased the heat transfer. As the width of the heat source decreased, the heat transfer enhancement was only moderate. Oild-Amer et al. [20] analyzed the effect of porous inserts between the heated blocks. They found that porous inserts increased the heat transfer rate on the vertical sides of the blocks. The heat transfer from multiple heated blocks with porous covers in a channel was studied by Huang et al. [21]. The global recirculation caused by the blocks substantially increased the heat transfer rate on both the top and the downstream faces of the second and the subsequent blocks.

This work was motivated by the fact that few numerical studies have addressed the effects of the size and spacing of the heated blocks on the fluid flow and the convective heat transfer. The lack of experimental data in this area has required the completion of experimental measurements for comparison with the numerical results.

This work numerically investigated the fluid flow behavior and the heat transfer mechanisms associated with a porous channel. The channel filled with a porous media made of sintered bronze beads was discretely heated through periodically spaced metallic blocks and cooled by air flow. Some typical cases were experimentally examined. The local temperatures and the heat transfer characteristics of each heated block were studied. The varied parameters were the average bead diameter (d), the relative block height (h/H), the relative block width (w/H), the relative block spacing (s/H), and the Reynolds number (Re). The findings can be used to improve the cooling performance of heated blocks, where the blocks are used to simulate heated electronic components, by sintered metallic porous media.

2 Numerical Analysis

2.1 Basic Assumptions and Governing Equations. Figure 1 presents the configuration of the problem studied herein. It involves air flow through a parallel plate channel with periodically spaced blocks on the bottom plate. The blocks are heated under isoflux conditions and the upper and bottom plates are assumed to be adiabatic. The air enters the channel at uniform temperature T_i and uniform velocity u_i. The other assumptions and simplifications are as follows: (1) the porous medium is homogenous and isotropic; (2) the fluid flow is steady state, laminar and incompressible; (3) the thermophysical properties of the fluid and porous media do not depend on temperature. Hence, the flow in the

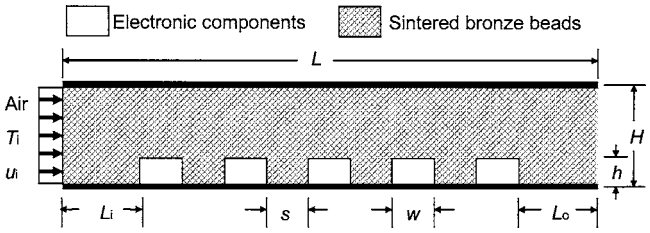

Fig. 1 Schematic diagram of the porous channel with heated electronic components

channel can be specified using the following volume-averaged conservation equations of continuity, momentum and energy [22–24].

$$\frac{\partial u}{\partial x}+\frac{\partial v}{\partial y}=0 \tag{1}$$

$$\frac{\rho_f}{\varepsilon^2}\left(u\frac{\partial u}{\partial x}+v\frac{\partial u}{\partial y}\right)=-\frac{\partial p}{\partial x}-\frac{\mu}{K}u-\frac{\rho_f C_F}{\sqrt{K}}(\sqrt{u^2+v^2})u+\frac{\mu}{\varepsilon}\left(\frac{\partial^2 u}{\partial x^2}+\frac{\partial^2 u}{\partial y^2}\right) \tag{2}$$

$$\frac{\rho_f}{\varepsilon^2}\left(u\frac{\partial v}{\partial x}+v\frac{\partial v}{\partial y}\right)=-\frac{\partial p}{\partial y}-\frac{\mu}{K}v-\frac{\rho_f C_F}{\sqrt{K}}(\sqrt{u^2+v^2})v+\frac{\mu}{\varepsilon}\left(\frac{\partial^2 v}{\partial x^2}+\frac{\partial^2 v}{\partial y^2}\right) \tag{3}$$

$$(\rho C_p)_f\left(u\frac{\partial T_f}{\partial x}+v\frac{\partial T_f}{\partial y}\right)=h_{fs}a_{fs}(T_s-T_f)+(k_f^*+k_d)\left(\frac{\partial^2 T_f}{\partial x^2}+\frac{\partial^2 T_f}{\partial y^2}\right) \tag{4}$$

$$0=h_{fs}a_{fs}(T_f-T_s)+k_s^*\left(\frac{\partial^2 T_s}{\partial x^2}+\frac{\partial^2 T_s}{\partial y^2}\right) \tag{5}$$

where K is the permeability, C_F is the inertial coefficient, ε is the porosity, k_s^* is the effective conductivity of the solid and depends on both the geometry of the porous medium and the conductivity of the solid, k_f^* is the effective conductivity of the fluid and is given simply as εk_f, k_d is the thermal dispersion conductivity, a_{fs} is the surface area of the fluid-solid interface per unit bulk volume of the packed bed, and h_{fs} is the heat transfer coefficient between the fluid stream and the solid matrix. Notably, the relevant empirical coefficients in the present numerical model, such as K, C_F, k_s^*, k_d, and h_{fs}, generally do not have universal values. This is because that these empirical coefficients mainly depend on the geometry of the porous medium, the thermal properties of the solid and the fluid, and the flow rate. Additionally, the sintered process changes the inner structure of the sintered porous material, resulting in different values of K, C_F, k_s^*, k_d, and h_{fs} from those for the non-sintered porous medium. Moreover, all these empirical coefficients are difficultly measured. This work contributes to build a numerical model for sintered porous channels by measuring the K, C_F, and k_s^* values and finding the suitable empirical formula of k_d and h_{fs} in the open literatures. The section of the test apparatus and instrumentation addresses the values of K, C_F, and k_s^* considered herein. The thermal properties, k_d, a_{fs}, and h_{fs}, of the sintered bronze beads are taken from Hwang and Chao [9], Hwang et al. [10], Chen and Hsu [25], Chen et al. [26], Kar and Dybbs [27], and Gamson et al. [28]

$$k_d=lD_t\,\mathrm{Pr}\,\mathrm{Re}_d\,k_f \tag{6}$$

$$l=\{1+(3d_p/H^*)[\exp(-H^*/3d_p)-1]\} \tag{7}$$

$$H^*=H \text{ for the regions between blocks}$$
$$=(H-h) \text{ for the regions above blocks} \tag{8}$$

$$h_{fs} = 0.004\left(\frac{d_v}{d_p}\right)^{0.35}\left(\frac{k_f}{d_p}\right)\mathrm{Pr}^{0.33}\,\mathrm{Re}_d^{1.35} \quad \text{for } \mathrm{Re}_d \leqslant 75$$

$$= 1.064\left(\frac{k_f}{d_p}\right)\mathrm{Pr}^{0.33}\,\mathrm{Re}_d^{0.59} \quad \text{for } \mathrm{Re}_d$$

$$\geqslant 350 \text{ for the porous medium}$$

$$= 0 \text{ for the blocks} \tag{9}$$

$$a_{fs} = 20.346(1-\varepsilon)\varepsilon^2/d_p \text{ for the porous medium}$$

$$= 0 \text{ for the blocks} \tag{10}$$

where l represents the wall function for transverse thermal dispersion, D_t is the thermal dispersion constant that equals 0.375, d_p is the average bead diameter; d_v $(=4\varepsilon/a_{fs})$ is the average void diameter, the bead Reynolds number Re_d is based on the bead diameter and the local velocity, and h_{fs} is evaluated by interpolation at $\mathrm{Re}_d=75-350$. Additionally, according to the results of Fu and Huang [29], the local Nusselt number distribution of the random porosity model are more similar to those of the constant porosity model than those of the variable porosity model. Therefore, a constant porosity value was used in this numerical simulation.

Equations (1)–(5) can be nondimensionalized by introducing the following variables:

$$X=\frac{x}{H},\quad Y=\frac{y}{H},\quad U=\frac{u}{u_i},\quad V=\frac{v}{u_i},\quad \mathrm{Pr}=\frac{\mu/\rho_f}{k_f/(\rho C_p)_f},\quad \mathrm{Da}=\frac{K}{H^2},$$

$$\mathrm{Re}=\frac{\rho_f u_i H}{\mu},\quad U_M=\frac{\sqrt{u^2+v^2}}{u_i},\quad \theta=\frac{T-T_i}{q_w H/k_f},\quad \mathrm{Nu}_{fs}=\frac{h_{fs}a_{fs}H^2}{k_f} \tag{11}$$

The vorticity-transport equation is determined by replacing the velocity components with the vorticity (ω) and the stream function (Ψ)

$$\omega = -\frac{\partial U}{\partial Y}+\frac{\partial V}{\partial X},\quad U=\frac{\partial \Psi}{\partial Y},\quad V=-\frac{\partial \Psi}{\partial X} \tag{12}$$

The dimensionless governing equations as follows:

$$-\omega = \frac{\partial^2\Psi}{\partial X^2}+\frac{\partial^2\Psi}{\partial Y^2} \tag{13}$$

$$U\frac{\partial \omega}{\partial X}+V\frac{\partial \omega}{\partial Y} = -\frac{\varepsilon^2}{\mathrm{Re}\cdot\mathrm{Da}}\omega-\frac{\varepsilon^2 C_F U_M}{\sqrt{\mathrm{Da}}}\omega+\frac{\varepsilon^2 C_F}{\sqrt{\mathrm{Da}}}\left(U\frac{\partial U_M}{\partial Y}-V\frac{\partial U_M}{\partial X}\right)$$
$$+\frac{\varepsilon}{\mathrm{Re}}\left(\frac{\partial^2\omega}{\partial X^2}+\frac{\partial^2\omega}{\partial Y^2}\right) \tag{14}$$

$$U\frac{\partial \theta_f}{\partial X}+V\frac{\partial \theta_f}{\partial Y} = \frac{\mathrm{Nu}_{fs}}{\mathrm{Re}\,\mathrm{Pr}}(\theta_s-\theta_f)+\frac{1}{\mathrm{Re}\,\mathrm{Pr}}\frac{k_f^*+k_d}{k_f}\left(\frac{\partial^2\theta_f}{\partial X^2}+\frac{\partial^2\theta_f}{\partial Y^2}\right) \tag{15}$$

$$0 = \mathrm{Nu}_{fs}(\theta_f-\theta_s)+\frac{k_s^*}{k_f}\left(\frac{\partial^2\theta_s}{\partial X^2}+\frac{\partial^2\theta_s}{\partial Y^2}\right) \tag{16}$$

In the blocks, $\mathrm{Da}=\Psi=0$, yielding $\omega=0$ and then $U=V=0$. Also, $\mathrm{Nu}_{fs}=k_f^*=k_d=0$.

2.2 Boundary Conditions. Figure 2 schematically depicts the numerical domain and the boundary conditions. Roache [30] elucidated the boundary conditions of the vorticity-transport equation. Additionally, when the blocks are employed to simulate the electronic components, two heat input approaches are typically utilized. One is isoflux at the block base and the other is uniform volumetric energy generation in the block. However, Young and Vafai [6] demonstrated that differences between the isotherms in the two heating cases are very small when the value of k_b/k_f is very large (k_b is the thermal conductivity of the block and k_f is the thermal conductivity of the fluid). The value of k_b/k_f in the present work is very high because the copper block is used as a heat spreader. Therefore, the isoflux condition is applied to the bottom surfaces of the blocks in this work. The temperature gradients of the solid phase and the fluid phase are zero on the adiabatic wall. The fluid is assumed to enter the inlet at a uniform temperature, T_i. The fluid phase at the exit is assumed to meet the zero diffusion condition. The following characteristics of the solid phase, reported by Hwang et al. [10], are assumed. At the interfaces between the blocks and the porous media, the nonslip condition, and the continuity of temperature and heat flux are assumed to apply

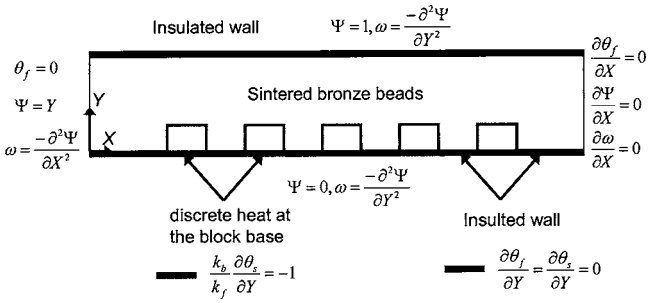

Fig. 2 Schematic diagram of numerical domain with boundary conditions

$$\frac{\partial \theta_s}{\partial X} = 1.29 l D_t\left(\frac{d_v}{d_p}\right)^{0.5}\left(\frac{k_f}{k_s^*}\right)\left(\frac{H}{d_v}\right)\mathrm{Pr}^{1.4}\,\mathrm{Re}_d^{1.5}\,\theta_s \quad \text{at } X=0 \tag{17}$$

$$\frac{\partial \theta_s}{\partial X} = -0.2776 l D_t\left(\frac{k_f}{k_s^*}\right)\left(\frac{H}{d_p}\right)\mathrm{Pr}^{1.4}\,\mathrm{Re}_d^{1.5}(\theta_s-\theta_f) \quad \text{at } X=L/H \tag{18}$$

$$U=V=0,\quad \theta_f=\theta_s,\quad k_b\frac{\partial\theta_s}{\partial N}=k_s^*\frac{\partial\theta_s}{\partial N}+k_f^*\frac{\partial\theta_f}{\partial N}$$
$$\text{at block/porous interfaces} \tag{19}$$

where l, Dt, d_p, d_v, and Re_d were defined according to Eqs. (6)–(10); k_b is the thermal conductivity of the block, and N is the dimensionless coordinate normal to the block surface. The validity and accuracy of the exit boundary conditions used herein was verified by comparing velocity and temperature profiles obtained for $L_o/H=0.93$ with those obtained for an extended computational domain $L_o/H=6$. The results had a good agreement between the two cases.

2.3 Numerical Procedure. The governing equations were discretized using the power-law scheme proposed by Patankar [31]. The stream function equation and the vorticity transport equation were solved simultaneously and iteratively [32]. The velocity components U and V were obtained from the stream function. When the velocity components had been determined, the energy equation was solved to yield the temperature distribution. All discretized algebraic equations were solved using the strong implicit solver (SIS) algorithm developed by Lee [33]. The convergence criterion was $\mathrm{Max}|(F^{(n)}-F^{(n-1)})/(F_{\max}^{(n)}-F_{\min}^{(n)})| \leqslant 1\times10^{-5}$, where F was Ψ, ω, θ_f or θ_s. The local Nusselt number (Nu) on the channel wall and the local Nusselt number (Nu_p) along the periphery of the block surface are defined as

$$\mathrm{Nu} = \frac{q_w H}{k_f(T_w-T_i)} = -\left(\frac{k_s^*}{k_f}\frac{\partial\theta_s}{\partial Y}+\frac{k_f^*}{k_f}\frac{\partial\theta_f}{\partial Y}\right)\Big/\,\theta_w \tag{20}$$

Table 1 Results from grid dependency simulations

Grid size	$\overline{\mathrm{Nu}}$ for the first block	$\overline{\mathrm{Nu}}$ for the third block	$\overline{\mathrm{Nu}}$ for the fifth block
201×81	1771.3	889.6	681.5
151×61	1771.2	889.6	681.5
151×41	1764.6	887.1	679.3
101×21	1752.3	880.7	675.4

$$\mathrm{Nu}_p = \frac{q_{w,p}H}{k_f(T_p - T_i)} = -\left(\frac{k_s^*}{k_f}\frac{\partial\theta_{s,p}}{\partial N} + \frac{k_f^*}{k_f}\frac{\partial\theta_{f,p}}{\partial N}\right)\Bigg/\theta_p \qquad (21)$$

where q_w is the heat flux of the heated wall, $q_{w,p}$ is the heat flux along the periphery of the block surface, θ_w is the dimensionless temperature on the channel wall conjugated with the blocks or the porous medium, θ_p is the dimensionless block surface temperature, and N is the dimensionless coordinate normal to the block surface. The average Nusselt number ($\overline{\mathrm{Nu}}$) for each block is the integral average value of Nu (defined in Eq. (20)). It is obtained from the block length.

2.4 Grid Dependency and Code Validation. A nonuniform rectangular grid system was employed. The typical case with sample-1, $L_i/H=0.93$, $L_o/H=0.93$, $n=5$, $h/H=0.36$, $s/H=0.47$, $w/H=0.47$, $\mathrm{Re}=3057$ was used for grid tests. Table 1 lists the results from grid dependency simulations. Based on the grid dependence study, the grid parameters (151×61) listed in the second row were used for all computations.

In order to validate the code, numerical results were compared with the relevant cases reported by Hadim [18]. Hadim [18] studied the problem that in a porous channel with four strip heat sources for $\varepsilon=0.97$, $C_F=0.1$, $L_i/H=1$, $L_o/H=7$, $n=4$, $h/H=0$, $s/H=1$, $w/H=1$, $\mathrm{Pr}=10$, and $(k_s^*+k_f^*)/k_f=1$ at $\mathrm{Da}=1\times10^{-6}$ and 1×10^{-3}, as well as $\mathrm{Re}=20$ and 1000. Since the numerical study performed by Hadim [18] was achieved by the one-equation model, a sufficiently large value was employed for Nu_{fs} in the present model. The results, as shown in Fig. 5, agree to better than 3% with data reported by Hadim [18].

3 Experiments

3.1 Test Apparatus and Instrumentation. The experimental setup displayed in Fig. 3 was divided into four main parts: (1) air supply system; (2) test section; (3) test specimens; and (4) data acquisition system. The air compressor (MITSUISEIKI 10 HP) blew air into the air tank. Then, the air flowed through a filter to remove the oil, water, and particles. Finally, the air entered the test section after it passed through the straightener made of an unheated porous specimen. The air flow rate was controlled by an electric digital flowmeter with the range of 0–1000 l/min. The test section was made of 40-mm-thick Bakelite. The dimensions of the channel section were 52 mm×8.5 mm. The channel was filled with test specimens of size 52 mm×8.5 mm×52 mm. The test specimens were made of sintered bronze beads with periodically inserted copper blocks. The separation between each pair of copper blocks of size 52 mm×3 mm×4 mm was 4 mm. A film heater was fixed on the bottom surface of the copper blocks. Available with the thermal grease as its adhesion agent, the top plate of the film heater was provided with 52 mm×8.5 mm ×52 mm Teflon material for insulation so as to prevent the stainless film heater from contacting the sintered porous channel, which would affect the thermocouple measurement signal. The wall heat fluxes supplied to the film heater from the electronic power were 1.5–4.3 W/cm^2 for 50–250 l/min flow rate.

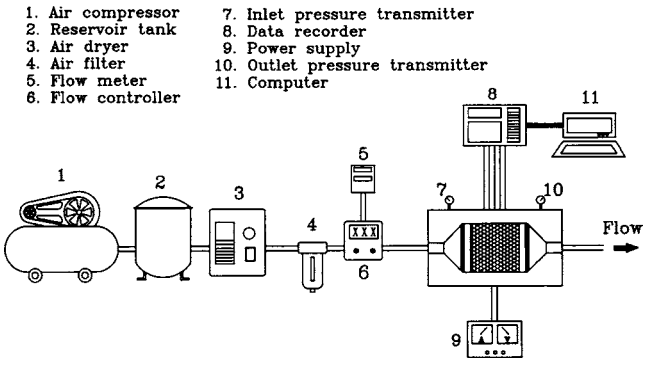

Fig. 3 Experimental apparatus

Table 2 Physical properties of sintered bronze beads

Samples	1	2
average bead diameter, d (mm)	0.70 (0.62–0.80)[a]	1.16 (1.00–1.42)[a]
porosity, ε	0.37	0.39
thermal conductivity, k_s^* (W/m °C)	10.73	10.45
permeability, $K\times10^{10}$ (m^2)	2.83	6.70
inertial coefficient, C_F	0.239	0.171

[a]The diameter ranges of beads

The average diameter of the sintered bronze beads in the channel was 0.70 mm and 1.16 mm. Table 2 provides the relevant parameters associated with the porous properties, including the permeability (K), the inertial coefficient (C_F), the effective solid conductivity (k_s^*), and others. The K and C_F values were determined by the method reported by Hunt and Tien [7]. The value of k_s^* was measured by performing several experiments of one-dimensional heat conduction (the test method can be found in Ref. [34]). The total error in the measurement of the effective solid thermal conductivity (k_s^*) was ±3.7%. Notably, the effective solid

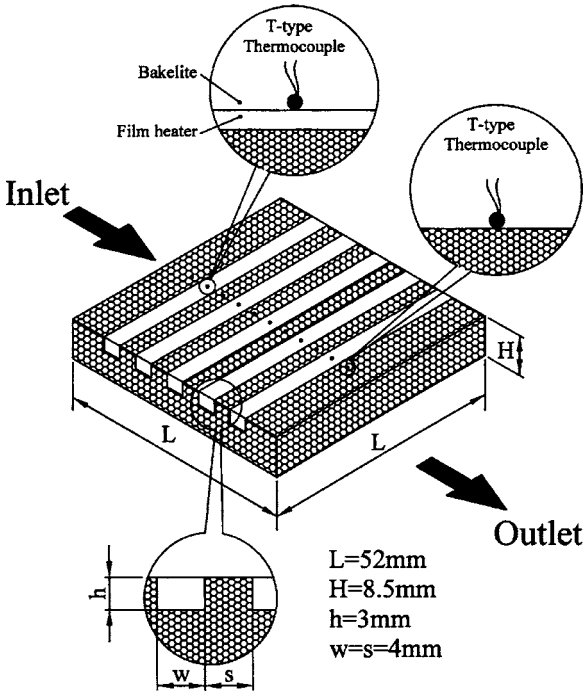

Fig. 4 Physical model of the test section and positions of thermocouples from bottom view

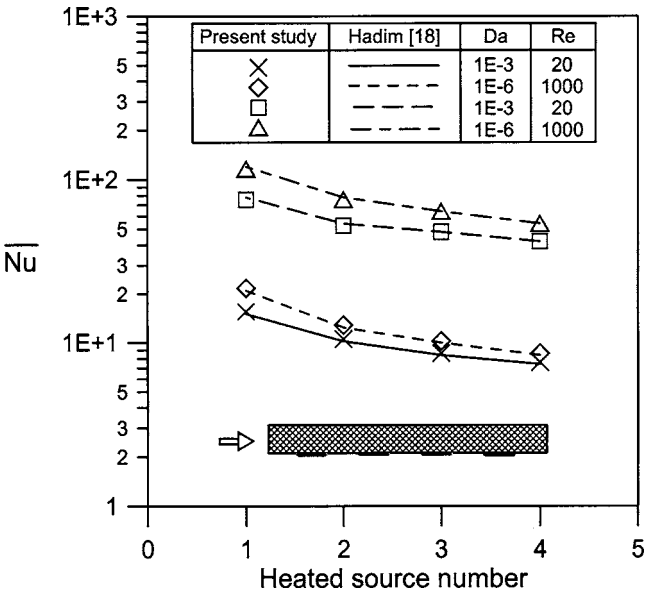

Fig. 5 Comparison of $\overline{Nu}$ on each heat source with that found in Ref. [18]

conductivity determined using $k_s(1-\varepsilon)$, which is commonly used in a numerical study of heat transfer in porous media, greatly exceeds the experimental value. Jiang et al. [15] found the same result.

Eleven OMEGA T-TT-30 thermocouples for measuring the wall temperature were embedded on the interior wall surface of the flow passage, as presented in Fig. 4. Another three thermocouples were employed to monitor the ambient temperature, the air temperature at the channel inlet, and the air temperature at the channel outlet. A total of 14 thermocouples were connected to the data recorder (YOKOGAWA DA100), which will transform the potential difference signal into a temperature value. All the temperature data printed out by the data recorder are then inputted into the computer and converted into data for further analysis. The inlet air temperature was about 23°C. The temperature difference of air between inlet and outlet was about 10–16°C. The wall temperatures were greater than 36°C at the fifth heated block. The system was assumed to be in a steady state when the temperature varied by no more than 0.2°C in 25 min.

3.2 Uncertainty Analysis. The maximum error in the flow rate was about ±5.0% at 50 l/min. The real temperature on the bottom surface of the test specimen should be estimated by $T_w - q_w\delta/k_g$, where δ was the distance between the temperature measurement point to the bottom surface of the test specimen, and k_g was the thermal conductivity of the combination of the thermal grease and the Teflon material. Since the δ was hardly estimated, the T_w was used to replace the real temperature on the bottom surface of the test specimen. Therefore, the errors in the temperature measurements were resulted from the inaccuracies in the recorder readings (about ±0.2°C), and the contact resistance between the film heater and the bottom surface of the test specimen (about ±2°C). The maximum errors in determining the heat flux (q_w), the channel height (H), and fluid conductivity (k_f) were estimated within ±3, ±1, and ±1%, respectively. Uncertainties in parameters were estimated by using the root-sum-square method of Kline and McClintock [35] and Moffat [36]. The experimental data obtained herein revealed that the uncertainties in the Reynolds number and the Nusselt number (as shown in Eq. (20)) were ±5.6 and ±22.0%, respectively.

4 Results and Discussion

The study was conducted to discuss the convective heat transfer in a rectangular channel filled with sintered bronze beads and periodically spaced heated blocks. The relevant varied parameters were h/H, s/H, w/H, Re, as listed in Table 3. The range of Reynolds numbers was Re=1019–5095.

4.1 Experimental Validation. Figures 6(*a*) and 6(*b*) compare the numerical predictions with the experimental result. Figure 6(*a*) shows the nondimensional wall temperature in the flow direction at various Reynolds numbers. The data reveal that the dimensionless wall temperature fell as the Reynolds number increased. This phenomenon is attributed to the effect of forced convection. The measured temperature difference ($T_w - T_i$), heat flux (q_w), and the uncertainties in the nondimensional temperature are listed in Table 4. The comparison results indicated that most of the numerical predictions were consistent with the measured temperature of the

Table 3 Relevant varied parameters for sample, h/H, s/H, w/H, Re

	$h/H=0.12$	$L_i/H=0.93$, $L_o/H=0.93$, $n=5$, Re=1019–5095 $h/H=0.36$	$h/H=0.59$
		Sample-1, $w/H=0.24$, ($L/H=3.962$)	
$s/H=0.235$	*Sample-1*, $w/H=0.47$, ($L/H=5.136$)	Sample-1, $w/H=0.47$, ($L/H=5.136$) Sample-2, $w/H=0.47$, ($L/H=5.136$)	Sample-1, $w/H=0.47$, ($L/H=5.136$)
	Sample-1, $w/H=0.24$, ($L/H=4.901$)	Sample-1, $w/H=0.24$, ($L/H=4.901$)	Sample-1, $w/H=0.24$, ($L/H=4.901$)
$s/H=0.470$	Sample-1, $w/H=0.47$, ($L/H=6.075$) Sample-2, $w/H=0.47$, ($L/H=6.075$)	Sample-1, $w/H=0.47$, ($L/H=6.075$) Sample-2, $w/H=0.47$, ($L/H=6.075$)	Sample-1, $w/H=0.47$, ($L/H=6.075$) Sample-2, $w/H=0.47$, ($L/H=6.075$)
		Sample-1, $w/H=0.24$, ($L/H=5.840$)	
$s/H=0.704$	Sample-1, $w/H=0.47$, ($L/H=7.014$)	Sample-1, $w/H=0.47$, ($L/H=7.014$) Sample-2, $w/H=0.47$, ($L/H=7.014$)	Sample-1, $w/H=0.47$, ($L/H=7.014$)

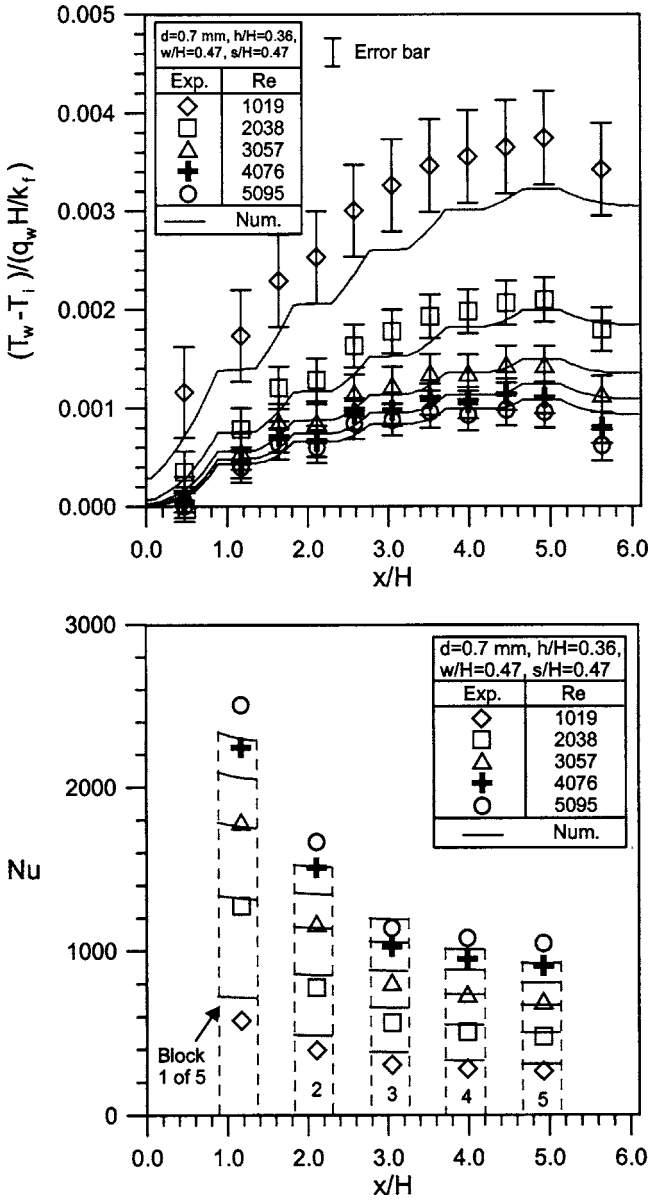

Fig. 6 Comparison of numerical predictions with experimental values (*a*) wall temperatures; (*b*) Nusselt numbers

wall. Figure 6(*b*) displays the Nusselt numbers for each heated block. Experimental results reveal that the Nusselt numbers at the walls of the upstream blocks exceeded those of the downstream blocks. Furthermore, the Nusselt numbers at the walls of the downstream blocks approached constants at a specified Reynolds number. The numerically predicted Nusselt number distributions

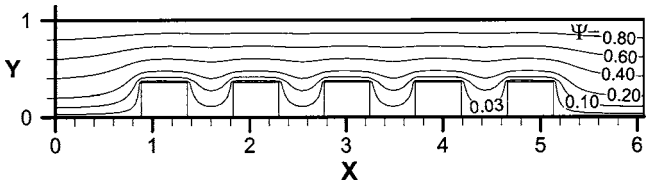

Fig. 7 Streamlines for *d*=0.7 mm, *h*/*H*=0.36, *w*/*H*=0.47, *s*/*H*=0.47, and Re=3057

at the walls were also consistent with the experimental data (the average deviation between numerical predictions and experimental data are less than 16%), indicating that the numerical model used herein accurately simulated the flow and thermal behavior in sintered porous channels that contained multiple heated blocks.

4.2 Flow Behavior and Heat Transfer Mechanism. Inserting metallic blocks into the porous media increased the complexity of the overall fluid flow behavior and the heat transfer mechanism. This section presents numerical results including streamlines, temperature contours, and velocity vectors for typical cases, to elucidate fluid flow behavior and the heat transfer mechanism.

Figure 7 depicts the streamlines in a typical case, with $d=0.70$ mm, $h/H=0.36$, $w/H=0.47$, $s/H=0.47$, and Re=3057. Unlike when many obstacles are present in an empty channel [6] or in a channel partially filled with porous material [18,19], no global recirculation occurred between blocks in a sintered porous channel. All numerical tests revealed this phenomenon, because the sintered bronze beads with low permeability prevented global

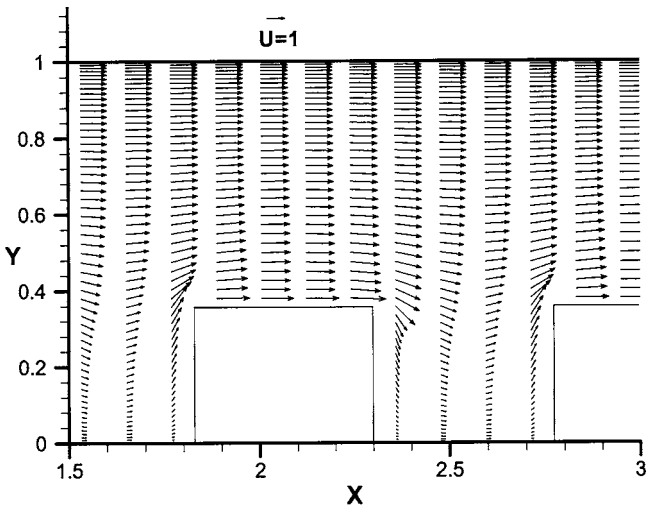

Fig. 8 Velocity vector field for *d*=0.7 mm, *h*/*H*=0.36, *w*/*H*=0.47, *s*/*H*=0.47, Re=3057, and around the second block

Table 4 Measured temperature difference (T_w-T_i) (°C) for *d*=0.70 mm

Re	$q_w(\times 10^{-4})$ (W/m^2)	x/H=	0.47	1.17	1.64	2.11	2.58	3.05	3.52	3.99	4.46	4.93	5.63	Average uncertainty in θ_w ±%[a]
1019	1.5		5.6	8.3	11.0	12.1	14.4	15.6	16.6	17.0	17.5	17.9	16.4	16.2
2038	3.2		3.6	8.2	12.5	13.4	16.9	18.5	20.0	20.6	21.4	21.8	18.6	14.4
3057	3.8		1.5	6.8	10.5	10.4	14.1	15.0	16.6	16.5	17.6	17.5	13.9	17.6
4076	4.3		0.6	6.3	10.0	9.4	13.3	13.8	15.4	14.9	16.1	15.6	11.3	19.3
5095	4.3		0.1	5.6	9.0	8.4	11.9	12.3	13.5	13.0	13.8	13.4	8.7	22.0

[a]Except the data at $x/H=0.47$

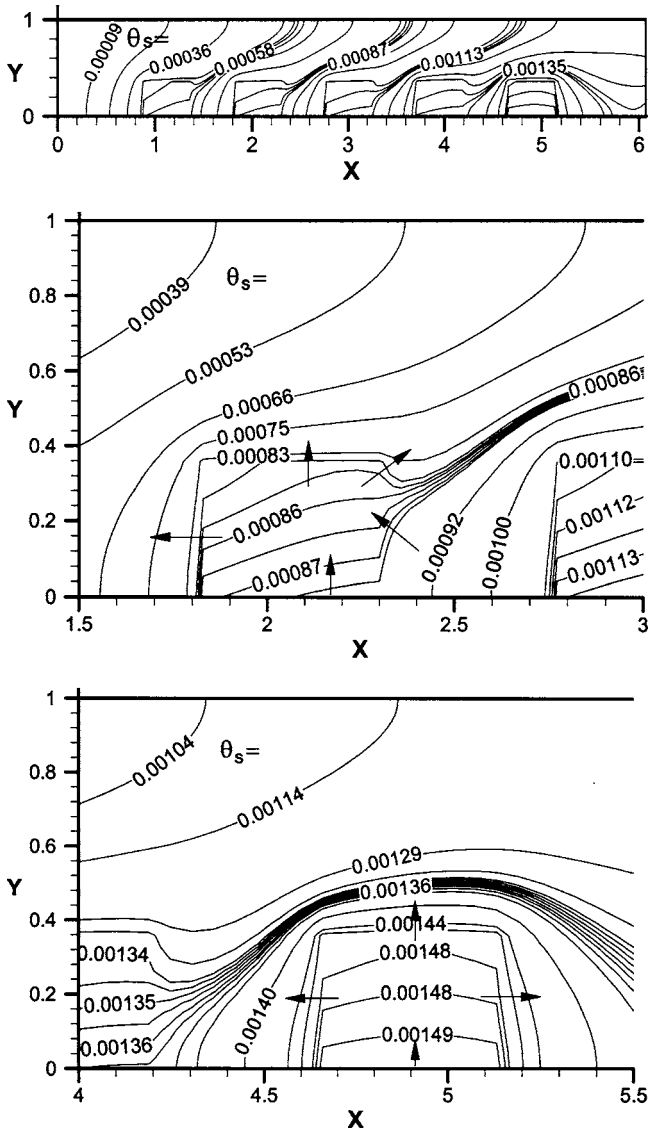

Fig. 9 Solid isotherms for d=0.7 mm, h/H=0.36, w/H=0.47, s/H=0.47, and Re=3057. (*a*) Solid temperature for all computational domain. (*b*) Solid temperature around the second block. (*c*) Solid temperature around the fifth block.

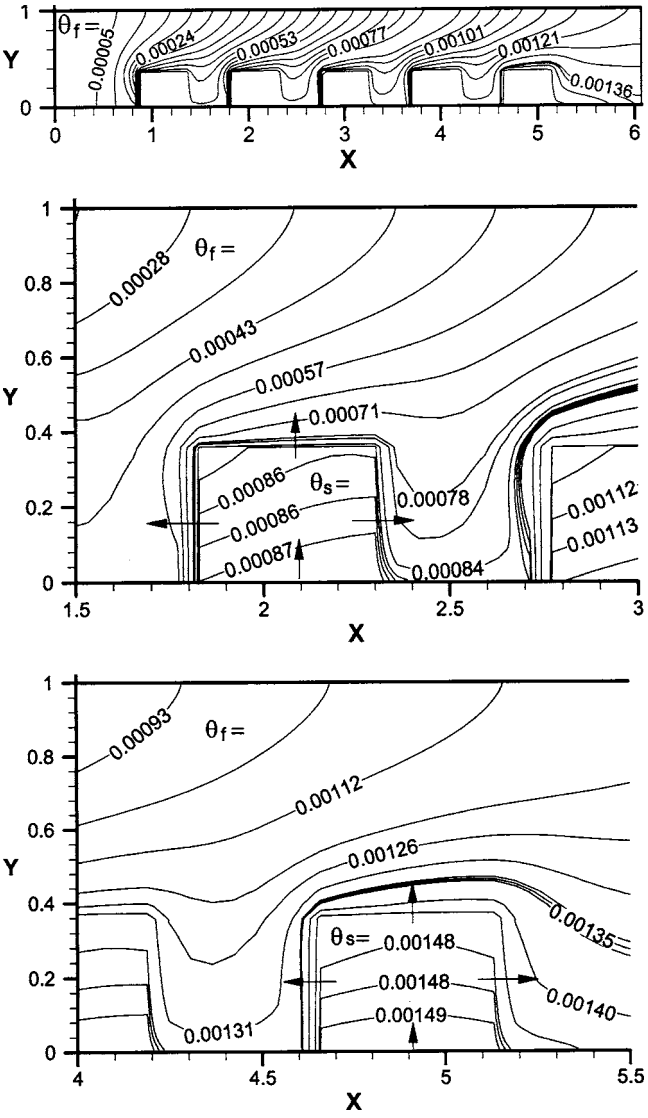

Fig. 10 Fluid isotherms for d=0.7 mm, h/H=0.36, w/H=0.47, s/H=0.47, and Re=3057 (Note: the isothermal in the block region is the block temperature). (*a*) Fluid temperature for all computational domain. (*b*) Fluid temperature around the second block. (*c*) Fluid temperature around the fifth block.

recirculation. It matches the results of earlier works [18,19], which indicated that the global recirculation did not extend to the flow in porous material but was confined to the open region of the channel. Figure 8 plots the velocity vectors for a selected parameter. The velocity vector between the second block and the third block was examined. This map also shows an absence of global recirculation, which greatly improves cooling. According to Martin et al. [21], who studied the application of porous inserts to enhance heat transfer in a recirculating flow over a backward-facing step, porous inserts not only prevent the formation of a global recirculation zone but also eliminate the locally minimal Nusselt number near the backward-face. This characteristic helps to reduce the locally maximal wall temperature. Additionally, the quantity of air that entered the bottom portions between the blocks was lower than the average flow rate and the flow velocity in the zone above the block was higher than the average velocity. These conditions implied that more heat was dissipated from the top face of the block than from other faces of the block. Figures 9 and 10 present the contours of the solid and fluid temperatures in a typical case, with d=0.70 mm, h/H=0.36, w/H=0.47, s/H=0.47, and Re=3057. The temperature distributions around the second block and the fifth block were plotted in detail to elucidate the heat transfer mechanism. Figure 9(*a*) demonstrates that the solid temperature distributions around the first four blocks were similar to each other and that around the fifth block differed from the others. The contours of solid temperature in Fig. 9(*b*) indicate that the metallic block absorbed heat from the heated bottom surface via two paths. The first path is direct conduction from the heated bottom surface; the other is indirect conduction through the porous media in the bottom portion of the right face of the block. Therefore, although the forced convective heat transfer between the blocks was low, the heat in those regions was transferred to the metallic block and then dissipated into the fluid that flowed over the zone above the block. However, in Figs. 9(*c*) and 10(*c*), the temperature contours reveal that the final block did not absorb heat from the porous media and none of the blocks took heat from the fluid. It needs to note that the isothermal in the block region shown in Fig. 10 is the block temperature. The purpose of plotting block isotherms in Fig. 10 is to present the temperature gradient and the heat transfer direction.

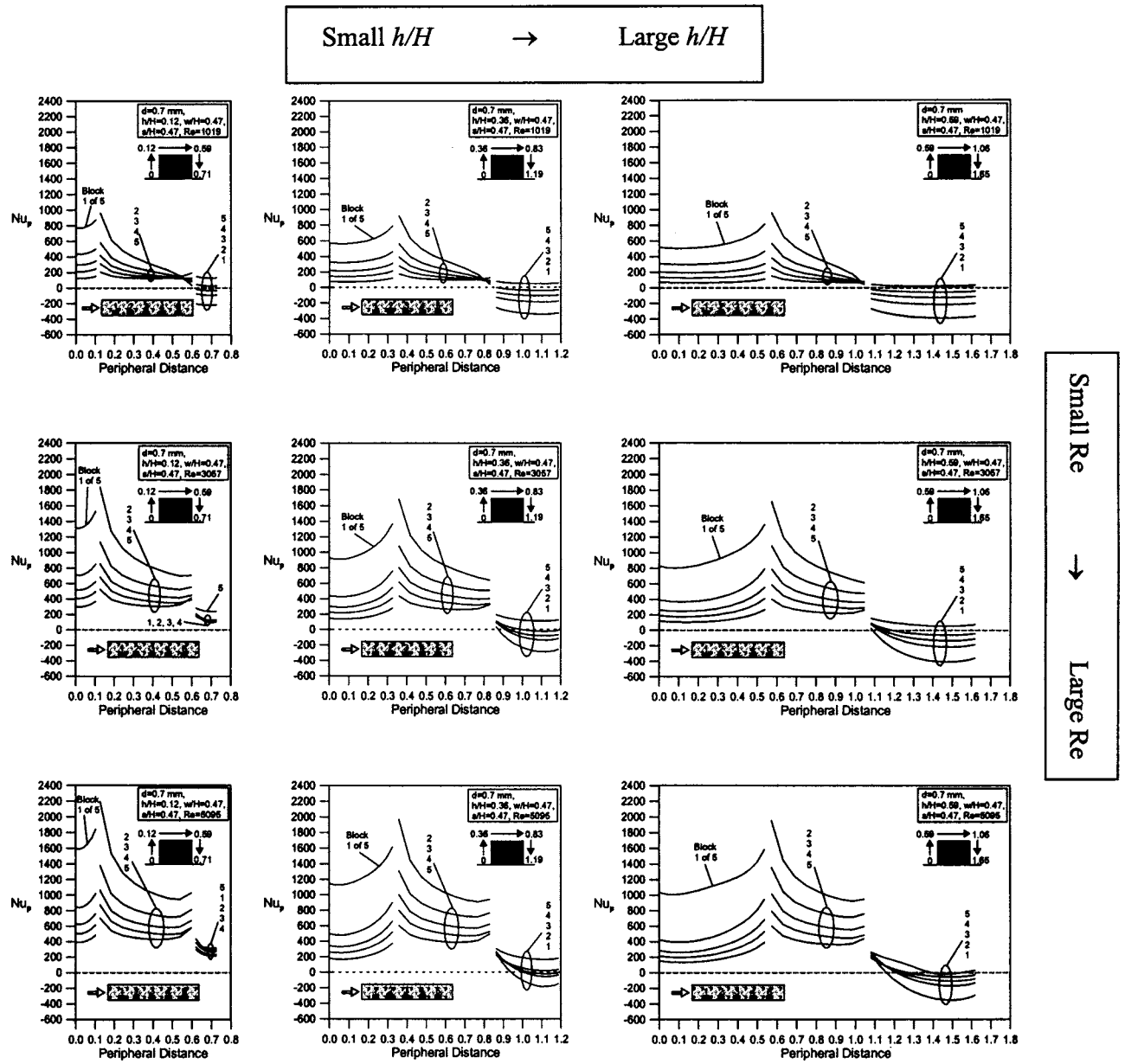

Fig. 11 Effects of h/H and Re on local Nusselt number distribution along the periphery of the block surface

4.3 Effects of Bead Diameter, Block Height, Length, Spacing, and Flow Rate on Thermal Characteristics. This section systematically addresses the effects of the parameters of interest, including block height, length, spacing, and flow rate, on the heat convection characteristics of the system, which include the Nusselt number distribution along the periphery of the heated block surface and the average Nusselt numbers for heated blocks.

4.3.1 Nusselt Number Distribution Along the Periphery of the Heated Block Surface. This section presents the local Nusselt number (Nu_p) distributions along the periphery of the block surface to clarify the differences among the heat transfers at all of the blocks in the porous channel. Figure 11 plots the effects of h/H and Re on Nu_p. The typical cases involved $d=0.7$ mm, $w/H=0.47$, $s/H=0.47$, various h/H values ($h/H=0.12-0.59$), and various Re values (Re=1019–5095). Figure 12 shows the effects of d, w/H, and s/H on Nu_p. The typical cases involved $h/H=0.36$, Re=5095, various d values ($d=0.7$ and 1.16 mm), various w/H values ($w/H=0.24$ and 0.47), and various s/H values ($s/H=0.24-0.7$). Nu_p at the left and top faces were lower in the downstream blocks than in the upstream blocks. On the left faces of the blocks, the Nu_p has maximal value at the upper corners because of fluid acceleration. Nu_p was largest at the left corner of the top faces declining rapidly to a local minimum value. In cases with small h/H, large Re and large s/H, Nu_p increased slightly near the right corner, because the blowing effect causes more fluid to turn around the right corner of the top face. The Nu_p at the right faces of the blocks varied differently. At the right faces, Nu_p was typically higher at the downstream blocks than at the upstream blocks. However, the Nu_p at the right faces of the upstream blocks increased more as h/H fell; Re increased or s/H increased, because as h/H falls, Re increases or s/H increases, and more cold flow enters the regions among the heated blocks. The first block had much larger Nu_p values along its left face than did the other blocks, because of the uniform entry flow. Therefore, the large Nu_p along the left face of the first block caused more heat to be transferred across its right face. Notably, the negative Nu_p along

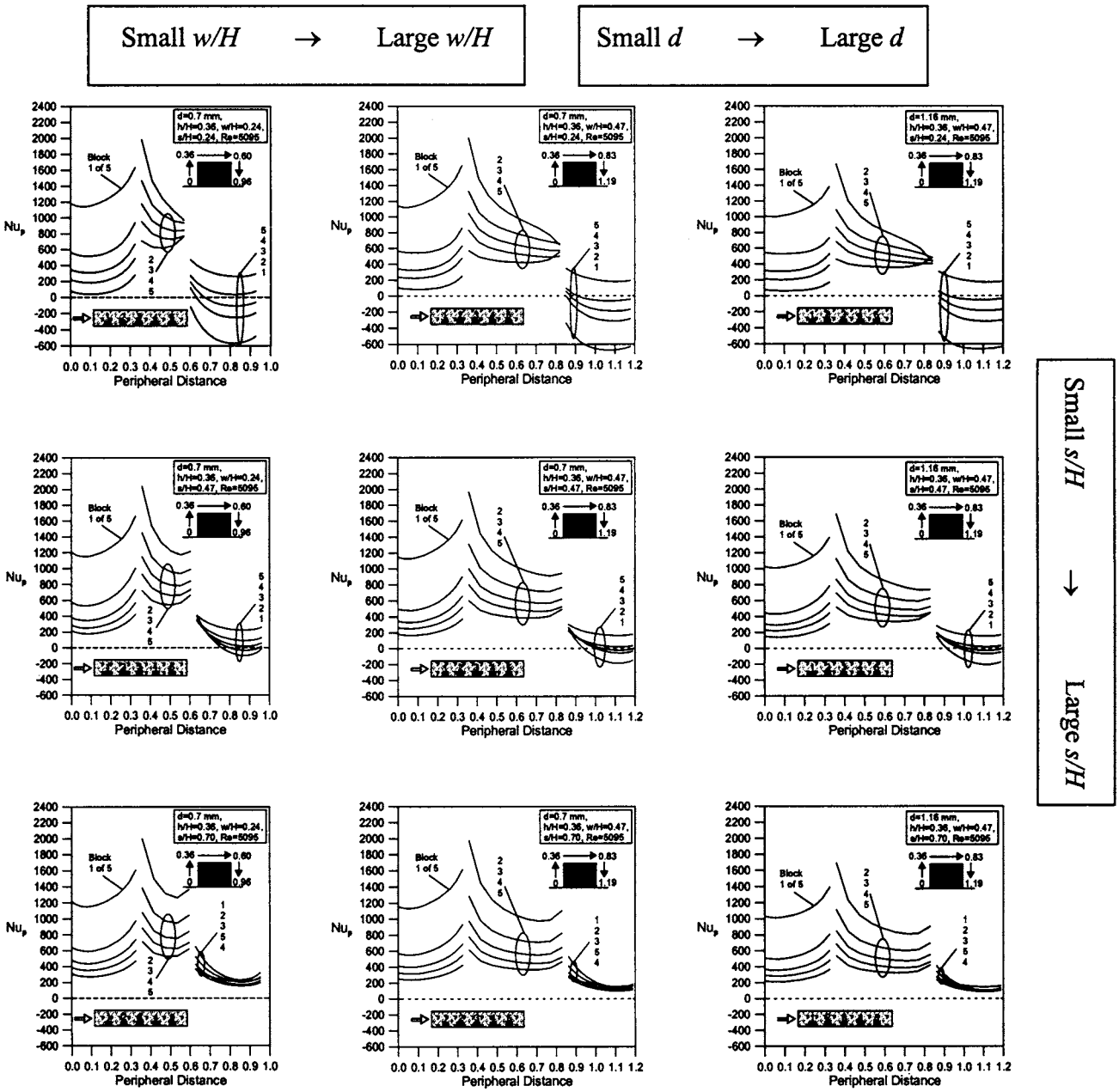

Fig. 12 Effects of *d*, *w*/*H*, *s*/*H* on local Nusselt number distribution along the periphery of the block surface

the right faces of the blocks gradually became positive as h/H fell; Re increased or s/H increased, especially in the upper portions of the right faces of the blocks.

4.3.2 Average Nusselt Numbers of Heated Blocks. Nu^* is taken as the average Nu for the bottom of the heated blocks to determine the average heat dissipation of the heated blocks for various d, h/H, w/H, s/H, and Re

$$\mathrm{Nu}^* = \overline{\mathrm{Nu}}\frac{w}{H} \tag{22}$$

where $\overline{\mathrm{Nu}}$ is the integral average value of the Nu (defined in Eq. (20)) determined from the block length. Figure 13 plots the average Nusselt number (Nu^*) of heated blocks with various d, h/H, w/H, s/H, and Re. The data reveals that for a specific h/H and Re, Nu^* is close to a particular value downstream. Restated, the array of heated blocks approaches the expected fully developed values. The average Nusselt number increased with h/H or Re in the fully developed region. The effect of h/H on the fully developed Nusselt number was stronger as Re increased and w/H decreased. Notably, a comparison of the Nu^* values at low w/H ($w/H=0.24$) and high w/H ($w/H=0.47$) reveals that in the former case, Nu^* is larger when h/H is higher ($h/H=0.59$), and in the latter case, Nu^* is larger when h/H is lower ($h/H=0.36$ and 0.12). In the fully developed region, the effects of s/H and d on the average Nusselt number were not so evident over the ranges of parameters considered herein. Some articles [4,37–40] have indicated that the fully developed Nu^* in a nonporous channel with periodically spaced heated blocks happened from the third row to the tenth row of the block array. This work arranged five heated blocks in the sintered porous channel. Using the deviation between two neighbor blocks as the reference of the fully developed Nusselt number, the difference in average Nusselt number decreased downstream and generally less than 10% was found between the fourth and fifth blocks for all numerical cases. There-

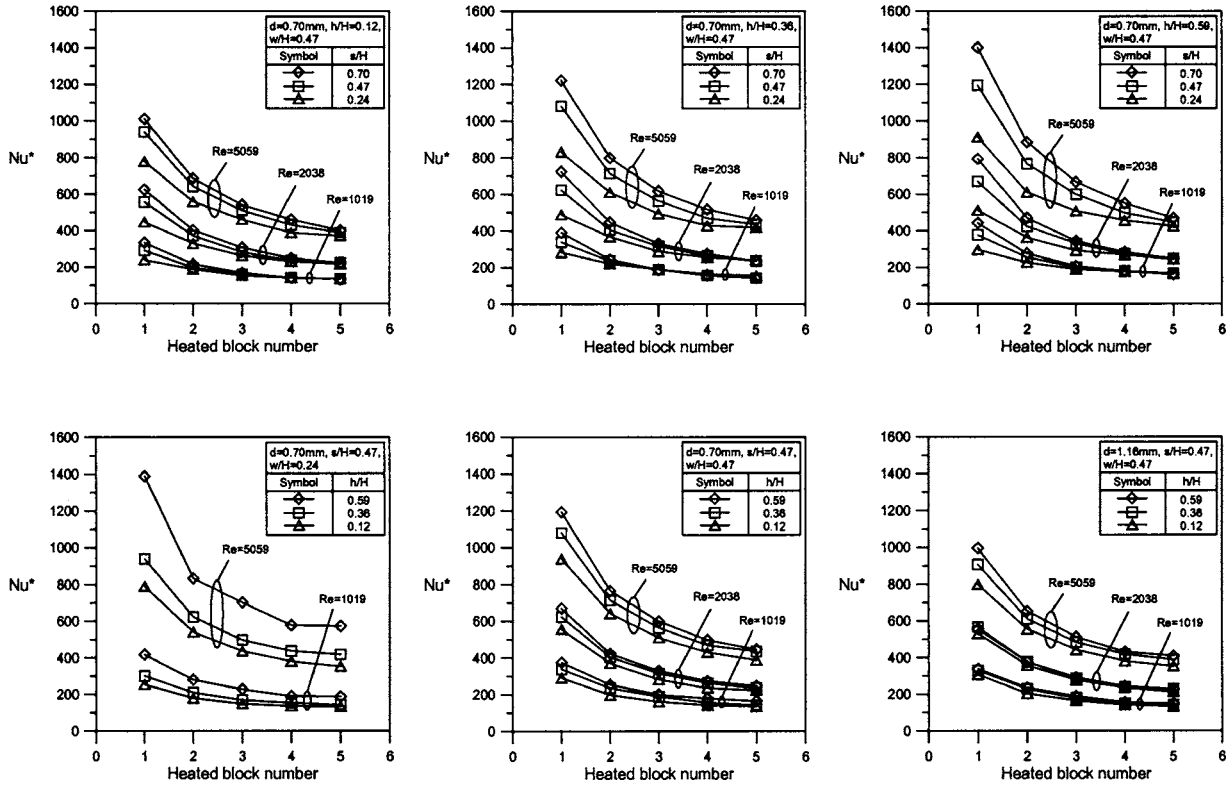

Fig. 13 Average Nusselt numbers on different blocks with various *d*, *h*/*H*, *w*/*H*, *s*/*H*, and Re

fore, Fig. 13 demonstrates that the Nu^* of the fifth block gradually reached the fully developed value. For ranges of parameters considered herein ($d=0.7$ and 1.16 mm, $h/H=0.12-0.59$, $w/H=0.24-0.47$, $s/H=0.24-0.7$, and $Re=1019-5059$), the Nu^* of the fifth block is between 133 and 573.

5 Conclusions

This work numerically investigated the fluid flow behavior and the heat transfer mechanism in a porous channel that contains periodically spaced heated metallic blocks. The results were experimentally validated for some typical cases. The porous medium was sintered bronze material. The varied parameters were the average bead diameter (d), the relative block height (h/H), the relative block width (w/H), the relative block spacing (s/H), and the Reynolds number (Re). The following conclusions were drawn:

1. The numerical predictions were consistent with the experimental results, indicating that the numerical model employed herein can accurately simulate the flow and thermal behavior in a sintered porous channel that contains multiple heated blocks.
2. No global recirculation occurred among the blocks in the sintered porous channel. The amount of air that entered the bottom regions between the blocks was lower than the average flow rate and the flow velocity in the zone above the block was higher than the average velocity. These conditions reveal that more heat was dissipated from the top face of the block than from other faces of the block.
3. Although less heat was transferred by forced convection in the regions among the blocks than elsewhere, the heat in those regions was transferred to the metallic block by conduction through the porous media, before being dissipated into the fluid that passed over the zone above the block. However, the final block did not absorb heat from the porous media and no block absorbed heat from the fluid.
4. On the left and top faces, Nu_p was lower at the downstream blocks. For the top faces, Nu_p was highest at the left corner, decreasing rapidly toward a local minimum value. In cases with low h/H, high Re, and high s/H values, Nu_p increased slightly near the right corner. Nu_p on the right faces was typically higher at the downstream blocks. However, Nu_p on the right faces of the upstream blocks increased more quickly as h/H fell, Re increased or s/H increased, than did the corresponding value of other blocks.
5. The average Nusselt number values (Nu^*) of upstream blocks exceeded those of downstream blocks and approached a constant value downstream for specific h/H and Re. The Nu^* increased with h/H or Re in the fully developed region. The effect of h/H on the fully developed Nusselt number became stronger as Re increased and w/H decreased. However, the effects of s/H and d on the fully developed Nusselt number were not very obvious over the ranges of parameters considered herein. The Nu^* of the fifth block gradually reached the fully developed value, being between 133 and 573.

Acknowledgment

The authors would like to thank the National Science Council of the Republic of China for financially supporting this research under Contract No. NSC 93-2622-E-270-003-CC3.

Nomenclature

a_{fs} = surface area of the fluid-solid interface per unit volume, m^{-1}
C_F = inertial coefficient
C_p = specific heat of fluid at constant pressure, J/kg/°C
d = average bead diameter, m
d_v = average void diameter $=4\varepsilon/a_{fs}$, m
Da = Darcy number, K/H^2
D_t = thermal dispersion constant

H = height of the channel, m
h = height of the block, m
h_{fs} = heat transfer coefficient between the fluid stream and the solid matrix, $W/m^2/°C$
K = Permeability, m^2
k = thermal conductivity, W/m/°C
l = wall function for transverse thermal dispersion
L = length of the channel, m
L_i = length of channel upstream from the blocks, m
L_o = length of channel downstream from the blocks, m
n = number of blocks
Nu = Nusselt number
p = pressure, Pa
Pr = Prandtl number
q_w = heat flux of the heated wall, W/m^2
$q_{w,p}$ = heat flux along the periphery of the block surface, W/m^2
Re = Reynolds number based on the height of channel, $\rho_f u_i H/\mu$
Re_d = Reynolds number based on the average bead diameter, $\rho_f\sqrt{u^2+v^2}d/\mu$
s = spacing of the block, m
T = temperature, °C
u = fluid flow velocity in the streamwise direction, m/s
U = dimensionless fluid flow velocity in the streamwise direction
U_M = dimensionless magnitude of the velocity, $\sqrt{u^2+v^2}/u_i$
v = fluid flow velocity in the crosswise direction, m/s
V = dimensionless fluid flow velocity in the crosswise direction
w = length of the block, m
x,y = Cartesian coordinates, m
X,Y = dimensionless Cartesian coordinates

Greek Symbols

ε = porosity
μ = viscosity of fluid, kg/m/s
θ = dimensionless temperature, $(T-T_i)/(q_w H/k_f)$
ρ = density, kg/m^3
ω = vorticity
Ψ = stream function

Superscripts

* = effective
$\bar{}$ = average

Subscripts

b = block
d = thermal dispersion
f = fluid
fs = fluid-solid interface
i = at the channel inlet
p = along the periphery of the block surface
s = solid matrix
w = channel wall

References

[1] Mahalingam, M., and Berg, H. M., 1984, "Thermal Trend in Component Level Packaging," Int. J. Hybrid Microelectron., **7**, pp. 1–9.
[2] Mahalingam, M., 1985, "Thermal Management in Semiconductor Device Packaging," Proc. IEEE, **73**, pp. 1396–1404.
[3] Kang, B. H., Jaluria, Y., and Tewari, S. S., 1990, "Mixed Convection Transport From an Isolated Heat Source Module on a Horizontal Plate," ASME J. Heat Transfer, **112**, pp. 653–661.
[4] Kim, S. Y., Sung, H. J., and Hyun, J. M., 1992, "Mixed Convection from Multiple-Layered Boards With Cross-Streamwise Periodic Boundary Conditions," Int. J. Heat Mass Transfer, **35**, pp. 2941–2952.
[5] Young, T. J., and Vafai, K., 1998, "Convective Cooling of a Heated Obstacle in a Channel," Int. J. Heat Mass Transfer, **41**, pp. 3131–3148.
[6] Young, T. J., and Vafai, K., 1998, "Convective Flow and Heat Transfer in a Channel Containing Multiple Heated Obstacles," Int. J. Heat Mass Transfer, **41**, pp. 3279–3298.
[7] Hunt, M. L., and Tien, C. L., 1988, "Effects of Thermal Dispersion on Forced Convection in Fibrous Media," Int. J. Heat Mass Transfer, **31**, pp. 301–309.
[8] Chou, F. C., Lien, W. Y., and Lin, S. H., 1992, "Analysis and Experiment of Non-Darcian Convection in Horizontal Square Packed-Sphere Channels—1. Forced Convection," Int. J. Heat Mass Transfer, **35**, pp. 195–205.
[9] Hwang, G. J., and Chao, C. H., 1994, "Heat Transfer Measurement and Analysis for Sintered Porous Channels," ASME J. Heat Transfer, **116**, pp. 456–464.
[10] Hwang, G. J., Wu, C. C., and Chao, C. H., 1995, "Investigation of Non-Darcian Forced Convection in an Asymmetrically Heated Sintered Porous Channel," ASME J. Heat Transfer, **117**, pp. 725–732.
[11] Peterson, G. P., and Chang, C. S., 1998, "Two-phase Heat Dissipation Utilizing Porous-Channels of High-Conductivity Material," ASME J. Heat Transfer, **120**, pp. 243–252.
[12] Calmidi, V. V., and Mahajan, R. L., 2000, "Forced Convection in High Porosity Metal Foams," ASME J. Heat Transfer, **122**, pp. 557–565.
[13] Angirasa, D., 2002, "Forced Convective Heat Transfer in Metallic Fibrous Materials," ASME J. Heat Transfer, **124**, pp. 739–745.
[14] Angirasa, D., 2002, "Experimental Investigation of Forced Convection Heat Transfer Augmentation With Metallic Fibrous Materials," Int. J. Heat Mass Transfer, **45**, pp. 919–922.
[15] Jiang, P. X., Li, M., Lu, T. J., Yu, L., and Ren, Z. P., 2004, "Experimental Research on Convection Heat Transfer in Sintered Porous Plate Channels," Int. J. Heat Mass Transfer, **47**, pp. 2085–2096.
[16] Jiang, P. X., Li, M., Ma, Y. C., and Ren, Z. P., 2004, "Boundary Conditions and Wall Effect for Forced Convection Heat Transfer in Sintered Porous Plate Channels," Int. J. Heat Mass Transfer, **47**, pp. 2073–2083.
[17] Rizk, T. A., and Kleinstreuer, C., 1991, "Forced Convective Cooling of a Linear Array of Blocks in Open and Porous Matrix Channels," Heat Transfer Eng., **12**, pp. 40–47.
[18] Hadim, A., 1994, "Forced Convection in Porous Channel With Localized Heat Sources," ASME J. Heat Transfer, **116**, pp. 465–472.
[19] Hadim, H. A., and Bethancourt, A., 1995, "Numerical Study of Forced Convection in a Partially Porous Channel With Discrete Heat Sources," ASME J. Electron. Packag., **117**, pp. 46–51.
[20] Ould-Amer, Y., Chikh, S., Bouhadef, K., and Lauriat, G., 1998, "Forced Convection Cooling Enhancement by Use of Porous Material," Int. J. Heat Fluid Flow, **19**, pp. 251–258.
[21] Huang, P. C., Yang, C. F., Hwang, J. J., and Chiu, M. T., 2005, "Enhancement of Forced-Convection Cooling of Multiple Heated Blocks in a Channel Using Porous Covers," Int. J. Heat Mass Transfer, **48**, pp. 647–664.
[22] Slattery, J. C., 1972, *Momentum, Energy and Mass Transfer in Continua*, McGraw-Hill, New York, pp. 57–65.
[23] Martin, A. R., Saltiel, C., and Shyy, W., 1998, "Heat Transfer Enhancement With Porous Inserts in Recirculating Flows," ASME J. Heat Transfer, **120**, pp. 458–467.
[24] Angirasa, D., and Peterson, G. P., 1999, "Forced Convection Heat Transfer Augmentation in a Channel With a Localized Heat Source Using Fibrous Materials," ASME J. Electron. Packag., **121**, pp. 1–7.
[25] Cheng, P., and Hsu, C. T., 1986, "Applications of Van Driest's Mixing Length Theory to Transverse Thermal Dispersion in Forced Convective Flow through a Packed Bed," Int. Commun. Heat Mass Transfer, **13**, pp. 613–625.
[26] Cheng, P., Hsu, C. T., and Chowdhury, A., 1988, "Forced Convection in the Entrance Region of a Packed Channel With Asymmetric Heating," ASME J. Heat Transfer, **110**, pp. 946–954.
[27] Kar, K. K., and Dybbs, A., 1982, "Internal Heat Transfer Coefficients of Porous Metals," *Proc. Winter Annual Meeting of ASME*, Phoenix, AZ, pp. 81–91.
[28] Gamson, B. W., Thodos, G., and Hougen, O. A., 1943, "Heat, Mass and Momentum Transfer in Flow of Gases," Trans. AIChE, **39**, pp. 1–35.
[29] Fu, W. S., and Huang, H. C., 1999, "Effects of a Random Porosity Model on Heat Transfer Performance of Porous Media," Int. J. Heat Mass Transfer, **42**, pp. 13–25.
[30] Roache, P. J., 1972, *Computational Fluid Dynamics*, *Hermosa*, Albuquerque, New Mexico, pp. 139–173.
[31] Patankar, S. V., 1980, *Numerical Heat Transfer and Fluid Flow*, McGraw-Hill, Hemisphere, New York, pp. 113–137.
[32] Hwang, G. J., and Cheng, K. C., 1970, "Boundary Vorticity Method for Convective Heat Transfer With Secondary Flow Application to the Combined Free and Forced Laminar Convection in Horizontal Tubes," *Proc. 4th Int. Heat Transfer Conf.*, Versailles, Paris, Vol. 4, Paper No. NC3.5.
[33] Lee, S. L., 1989, "A Strong Implicit Solver for Two-Dimensional Elliptic Differential Equations," Numer. Heat Transfer, Part B, **16**, pp. 161–178.
[34] Calmidi, V. V., and Mahajan, R. L., 1999, "The Effective Thermal Conductiv-

ity of High Porosity Fibrous Metal Foams," ASME J. Heat Transfer, **121**, pp. 466–471.
[35] Kline, S. J., and Mcclintock, F. A., 1953, "Describing Uncertainties in Single-Sample Experiments," Mech. Eng. (Am. Soc. Mech. Eng.), **75**, Jan., pp. 3–8.
[36] Moffat, R. J., 1986, "Contributions to the Theory of Single-Sample Uncertainty Analysis," ASME J. Fluids Eng., **104**, pp. 250–260.
[37] Souza Mendes, P. R., and Santos, W. F. N., 1987, "Heat Transfer and Pressure Drop Experiments in Air-Cooled in Electronic-Component Arrays," J. Thermophys. Heat Transfer, **1**, pp. 373–378.
[38] Garimella, S. V., and Eibeck, P. A., 1990, "Heat Transfer Characteristics of an Array of Protruding Elements in Single-Phase Forced Convection," Int. J. Heat Mass Transfer, **33**, pp. 2659–2669.
[39] Lehmann, G. L., and Pembroke, J., 1991, "Forced Convection Air Cooling of Simulated Low Profile Electronic Components: Part 1-Base Case," ASME J. Electron. Packag., **113**, pp. 21–26.
[40] Jubran, B. A., Swiety, S. A., and Hamdan, M. A., 1996, "Convective Heat Transfer and Pressure Drop Characteristics of Various Array Configurations to Simulate the Cooling of Electronic Modules," Int. J. Heat Mass Transfer, **39**, pp. 3519–3529.

Heat Conduction in Nanofluid Suspensions

Peter Vadasz
Professor and Chair
Fellow ASME
e-mail: peter.vadasz@nau.edu
Department of Mechanical Engineering,
Northern Arizona University,
P.O. Box 15600,
Flagstaff, AZ 86001

The heat conduction mechanism in nanofluid suspensions is derived for transient processes attempting to explain experimental results, which reveal an impressive heat transfer enhancement. In particular, the effect of the surface-area-to-volume ratio (specific area) of the suspended nanoparticles on the heat transfer mechanism is explicitly accounted for, and reveals its contribution to the specific solution and results. The present analysis might provide an explanation that settles an apparent conflict between the recent experimental results in nanofluid suspensions and classical theories for estimating the effective thermal conductivity of suspensions that go back more than one century (Maxwell, J.C., 1891, Treatise on Electricity and Magnetism). Nevertheless, other possible explanations have to be accounted for and investigated in more detail prior to reaching a final conclusion on the former explanation. [DOI: 10.1115/1.2175149]

Keywords: nanofluids, nanoparticles suspension, heat transfer enhancement, effective thermal conductivity, effective heat capacity, dual-phase-lagging

1 Introduction

The reported breakthrough in substantially increasing the thermal conductivity of fluids by adding very small amounts of suspended metallic or metallic oxide nanoparticles (Cu, CuO, Al_2O_3) to the fluid (Eastman et al. [1], Lee et al. [2]), or alternatively using nanotube suspensions (Choi et al. [3], Xuan and Li [4]) conflicts with the classical theories (Maxwell [5], Batchelor [6], Batchelor and Green [7], Hamilton and Crosser [8], Jeffrey [9], Davis [10], Lu and Lin [11], Bonnecaze and Brady [12,13]) of estimating the effective thermal conductivity of suspensions. A very small amount (less than 1% in terms of volume fraction) of copper nanoparticles was reported to improve the measured thermal conductivity of the suspension by 40% (Eastman et al. [1], Lee et al. [2]), while over a 150% improvement of the effective thermal conductivity at a volume fraction of 1% was reported by Choi et al. [3] for multiwalled carbon nanotubes suspended in oil. The procedure used by Eastman et al. [1] for producing nanofluids containing metallic particles and dispersing them into ethylene glycol resulted in very little agglomeration. In the case of nanotube suspensions Choi et al. [3] indicate that well dispersed and stable suspensions were produced and tested. The reported experimental results for the effective thermal conductivity undertaken by using the transient hot wire (THW) method are substantially greater than the predictions based on existing theories and models. The argument laid forward by Eastman et al. [1] for explaining such an impressive enhancement of the effective thermal conductivity of the suspension is the fact that "*…the surface-area-to volume ratio is 1000 times larger for particles with a 10 nm diameter than for particles with a 10 μm diameter…*" and that "*an obvious shortcoming*" in the classical theory of estimating the effective thermal conductivity of suspensions "*is the lack of any predicted dependence of conductivity on particle size….it does not account for the orders-of-magnitude increase in surface-area-to-volume ratio that accompany decreasing particle size into the nanocrystalline regime.*" Possible explanations for the divergence between theory and experiments were suggested and explored very basically by Keblinski et al. [14]. Brownian motion of the particles, molecular-level layering of the liquid at the liquid/particle interface, the nature of heat transport within the nanoparticles and effects of nanoparticle clustering were investigated. While these investigations were not done in detail but mainly at the very basic level, Keblinski et al. [14] show that the "*key factors in understanding thermal properties of nanofluids are the ballistic, rather than diffusive, nature of heat transport in the nanoparticles, combined with direct or fluid mediated clustering effects that provide paths for rapid heat transport*." Recent research results presented by Xue et al. [15] eliminate the molecular-level layering of the liquid at the liquid/particle interface as a possible heat transfer enhancement mechanism. Xue et al. [15] conclude that "*the experimentally observed large enhancement of thermal conductivity in suspensions of solid nanosize particles (nanofluids) can not be explained by altered thermal transport properties of the layered liquid*." Furthermore, while originally Keblinski et al. [14] estimated that "*…Brownian motion is too slow to transport significant amounts of heat through a nanofluid, a conclusion supported by the results of Molecular Dynamics simulations…*" recent research efforts such as Prasher et al. [16], Das et al. [17], Kumar et al. [18], and Jang and Choi [19] show although in a very preliminary fashion, practically via an order of magnitude analysis, that Brownian motion may explain the substantial enhancement of the effective thermal conductivity. Indeed, Keblinski et al. [14] suggested (although did not investigate) a possibility where Brownian motion combined with ballistic phonon effects may provide a mechanism for such enhancement. On the other hand the ballistic phonon transport alone is known to be a substantially less effective mechanism of heat transfer than diffusion as presented in detailed studies at the nanoscale level by Chen [20–22]. Additional possible mechanisms for enhancement of heat transfer in nanofluid suspensions may also include thermo/electrophoresis and natural convection driven by the suspended nanoelements (nanoparticles or nanotubes).

However, while the reported results are a direct consequence of the presence of nanoelements (nanoparticles or nanotubes) in the suspension, the measurements were not performed at the nanoscale, but rather at the macro/mesoscale. Therefore, the interest should not be focused only on what occurs at the nanoscale but rather on how the heat transfer at the macro/mesoscale is substantially affected by a very small presence (less than 1% in volume) of an extremely small concentration of suspended nanoelements (nanoparticles or nanotubes).

The present investigation demonstrates that the transient heat conduction process in suspensions is fully consistent with the classical method of estimating the effective thermal conductivity of suspensions and may provide a valid explanation for the appar-

Contributed by the Heat Transfer Division of ASME for publication in the JOURNAL OF HEAT TRANSFER. Manuscript received March 2, 2005; final manuscript received October 7, 2005. Review conducted by Jay M. Khodadadi.

ent heat transfer enhancement revealed experimentally. Note that Maxwell's [5] results as well as their extensions (Batchelor [6], Batchelor and Green [7], Hamilton and Crosser [8], Jeffrey [9], Davis [10], Lu and Lin [11], Bonnecaze and Brady [12,13]) demonstrating the existence of a constant effective thermal conductivity were derived at steady state and such an effective thermal conductivity might not be existent during transients. Furthermore, if it does exist, the results presented here suggest that a correction to the analytical formulation of the THW method is required when the latter is applied to the evaluation of the effective thermal conductivity of suspensions.

The method adopted in this analysis is basically a variation of the classical method applied to heat conduction in porous media (Nield and Bejan [23]) adapted to the problem of heat conduction in suspensions. In the respective formulation it is already evident that the transient heat conduction in suspensions is controlled not only by the effective thermal conductivity but also by a fluid-to-solid heat transfer coefficient that accounts for the heat flux at the fluid-solid interface. The latter includes the effect of the surface-area-to-volume ratio (specific area) as well as the impact of the heat capacity of the solid particles, which introduce a delayed response to any temperature variation in the neighboring fluid.

While the results presented may provide a possible explanation for the apparent heat transfer enhancement revealed experimentally, there are other possible macroscale explanations that might contribute to the latter, such as hyperbolic heat conduction (Vadasz, Govender, and Vadasz, [24]), particle driven natural convection, convection induced by electrophoresis, thermophoresis, etc.

Throughout the paper all variables carrying the subscript $(\cdot)_*$ represent dimensional values while variables lacking the subscript are dimensionless. Specific dimensional values of variables also carry the subscript $(\cdot)_*$ in order to distinguish them from their corresponding dimensionless ones. Constant property symbols, although dimensional do not carry the $(\cdot)_*$ subscript, for maintaining simplicity of notation.

2 Transient Hot Wire Method for Estimating the Thermal Conductivity

An essential component in the following analysis is the application of the (THW) method for estimating experimentally the thermal conductivity of the nanofluid suspension. The THW method is well established as the most accurate, reliable and robust technique (Hammerschmidt and Sabuga [25]) for evaluating the thermal conductivity of fluids (De Groot, Kestin, and Sookiazian [26], Healy, De Groot, and Kestin [27], Kestin and Wakeham, [28]) and solids (Assael et al. [29]). It replaced the steady state methods primarily because of the difficulty in determining that steady state conditions have indeed been established and for fluids the difficulty in preventing the occurrence of natural convection and consequently the difficulty in eliminating the effects of natural convection on the heat flux. The THW method consists in principle of determining the thermal conductivity of a selected material/fluid by observing the rate at which the temperature of a very thin platinum (or alternatively tantalum) wire (5–80 μm in diameter) increases with time after a step change in voltage has been applied to it. The platinum (tantalum) wire is embedded vertically in the selected material/fluid (see Fig. 1(*a*)) and serves as a heat source as well as a thermometer. The temperature of the wire is established by measuring its electrical resistance, the latter being related to the temperature via a well-known relationship. A Wheatstone bridge is used to measure the electrical resistance R_w of the wire. The electrical resistance of a potentiometer R_3 is adjusted until the reading of the galvanometer G shows zero current. When the bridge is balanced as indicated by a zero current reading on the galvanometer G, the value of R_w can be established from the known electrical resistances R_1, R_2, and R_3 by using the balanced Wheatstone bridge relationship $R_w = R_1 R_2 / R_3$.

While the application of the method to solids and gases is straightforward its corresponding application to electrically conducting liquids needs further attention. The experiments conducted in nanofluid suspensions listed above [1–4] used a thin electrical insulation coating layer to cover the platinum wire instead of using the bare metallic wire, a technique developed by Nagasaka and Nagashima [30]. The latter is aimed at preventing problems such as electrical current flow through the liquid causing ambiguity of the heat generation in the wire. Alternatively, Assael et al. [31] used tantalum wires, which were anodized in situ to form a coating layer of tantalum pentoxide (Ta_2O_5) which is an electrical insulator.

Because of the very small diameter (micrometer size) and high thermal conductivity of the platinum wire the latter can be regarded as a line source in an otherwise infinite cylindrical medium. The rate of heat generated per unit length (l_*) of platinum wire is therefore $\dot{q}_{l_*} = iV/l_*$ W m^{-1}, where i is the electric current flowing through the wire and V is the voltage drop across the wire.

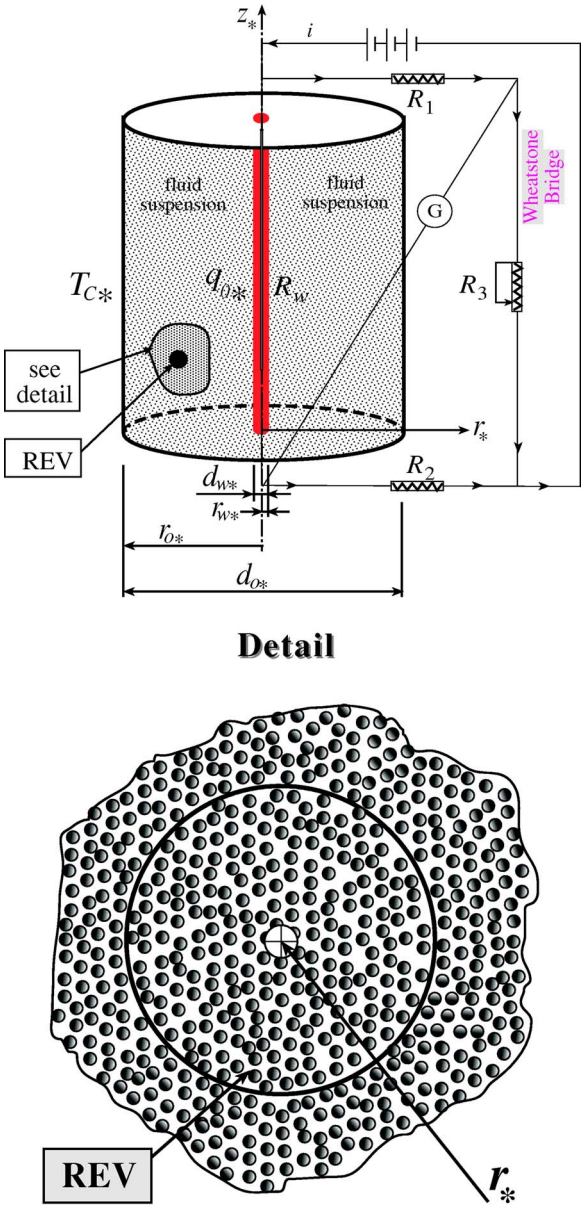

Fig. 1 (*a*) An embedded platinum (tantalum) hot wire within a nanofluid suspension in a cylindrical container. (*b*) Graphical representation of the averaging method for suspended solid particles in a fluid using a REV.

Solving for the radial heat conduction due to this line heat source leads to a temperature solution in the following closed form that can be expanded in an infinite series as follows

$$T_* = \frac{\dot{q}_{l_*}}{4\pi k}\mathrm{Ei}\left(\frac{r_*^2}{4\alpha t_*}\right) = \frac{\dot{q}_{l_*}}{4\pi k}\left[-\gamma + \ln\left(\frac{4\alpha t_*}{r_*^2}\right) + \frac{r_*^2}{4\alpha t_*} - \frac{r_*^4}{64\alpha^2 t_*^2} + \frac{r_*^6}{1152\alpha^3 t_*^3} - \cdots\right] \quad (1)$$

where $Ei(\cdot)$ represents the exponential integral function, and $\gamma = \ln(\sigma) = 0.5772156649$ is Euler's constant. For a line heat source embedded in a cylindrical cell of infinite radial extent and filled with the test fluid one can use the approximation $r_*^2/4\alpha t_* \ll 1$ in Eq. (1) to truncate the infinite series and yield

$$T_* \approx \frac{\dot{q}_{l^*}}{4\pi k}\left[-\gamma + \ln\left(\frac{4\alpha t_*}{r_*^2}\right) + O\left(\frac{r_*^2}{4\alpha t_*}\right)\right] \quad (2)$$

Equation (2) reveals a linear relationship, on a logarithmic time scale, between the temperature and time. Therefore, one way of evaluating the thermal conductivity is from the slope of this relationship evaluated at $r_* = r_{w^*}$, for example, r_{w^*} being the radius of the platinum wire. For $r_* = r_{w^*}$ the condition for the series truncation $r_{w^*}^2/4\alpha t_* \ll 1$ can be expressed in the following equivalent form that provides the validity condition of the approximation in the form

$$t_* \gg \frac{r_{w^*}^2}{4\alpha} \quad (3)$$

The value of $t_{o^*} = r_{w^*}^2/4\alpha$ provides a validity condition of the experimental readings, i.e., $t_* \gg t_{o^*}$. For any two readings of temperature T_{1^*} and T_{2^*} recorded at times t_{1^*} and t_{2^*} respectively, the temperature difference $(T_{2^*} - T_{1^*})$ can be approximated by using Eq. (2), as long as the latter validity condition is fulfilled, in the form

$$(T_{2^*} - T_{1^*}) \approx \frac{iV}{4\pi k l_*}\left[\ln\left(\frac{t_{2^*}}{t_{1^*}}\right)\right] \quad (4)$$

where we replaced the heat source with its explicit dependence on i, V and l_*, i.e., $\dot{q}_{l^*} = iV/l_*$. From Eq. (4) one can express the thermal conductivity k explicitly in the form

$$k \approx \frac{iV}{4\pi(T_{2^*} - T_{1^*})l_*}\left[\ln\left(\frac{t_{2^*}}{t_{1^*}}\right)\right] \quad (5)$$

Equation (5) is a very accurate way of estimating the thermal conductivity as long as the validity conditions for appropriateness of the problem derivations used above are fulfilled. A finite length of the platinum (tantalum) wire, the finite size of the cylindrical container, the heat capacity of the platinum (tantalum) wire, and possibly natural convection effects are examples of possible deviations of any realistic system from the one used in deriving Eq. (5). De Groot et al. [26], Healy et al. [27], and Kestin and Wakeham [28] introduce an assessment of these deviations and possible corrections to the THW readings to improve the accuracy of the results. In general all the deviations indicated above could be eliminated via the proposed corrections provided the validity condition listed in Eq. (3) is enforced as well as an additional condition that ensures that natural convection is absent. The validity condition (3) implies the application of Eq. (5) for long times only. However, when evaluating this condition (3) to data used in the nanofluid suspensions experiments considered in this paper one obtains explicitly the following values. For a 76.2 μm diameter of platinum wire used by Eastman et al. [1], Lee et al. [2], Choi et al. [3], and an electrical insulation coating thickness of 10 μm, the wire radius is $r_{w^*} = 4.81 \times 10^{-5}$ m leading to $t_{o^*} = r_{w^*}^2/4\alpha = 13.7$ ms for ethylene glycol and $t_{o^*} = r_{w^*}^2/4\alpha = 7.2$ ms for oil, leading to the validity condition $t_* \gg 13.7$ ms for ethylene glycol and $t_* > 7.2$ ms for oil. The long times beyond which the solution (5) can be used reliably are therefore of the order of hundreds of milliseconds, not so long in the actual practical sense. On the other hand the experimental time range is limited from above as well in order to ensure the lack of natural convection that develops at longer time scales. Xuan and Li [6] estimate this upper limit for the time that an experiment may last before natural convection develops as about 5 s. They indicate that "*An experiment lasts about* 5 s. *If the time is longer, the temperature difference between the hot-wire and the sample fluid increases and free convection takes place, which may result in errors*." Lee et al. [2] while using the THW method and providing experimental data in the time range of 1–10 s, indicate in their Fig. 3 the "*valid range of data reduction*" to be between 3–6 s. Our estimations evaluated above confirm these lower limits as a very safe constraint and we assume that the upper limits listed by Xuan and Li [6] and Lee et al. [2] are also good estimates. Within this time range the experimental results should produce a linear relationship, on a logarithmic time scale, between the temperature and time.

3 Problem Formulation of Heat Conduction in Suspensions and Dual-Phase-Lagging

To investigate the transient heat conduction in a fluid containing suspended solid particles (Figs. 1(*a*) and 1(*b*)) one considers the phase-averaged equations. The averaging process over a representative elementary volume (REV) V_{REV} (Fig. 1(*b*)) can be represented by introducing the following definitions: $V_{\mathrm{REV}} = V_{s,\mathrm{REV}} + V_{f,\mathrm{REV}}$, where $V_{s,\mathrm{REV}}$ and $V_{f,\mathrm{REV}}$, are the volumes occupied by the solid and fluid phases within the REV, respectively, and $\varepsilon = V_{s,\mathrm{REV}}/V_{\mathrm{REV}}$ is the volume fraction of the solid phase. Then, for the local temperature variable of any solid particle j, T_{sj^*}, and for the corresponding local temperature variable of the fluid, T_{fl^*}, one can evaluate the average temperatures over the REV in the form $T_{s^*} = (\Sigma_{i=1}^{np} T_{sj^*})/n_p$, where $n_p = nV_{\mathrm{REV}}$ is the number of solid particles within the REV while n is the number of solid particles per unit volume, and $T_{f^*} = (\int_{V_f} T_{\mathrm{fl}^*} dV)/V_f$. As a result, one obtains the average temperatures of the solid and fluid phases, respectively, associated with the REV located at the coordinates of its centroid, $\mathbf{r}_*$. As the REV can be moved within the domain its centroid moves to different spatial coordinates and the resulting average phase temperatures vary. The results are the average temperature functions $T_{s^*}(\mathbf{r}_*, t_*)$ and $T_{f^*}(\mathbf{r}_*, t_*)$, where $\mathbf{r}_*$ are the coordinates of the centroid at any given position. The resulting phase-averaged equations have the form

$$\gamma_s \frac{\partial T_{s^*}}{\partial t_*} = h(T_{f^*} - T_{s^*}) \quad (6)$$

$$\gamma_f \frac{\partial T_{f^*}}{\partial t_*} = k_e \nabla_*^2 T_{f^*} - h(T_{f^*} - T_{s^*}) \quad (7)$$

where $T_{f^*}(\mathbf{r}_*, t_*)$, $T_{s^*}(\mathbf{r}_*, t_*)$ are average temperature values for the fluid and solid phases respectively taken over a REV that is large enough to be statistically valid but sufficiently small compared to the size of the domain. In Eqs. (6) and (7) $\gamma_s = \rho_s c_s$ and $\gamma_f = \rho_f c_p$ represent the heat capacity of the solid and fluid phases, respectively, with ρ_s and ρ_f being the density of the solid and fluid phases, respectively, and c_s and c_p being the specific heat of the solid and fluid phases, respectively. Similarly, k_e is the effective thermal conductivity of the fluid as established by Maxwell [5] and developed further including higher order corrections and other than spherical particle geometries by Batchelor [6], Batchelor and Green [7], Hamilton and Crosser [8], Jeffrey [9], Davis [10], Lu and Lin [11], Bonnecaze and Brady [12,13]. Note that $T_{s^*}(\mathbf{r}_*, t_*)$ is a function of the space variables represented by the position vector $\mathbf{r}_* = r_*\hat{\mathbf{e}}_r + \phi_*\hat{\mathbf{e}}_\phi + z_*\hat{\mathbf{e}}_z$, in addition to its dependence on time, because $T_{s^*}(\mathbf{r}_*, t_*)$ depends on $T_{f^*}(\mathbf{r}_*, t_*)$ as explicitly stated in Eq.

(6), although no spatial derivatives appear in Eq. (6). The reason for the lack of macroscopic level conduction mechanism in Eq. (6) representing the heat transfer within the solid phase is the fact that the solid particles represent the dispersed phase in the fluid suspension and therefore the solid particles can conduct heat between themselves only via the neighboring fluid. When steady state is accomplished $\partial T_{s^*}/\partial t_* = \partial T_{f^*}/\partial t_* = 0$ leading to local thermal equilibrium between the solid and fluid phases, i.e., $T_{s^*}(\mathbf{r}) = T_{f^*}(\mathbf{r})$. At steady state, therefore, Maxwell's [5] method and its further derivations (Batchelor [6], Batchelor and Green [7], Hamilton and Crosser [8], Jeffrey [9], Davis [10], Lu and Lin [11], Bonnecaze and Brady [12,13]) can be applied to evaluate the effective thermal conductivity k_e of the suspension. The parameter h, carrying units of W m^{-3} K^{-1}, represents an integral heat transfer coefficient for the heat conduction at the solid-fluid interface within an REV. It is assumed to be independent of time and its general relationship to the surface-area-to-volume ratio (specific area) is derived in Appendix A.

For the particular case pertaining to this investigation that consists of a thin hot wire embedded in a cylindrical container insulated on its top and bottom sides as presented in Fig. 1 one can assume that the heat is transferred in the radial direction only leading to the sensible assumption that $\partial T_{s^*}/\partial \phi_* = \partial T_{s^*}/\partial z_* = \partial T_{f^*}/\partial \phi_* = \partial T_{f^*}/\partial z_* = 0$, hence rendering Eqs. (6) and (7) to the following operator form

$$\begin{bmatrix} \left(\gamma_s \dfrac{\partial}{\partial t_*} + h\right) & -h \\ -h & \left(\gamma_f \dfrac{\partial}{\partial t_*} - k_e \dfrac{1}{r_*}\dfrac{\partial}{\partial r_*}\left(r_* \dfrac{\partial}{\partial r_*}\right) + h\right) \end{bmatrix} \begin{bmatrix} T_{s^*} \\ T_{f^*} \end{bmatrix} = 0 \tag{8}$$

subject to the following boundary and initial conditions

$$r_* = r_{o^*}: T_{f^*} = T_{C^*} = \text{const}$$

$$r_* = r_{w^*}: q_{fr^*} = -k_e \left(\frac{\partial T_{f^*}}{\partial r_*}\right)_{r_{w^*}} = q_{o^*} = \text{const} \Rightarrow \left(\frac{\partial T_{f^*}}{\partial r_*}\right)_{r_{w^*}} = -\frac{q_{o^*}}{k_e}$$

$$t_* = 0: T_{f^*} = T_{s^*} = T_{C^*} = \text{const} \tag{9}$$

where T_{C^*} is the ambient temperature and q_{o^*} is the heat flux over the fluid-platinum-wire interface that is related to the Joule heating of the platinum wire in the form $q_{o^*} = iV/(\pi d_{w^*} l_*)$, where d_{w^*} and l_* are the diameter and the length of the platinum wire, respectively.

The coupling between the two equations via the term $h(T_{f^*} - T_{s^*})$ can be removed by evaluating the operator determinant leading to

$$\left[\left(\gamma_s \frac{\partial}{\partial t_*} + h\right)\left(\gamma_f \frac{\partial}{\partial t_*} - k_e \frac{1}{r_*}\frac{\partial}{\partial r_*}\left(r_* \frac{\partial}{\partial r_*}\right) + h\right) - h^2\right] T_{i^*} = 0 \quad \forall\, i = s, f \tag{10}$$

where the index i can take the values s representing the solid phase or f standing for the fluid phase. Assuming that the value of the heat transfer coefficient h is independent of time one can present Eq. (10) explicitly after dividing it by $h(\gamma_s + \gamma_f)$ in the form

$$\tau_q \frac{\partial^2 T_*}{\partial t_*^2} + \frac{\partial T_*}{\partial t_*} = \alpha_e \left[\frac{1}{r_*}\frac{\partial}{\partial r_*}\left(r_* \frac{\partial T_*}{\partial r_*}\right) + \frac{\tau_T}{r_*}\frac{\partial}{\partial r_*}\left(r_* \frac{\partial^2 T_*}{\partial r_* \partial t_*}\right)\right] \tag{11}$$

where the index i was removed as the intention is to use this equation from this point onwards to represent the effective fluid phase, and the following notation was used

$$\tau_q = \frac{\gamma_s \gamma_f}{h(\gamma_s + \gamma_f)}; \quad \alpha_e = \frac{k_e}{(\gamma_s + \gamma_f)}; \quad \tau_T = \frac{\gamma_s k_e}{h(\gamma_s + \gamma_f)\alpha_e} = \frac{\gamma_s}{h} \tag{12}$$

In Eq. (12) τ_q and τ_T are the heat flux and temperature related time lags linked to the dual-phase-lagging (DuPhlag) to be discussed below, while α_e is the effective thermal diffusivity of the suspension. It may be observed from Eq. (12) that there is a dual effect of the heat capacities on the effective parameters of the uncoupled system in the sense that the heat flux time lag τ_q is affected by the heat capacities of the solid and fluid phases as thermal capacitors connected in series following the relationship $1/\gamma_e^s = 1/\gamma_s + 1/\gamma_f = (\gamma_s + \gamma_f)/\gamma_s \gamma_f$, while the effective thermal diffusivity is affected by the heat capacities of the solid and fluid phases as thermal capacitors connected in parallel following the relationship $\gamma_e^p = (\gamma_s + \gamma_f)$. The boundary and initial conditions applicable to the uncoupled equation (11) are obtained from the original boundary and initial conditions (9) in combination with Eq. (7) and include two initial conditions because Eq. (11) is second order in time

$$r_* = r_{o^*}: T_{f^*} = T_{C^*}$$

$$r_* = r_{w^*}: q_{fr^*} = -k_e \left(\frac{\partial T_{f^*}}{\partial r_*}\right)_{r_{w^*}} = q_{o^*} = \text{const} \Rightarrow \left(\frac{\partial T_{f^*}}{\partial r_*}\right)_{r_{w^*}} = -\frac{q_{o^*}}{k_e}$$

$$t_* = 0: T_{f^*} = T_{C^*} \quad \text{and} \quad \left(\frac{\partial T_{f^*}}{\partial t_*}\right)_{t_*=0} = 0 \tag{13}$$

Equation (11) is identical to the one obtained by replacing the Fourier Law and the fluid-solid interface heat transfer with a DuPhlag constitutive relationship between the heat flux and temperature gradient (Tzou [32,33]) in the form

$$\mathbf{q}_*(\mathbf{r}_*, t_* + \tau_q) = -k_e \nabla_* T_*(\mathbf{r}_*, t_* + \tau_T) \tag{14}$$

where the relationship between the heat flux and temperature gradient is not instantaneous but rather affected by two time lags, a heat flux time lag τ_q, and a temperature gradient time lag, τ_T. By expanding Eq. (14) in a Taylor series in time one obtains

$$\mathbf{q}_*(\mathbf{r}_*, t_*) + \tau_q \frac{\partial \mathbf{q}_*}{\partial t_*}(\mathbf{r}_*, t_*) + O(\tau_q^2) = -k_e \left[\nabla T_*(\mathbf{r}_*, t_*) + \tau_T \frac{\partial(\nabla_* T_*)}{\partial t_*}(\mathbf{r}_*, t_*) + O(\tau_T^2)\right] \tag{15}$$

Truncating the Taylor series by including terms up to order $O(\tau_q)$ and $O(\tau_T)$ yields

$$\mathbf{q}_* + \tau_q \frac{\partial \mathbf{q}_*}{\partial t_*} = -k_e \left[\nabla_* T_* + \tau_T \frac{\partial(\nabla_* T_*)}{\partial t_*}\right] \tag{16}$$

This DuPhlag formulation is applied to the thermal conduction energy equation for the effective medium

$$\gamma_e \frac{\partial T_*}{\partial t_*} + \nabla_* \cdot \mathbf{q}_* = 0 \tag{17}$$

by replacing the fluid-solid interface heat transfer term with the DuPhlag formulation. Applying now the $(\nabla_* \cdot)$ operator in Eq. (16) produces

$$\left[1 + \tau_q \frac{\partial}{\partial t_*}\right] \nabla_* \cdot \mathbf{q}_* = -k_e \left[1 + \tau_T \frac{\partial}{\partial t_*}\right] \nabla_*^2 T_* \tag{18}$$

Substituting $\nabla_* \cdot \mathbf{q}_* = -\gamma_e \partial T_*/\partial t_*$ from Eq. (17) into Eq. (18) and dividing the resulting equation by γ_e yields the equation for the temperature of the effective medium due to DuPhlag, in a form which is identical to Eq. (11) if the ∇_*^2 operator is replaced with its one-dimensional version $(1/r_*)\partial/\partial r_*[r_* \partial(\cdot)/\partial r_*]$, as follows

$$\tau_q \frac{\partial^2 T_*}{\partial t_*^2} + \frac{\partial T_*}{\partial t_*} = \alpha_e \left[\nabla_*^2 T_* + \tau_T \nabla_*^2 \left(\frac{\partial T_*}{\partial t_*} \right) \right] \tag{19}$$

where γ_e, α_e, τ_q, and τ_T are effective parameters which the DuPhlag formulation cannot relate to the specific properties of the individual phases. However, the original derivation presented above resulting in Eq. (11) clearly identifies the explicit form of these effective coefficients and their accurate relationship with the properties of the individual phases in the suspension.

A direct and very important property of these parameters is obtained in evaluating the ratio τ_T/τ_q by using Eq. (12) leading to the following result

$$\beta = \frac{\tau_T}{\tau_q} = 1 + \frac{\gamma_s}{\gamma_f} > 1 \tag{20}$$

Since the ratio of positive valued properties in the second term of Eq. (20) is always positive, the time lags ratio is always greater than 1, i.e., $\tau_T/\tau_q > 1$. The latter conclusion, which is identical to DuPhlag conduction in porous media (Vadasz [34–36]) and is based on a physical argument, has a profound impact on the following results. It applies generally to Fourier heat conduction in suspensions subject to the interface heat transfer formulation presented in Eqs. (6) and (7), and is not restricted to any specific geometry or any specific boundary conditions.

4 Analytical Solution

In order to produce an analytical solution to the problem it is convenient to render Eq. (11) into a dimensionless form by introducing the following dimensionless variables

$$\mathbf{q} = \frac{\mathbf{q}_*}{q_{o^*}}; \quad T = \frac{(T_* - T_{C^*})k_e}{q_{o^*} r_{o^*}}; \quad r = \frac{r_*}{r_{o^*}}; \quad t = \frac{\alpha_e t_*}{r_{o^*}^2} \tag{21}$$

leading to

$$\mathrm{Fo}_q \frac{\partial^2 T}{\partial t^2} + \frac{\partial T}{\partial t} = \frac{1}{r}\frac{\partial}{\partial r}\left(r \frac{\partial T}{\partial r} \right) + \mathrm{Fo}_T \frac{1}{r}\frac{\partial}{\partial r}\left(r \frac{\partial^2 T}{\partial r \partial t} \right) \tag{22}$$

where the following two dimensionless groups representing a heat flux Fourier number, Fo_q, and a temperature Fourier number, Fo_T, emerged. These Fourier numbers are defined in the form

$$\mathrm{Fo}_q = \frac{\alpha_e \tau_q}{r_{o^*}^2}; \quad \mathrm{Fo}_T = \frac{\alpha_e \tau_T}{r_{o^*}^2} \tag{23}$$

and the ratio between them is identical to the ratio between the time lags, i.e., $\mathrm{Fo}_T/\mathrm{Fo}_q = \tau_T/\tau_q$. The applicable dimensionless boundary and initial conditions are obtained by rendering Eq. (13) dimensionless using the scales introduced by Eq. (21) in the form

$$r = 1: T = 0 \tag{24}$$

$$r = r_w: q_r = -\left(\frac{\partial T}{\partial r} \right)_{r_w} = 1 \Rightarrow \left(\frac{\partial T}{\partial r} \right)_{r_w} = -1 \tag{25}$$

$$t = 0: T = 0 \quad \text{and} \quad \left(\frac{\partial T}{\partial t} \right)_{t=0} = 0 \tag{26}$$

Prior to presenting the analytical solution to the DuPhlag problem represented by Eqs. (22) and (24)–(26) it is of interest to present the case corresponding to the Fourier solution because this will be our reference case, the one being used in the experimental evaluation of the effective thermal conductivity when using the THW method. It can be observed that Eq. (22) degenerates to the Fourier thermal diffusion equation when $\mathrm{Fo}_q = \mathrm{Fo}_T = 0$, corresponding to $\tau_q = \tau_T = 0$. The latter may occur either when the heat capacity of the solid is excessively low, i.e., when $\gamma_s \to 0$, or when the fluid-solid interface heat transfer coefficient is excessively large, i.e., when $h \to \infty$ as can be observed from Eq. (12). In such cases the Fourier thermal diffusion solution applies and can be presented in the classical form (e.g., Özisik [37])

$$T = -r_w \ln(r) + \sum_{n=1}^{\infty} A_n e^{-\kappa_n^2 t} \left[Y_o(\kappa_n) J_o(\kappa_n r) - J_o(\kappa_n) Y_o(\kappa_n r) \right] \tag{27}$$

where $J_o(\kappa_n r)$ and $Y_o(\kappa_n r)$ are the order 0 Bessel functions of the first and second kind, respectively. The eigenvalues κ_n are the roots of the equation

$$J_o(\kappa_n) Y_1(\kappa_n r_w) - Y_o(\kappa_n) J_1(\kappa_n r_w) = 0,$$

and the coefficient A_n is established from the initial condition $(T)_{t=0} = 0$ in the form

$$A_n = \frac{\pi^2 r_w J_1^2(\kappa_n r_w) \left[Y_o(\kappa_n) J_o(\kappa_n r_w) - J_o(\kappa_n) Y_o(\kappa_n r_w) \right]}{2\left[J_o^2(\kappa_n r_w) - J_1^2(\kappa_n r_w) \right]}$$

The analytical solution to the DuPhlag equation (22) subject to the boundary conditions (24) and (25) and initial conditions (26) is obtained by superposition of the steady state, $T_{\mathrm{st}}(r)$, and transient $T_{\mathrm{tr}}(r,t)$, solutions in the form

$$T = T_{\mathrm{st}}(r) + T_{\mathrm{tr}}(r,t) \tag{28}$$

The steady state part of the solution is governed by the equation

$$\frac{d}{dr}\left(r \frac{dT_{\mathrm{st}}}{dr} \right) = 0 \tag{29}$$

which is simply integrated subject to the boundary conditions

$$r = 1: T_{\mathrm{st}} = 0; \quad r = r_w: \left(\frac{dT_{\mathrm{st}}}{dr} \right)_{r_w} = -1 \tag{30}$$

to yield the steady state solution in the form

$$T_{\mathrm{st}} = -r_w \ln(r) \tag{31}$$

The transient solution is governed by the equation

$$\mathrm{Fo}_q \frac{\partial^2 T_{\mathrm{tr}}}{\partial t^2} + \frac{\partial T_{\mathrm{tr}}}{\partial t} = \frac{1}{r}\frac{\partial}{\partial r}\left(r \frac{\partial T_{\mathrm{tr}}}{\partial r} \right) + \mathrm{Fo}_T \frac{1}{r}\frac{\partial}{\partial r}\left(r \frac{\partial^2 T_{\mathrm{tr}}}{\partial r \partial t} \right) \tag{32}$$

which is subject to the homogeneous boundary conditions

$$r = 1: T_{\mathrm{tr}} = 0; \quad r = r_w: \left(\frac{\partial T_{\mathrm{tr}}}{\partial r} \right)_{r_w} = 0 \tag{33}$$

and the initial conditions

$$t = 0: T_{\mathrm{tr}} = -T_{\mathrm{st}}(r) = r_w \ln(r) \quad \text{and} \quad \left(\frac{\partial T_{\mathrm{tr}}}{\partial t} \right)_{t=0} = 0 \tag{34}$$

The solutions to Eq. (32) subject to the boundary conditions (33) and initial conditions (34) is obtained by separation of variables and expansion in terms of orthogonal eigenfunctions in the form $T_{\mathrm{tr}} = S(t)R(r)$, which upon substitution into Eq. (32) produces the following eigenvalue-eigenfunction problems

$$\frac{1}{r}\frac{\mathrm{d}}{\mathrm{d}r}\left(r \frac{\mathrm{d}R_{\mathrm{on}}}{\mathrm{d}r} \right) + \kappa_n R_{\mathrm{on}} = 0 \tag{35}$$

subject to the homogeneous boundary conditions

$$r = 1: R_{\mathrm{on}} = 0; \quad r = r_w: \left(\frac{\mathrm{d}R_{\mathrm{on}}}{\mathrm{d}r} \right)_{r_w} = 0 \tag{36}$$

and

$$\frac{d^2 S_n}{dt^2} + c_{fn} \frac{dS_n}{dt} + \omega_n^2 S_n = 0 \tag{37}$$

where

$$c_{fn} = \frac{(1 + \kappa_n^2 \mathrm{Fo}_T)}{\mathrm{Fo}_q}; \quad \omega_n^2 = \frac{\kappa_n^2}{\mathrm{Fo}_q} \tag{38}$$

Equation (35) is the Bessel equation of order 0, producing solutions in the form of Bessel functions

$$R_{\mathrm{on}} = A_1 J_o(\kappa_n r) + A_2 Y_o(\kappa_n r) \tag{39}$$

where $J_o(\kappa_n r)$ and $Y_o(\kappa_n r)$ are the order 0 Bessel functions of the first and second kind, respectively. Applying the boundary conditions (36) one obtains the equation for the eigenvalues in the form

$$J_o(\kappa_n) Y_1(\kappa_n r_w) - Y_o(\kappa_n) J_1(\kappa_n r_w) = 0 \tag{40}$$

where $J_1(\kappa_n r_w)$ and $Y_1(\kappa_n r_w)$ are the order 1 Bessel functions of the first and second kind, respectively. This equation for the eigenvalues (40) as well as the eignefunctions (39) are identical to the ones obtained for Fourier thermal diffusion as observed in Eq. (27) and the text following it. The boundary conditions also yield the following form for the eignefunctions

$$R_{\mathrm{on}} = A_n [Y_o(\kappa_n) J_o(\kappa_n r) - J_o(\kappa_n) Y_o(\kappa_n r)] \tag{41}$$

On the other hand, Eq. (37) is the equation of a linear damped oscillator that allows in principle, overdamped, critically-damped and underdamped solutions depending on the values of c_{fn} and ω_n^2. The solution to Eq. (37) is obtained by solving the auxiliary equation for the eigenvalues λ_n

$$\lambda_n^2 + c_{fn} \lambda_n + \omega_n^2 = 0 \tag{42}$$

where c_{fn} and ω_n^2 are defined by Eq. (38). Hence, the solutions for the eigenvalues λ_n are

$$\lambda_{n1} = -\frac{c_{fn}}{2}\left[1 + \sqrt{1 - 4\frac{\omega_n^2}{c_{fn}^2}}\right] \tag{43}$$

$$\lambda_{n2} = -\frac{c_{fn}}{2}\left[1 - \sqrt{1 - 4\frac{\omega_n^2}{c_{fn}^2}}\right] \tag{44}$$

producing the complete solution in the form

$$T = -r_w \ln(r) + \sum_{n=1}^{\infty} [B_{1n} e^{\lambda_{n1} t} + B_{2n} e^{\lambda_{n2} t}][Y_o(\kappa_n) J_o(\kappa_n r) - J_o(\kappa_n) Y_o(\kappa_n r)] \tag{45}$$

The solution $S_n(t)$ represented by the terms in the first brackets in Eq. (45) is overdamped if for some values of $n \geq 1$ the condition $4\omega_n^2 < c_{fn}^2$ is satisfied, leading to real values of λ_{n1} and λ_{n2}, and to the solution (45) above, it is critically damped if for some value of $n = n_{\mathrm{cr}} \geq 1$ the condition $4\omega_{n,\mathrm{cr}}^2 = c_{fn,\mathrm{cr}}^2$ is satisfied, corresponding to $\lambda_{n1} = \lambda_{n2} = \lambda_{n,\mathrm{cr}} = -c_{fn,\mathrm{cr}}/2$, leading to a solution of the form $[B_{1n,\mathrm{cr}} e^{\lambda_{n,\mathrm{cr}} t} + B_{2n,\mathrm{cr}} t e^{\lambda_{n,cr} t}][Y_o(\kappa_{n,cr}) J_o(\kappa_{n,\mathrm{cr}} r) - J_o(\kappa_{n,\mathrm{cr}}) Y_o(\kappa_{n,\mathrm{cr}} r)]$ and it is underdamped if for some values of $n \geq 1$ the condition $4\omega_n^2 > c_{fn}^2$ is satisfied producing complex values of λ_{n1} and λ_{n2} in the form $\lambda_{n1} = \lambda_{rn} + i\lambda_{in}$, $\lambda_{n2} = \lambda_{rn} - i\lambda_{in}$, leading to the following form of the solution $e^{\lambda_{rn} t}[B_n e^{i\lambda_{in} t} + B_n^* e^{-i\lambda_{in} t}][Y_o(\kappa_n) J_o(\kappa_n r) - J_o(\kappa_n) Y_o(\kappa_n r)]$ where B_n^* stands for the complex conjugate of B_n.

The condition for underdamped solutions and its associated oscillations is further explored to obtain explicit criteria in terms of the primitive parameters of the original system. By using the definitions from Eq. (38) it produces the condition for underdamped and critically-damped solutions in the form

$$\frac{c_{fn}^2}{4\omega_n^2} = \frac{[1 + \mathrm{Fo}_T \kappa_n^2]^2}{4\,\mathrm{Fo}_q \kappa_n^2} \leq 1 \tag{46}$$

where the equality part applies to critically-damped solutions. An analysis of inequality (46) presented in Appendix B yields the following necessary and sufficient condition for underdamped and critically-damped solutions to materialize

$$\beta = \frac{\mathrm{Fo}_T}{\mathrm{Fo}_q} = \frac{\tau_T}{\tau_q} \leq 1 \tag{47}$$

However Eq. (20) shows that based on physical arguments the time lag ratio τ_T/τ_q is always greater than 1, i.e., $\tau_T/\tau_q > 1$. Therefore, underdamped (oscillatory) solutions, which require according to Eq. (47) that $\tau_T/\tau_q < 1$, are being ruled out. Similarly, since the condition for critically-damped solutions is $\mathrm{Fo}_T/\mathrm{Fo}_q = \tau_T/\tau_q = 1$, but in reality this ratio is greater than 1, i.e., $\tau_T/\tau_q > 1$, critically-damped solutions are ruled out as well, meaning that the eignevalues λ_{n1} and λ_{n2}, are real, distinct, and negative. Therefore, solution (45) represents the complete form of the solution.

The values of the coefficients B_{1n} and B_{2n} are being evaluated by using the two initial conditions presented in Eq. (26) or (34). By applying the initial condition $(\partial T/\partial t)_{t=0} = 0$ with the solution (45) yields a relationship between the coefficients B_{1n} and B_{2n} in the form $B_{2n} = -(\lambda_{n1}/\lambda_{n2}) B_{1n}$ transforming Eq. (45) to its final form

$$T = -r_w \ln(r) + \sum_{n=1}^{\infty} B_n [\lambda_{n2} e^{\lambda_{n1} t} - \lambda_{n1} e^{\lambda_{n2} t}][Y_o(\kappa_n) J_o(\kappa_n r) - J_o(\kappa_n) Y_o(\kappa_n r)] \tag{48}$$

By applying now the other initial condition $(T)_{t=0} = 0$ to Eq. (48), multiplying Eq. (48) by $R_{om} = Y_o(\kappa_m) J_o(\kappa_m r) - J_o(\kappa_m) Y_o(\kappa_m r)$, integrating the result over the domain $r \in [r_w, 1]$ while using the orthogonal properties of Bessel functions

$$\int_{r_w}^{1} R_{\mathrm{on}}(\kappa_n, r) R_{om}(\kappa_m, r) r\, dr = \begin{cases} 0 & \text{for } m \neq n \\ N(\kappa_n) & \text{for } m = n \end{cases} \tag{49}$$

where $N(\kappa_n) = \int_{r_w}^{1} r R_{\mathrm{on}}^2(\kappa_n, r) dr$ is the norm, produces the following result for B_n

$$B_n = \frac{-r_w [Y_o(\kappa_n) J_o(\kappa_n r_w) - J_o(\kappa_n) Y_o(\kappa_n r_w)]}{(\lambda_{2n} - \lambda_{1n}) \kappa_n^2} \frac{1}{N(\kappa_n)} \tag{50}$$

The norm evaluated for this problem is presented in the form

$$\frac{1}{N(\kappa_n)} = \frac{\pi^2}{2} \frac{\kappa_n^2 J_1^2(\kappa_n r_w)}{[J_1^2(\kappa_n r_w) - J_o^2(\kappa_n r_w)]} \tag{51}$$

and therefore the explicit form of the coefficient B_n in the final form of the solution (48) is

$$B_n = \frac{\pi^2 r_w J_1^2(\kappa_n r_w)[Y_o(\kappa_n) J_o(\kappa_n r_w) - J_o(\kappa_n) Y_o(\kappa_n r_w)]}{2(\lambda_{n2} - \lambda_{n1})[J_o^2(\kappa_n r_w) - J_1^2(\kappa_n r_w)]} \tag{52}$$

where λ_{n1} and λ_{n2} are defined by Eqs. (43) and (44), respectively, and $\kappa_n \forall n = 1, 2, 3, \ldots$ are the solutions of the eignevalues equation (40).

5 Corrections to Experimental Data

In order to derive the deviations from the Fourier to the DuPhlag thermal conduction solutions and evaluate the required corrections to the THW experimental method to render it applicable to suspensions we use the corresponding Fourier solution to the same problem by using Eq. (27) leading to the following dimensional solution for the wire temperature $T_{w^*}(t)$ at $r = r_w$

$$[T_{w^*}(t) - T_{C^*}] = \frac{q_{o^*} r_{o^*}}{k_{\mathrm{app}}} [-r_w \ln(r_w) + f(t)] \tag{53}$$

where k_{app} is the apparent effective thermal conductivity and

$$f(t) = \sum_{n=1}^{\infty} C_n \exp(-\kappa_n^2 t) \tag{54}$$

The coefficient C_n is defined in the form

$$C_n = \frac{\pi^2 r_w J_1^2(\kappa_n r_w)[Y_o(\kappa_n)J_o(\kappa_n r_w) - J_o(\kappa_n)Y_o(\kappa_n r_w)]^2}{2[J_o^2(\kappa_n r_w) - J_1^2(\kappa_n r_w)]} \quad (55)$$

When evaluating the thermal conductivity by applying the THW method and using the Fourier Law one obtains from Eq. (53)

$$k_{\text{app}} = \frac{q_{o^*} r_{o^*}}{[T_{w^*}(t) - T_{C^*}]}[-r_w \ln(r_w) + f(t)] \quad (56)$$

where the temperature difference $[T_{w^*}(t) - T_{C^*}]$ is represented by the recorded experimental data and the value of the heat flux at the fluid-platinum-wire interface q_{o^*} is evaluated from the Joule heating of the hot wire in the form $q_{o^*} = iV/2\pi r_{w^*} l_*$, where $2\pi r_{w^*} l_*$ is the heat transfer area of the hot wire, with l_* being the length of the platinum wire, i is the electric current flowing through the wire, and V is the voltage drop across the wire.

A method of synthetic experimental emulation data (SEED) is applied now to evaluate the deviation between Fourier and Dual-Phase-Lagging thermal conduction. According to the SEED method one assumes that the data expressed by $[T_{w^*}(t) - T_{C^*}]$ represent a different than Fourier conduction solution, in this case a DuPhlag thermal conduction solution. Then we substitute in Eq. (56) the values of $[T_{w^*}(t) - T_{C^*}]$ obtained from the DuPhlag solution expressed by Eq. (48) in the form

$$[T_{w^*} - T_{C^*}] = \frac{q_{o^*} r_{o^*}}{k_{\text{act}}}[-r_w \ln(r_w) + g(t)] \quad (57)$$

where k_{act} is the actual effective thermal conductivity and

$$g(t) = \sum_{n=1}^{\infty} \tilde{C}_n[\lambda_{n2} \exp(\lambda_{n1} t) - \lambda_{n1} \exp(\lambda_{n2} t)] \quad (58)$$

The coefficient $\tilde{C}_n$ is related to C_n defined in Eq. (54) by the following relationship

$$\tilde{C}_n = \frac{C_n}{(\lambda_{n2} - \lambda_{n1})} \quad (59)$$

where λ_{n1} and λ_{n2} are defined by Eqs. (43) and (44), respectively. Following the substitution of the values of $[T_{w^*}(t) - T_{C^*}]$ obtained from the DuPhlag solution expressed by Eq. (57) into Eq. (56) leads to the following ratio between the apparent and actual effective thermal conductivities

$$\sigma = \frac{k_{\text{app}}}{k_{\text{act}}} = \frac{[-r_w \ln(r_w) + f(t)]}{[-r_w \ln(r_w) + g(t)]} \quad (60)$$

where k_{app} is the apparent effective thermal conductivity obtained from the Fourier conduction solution while k_{act} is the actual effective thermal conductivity that corresponds to data that follow the DuPhlag conduction, and where $f(t)$ can be evaluated from Eq. (54) while $g(t)$ is evaluated from Eq. (58). The ratio between the two will provide the deviation of the apparent effective thermal conductivity from the actual one.

The dimensional values used in the computational results are identical to the ones used in the experimental setup of Eastman et al. [1], Lee et al. [2] for metals and metal oxides suspended in ethylene glycol, or alternatively for nanotube suspensions in oil used by Choi et al. [3]. Equation (60) can be evaluated as a function of time for any given values of Fourier numbers, Fo_q, Fo_T. The dependence of the results on the Fourier numbers is established due to the dependence of the DuPhlag eigenvalues on Fo_q and Fo_T, which are needed in the evaluation of $g(t)$. Other than that the thermal conductivity ratio depends only on the dimensionless time and on the value of $r_w = r_{w^*}/r_{o^*}$. To convert the thermal conductivity ratio and express it in terms of the dimensional values of time we use the scaling definition introduced by Eq. (21) in the form $t_* = (r_{o^*}^2/\alpha_e)t$. We use a value of $r_{o^*} = 0.025$ m which is the radius of the cylindrical container used by Eastman et al. [1], Lee et al. [2], and Choi et al. [3], and two different values of effective thermal diffusivity α_e corresponding to copper in ethylene glycol and carbon nanotubes in oil, respectively. The effective thermal conductivity used to evaluate the effective thermal diffusivity was evaluated by using the Hamilton and Crosser [8] equations that represent an application of Maxwell's equation [5] to other than the spherical geometry. As a result, for copper nanoparticles in ethylene glycol at a volumetric solid fraction of $\varepsilon = 0.01$ one obtains the values of $\alpha_e = 4.227 \times 10^{-8}$ m^2 s^{-1}, $k_e = 0.257$ W m^{-1} K^{-1} and a time lags ratio of $\beta = \tau_T/\tau_q = \text{Fo}_T/\text{Fo}_q = 2.2857$. The corresponding values for carbon nanotubes suspended in oil are $\alpha_e = 8.045 \times 10^{-8}$ m^2 s^{-1}, $k_e = 0.154$ W m^{-1} K^{-1} and a time lag ratio of $\beta = \tau_T/\tau_q = \text{Fo}_T/\text{Fo}_q = 1.113$. Consequently the time conversion from dimensionless to dimensional follows the respective factoring $t_* = (r_{o^*}^2/\alpha_e)t = 1.479 \times 10^4 t$ s for copper nanoparticles suspended in ethylene glycol, and $t_* = 7.769 \times 10^3 t$ s for carbon nanotubes suspended in oil. The same values produce the following validity time range for the application of the THW method as indicated by Eq. (3) and the text following Eq. (5) in the form 13.7 ms $\ll t_* <$ 5 s for copper nanoparticles suspended in ethylene glycol and 7.2 ms $\ll t_* <$ 5 s for carbon nanotubes suspended in oil. A value of $r_w = 2 \times 10^{-3}$ was used in all computations. If the relationships for h that are applicable to porous media are being (without justification) extrapolated to include nanofluid suspensions one evaluates very large values of h leading to very small values for the time lags τ_q and τ_T, and consequently very small values of the Fourier numbers, Fo_q and Fo_T. However, further and a different dependence of h on particle size is anticipated when the particle size is reduced to the nanoscale level predominantly when the ballistic rather than diffusive nature of heat transfer becomes dominant (Chen [20–22]) and hence reducing by a few orders of magnitude the rate of heat transfer, implying a consequential reduction of the value of h to compensate for the otherwise substantial increase of h as the particle size decreases. The latter opposing trends in the variation of the value of h as the particle size is reduced to the nanoscale level suggest much larger values for the time lags τ_q and τ_T, and consequently larger values of the Fourier numbers, Fo_q and Fo_T. Therefore, a wide range of Fourier numbers Fo_q and Fo_T spanning over a few orders of magnitude (but still quite small Fourier number values) was used in order to compensate for the lack of accurate knowledge of the value of the solid-fluid interface heat transfer coefficient h, especially for nanoscale suspensions, as discussed in Appendix A. The Fourier number ratio $\beta = \text{Fo}_T/\text{Fo}_q$ used was as indicated above for copper nanoparticles suspended in ethylene glycol and carbon nanotubes suspended in oil, respectively. Therefore, for each one of these types of suspensions, a variation of Fo_q was applied while the corresponding value of Fo_T can be evaluated by $\text{Fo}_T = \beta \text{Fo}_q$ with the values of β consistent with the ones listed above.

To conclude so far, a correction factor σ, as presented in Eq. (60), can be used in connection with the THW method in order to apply the latter method to suspended particles in fluids.

6 Results and Discussion

The evaluated dimensionless wire temperature at $r_* = r_{w^*}$ as a function of the dimensional time corresponding to either nanoparticles suspended in ethylene glycol and carbon nanotubes suspended in oil and a range of values of Fo_q varying between $\text{Fo}_q = 10^{-4}$ and $\text{Fo}_q = 10^{-6}$ is presented in Figs. 2–7 on a logarithmic time scale. The objective of the wire temperature results is to observe whether the DuPhlag solution produces results that are approximately linear in time on a logarithmic time scale, as the Fourier solution is anticipated to produce, especially for the time ranges indicated above. The latter is particularly important because the experimental results presented by Eastman et al. [1], Lee et al. [2], and Choi et al. [3] do not include the wire temperature as a function of time used to evaluate the effective thermal con-

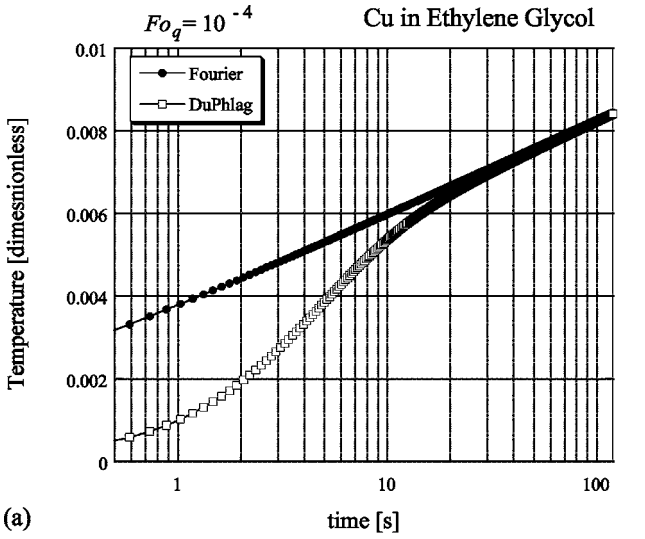

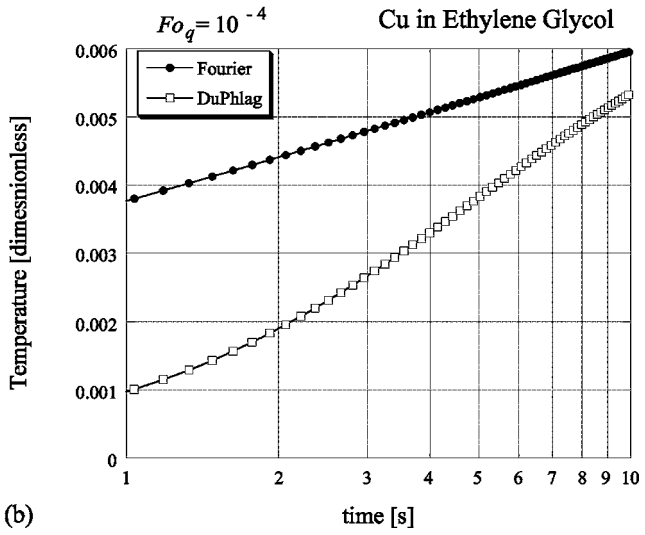

Fig. 2 The dimensionless wire temperature corresponding to the Fourier as well as the DuPhlag solutions as a function of time, on a logarithmic time scale, for a Fourier number of $Fo_q = 10^{-4}$ and for copper nanoparticles suspended in ethylene glycol. (*a*) Transient solution for the time range 0.5 s$<t_*<$120 s; (*b*) detail within the time range 1 s$<t_*<$10 s.

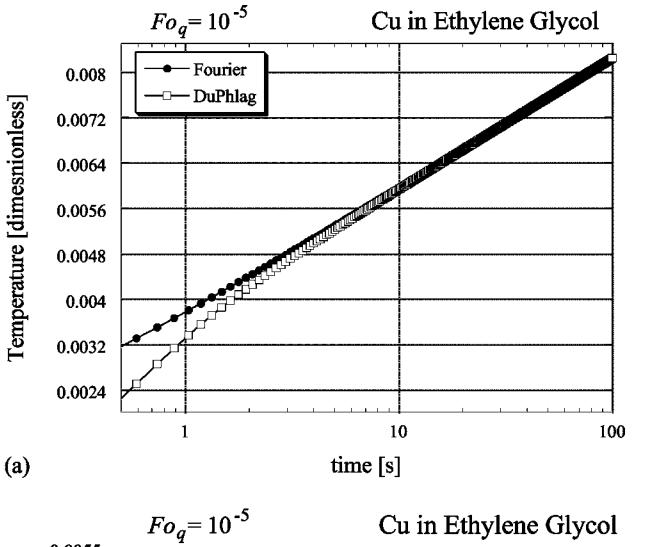

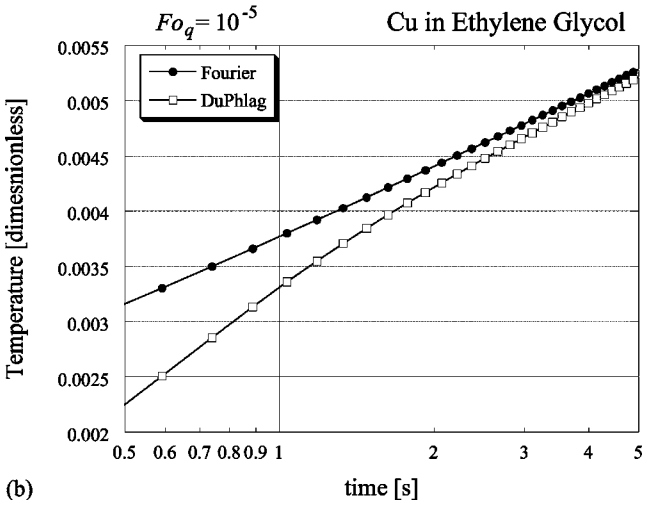

Fig. 3 The dimensionless wire temperature corresponding to the Fourier as well as the DuPhlag solutions as a function of time, on a logarithmic time scale, for a Fourier number of $Fo_q = 10^{-5}$ and for copper nanoparticles suspended in ethylene glycol. (*a*) Transient solution for the time range 0.5 s$<t_*<$100 s; (*b*) detail within the time range 0.5 s$<t_*<$5 s.

ductivity, with the only exception of a calibration result for the fluid without the suspended nanoparticles which was presented by Lee et al. [2]. Initial evaluation of the Fourier dimensionless solution (53) was compared first to the "THW" wire temperature solution evaluated based on a dimensionless form of Eq. (2) clearly identifying a straight line on a logarithmic time scale and very small deviations between the two. Actually for dimensional times above 1 s the relative deviations between the two are less than 5% with less than 1% deviations for times larger than 3 s.

The dimensionless wire temperature corresponding to the Fourier as well as the DuPhlag solutions as a function of time is presented on a logarithmic time scale in Fig. 2(*a*) for a Fourier number of $Fo_q = 10^{-4}$ and for copper nanoparticles in ethylene glycol. The solution presented in the figure represents the transient, and the time range does not include the steady state. The DuPhlag solution overlaps with the Fourier solution for long times. The corresponding results zoomed within the short time range $1\ \text{s} < t_* < 10\ \text{s}$ are presented in Fig. 2(*b*) showing that within this time range the DuPhlag solution produces results that can be seen as approximately linear in time on a logarithmic time scale, while the Fourier solution is almost accurately linear in time on a logarithmic time scale, however their slopes are substantially different. Similar results that apply to copper nanoparticles in ethylene glycol and a Fourier number of $Fo_q = 10^{-5}$ are presented in Fig. 3(*a*) where the overlapping between the DuPhlag and the Fourier solutions at long times is evident. The corresponding results zoomed within the short time range $0.5\ \text{s} < t_* < 5\ \text{s}$ are presented in Fig. 3(*b*). They show that within this time range the DuPhlag solution produces results that are approximately linear in time on a logarithmic time scale, while the Fourier solution is accurately linear in time on a logarithmic time scale, however different slopes are generally associated with each solution. The results applicable to copper nanoparticles in ethylene glycol and a Fourier number of $Fo_q = 10^{-6}$ are presented in Fig. 4 within the short time range $0.5\ \text{s} < t_* < 5\ \text{s}$, where the overlapping between the DuPhlag and the Fourier solutions at almost all times is revealed. A slight variation between the DuPhlag and Fourier solutions within the initial short time range is noticed. Both the DuPhlag and Fourier results are almost accurately linear in time on a logarithmic time scale, their slopes however varying at short times.

The dimensionless wire temperature corresponding to the Fou-

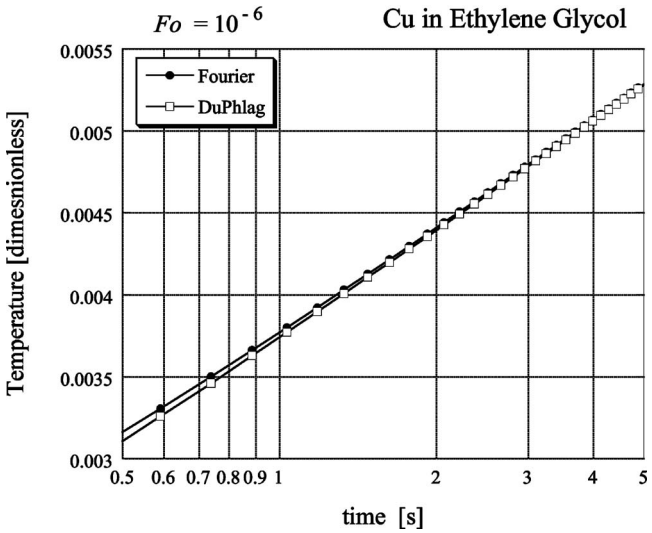

Fig. 4 The dimensionless wire temperature corresponding to the Fourier as well as the DuPhlag solutions as a function of time, on a logarithmic time scale, for a Fourier number of $Fo_q = 10^{-6}$ and for copper nanoparticles suspended in ethylene glycol. Detail of the transient solution for the time range 0.5 s $< t_* <$ 5 s.

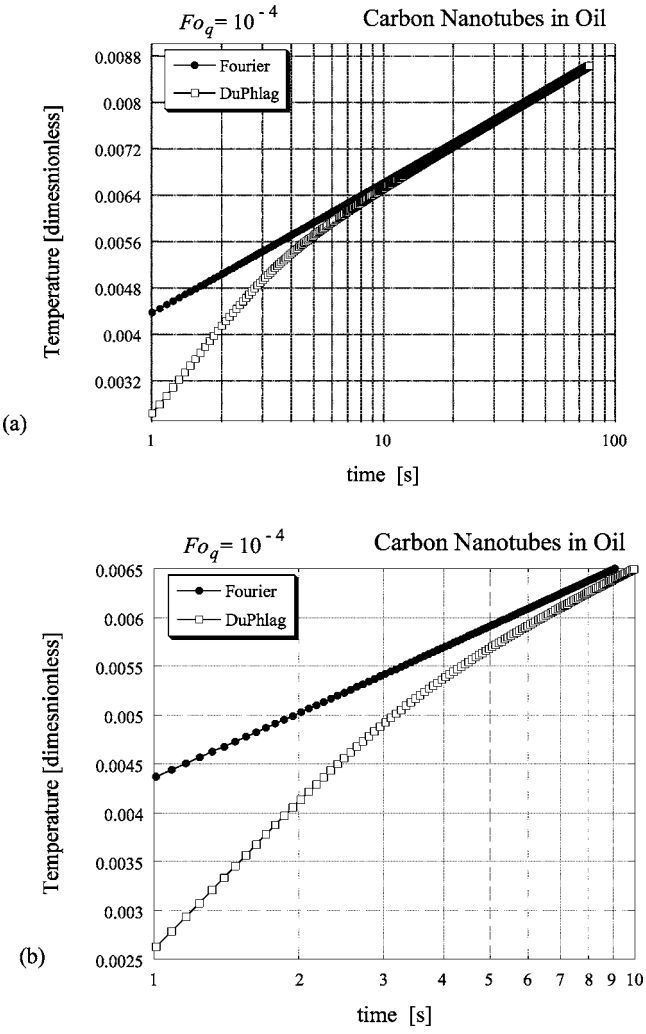

Fig. 5 The dimensionless wire temperature corresponding to the Fourier as well as the DuPhlag solutions as a function of time, on a logarithmic time scale, for a Fourier number of $Fo_q = 10^{-4}$ and for for carbon nanotubes suspended in oil. (*a*) transient solution for the time range 1 s $< t_* <$ 100 s; (*b*) detail within the time range 1 s $< t_* <$ 10 s.

rier as well as the DuPhlag solutions as a function of time is presented on a logarithmic time scale in Fig. 5(*a*) for a Fourier number of $Fo_q = 10^{-4}$ and for carbon nanotubes in oil. The DuPhlag solution overlaps with the Fourier solution at long times. The corresponding results zoomed within the short time range 1 s $< t_* <$ 10 s are presented in Fig. 5(*b*). The results show that within this time range the DuPhlag solution does not produce results that are approximately linear in time on a logarithmic time scale unless a smaller time range window is used, while the Fourier solution is almost accurately linear in time on a logarithmic time scale. Their corresponding slopes are substantially different. Similar results that apply to carbon nanotubes in oil and a Fourier number of $Fo_q = 10^{-5}$ are presented in Fig. 6 within the short time range 0.5 s $< t_* <$ 5 s, where the overlapping between the DuPhlag and the Fourier solutions at longer times is evident. The figure shows that within this short time range both the DuPhlag as well as the Fourier solutions produce results that are linear in time on a logarithmic time scale, however different slopes are generally associated with each solution. The results applicable to carbon nanotubes in oil and a Fourier number of $Fo_q = 10^{-6}$ zoomed within the short time range 0.5 s $< t_* <$ 5 s are presented in Fig. 7 where the overlapping between the DuPhlag and the Fourier solutions at almost all times is revealed. A slight variation between the DuPhlag and Fourier solutions within the initial short time range is noticed. Both the DuPhlag and Fourier results are accurately linear in time on a logarithmic time scale. The linearity of the wire temperature with time on a logarithmic time scale that was at least approximately revealed in most of the results presented above cannot be used to distinguish a priori between experimental data whether they belong to Fourier or DuPhlag unless moderate or large values of the Fourier number, i.e., $Fo_q \geq 10^{-5}$, are considered. The latter may therefore confirm the validity of one of the models as the correct one if the previously mentioned range of Fourier numbers applies. Otherwise there is no easy way to distinguish between the two.

The results of the ratio between the "apparent" and "actual" effective thermal conductivities following Eq. (60) and corresponding to data of copper nanoparticles suspended in ethylene glycol compared with carbon nanotubes suspended in oil are presented in Fig. 8 for a Fourier number of $Fo_q = 10^{-4}$. An effective thermal conductivity ratio that varies between $k_{app}/k_{act} = 1.4$ and beyond $k_{app}/k_{act} = 5$ was evaluated for carbon nanotubes in oil, while this ratio varies between $k_{app}/k_{act} = 1.05$ and beyond $k_{app}/k_{act} = 5$ for copper nanoparticles suspended in ethylene glycol. The corresponding effective thermal conductivity ratio results for a Fourier number of $Fo_q = 10^{-5}$ is presented in Fig. 9. The figure reveals a variation of the effective thermal conductivity ratio that may go beyond $k_{app}/k_{act} = 1.5$ for times below 1 s for both copper nanoparticles suspended in ethylene glycol as well as for carbon nanotubes in oil. Results for a very small Fourier number value of $Fo_q = 10^{-6}$ are presented in Fig. 10 where values of up to and beyond $k_{app}/k_{act} = 1.3$ can be reached for times below 0.5 s.

The fact that the effective thermal conductivity ratio varies substantially with time within the time range considered and used in the experiments makes a definite resolution to the experimental puzzle inconclusive, unless the experimental wire temperature versus time data become available for analysis. Nevertheless the results presented in this paper may provide a valid explanation. The computed analytical results show that the apparent thermal conductivity evaluated via the Fourier conduction constitutive relationship in conjunction with the THW experimental method could indeed produce results that show substantial apparent enhancement of the effective thermal conductivity of the nanofluid

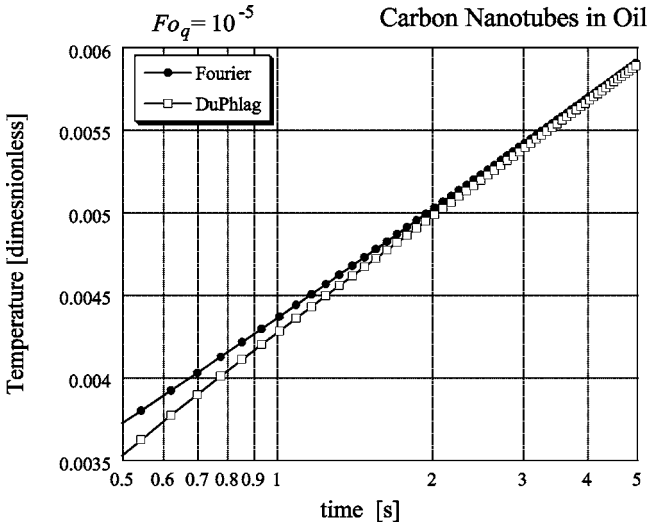

Fig. 6 The dimensionless wire temperature corresponding to the Fourier as well as the DuPhlag solutions as a function of time, on a logarithmic time scale, for a Fourier number of $Fo_q = 10^{-5}$ and for carbon nanotubes suspended in oil. Detail within the time range 0.5 s$<t_*<$5 s.

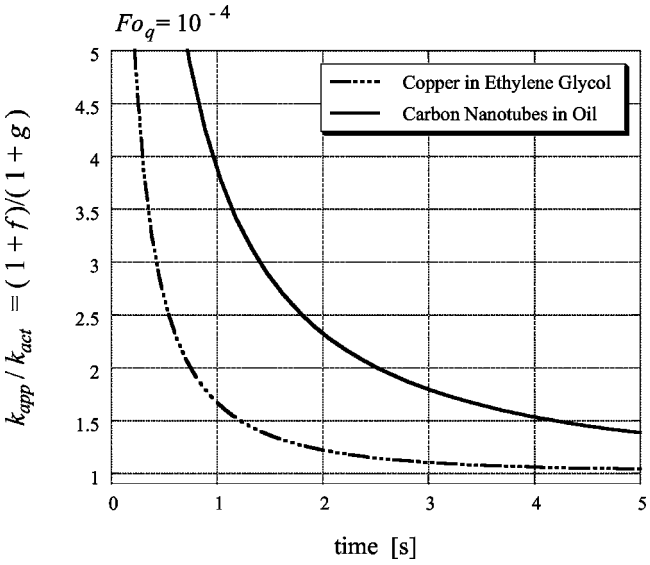

Fig. 8 The ratio between the "apparent" and "actual" effective thermal conductivities following Eq. (60) and corresponding to copper nanoparticles suspended in ethylene glycol compared with carbon nanotubes suspended in oil for a Fourier number of $Fo_q = 10^{-4}$

suspension if the actual conduction process is governed by a thermal conduction process as derived in the present paper. A correction factor σ is to be used in the latter case to convert the THW data to values appropriate for suspensions. (Note: the thermal conductivity obtained from the Fourier solution is constant, i.e., independent of time. However, the ratio between the derivations of the thermal conductivity via Fourier and DuPhlag methods varies in time.)

Future research should focus on the development of an accurate estimate for the solid-fluid interface heat transfer coefficient, h, as the particle size is reduced. The latter will allow an accurate and directly applicable correction to the THW data, which will make the THW experimental method useful in its application to suspensions.

7 Conclusions

An attempt in explaining experimental results, which reveal an impressive heat transfer enhancement in nanofluid suspensions was derived based on the heat conduction mechanism for transient processes in suspensions. The effect of the surface-area-to-volume ratio (specific area) of the suspended nanoparticles on the heat transfer mechanism was shown to impact substantially on the solution and results. The results show that an apparent effective thermal conductivity enhancement of the same quantitative values as the experiments suggest can be obtained if the solid-fluid interface heat transfer mechanism is accounted for, leading to DuPhlag conduction. The analysis provides a possible explanation that settles the apparent conflict between the recent experimental re-

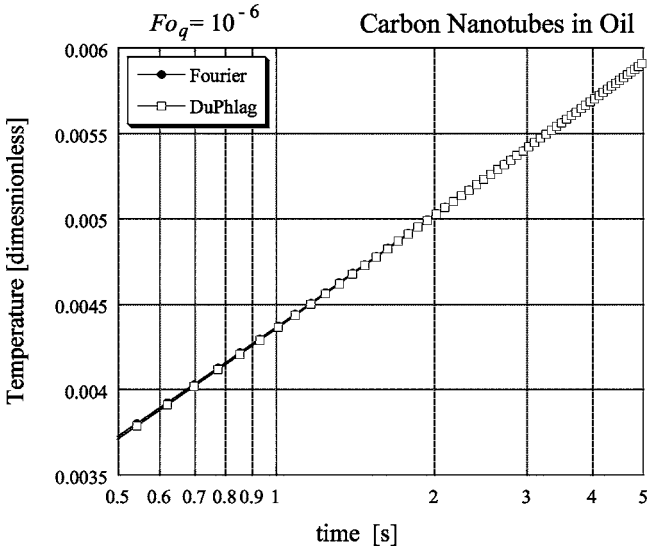

Fig. 7 The dimensionless wire temperature corresponding to the Fourier as well as the DuPhlag solutions as a function of time, on a logarithmic time scale, for a Fourier number of $Fo_q = 10^{-6}$ and for for carbon nanotubes suspended in oil. Detail within the time range 0.5 s$<t_*<$5 s.

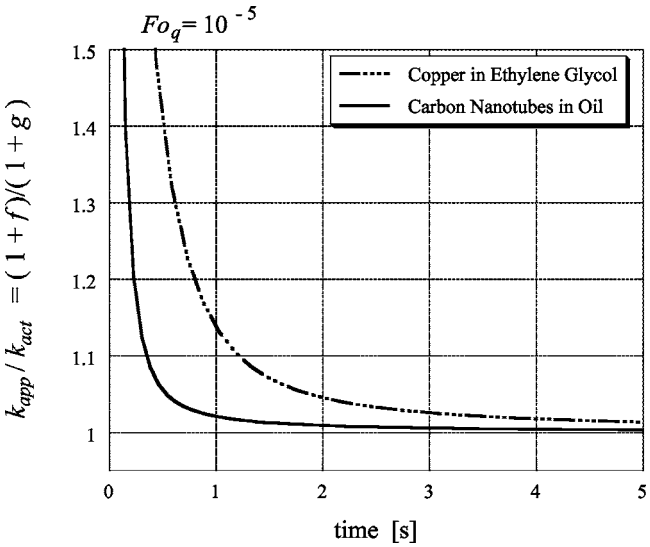

Fig. 9 The ratio between the "apparent" and "actual" effective thermal conductivities following Eq. (60) and corresponding to copper nanoparticles suspended in ethylene glycol compared to carbon nanotubes suspended in oil for a Fourier number of $Fo_q = 10^{-5}$

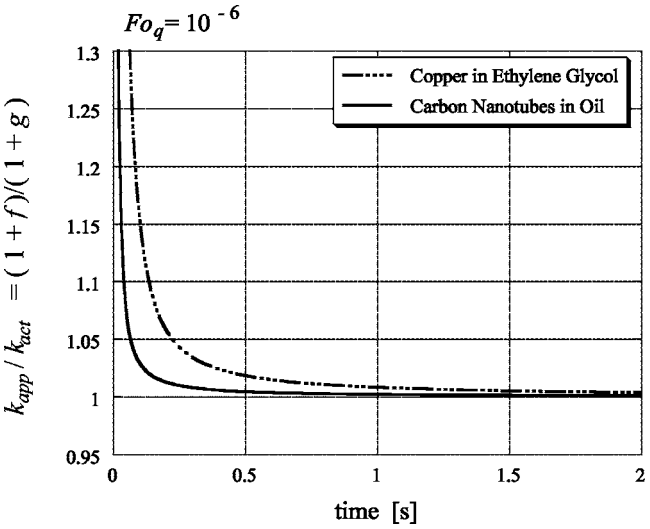

Fig. 10 The ratio between the "apparent" and "actual" effective thermal conductivities following Eq. (60) and corresponding to copper nanoparticles suspended in ethylene glycol compared with carbon nanotubes suspended in oil for a Fourier number of $Fo_q = 10^{-6}$

sults in nanofluid suspensions and classical theories for estimating the effective thermal conductivity of suspensions. Nevertheless, other possible mechanisms have to be accounted for and investigated in more detail prior to reaching a final conclusion. In this respect the present results do not provide a definite conclusion to settle the puzzle.

Appendix A

The parameter h, carrying units of $\mathrm{W\,m^{-3}\,K^{-1}}$, represents an integral heat transfer coefficient for the heat conduction at the solid-fluid interface within an REV. Its general relationship to the surface-area-to-volume ratio (specific area) is derived in this appendix. The author is not aware of any investigations attempting to evaluate a relationship for the heat transfer coefficient h in fluid suspensions, however some relationships are available for the respective coefficient in fluid saturated porous media (Quintard and Whitaker [38], Alazmi and Vafai [39], Amiri and Vafai [40], Wakao, Kaguei, and Funazkri [41], Wakao and Kaguei [42], Kuwahara, Shirota, and Nakayama [43]). Most of the reported evaluations of h in porous media, such as Alazmi and Vafai [39], Amiri and Vafai [40], Wakao et al. [41], Wakao and Kaguei [42], Kuwahara, Shirota, and Nakayama [43], were derived with a particular focus on convection rather than conduction heat transfer. Their applicability and accuracy for conduction are therefore questionable. Nevertheless, the common aspects of all these derivations or empirical relationships and their conversion to fluid suspensions can be summarized as follows. Consider A_{if} as the interface heat transfer area and V_p the volume of one suspended particle. Then, one can define the *specific area*, a_{if} in $\mathrm{m^{-1}}$, of one particle as the interface area per unit volume of solid particle in the form $a_{if}=A_{if}/V_p$. Based on this definition the specific area of a sphere is $(a_{if})_{\mathrm{sphere}}=6/d_p$, where d_p is the spherical particle's diameter, and the specific area of a cylinder excluding the top and bottom surfaces is $(a_{if})_{\mathrm{cylinder}}=4/d_p$, where d_p is the cylindrical particle's diameter. For N particles in a suspension that has a total volume V_{tot} the total interface heat transfer area is $A_{sf}=NA_{if}$, the total volume of the solid phase is $V_s=NV_p$, and the specific area of all particles per unit volume of suspension, $a_{sf}=A_{sf}/V_{\mathrm{tot}}$, can be obtained from the following derivation

$$a_{if} = \frac{NA_{if}}{NV_p} = \frac{A_{sf}}{V_s} = \frac{A_{sf}}{V_{\mathrm{tot}}}\frac{V_{\mathrm{tot}}}{V_s} = \frac{1}{\varepsilon}\frac{A_{sf}}{V_{\mathrm{tot}}} = \frac{a_{sf}}{\varepsilon} \tag{A1}$$

where the definition of the solid fraction as $\varepsilon=V_s/V_{\mathrm{tot}}$ was introduced leading to

$$a_{sf} = \varepsilon a_{if} \tag{A2}$$

For spherical particles suspended in the fluid $a_{sf}=6\varepsilon/d_p$ and for long cylindrical particles (neglecting the effect of the top and bottom surfaces on heat transfer) $a_{sf}=4\varepsilon/d_p$. We can therefore separate the direct effect of the specific heat transfer area on the heat transfer coefficient h in fluid suspensions in the form

$$h = h_{sf}a_{sf} = \varepsilon h_{sf}a_{if} \tag{A3}$$

where $h_{sf}=h/a_{sf}$ is the specific heat transfer coefficient carrying units of $\mathrm{W\,m^{-2}\,K^{-1}}$. Now let us consider the heat flux, q_{if^*} in $\mathrm{W\,m^{-2}}$, at the interface of one particle leading to the rate of heat-transferred to/from that particle (or the rate of internal energy gained/lost per unit time) as $\dot{Q}_{if}=q_{if}A_{if}$ in W. For the whole suspension the total rate of heat-transferred to/from the solid phase is $\dot{Q}_{\mathrm{tot}}=Nq_{if}A_{if}$ and within an REV containing n solid particles per unit volume ($n=N/V_{\mathrm{tot}}$) the rate of heat-transferred to/from the solid phase per unit volume, $\dot{Q}_{sf}=\dot{Q}_{\mathrm{tot}}/V_{\mathrm{tot}}$ is

$$\dot{Q}_{sf} = nq_{if}A_{if} = nV_pa_{if}q_{if} = \varepsilon a_{if}q_{if} = a_{sf}q_{if} \tag{A4}$$

The representation used in Eqs. (6) and (7) for this rate of heat transferred between the phases per unit volume of suspension was

$$\dot{Q}_{sf} = h(T_{f^*} - T_{s^*}) = h_{sf}a_{sf}(T_{f^*} - T_{s^*}) \tag{A5}$$

Combining Eqs. (A4) and (A5) yields the definition of the heat transfer coefficient in the form

$$h = \frac{\dot{Q}_{sf}}{(T_{f^*} - T_{s^*})} = \frac{q_{if}}{(T_{f^*} - T_{s^*})}a_{sf} \tag{A6}$$

and the specific heat transfer coefficient

$$h_{sf} = \frac{\dot{Q}_{sf}}{(T_{f^*} - T_{s^*})a_{sf}} = \frac{q_{if}}{(T_{f^*} - T_{s^*})} \tag{A7}$$

The general form of the relationships derived theoretically or empirically for the evaluation of the heat transfer coefficient in porous media has the form

$$\mathrm{Ni} = \frac{hd_p^2}{k_f} = s(\varepsilon, k_f/k_s) \tag{A8}$$

where Ni is Nield number (Nield [44]) d_p is a characteristic length of the solid phase (particle size), and $s(\varepsilon, k_f/k_s)$ is a function of the solid fraction ε and the fluid-to-solid thermal conductivity ratio k_f/k_s. The implication of Eq. (A8) is that the heat transfer coefficient is related to the particle size by the inversely quadratic relationship

$$h = \frac{k_f}{d_p^2}s(\varepsilon, k_f/k_s) \tag{A9}$$

While the particular form of the function $s(\varepsilon, k_f/k_s)$ and its possible further dependence on the particle size as well, especially as the particle size is reduced to nanoscale levels, is not established for the case of suspensions, the general dependence of the heat transfer coefficient on the particle size is evident. This dependence of the heat transfer coefficient on the particle size introduces the effect of the surface-area-to-volume ratio (specific area) that was claimed by Eastman et al. [1] to be missing in the classical models of evaluating the effective thermal conductivity of the suspension. One should however bear in mind that further dependence on particle size is anticipated as the particle size is reduced to the nanoscale level predominantly when the ballistic rather than dif-

fusive nature of heat transfer becomes dominant (Chen [20–22]) and hence reducing the rate of heat transfer, implying a consequential reduction of the value of h to somewhat compensate for the otherwise substantial increase of h as the particle size is reduced. In addition one may anticipate an increase of h due to Brownian motion induced nanoconvection [19] or a decrease due to the exceptionally small interface thermal conductance [45]. The latter opposing trends in the variation of the value of h as the particle size is reduced to the nanoscale level suggest much larger values for the time lags τ_q and τ_T, and consequently larger values of the Fourier numbers, Fo_q and Fo_T.

Appendix B

The condition for underdamped and critically-damped solutions to Eq. (37) was identified in Eq. (46) and is expressed in the form

$$\frac{c_{fn}^2}{4\omega_n^2} = \frac{(1+\kappa_n^2\,\mathrm{Fo}_T)^2}{4\kappa_n^2\,\mathrm{Fo}_q} \leqslant 1 \tag{B1}$$

where the equality part applies to the critically-damped solution, and the inequality to underdamped solutions. Inequality (B1) can be expanded to yield

$$\kappa_n^4 + 2\frac{(\mathrm{Fo}_T - 2\,\mathrm{Fo}_q)}{\mathrm{Fo}_T^2}\kappa_n^2 + \frac{1}{\mathrm{Fo}_T^2} \leqslant 0 \tag{B2}$$

which has the quadratic form

$$y \equiv \kappa_n^4 + b\kappa_n^2 + c \leqslant 0 \tag{B3}$$

where $b=2(\mathrm{Fo}_T-2\,\mathrm{Fo}_q)^2/\mathrm{Fo}_T^2$ and $c=1/\mathrm{Fo}_T^2>0$. By treating κ_n^2 as a continuous variable, the function $y\equiv\kappa_n^4+b\kappa_n^2+c$ represents a parabola, which has a minimum at $\kappa_n^2=-b/2$. Given the established fact that $c=1/\mathrm{Fo}_T^2>0$, the relevant case consistent with real κ_n values is linked to $b<0$ or explicitly to $(\mathrm{Fo}_T-2\,\mathrm{Fo}_q)<0$. For $b<0$ an underdamped solution is in principle possible provided the roots of the quadratic equation $y\equiv\kappa_n^4+b\kappa_n^2+c=0$ are real. The latter implies that the following roots $\kappa_{n1,2}^2=-b[1\pm\sqrt{1-4c/b^2}]/2$ have to be real in order to obtain two real and positive, distinct or identical values of κ_n^2. For the latter to occur, the discriminant (b^2-4c) must be nonnegative leading to

$$\frac{4}{\mathrm{Fo}_T^2}\left[1-\frac{2\,\mathrm{Fo}_q}{\mathrm{Fo}_T}\right]^2 - \frac{4}{\mathrm{Fo}_T^2} \geqslant 0 \tag{B4}$$

Further expansion of the left-hand side of inequality (B4) produces the final condition for underdamped and critically-damped solutions in the form

$$\frac{\mathrm{Fo}_T}{\mathrm{Fo}_q} = \frac{\tau_T}{\tau_q} \leqslant 1 \tag{B5}$$

where the equality part is applicable to the critically-damped solution, while the inequality is the condition for underdamped solutions.

References

[1] Eastman, J. A., Choi, S. U. S., Li, S., Yu, W., and Thompson, L. J., 2001, "Anomalously Increased Effective Thermal Conductivities of Ethylene Glycol-Based Nanofluids Containing Copper Nanoparticles" Appl. Phys. Lett., **78**, pp. 718–720.

[2] Lee, S., Choi, S. U.-S., Li, S., and Eastman, J. A., 1999, "Measuring Thermal Conductivity of Fluids Containing Oxide Nanoparticles," ASME J. Heat Transfer, **121**, pp. 280–289.

[3] Choi, S. U. S., Zhang, Z. G., Yu, W., Lockwood, F. E., and Grulke, E. A., 2001, "Anomalous Thermal Conductivity Enhancement in Nanotube Suspensions," Appl. Phys. Lett., **79**, pp. 2252–2254.

[4] Xuan, Y., and Li, Q., 2000, "Heat Transfer Enhancement of Nanofluids," Int. J. Heat Mass Transfer, **21**, pp. 58–64.

[5] Maxwell, J. C., 1891, *A Treatise on Electricity and Magnetism*, 3rd ed., Clarendon Press, 1954 reprint, Dover, New York, pp. 435–441.

[6] Batchelor, G. K., 1972, "Sedimentation in a Dilute Dispersion Of Spheres," J. Fluid Mech., **52**, pp. 45–268.

[7] Batchelor, G. K., and Green, J. T., 1972, "The Hydrodynamic Interaction of Two Small Freely-Moving Spheres in a Linear Flow Field," J. Fluid Mech., **56**, pp. 375–400.

[8] Hamilton, R. L., and Crosser, O. K., 1962, "Thermal Conductivity of Heterogeneous Two-Component Systems," Ind. Eng. Chem. Fundam., **1**, pp. 187–191.

[9] Jeffrey, D. J., 1973, "Conduction Through a Random Suspension of Spheres," Proc. R. Soc. London, Ser. A, **335**, pp. 355–367.

[10] Davis, R. H., 1986, "The Effective Thermal Conductivity of a Composite Material With Spherical Inclusions," Int. J. Thermophys., **7**, pp. 609–620.

[11] Lu, S., and Lin, H., 1996, "Effective Conductivity of Composites Containing Aligned Spheroidal Inclusions of Finite Conductivity," J. Appl. Phys., **79**, pp. 6761–6769.

[12] Bonnecaze, R. T., and Brady, J. F., 1990, "A Method for Determining the Effective Conductivity of Dispersions of Particles," Proc. R. Soc. London, Ser. A, **430**, pp. 285–313.

[13] Bonnecaze, R. T., and Brady, J. F., 1991, "The Effective Conductivity of Random Suspensions of Spherical Particles," Proc. R. Soc. London, Ser. A, **432**, pp. 445–465.

[14] Keblinski, P., Phillpot, S. R., Choi, S. U. S., and Eastman, J. A., 2002, "Mechanisms of Heat Flow in Suspensions of Nano-Sized Particles (Nanofluids)," Int. J. Heat Mass Transfer, **45**, pp. 855–863.

[15] Xue, L., Keblinski, P., Phillpot, S. R., Choi, S. U.-S., and Eastman, J. A., 2004, "Effect of Fluid Layering at the Liquid-Solid Interface on Thermal Transport," Int. J. Heat Mass Transfer, **47**, pp. 4277–4284.

[16] Prasher, R., Bhattacharya, P., and Phelan, P. E., 2005, "Thermal Conductivity of Nanoscale Colloidal Solutions (Nanofluids)," Phys. Rev. Lett., **94**, p. 025901.

[17] Das, S. K., Putra, N., Thiesen, P., and Roetzel, W., 2003, "Temperature Dependence of Thermal Conductivity Enhancement for Nanofluids," ASME J. Heat Transfer, **125**, pp. 567–574.

[18] Kumar, D. H., Patel, H. E., Rajeev Kumar, V. R., Sundararajan, T., Pradeep, T., and Das, S. K., 2004, "Model for Heat Conduction in Nanofluids," Phys. Rev. Lett., **93**, p. 144301.

[19] Jang, S. P., and Choi, S. U.-S., 2004, "Role of Brownian Motion in the Enhanced Thermal Conductivity of Nanofluids," Appl. Phys. Lett., **84**(21), pp. 4316–4318.

[20] Chen, G., 1996, "Nonlocal and Nonequilibrium Heat Conduction in the Vicinity of Nanoparticles," ASME J. Heat Transfer, **118**, pp. 539–545.

[21] Chen, G., 2000, "Particularities of Heat Conduction in Nanostructures," J. Nanopart. Res., **2**, pp. 199–204.

[22] Chen, G., 2001, "Balistic-Diffusive Heat-Conduction Equations," Phys. Rev. Lett., **86**(11), pp. 2297–2300.

[23] Nield, D., and Bejan, A., 1999, *Convection in Porous Media*, 2nd ed., Springer, New York.

[24] Vadasz, J. J., Govender, S., and Vadasz, P., 2005, "Heat Transfer Enhancement in Nanofluids Suspensions: Possible Mechanisms and Explanations," Int. J. Heat Mass Transfer, **48**, pp. 2673–2683.

[25] Hammerschmidt, U., and Sabuga, W., 2000, "Transient Hot Wire (THW) Method: Uncertainty Assessment," Int. J. Thermophys., **21**, pp. 1255–1278.

[26] De Groot, J. J., Kestin, J., and Sookiazian, H., 1974, "Instrument to Measure the Thermal Conductivity of Gases," Physica (Utrecht), **75**, pp. 454–482.

[27] Healy, J. J., de Groot, J. J., and Kestin, J., 1976, "The Theory of the Transient Hot-Wire Method for Measuring Thermal Conductivity," Physica, **82C**, pp. 392–408.

[28] Kestin, J., and Wakeham, W. A., 1978, "A Contribution to the Theory of the Transient Hot-Wire Technique for Thermal Conductivity Measurements," Physica A, **92**, pp. 102–116.

[29] Assael, M. J., Dix, M., Gialou, K., Vozar, L., and Wakeham, W. A., 2002, "Application of the Transient Hot-Wire Technique to the Measurement of the Thermal Conductivity of Solids," Int. J. Thermophys., **23**, 615–633.

[30] Nagasaka, Y., and Nagashima, A., 1981, "Absolute Measurement of the Thermal Conductivity of Electrically Conducting Liquids by the Transient Hot-Wire Method," J. Phys. E, **14**, pp. 1435–1440.

[31] Assael, M. J., Chen, C.-F., Metaxa, I., and Wakeham, W. A., 2004, "Thermal Conductivity of Suspensions of Carbon Nanotubes in Water," Int. J. Thermophys., **25**, 971–985.

[32] Tzou, D. Y., 1997, *Macro-to-Microscale Heat Transfer The Lagging Behavior*, Taylor and Francis, Washington, D.C.

[33] Tzou, D. Y., 2001, "Temperature-Dependent Thermal Lagging in Ultrafast Laser Heating," Int. J. Heat Mass Transfer, **44**, pp. 1725–1734.

[34] Vadasz, P., 2005, "Explicit Conditions for Local Thermal Equilibrium in Porous Media Conduction," Transp. Porous Media, **59**, pp. 341–355.

[35] Vadasz, P., 2005, "Absence of Oscillations and Resonance in Porous Media Dual-Phase-Lagging Fourier Heat Conduction," ASME J. Heat Transfer, **127**, pp. 307–314.

[36] Vadasz, P., 2005, "Lack of Oscillations in Dual-Phase-Lagging Heat Conduction for a Porous Slab Subject to Imposed Heat Flux and Temperature," Int. J. Heat Mass Transfer, **48**(14), pp. 2822–2828.

[37] Özisik, M. N., 1993, *Heat Conduction*, 2nd ed., Wiley, New York.

[38] Quintard, M., and Whitaker, S., 1995, "Local Thermal Equilibrium for Transient Heat Conduction: Theory and Comparison With Numerical Experiments," Int. J. Heat Mass Transfer, **38**, pp. 2779–2796.

[39] Alazmi, B., and Vafai, K., 2002, "Constant Wall Heat Flux Boundary Conditions in Porous Media Under Local Thermal Nonequilibrium Conditions," Int. J. Heat Mass Transfer, **45**, pp. 3071–3087.

[40] Amiri, A., and Vafai, K., 1994, "Analysis of Dispersion Effects and Non-Thermal Equilibrium, Non-Darcian, Variable Porosity Incompressible Flow

Through Porous Media," Int. J. Heat Mass Transfer, **37**, pp. 934–954.
[41] Wakao, N., Kaguei, S., and Funazkri, T., 1979, "Effect of Fluid Dispersion Coefficients on Particle-to-Fluid Heat Transfer Coefficients in Packed Beds," Chem. Eng. Sci., **34**, pp. 325–336.
[42] Wakao, N., and Kaguei, S., 1982, "Effect of Fluid Dispersion Coefficients on Particle-to-Fluid Heat Transfer Coefficients in Packed Beds," *Heat and Mass Transfer in Packed Beds*, Gordon and Breach, New York.
[43] Kuwahara, F., Shirota, M., and Nakayama, A., 2001, "A Numerical Study of Interfacial Convective Heat Transfer Coefficient in Two-Energy Equation Model for Convection in Porous Media," Int. J. Heat Mass Transfer, **44**, pp. 1153–1159.
[44] Nield, D. A., 1998, "Effects of Local Thermal Nonequilibrium in Steady Convective Processes in a Saturated Porous Medium: Forced Convection in a Channel," J. Porous Media, **1**, pp. 181–186.
[45] Huxtable, S. T., Cahill, D. G., Shenogin, S., Xue, L., Ozisik, R., Barone, P., Usrey, M., Strano, M. S., Siddons, G., Shim, M., and Keblinski, P., 2003, "Interfacial Heat Flow in Carbon Nanotube Suspensions," Nat. Mater., **2**, pp. 731–734.

Study of Infrared CO_2 Radiation From Liquid-Fueled Combustor

Y. Levy

M. Lev
e-mail: aerysml@aerodyne.technion.ac.il

V. Ovcharenko

Israel Institute of Technology,
Faculty of Aerospace Engineering,
Haifa, 32000, Israel

The combustor that is a 30% flat (rectangular) model of an annular turbojet-engine combustion chamber was studied. It gave a turbulent nonpremixed kerosene-air flame with equivalence ratios within the range of 0.15–0.75. Measurements of CO_2 infrared radiation were performed on exhaust gases from a combustor. The infrared radiation images were obtained by an IR camera equipped with a narrow bandpass filter that falls on the CO_2 fundamental band. Temperature profiles were measured by the thermocouple at the combustor outlet. The in-house program INFRAD was used to calculate infrared radiation from the CO_2 component of the efflux gases from the combustor. The calculation was performed, taking into account the effects of radiation emission and absorption along an optical path. The calculations that allow prediction of "apparent" gas temperatures are those expected to be read by the IR camera. The calculated results are compared with experimental measurements. They are found to be in close agreement.
[DOI: 10.1115/1.2175153]

Keywords: combustion, IR optical diagnostics, infrared radiation calculation

1 Introduction

For a long time laboratory flames have been successfully investigated by studying their radiation emission [1–5]. The emission diagnostics can reveal the flame structure, temperature, data on the chemical composition, and the combustion processes [5,6]. Less has been published about the applications of these methods to practical nonpremixed combustions employing liquid fuels. During the last decades, commercial optical instruments were developed allowing radiation mapping and spectral imaging of intricate combustion environments such as engine chambers and rocket exhaust plumes [5,7,8]. On the other hand, comprehensive computer codes, simulating combustion in complicated nonuniform nonisothermal conditions became available [5,6]. Based on CFD simulation, molecular radiation emission can be calculated for comparison with experimental data.

The maximum intensity of combustion radiation falls on the near-infrared (NIR) spectral range. The main IR radiators of combustion gases are CO_2, H_2O, CO, and carbon soot particles. Typical combustion zones are transparent for IR radiation to various extents, depending on the radiation wavelength. In many cases they are transparent enough to collect radiation not only from layers close to the observed surface but also from the whole optical path. Difficulty arises from the interpretation of the radiation, accumulated from the whole optical path, along which the gas is usually nonuniform and nonisothermal. The problem of obtaining the temperatures and species concentrations along an optical path from the radiation data is known as an "inverse problem" and it is far from being solved in general. It seems that a solution of the problem in the infrared range depends on: (a) developing multiwave imaging, that allows different transparency for different wavelengths, and (b) developing an infrared emission tomography technique, in which images at different viewing angles are obtained. However, the radiation data measured from outside the gas flow reflects changes that can occur inside the flow. It can serve for monitoring the gas flow. The solution of a "direct problem" (that is finding the radiation output from gas thermodynamic data) in a specific case helps in understanding the results of monitoring.

In the present work, the CO_2 infrared emission from efflux gases of a practical combustor, with a nonpremixed liquid-fueled flame, was investigated. The IR images of the efflux were obtained by an IR camera. The camera was equipped with a narrow bandpass filter, with transmittance band that lies within the fundamental CO_2 radiation band. No other molecular species radiate within the filter transmittance band. Simulation of the IR radiation was carried out, based on thermocouple measurements of temperatures in the efflux gases. The radiation transfer equation was solved numerically taking into account the emission and absorption of radiation along the lines-of-sight. Comparison of the simulated and measured results is needed to improve the reliability of the diagnostic method. The objective of the present study is to develop a radiation diagnostic method, to enable fast evaluation of the exhaust gases characteristics in full-scale turbojet combustors.

2 Combustor Design and Performance

The combustor, used in the present study, is shown in Fig. 1. It is a 30% flat sector model of reversed flow annular combustor of a small turbojet engine. This model was designed to study its internal flow and ignition processes. Three L-shaped vaporizers (out of 10 in the complete engine) are incorporated in the model, but in the present experiment only two, adjacent to the igniter, were used. The air feed duct is connected to the combustor in a reverse-flow arrangement. The liner contains three series of air inlets. One set of holes of 0.8 mm diameter in the liner front (Fig. 1); two others with larger different diameters are drilled in the outer and inner liner walls to form the optimized graduated air admission. The combustor has a rectangular exit of 210×30 mm^2 cross section. We define a Cartesian coordinate system with its origin in exit plane, see Fig. 1 (A-A). The combustor and liner profiles, as well as the system of air inlets in the outer and inner liner walls, shown in Fig. 1, are equivalent to those in a real engine.

Nonpremixed kerosene/air combustion process takes place, and can be observed, inside the model combustor through quartz or sapphire windows. The fuel mass flow-rate was varied from 1 g/s to 3 g/s and the air mass airflow rate was fixed at a value of 100 g/s. This corresponds to global equivalence ratios of 0.15, 0.3, and 0.45. The Reynolds number $\mathrm{Re} \sim 18,000$ for the model is the same as for the real engine combustor.

Contributed by the Heat Transfer Division of ASME for publication in the JOURNAL OF HEAT TRANSFER. Manuscript received July 19, 2005; final manuscript received November 6, 2005. Review conducted by Walter W. Yuen. Paper presented at the ASME Turbo Expo 2005: Land, Sea and Air (GT2005), June 6–9, 2005, Reno, Nevada, USA.

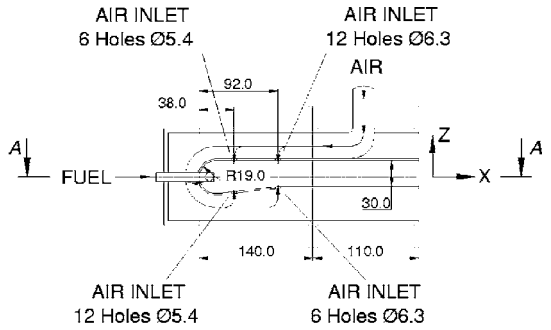

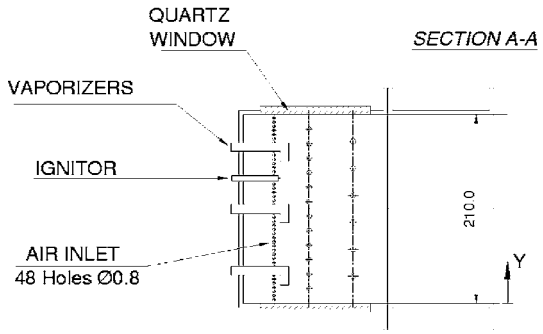

Fig. 1 Combustor (all units in mm)

3 Chemical Composition of the Combustion Products

Normally, the kerosene combustion products are carbon dioxide, water vapor, nitrogen, and oxygen. The reaction between hydrocarbon fuel and "theoretical air" (molar concentration of 21% O_2 and 79% N_2) at stoichiometric condition can be written as

$$C_xH_y + (x + y/4)O_2 + 3.76(x + y/4)N_2 = xCO_2 + (y/2)H_2O + 3.76(x + y/4)N_2 \quad (1)$$

For combustion with excess air ($Ø < 1$), evaluation of the exhaust gases' composition should also consider the specific equivalence ratio, Ø. Assuming the equivalent kerosene molecular formula to be $C_{12}H_{24}$ ($x=12, y=24$):

$$ØC_{12}H_{24} + 18O_2 + 67.68N_2 = 12\,Ø\,CO_2 + 12\,Ø\,H_2O + 18(1 - Ø)O_2 + 67.68N_2 \quad (2)$$

the mole fraction of combustion products can be found (Table 1).

4 Temperature Measurements in the Combustor Exhaust Gases

The exhaust gases are not isothermal, mainly due to nonuniform fuel injection and discrete air inlets. The operational regime used, in which two vaporizers operated within the combustor, causes temperature asymmetry across the exhaust. The aerodynamic flow pattern in the combustor and the heat release are also nonuniform. Radiation calculation of nonisothermal gas requires knowledge of gaseous temperature distribution in the combustion chamber. To simulate the exhaust temperature field, temperature profiles were measured by a thermocouple (Pt/Pt13%Rh thermocouple, with a junction of 1 mm in diameter). The most significant error in temperature measurement by an unshielded thermocouple originates from the heat loss through radiation from the thermocouple junction. The heat balance for the junction is described by the equation:

$$h(T_g - T_{tc}) = \varepsilon\sigma(T_{tc}^4 - T_{amb}^4) \quad (3)$$

where h is the convective heat transfer coefficient, ϵ is the thermocouple emissivity, and σ is the Stefan-Boltzmann constant, T_g is the gas temperature, T_{tc} is the thermocouple temperature, and T_{amb} is the ambient temperature. An emissivity value of 0.2 was accepted for the platinum alloy thermocouple bead [9]. An estimation of the Nusselt number is required in order to obtain the convective heat transfer coefficient. It was estimated as Nu=10, using an empirical dependence of Nu as a function of $Re_d^{0.54}\,Pr^{0.33}$. The Reynolds number $Re_d=300$ was estimated based on the thermocouple junction diameter d and the flow velocity (about 70 m/s) at the combustor exit. The Prandtl number was assumed to be Pr=0.7, typical for combustion gases. The discrepancy between a measured temperature and real gas temperature increases when the gas temperature increases. It is negligible up to a temperature of 1000 K and is about 180 K at a temperature of 2000 K. These discrepancies were calculated for each temperature and the experimentally obtained temperature values were corrected.

The time constant of the thermocouple is estimated by the equation:

$$\tau = mc/hA \quad (4)$$

where m is the mass of the thermocouple junction, c is the thermocouple specific heat capacity, h is the convective heat transfer coefficient, and A is the surface area of the thermocouple junction. This gives $\tau=0.5$ s. This value is larger than the turbulence time scale (about 30 ms for flow velocities of about 70 m/s). Consequently, only average values are detected. It can be noted here that the oscillation of the measured apparent temperature, obtained by the thermocamera has a wavelength of 20 mm (along the X-axis).

The temperature measurements were performed along two lines: transverse (Y-axis) and longitudinal (X-axis) to the flow. The transverse line was selected at the exit plane at the midheight of the combustor exit. The measured transverse temperatures are shown in Fig. 2 for the regimes with equivalence ratios of 0.15, 0.3, and 0.45. The transverse profiles, normalized to the maximum temperature, differ in the various regimes by no more than 4%. The combustion is not symmetrical in the combustion chamber. This is due to several reasons. As can be seen from Fig. 1, the fuel

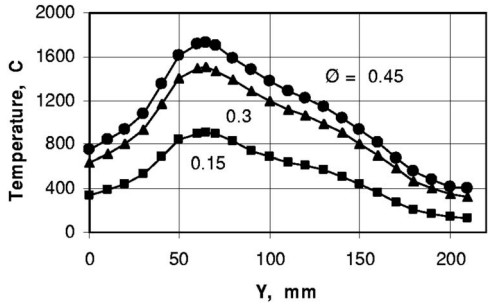

Fig. 2 Measured temperature profiles along the *Y*-axis for different equivalence ratios, *X*=10 mm, *Z*=0 mm

Table 1 Mole fraction of the combustion products in different regimes

Combustion products	Equivalence ratios		
	0.15	0.3	0.45
CO_2	0.02	0.04	0.06
H_2O	0.02	0.04	0.06
O_2	0.18	0.14	0.11
N_2	0.78	0.78	0.77

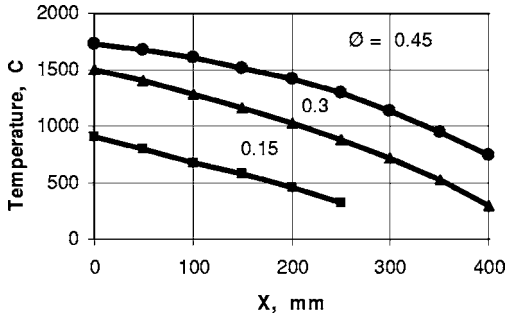

Fig. 3 Measured temperature profiles along the *X*-axis for different equivalence ratios, *Y*=65 mm, *Z*=0 mm

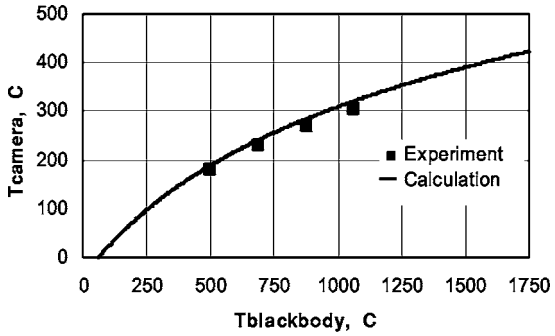

Fig. 4 Comparison of experimental and calculated apparent blackbody temperature read by a PM390 camera with the 4.6 μm filter

is supplied by two neighboring injectors, which are located closer to one side of the combustor than to the other side. Because of this, the combustion zone is moved to one side of the combustor. The air is supplied through the symmetrical sequences of holes that produce nonsymmetrical aerodynamics with respect to the combustion zone. It is obvious that the energy losses are also nonsymmetrical in this combustion geometry. All the above factors lead to the appearance of a peak in the transverse temperature profile, which is closer to one side of the combustor.

The measured longitudinal profiles for the same regimes are shown in Fig. 3. The location of maximum temperature on the *Y*-axis is the same for all regimes. The maximum gas temperature at the combustor exit plane can serve as a characteristic of a given regime. Characteristic temperatures of 910°C, 1500°C, and 1720°C were obtained for the studied regimes. To simulate the complete temperature field in the *X*-Y plane, at the midheight of the combustor exit ($Z=0$), it was accepted that any normalized transverse temperature profile is preserved in each *X*-coordinate. The value of the maximum temperature in a transverse profile is assumed to be the measured value as presented in Fig. 3.

5 Experimental IR Radiation Study

Imaging of the combustor exhaust gases was performed by an infrared camera ThermaCAM® PM 390 [8]. The PM 390 camera is intended for general infrared inspections in a spectral range of 3.4–5.0 μm and can be used for planar and local temperature measurements. Image acquisition rate of the thermocamera is 50–60 Hz. The filter used with the camera was a near-infrared interference filter (Oriel Instruments) with peak transmittance of about 80% at 4.6 μm and bandwidth 0.2 μm. This filter was chosen because its transmittance band is located within the spectral interval of the fundamental vibrational-rotational emission band of the carbon dioxide molecule. IR spectral transmittance of the 4.6 μm filter was measured in the working range. The transmittance of the filter was exploited in calculations of IR radiation. The imaging was performed from a distance of 2.0 m. The spatial resolution of the images is about 2.2 mm/pixel for a distance of 2 m.

The IR camera is calibrated by blackbody radiation and its readings indicate temperature units. Hence a temperature indication corresponds to the blackbody radiation integrated over the range of the camera sensitivity according to its spectral response. The temperature read by the camera is the real temperature only if the monitored surface radiates like a blackbody, or like a gray body, of which the emissivity is constant, at least, within the range of sensitivity. The emissivity value is installed through the camera operational menu.

The gas, in principle, is not a blackbody-like radiator. Besides, the transmittance band of the applied 4.6 μm filter is narrower than the range of camera sensitivity. Therefore, the camera operation while using that filter is inconsistent with the calibration by a blackbody continuum. The temperature read by the camera is an apparent, or effective, temperature, T_{eff}, which represents a total radiation over the range of spectral sensitivity. It is assumed that the camera operates in a linear range of radiation intensity, and a temperature read by the camera depends only on the number of watts acting on the sensor, and not on the energy spectral distribution. These assumptions were checked by measurement of blackbody temperatures, read by the camera, equipped with the 4.6 μm filter, and by corresponding numerical simulation, using data of the filter transparency and the camera total response. The measured and calculated results are in a good agreement, as can be seen in Fig. 4.

Carbon dioxide CO_2 is the main radiating species in the combustion products. In spite of significant amounts of water vapor, its emittance in the considered range is much lower. However, the radiation of H_2O is present and should be taken into account. Because the equivalence ratio is small, it was assumed that the quantity of carbon monoxide (CO) in the combustion products is negligible [3,4]. Also the emittance of carbon monoxide in the considered spectral range is significantly lower than the emittance of CO_2. The possible presence of carbon monoxide (CO) in the exhaust gases cannot essentially change the measured or calculated results.

Figure 5 shows examples of exhaust gas images performed by the IR camera equipped with the 4.6 μm filter. The temperature values along the *X*-axis at the exhaust centerline (at midheight of the combustor exit), read by the IR camera, are presented in Fig. 6. The thermocamera image of IR radiation shows a two-dimensional temperature map of the object according to its calibration. Temperatures T_{eff} along the centerline of the flow were read from images recorded during the experiment. There is a certain dispersion of the temperatures at similar points of several images, especially in the regimes with high equivalence ratios. The dispersion of the apparent temperature is believed to be associated with the flow turbulence, causing oscillations of the temperature and radiation. Therefore, the temperatures in each point were averaged over five images. These averaged temperatures

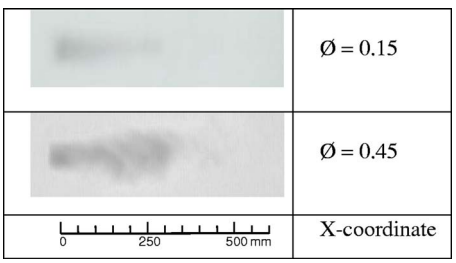

Fig. 5 Planar CO_2 radiation images of exhaust gases obtained with a 4.6 μm filter for two equivalence ratios

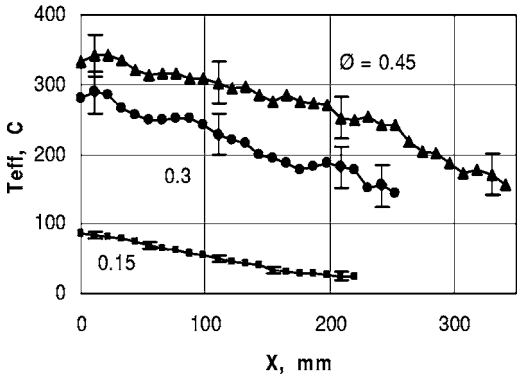

Fig. 6 Measured T_{eff}, averaged over five images (4.6 μm filter)

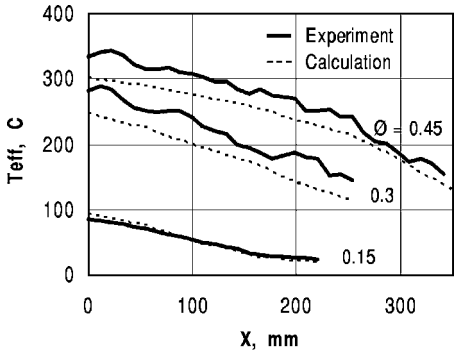

Fig. 7 Experimental and calculated temperature profile along the *X*-axis for different equivalence ratio, *Z*=0 mm, 4.6 μm filter

along the centerline of the flow images are shown in Fig. 6 with standard deviations (bars). It can be seen that the temperatures read by the thermocamera, along the line with maximum temperatures ($Y=65$ mm), are much lower than those measured by the thermocouple. This result was expected because the temperature read by the thermocamera does not correspond to any real temperature in the flow. It is an apparent temperature corresponding to the IR radiation received by the thermocamera. The apparent temperatures are determined by the emitted radiative energy, collected along optical paths from the hot gas volume, by transmittances of the gas, by camera optics and filter, and by camera sensitivity.

6 Results and Discussion

The in-house INFRAD program was developed for the numerical study of the spectral and radiative properties of hot gases in the IR spectral range [5]. The program calculates the radiation transfer for nonuniform and nonisothermal molecular gases. It uses a technique, known as a statistical narrow-band model. The radiative transfer in the narrow band model is formulated for an array of many lines with centers confined to a narrow spectral interval $\Delta\omega$ (ω is a wave number). The average radiance $\overline{N}$ in a band $\Delta\omega$ for a nonuniform optical path segment from $s=0$ to $s=S$ is

$$\overline{N} = -\int_0^S N_\omega^0(s)\frac{d\overline{\tau}(s)}{ds}ds \tag{5}$$

The band $\Delta\omega$ should be small enough that the Planck function $N_\omega^0(s)$ can be considered as approximately constant across $\Delta\omega$. $\overline{\tau}(s)$ is the average spectral transmittance for the $\Delta\omega$:

$$\overline{\tau}(s) = \frac{1}{\Delta\omega}\int_{\Delta\omega}\tau_\omega(\omega,s)d\omega, \tag{6}$$

where $\tau_\omega(\omega,s)$ is the spectral transmittance within $\Delta\omega$. The number of lines in $\Delta\omega$ is large, therefore $\tau_\omega(\omega,s)$ is a rapidly fluctuating function of ω.

An introduction and details of the problem can be found in the *Handbook of Infrared Radiation* [2]. Detailed analysis of the different band models and all mathematical details are given in [10]. The approach was tested in [11]. The code INFRAD, is based on the mathematical analyses conducted in [10] and was directly tested in [5]. The spectral resolution, given by the code, is determined by the available band model parameters data, and is 5 cm^{-1} in wave numbers for the present work. The input to the program includes temperature, pressure, and species mole fraction. The program can simulate the radiation emitted from a local surface area.

The mole fractions are required for IR radiation calculation. Because they are unknown during the experiment, an assumption is made that the measured temperatures are as of adiabatic flame temperatures. Then the equivalence ratios can be calculated, assuming the kerosene formula as $C_{12}H_{24}$. The pressure was taken at $P=1$ bar everywhere in the efflux flow. The mole fractions of the equilibrium combustion products were calculated according to the local temperature and equivalence ratio [3]. The temperature field in the plane X-Y was obtained from the thermocouple measuring in compliance with the regime. The radiation at the centerline, observed from a combustor narrow side, was computed with respect to the X-coordinate.

To compare the experimental apparent temperature (obtained by the thermocamera) with predictions from the INFRAD program, integration of the predicted spectral radiations was conducted over a spectral interval of camera sensitivity. The transmission of the filter and the camera response were taken into account. These integrals were compared with similar integrals of the blackbody at different temperatures. We assume that the apparent temperature of the gas is that of a blackbody, which emits equal total radiation (taking into account the camera and filter characteristics).

The calculation of IR radiation, observed through the 4.6 μm filter, including the effect of a certain amount of carbon soot particles, shows that the occurrence of the soot adds no more than 4% to the integral radiation energy. The calculations show that radiation intensity of water vapor in this spectral range is about one order of magnitude less than the radiation of CO_2. Thus CO_2 molecules contribute the dominant radiation passing through the filter band.

Figure 7 shows averaging over five measurement temperature data and simulated apparent temperatures along X, for the camera equipped with the 4.6 μm filter. Excellent agreement can be seen in the regime with the equivalence ratio 0.15 and some discrepancy is observed in the regimes with the equivalence ratio 0.3 and 0.45. The camera indicates temperature values higher than the predicted temperatures based on thermocouple measurements. Two sources of this discrepancy can be surmised. One is a wrong accounting for temperature losses by the thermocouple. This can lead to the higher measured temperature and to the higher result in the calculated radiation. Another obvious error is the assumption that the measured temperatures are the adiabatic flame temperatures. The adiabatic temperature based on the flow rate measurements, or global adiabatic temperature, can serve only as a calculated characteristic parameter, which reflects the overall equivalence ratio and shows a certain mean temperature in the flow. Due to nonperfect mixing and intense turbulence, special variations exist in the equivalence ratio and therefore also in the local temperatures. The thermocouple measurements at the exit plane reflect more or less the local adiabatic temperature in the combustor. This assumption is more accurate with the heat losses while the flow passes from the combustion zone to the exit plane

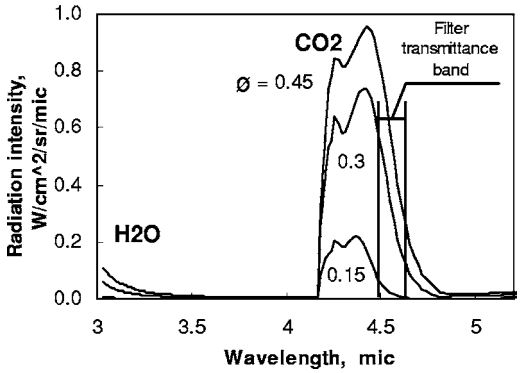

Fig. 8 Calculated CO_2 radiance spectra for different equivalence ratios, $X=0$ mm, $Z=0$ mm

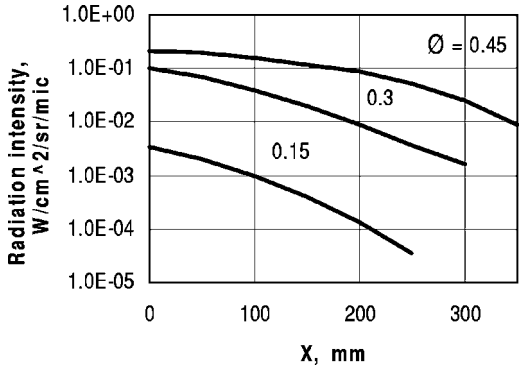

Fig. 9 Calculated radiation intensity at 4.6 μm depending on the X-coordinate for different equivalence ratio, $Z=0$ mm

are minimal. However, these losses are not negligible. By considering the thermocouple-measured temperatures as adiabatic temperatures, an error is introduced in finding CO_2 mole fractions in the exit plane. This error contributes to the discrepancy, which can be seen between the predicted apparent temperatures and measured ones. If the real adiabatic temperatures are higher, the calculated mole fractions of CO_2 are higher. This leads to an increase of the calculated radiation and, correspondingly, to higher predicted apparent temperatures. This discrepancy increases in the regimes with higher equivalence ratios because the heat losses are more significant in these regimes and the difference between the local adiabatic temperature and the value measured by the thermocouple is larger. To estimate the effect of variation of CO_2 molar fraction on the evaluated temperature, it was assumed that perfect mixing takes place in the combustor, and species mole fractions are uniform at the combustor exit plane and equal to the average value (obtained from the chemical balanced equation). Due to this approach, in regions of high temperatures the evaluated CO_2 mole fraction will be lower than the real values. The discrepancy in the predicted apparent temperature is within the range of 20–40 deg.

The characteristics wavelength of temperature oscillations, as observed by the thermocamera, along the X-axis were about 20 mm. The image acquisition rate of the thermocamera is 50 or 60 Hz. Thus the time response is less than 20 ms, and therefore the oscillations of the effective temperature are observed in the images. In order to compare results of temperature values based on the thermocouple measurements with temperatures measured by the thermocamera, several recorded images were used to smooth the oscillations by averaging the temperature at each point. It was found that there are, practically, no oscillations in the regimes with an equivalence ratio of 0.15; in terms of effective temperatures they are less than 2% of the apparent temperature (90 °C), i.e., about 2 °C. The oscillations in the regimes with equivalence ratios of 0.3–0.45 are about 7% that allows smoothing them using only five images. It is believed that the oscillations are small enough and turbulence/radiation interactions do not affect the radiation values. In the following a possible explanation of the oscillations in the efflux flow is given. In the regime with the global equivalence ratio of 0.15, the whole fuel is burned out at the combustion zones, where only part of the air is supplied. In regimes with global equivalence ratios of 0.3–0.45, the air supplied to the combustion zones is not sufficient for complete combustion of all the fuel. An amount of the fuel passes to the dilution zone. It is possible that a small amount of the unburned fuel exits the combustor and postcombustion occurs downstream of the exit plane; hence oscillations are observed in the IR radiation.

Figure 8 shows the calculated spectral radiation intensity emitted from the combustor efflux at $X=0$ mm for different equivalence ratios. The radiation within the range 3.0–3.5 μm is produced by water vapor. The range of 3.5–4.2 μm represents a spectral window where no radiation of molecular species occurs. The radiation within the range of 4.2–4.8 μm is due to the CO_2 fundamental band. From the wavelength of 4.7 μm the radiation of the water vapor spectral band begins. The vertical lines show the filter transmittance band, used for the IR measurements. This band is within the strong CO_2 radiation band. However, its location on the edge of the band ensures a weak absorption and allows us to obtain radiation from the whole optical path. The calculated total transparency of the gas in the transverse direction is about 0.8–0.9. Figure 9 shows the calculated radiance intensity at 4.6 μm depending on the X-coordinate for different equivalence ratio at $Z=0$ mm. Unlike the effective temperature, the spectral radiance intensity is a characteristic independent of the thermocamera and characterizes a specific optical path. It can also be expressed in terms of temperatures, by recalculating it to the brightness temperature (temperature of a blackbody with equal radiation intensity in a specific wavelength).

7 Conclusions

A diagnostic method for efflux gas monitoring was proposed and tested in a liquid-fueled model of a jet engine's combustor. The method is based on measuring infrared emission from combustor efflux flow.

Measurements of temperature profiles at the combustor exit plane revealed similar profiles even with different equivalence ratios and the consequent different maximum temperature values. This fact allows that an apparent temperature can serve as a characteristic temperature of the combustion gases. The method can be used for fast retrieval of the apparent temperature field in different combustion systems. Upon calibration, variation from nominal values in the apparent temperature fields can be easily detected.

It should be noted that the use of several filters with an IR camera will increase the power of the gas flow monitoring by the IR camera. Particularly, obtaining mole fractions of different species in combustion products is possible.

References

[1] Edwards, D. K., 1960, "Absorption by Infrared Bands of Carbon Dioxide Gas at Elevated Pressures and Temperatures," J. Opt. Soc. Am., **50**, pp. 617–626.
[2] Ludwig, C. B., Malkmus, W., Reardon, J. E., and Thomson, J. A. L., 1973, *Handbook of Infrared Radiation from Combustion Gases*, NASA SP-3080.
[3] Turns, S. R., 2000, *An Introduction to Combustion, Concept and Applications*, 2nd ed., McGraw-Hill Higher Education, Boston.
[4] Baukal, C. E., 2001, *The John Zink Combustion Handbook*, R. Schwartz, ed., CRC Press, London.
[5] Avital, G., Cohen, Y., Gamss, L., Kanelbaum, Y., Macales, J., Trieman, B., Yaniv, S., Lev, M., Stricker, Y., Sternlieb, A., 2001, "Experimental and Computational Study of Infrared Emission from Underexpanded Rocket Exhaust Plumes," J. Thermophys. Heat Transfer, **15**, pp. 377–383.

[6] Jun, J. I., Sivathanu, Y. R., and Gore, J. P., 2000, "Thermal Radiation Properties of Turbulent Lean Premixed Methane Air Flames," in *Proceedings of the Combustion Institute*, Vol. 28, pp. 391–398.
[7] Kirby, B. J., and Hanson, R. K., 2000, "Imaging of CO and CO_2 Using Infrared Planar Laser-Induced Fluorescence," in *Proceedings of the Combustion Institute*, Vol. 28, pp. 253–259.
[8] http://www.x20.org/FLIR.htm, Infrared PM390 radiometer.
[9] Bradley, D., and Entwistle, A. G., 1961, "Determination of the Emissivity, for Total Radiation, of Small Diameter Platinum-10% Rhodium Wires in the Temperature Range 600–1450°C," Br. J. Appl. Phys., **12**, pp. 708–711.
[10] Young, S. J., 1977, "Nonisothermal Band Model Theory," J. Quant. Spectrosc. Radiat. Transf., **18**, pp. 1–28.
[11] Young, S. J., 1977, "Evaluation of Nonisothermal Band Model for H_2O," J. Quant. Spectrosc. Radiat. Transf., **18**, pp. 29–35.

Numerical and Experimental Investigation of Thermal Signatures of Buried Landmines in Dry Soil

F. Moukalled

N. Ghaddar[1]
ASME Fellow
e-mail: farah@aub.edu.lb

H. Kabbani

N. Khalid

Faculty of Engineering and Architecture,
American University of Beirut,
Beirut, Lebanon

Z. Fawaz
Ryerson University,
School Aerospace Engineering,
Toronto, Canada, M5B 2K3

This paper reports a numerical and experimental investigation conducted to study the thermal signature of buried landmines on soil surface. A finite-volume-based numerical model was developed to solve the unsteady three-dimensional heat transport equation in dry homogeneous soil with a buried mine. Numerical predictions of soil thermal response were validated by comparison with published analytical and numerical values in addition to data obtained experimentally. Experiments were performed inside an environmental chamber and soil temperatures were measured during cooling, using two measurement techniques, after exposing the soil surface to a radiant heat flux for a specified period. In the first technique, the temporal variation of the surface and internal soil temperatures were recorded using thermocouples. In the second technique, the soil surface temperature was measured using an infrared camera that revealed the thermal signature of the mine. The transient temperature profiles generated numerically agreed with measurements, and the difference between predicted and measured values was less than 0.3°C at both the soil surface and in depth. The accurate matching of numerical and IR images at the surfaces was found to strongly depend on the use of a smaller soil thermal conductivity at the surface than at greater depths. The numerical model was used to predict the dependence of the peak thermal contrast on time, depth, and heating period. The thermographic analysis, when combined with numerical predictions, holds promise as a method for detecting shallowly buried land mines. [DOI: 10.1115/1.2176681]

Keywords: infrared imaging, detection of buried objects, soil thermal response to unsteady surface heating, finite-volume method

1 Introduction

Objects of dissimilar thermal capacitance absorb and release heat at different rates and as such have different infrared (IR) emission characteristics. Therefore, a buried mine heats up and cools down at a rate different from the surrounding soil. This unequal heat transfer rate manifests itself on the surface above the mine through either a higher or a lower soil surface temperature than the surface temperature at a location away from the mine. This variation in temperature is denoted in the literature by thermal signature [1–3] and appears as a thermal contrast in an image taken by an IR camera. Simard [2,3] thoroughly explained the various thermal mechanisms affecting the temperature contrast and related them to the "*volume*" and "*surface*" effects. The *volume* effect results in an alteration of the heat flow due to the presence of the buried mine. The surface effect, which enhances the mine's signature, is present whenever the soil layer above and around the mine is disturbed (e.g., during the first few weeks after burial). According to numerous studies, IR systems hold promise as a support technology for specific mine-detection situations [4]. The IR technology, which has the key advantage of being passive, could be remotely utilized by aerial search, and could cover a large area in a relatively short time [4]. Infrared thermography is best suited for identifying minefields (global area search), rather than searching for individual mines (local area search) [5]. Nevertheless, a few projects using IR technology aimed at searching for individual mines. One such project involved developing a short range IR system based on an 8–12 μm IR sensor and using neural networks for pattern recognition after segmentation of the image. Reported results indicate that the system is capable of achieving a successful mine-detection rate of 90% [6].

Besides accuracy, it is highly desirable for any potential landmine detection technology to be quick and minimally intrusive. IR technology, as a means for remotely detecting buried landmines, has the potential of combining these desirable features. Since the detection of mines using IR technology is via an image for the soil surface, its degree of success depends on a number of factors including burial depth, soil attributes, moisture content, mine properties, as well as the time of day during when the scanning is performed. Bruschini and Gros [7] assessed the potential of using IR imaging as a landmine detection technology and described its advantages and limitations. They estimated that IR images could spot the presence of an antitank mine at a maximum burial depth of 10–15 cm. Their work also indicated that the results of IR imaging depend heavily on environmental conditions. In a recent paper, Deans et al. [8] presented experimental results of a thermal imaging method using microwave heating to enhance the visibility of buried landmines. They concluded that discovery of mines buried in dry sand is possible up to a burial depth of 2 cm, which differs significantly from the 10–15 cm suggested by Bruschini and Gros [7]. Consequently, the depth at which mines are detectable by an IR sensor strongly depends on the type of mines and the type of soil in which they are buried.

Hermann and Ian [9] investigated experimentally the enhancement of thermal signature of buried landmines using IR sensors through volumetric heating via microwave energy sources. In ad-

[1]Corresponding author.

Contributed by the Heat Transfer Division of ASME for publication in the JOURNAL OF HEAT TRANSFER. Manuscript received April 27, 2005; final manuscript received October 25, 2005. Review conducted by Ramendra P. Roy. Paper presented at the 2005 ASME Heat Transfer Summer Conference (HT2005), July 15–22, 2005, San Francisco, California, USA.

dition, the authors presented a one-dimensional model for microwave absorption and heat dissipation by moisture-laden soils with a surrogate buried landmine to model the enhancement of the signature. Mitchell et al. [10] studied the detection of antipersonnel landmines by taking thermal images of the soil surface after spraying it by hot water with an array of jets. The variation in conduction and radiation heat transfer due to the water blocked by the mine and the heating of the mine itself, affected the transient temperature profiles at the soil surface and reflected the presence of the buried mine. Moreover, to reduce the false alarm mitigation (FAM) three quantitative numbers based on gray contrast, temperature gradient, and apparent thermal width were used as indicators. Deepak et al. [11] applied other FAM reduction techniques using three indicators based on circularity, gray scale moment, and reflection symmetry. The study reported reduction in false alarms by factors ranging from four to twelve depending on the mine size.

Recently, Khanafer and Vafai [12] analyzed numerically using the finite-element method effect of surface roughness on thermal signature of buried landmines over a diurnal cycle. In their work, an antitank mine was simulated taking into consideration the effect of its striker mechanism. Khanafer et al. also studied the effect on the soil surface temperature of the mine's outer metal case and its top air gap [13]. Their results show that the thin metal outer case and the top air space of a buried antipersonnel mine have a noticeable effect on the intensity of the landmine signature over a diurnal cycle.

Lopez et al. [1,14] investigated landmine detection numerically and experimentally using, respectively, the finite difference method and infrared technology. Their work [14] consisted of comparing thermal signatures in bare soil generated using a three-dimensional thermal model against signatures obtained from infrared images in order to infer the presence of buried objects. Then, Lopez et al. [14] classified these detected objects into either mine or no-mine categories by solving an inverse heat transfer problem. The analysis of the time evolution of perturbations created by such objects constituted the basis of the classification procedure. Moreover, Sendur and Baertlein [15] conducted a similar study to illustrate the effect of the buried landmines on the surface temperature distribution. Results reported [14,15] good agreement in the measured and predicted thermal contrast at the surface of the soil. However, the difference between the predicted and measured absolute temperatures at the surface [14,15] and in the soil [14] were higher (of ±1°C to ±2°C) showing lower matching levels.

From the above, it seems that combining numerical techniques with infrared technology holds a promise with regard to developing a powerful tool for the detection of buried landmines. To this end, the aim of this investigation is to develop a three-dimensional thermal model using a control volume approach to better understand the unsteady heat transport in soil with buried landmines and to predict accurately the soil surface temperature and surface thermal contrast. The model is validated by comparing generated results against available theoretical/numerical values and against measurements taken at controlled ambient conditions in an environmental chamber using both an IR video camera of high thermal resolution and thermocouples embedded in the soil. The temporal variation of the soil surface temperature is generated by subjecting the soil surface to radiant heating for a specified time interval followed by convection cooling. The formulation and validation of the numerical model represent the first step toward the future development of an IR-based tool for detecting buried landmines using both the expected absolute surface temperature and the strength of the thermal contrast as parameters in the mine identification technique.

2 Soil Thermal Model Formulation

A schematic of the physical situation and heat exchange processes is depicted in Fig. 1. The three-dimensional transient heat

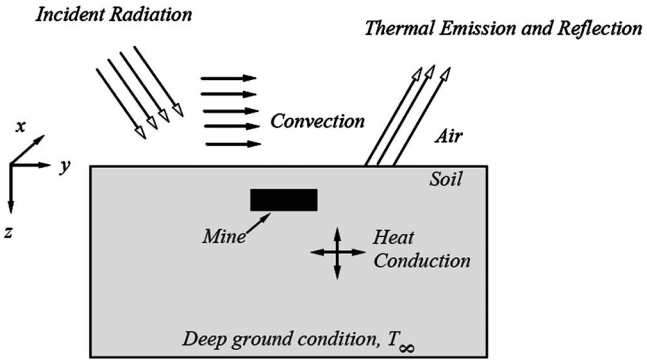

Fig. 1 The soil bed and the embedded mine

conduction equation governs the transport of heat in both soil and mine. Moreover, the target objects buried in it are modeled as isotropic solids. Assuming negligible temporal variation of the moisture content, the resulting governing equations for the soil and the mine can be written as

$$\text{Soil:} \quad \frac{\partial}{\partial t}(\rho c T)_s = \nabla(k \nabla T)_s \tag{1}$$

$$\text{Mine:} \quad \frac{\partial}{\partial t}(\rho c T)_m = \nabla(k \nabla T)_m \tag{2}$$

Where ρ, c, k, and T are the density, specific heat, thermal conductivity, and temperature, respectively. The subscripts s and m refer to soil and mine, respectively. The boundary conditions applicable at the boundaries of the physical domain are given by

$$\text{At the soil surface:} \quad \mathbf{n} \cdot k_s \nabla T_s = q_{\text{net}} \tag{3a}$$

$$\text{At the mine surface:} \quad \mathbf{n} \cdot k_s \nabla T_s = \mathbf{n} \cdot k_m \nabla T_m \tag{3b}$$

$$\text{At vertical boundaries:} \quad \mathbf{n} \cdot k_s \nabla T_s = 0 \tag{3c}$$

$$\text{At the deep soil below the mine:} \quad T_s \rightarrow T_\infty \tag{3d}$$

where $\mathbf{n}$ represents the normal unit vector, T_∞ the deep soil temperature below the buried mine, and q_{net} the net heat flux into the top surface of the soil given by

$$q_{\text{net}} = q_{\text{conv}} + q_{\text{rhs}} - q_{\text{emis}} \tag{4}$$

where q_{conv} is the convective heat transfer between the surface of the soil and the ambient air, q_{rhs} is the incident radiation heat flux on soil surface, $q_{\text{emis}}$is the gray body emission from the soil's surface. In this work, the soil is assumed dry and therefore the latent cooling of the ground caused by evapotranspiration and condensation is neglected. Convective heat transfer between the soil and the surrounding air is expressed as

$$q_{\text{conv}} = Ah(T_\infty - T_s) \tag{5}$$

In Eq. (5), h is the convective heat transfer coefficient at the soil surface and A the surface area. Initially, the soil, ambient air, and mine are considered to be at the same uniform temperature T_∞. Moreover, assuming the ground surface to behave as a grey body, the long-wave radiation between the soil surface and the room surfaces can be expressed as

$$q_{\text{emis}} = \sigma\varepsilon(T_s^4 - T_\infty^4) \tag{6}$$

where $\sigma = 5.67 * 10^{-8}$ W/m^2 K^4 is the Stefan-Boltzmann constant, ε is the mean emissivity of the room surfaces, and T_s is the soil's surface temperature. The temperatures of the surfaces surrounding the soil-mine configuration in the environmental chamber are assumed the same as that of the room air temperature.

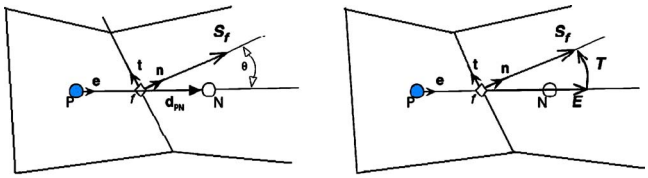

Fig. 2 A schematic showing the treatment of the diffusion term

3 Numerical Analysis

3.1 The Discretization Process. The discretization of the heat conduction equation is performed following the finite-volume method. In this approach, the solution domain is divided into a set of discrete and nonoverlapping elements or control volumes, each associated with a grid point located at its geometric center. The discretization process is a two-step procedure. In step 1, the equations are integrated over a control volume to obtain a discretized description of the conservation laws. In step 2, an interpolation profile is used to relate some of the discretized terms from step 1 to the discrete nodes in the solution domain.

To perform step 1, Eq. (1) or (2) (with the subscript *s* or *m* dropped) is integrated over a control volume with the flux components transformed into surface integrals using Green's theorem [16]. This procedure yields

$$\int_V \frac{\partial(\rho cT)}{\partial t} dV = \oint_{\partial S} (k \nabla T) d\mathbf{S} \tag{7}$$

The discrete form is obtained by replacing the surface integrals of the flux terms by discrete summations over the faces of the control volume, and the volume integral by the product of the integrand at the cell center and the cell volume. Upon substitution into Eq. (7), the resulting discrete equation is written as

$$\frac{\partial(\rho cT)}{\partial t} V_P - \sum_{f=nb(P)} \Gamma \nabla \mathbf{T}_f \cdot \mathbf{S}_f = 0 \tag{8}$$

where $\mathbf{S}_f$ represents the surface area of the control volume face f and $nb(P)$ the faces of cell P.

In step 2, Eq. (8) is transformed into an algebraic equation with the time derivative approximated using an Euler-implicit formulation to yield

$$\frac{\partial(\rho cT)}{\partial t} V_P = \frac{(\rho cT)_P - (\rho cT)_P^o}{\Delta t} V_P \tag{9}$$

Moreover, the diffusion flux of T through the control volume face f can be written as

$$(-k \nabla T)_f \cdot \mathbf{S}_f = (-k \nabla T)_f \cdot \mathbf{E}_f + (-k \nabla T)_f \cdot \mathbf{T}_f \tag{10}$$

where the two vectors $\mathbf{E}$ and $\mathbf{T}$ satisfy the relation $\mathbf{S}=\mathbf{E}+\mathbf{T}$, with $\mathbf{E}$ being collinear with $\mathbf{d}_{PF}$, the vector joining the grid points P and F straddling the control volume face (Fig. 2). The first term on the right-hand side of Eq. (10) represents a contribution similar to the one obtained on orthogonal grids (i.e., involving T_F and T_P), while the second term on the right-hand side is called cross diffusion or nonorthogonal diffusion and is due to the nonorthogonality of the grid system. Several options are available for the decomposition of $\mathbf{S}$. The over-relaxed approach, in which $\mathbf{T}$ is selected to be perpendicular to $\mathbf{S}$ (i.e., $E=S/\cos\theta$, θ being defined in Fig. 2 and E and S are the magnitudes of $\mathbf{E}$ and $\mathbf{S}$, respectively), is found to be the most stable even when using highly distorted grids. In this approach, the importance of the term involving T_P and T_F increases with increasing grid nonorthogonality. For an orthogonal grid, all variations yield the same numerical discretization. Expanding Eq. (10) using a fully implicit scheme in time, the expression for the diffusion flux becomes

$$(-k \nabla T)_f \cdot \mathbf{S}_f = -k_f \left(\frac{T_F - T_P}{d_{PF}} \mathbf{E}_f + (\nabla T)_f \cdot \mathbf{T}_f \right) \tag{11}$$

where E_f is the magnitude of $\mathbf{E}_f$, and the cross-diffusion term is treated as a source term in a deferred correction manner, with its value computed explicitly using the current T field. By substituting Eqs. (9) and (11) in Eq. (8), the following algebraic equation is obtained:

$$(a_P^t + a_P^D) T_P + \sum_{F=NB(P)} a_F^D T_F = a_P^t T_P^0 \tag{12}$$

where the superscripts t and D indicate coefficients obtained from the discretization of the transient term and of the diffusion fluxes, respectively, and the superscript ^{0} designates a value from the previous time step.

To improve the robustness of the solution procedure, which is iterative in nature, the equations are usually under relaxed. Denoting the under relaxation factor by urf, Eq. (12) becomes

$$\left(\frac{a_P^t + a_P^D}{\text{urf}} \right) T_P + \sum_{F=NB(P)} a_F^D T_F = a_P^t T_P^0 + \left(\frac{1 - \text{urf}}{\text{urf}} \right) (a_P^t + a_P^D) T_P^{(n)} \tag{13}$$

where the superscript (n) refers to values taken from the previous iteration. This equation can be rewritten as

$$a_P T_P + \sum_{F=NB(P)} (a_F T_F) = b_P \tag{14}$$

with the coefficients given by

$$a_F = -k_f \frac{\mathbf{E}_f}{d_{PF}} \qquad a_P = a_P^t - \sum_{F=NB(P)} a_F$$

$$b_P = a_P^t T_P^0 + \left(\frac{1 - \text{urf}}{\text{urf}} \right) (a_P^t + a_P^D) T_P^{(n)} + \sum_{f=nb(P)} (k \nabla T)_f \cdot \mathbf{T}_f \tag{15}$$

The system of algebraic equations is solved iteratively using a line-by-line tri-diagonal matrix algorithm [16]. Moreover, grid networks are generated using the transfinite interpolation technique [17]. Furthermore, since a conservative scheme is used, arranging the control volume face to coincide with the mine interface ensures energy balance at the mine-soil surface of contact [16] and forces Eq. (3*b*) to be satisfied identically.

3.2 Validation of the Thermal Model. The above-described numerical procedure was implemented in a finite volume code and validated by solving several problems of which two tests are presented next.

3.2.1 Test 1: Temperature Distribution in a Semi-Infinite Wall. A soil column of depth 2 m represents the semi-infinite wall, with the soil having a density of 2000 kg/m^3, a thermal conductivity of 2.511 W/m K, and a heat capacity of 837.2 J/kg K as used by Khanafer and Vafai [12]. Initially, the soil is maintained at a uniform temperature of value 293 K. At time $t>0$, the surface temperature of the soil is increased to 310 K and the temporal evolution of temperature profiles in the soil are predicted using the developed numerical code. Predicted profiles after 1, 4, 9, 16, and 25 h are compared in Fig. 3(*a*) against the exact analytical profiles, assuming that heat flows in the vertical direction only. As shown, the numerical code reproduces accurately the analytical profiles, with numerical predictions falling right on top of analytical values. This is an indication of the correct implementation of the unsteady and conduction terms in the governing equation.

3.2.2 Test 2: Reproduction of Khanafer and Vafai [16] predictions. As a further check for accuracy, soil temperature profiles in the presence of a buried landmine reported by Khanafer and Vafai [12] following a finite-element approach were repro-

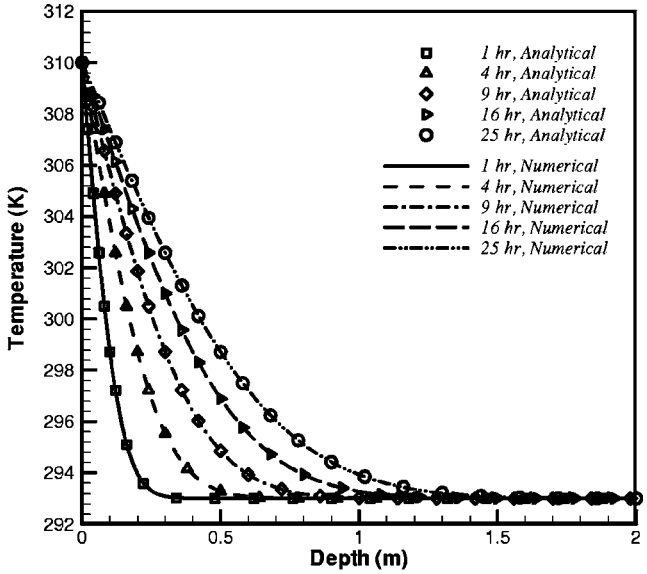

Fig. 3 A plot showing (*a*) comparison of soil temperature profiles generated numerically and analytically for the semi-infinite heat conduction problem, (*b*) comparison of predicted soil temperature profiles in the presence of a buried mine against those reported by Khanafer and Vafai [12]

duced. The simulated mine radius and height in the study were 0.125 m and 0.0833 m, respectively. The properties used in their work were: Trinitrotoluene (TNT) thermal conductivity $=0.22344$ W/m K, soil thermal conductivity$=2.5$ W/m K, soil density$=2000$ kg/m^3, and soil heat capacity$=837$ J/kg K. Computations were repeatedly performed while refining the mesh and varying the time step until a grid and time step independent solution was reached. Predicted temperature profiles at two depths of 0.076 m and 0.1193 m are compared against similar results reported in [12]. As depicted, predictions are in good agreement with each other. The slight difference in values is attributed to some error introduced while extracting data from small figures for comparison and to the different mesh and time step used. A fixed time step of 30 s is used in this work, while Khanafer and Vafai [12] used a variable time step with a minimum value of 0.36 s.

4 Experimental Methodology

As mentioned earlier, the current work is the first foundation in a large-scale project aiming at developing an IR-based system for the detection of buried landmines. The objective of this phase is to develop the numerical model that will be used in generating a database against which infrared images will be compared for inferring the presence or non-presence of landmines. Therefore, it is essential for this tool to be capable of generating accurate predictions. Furthermore, to fine tune the model, it is necessary to compare numerical predictions against experimental data. Recording these measurements in outdoor conditions requires accurate weather and solar radiation data. To reduce the complexity of the problem and validate the numerical tool, indoor experiments were conducted at controlled temperature and humidity conditions inside an environmental chamber. The soil surface was exposed to radiant heat flux for a short period of time and the thermal response of the soil surface as well as the inner shallow layers of the soil were monitored while cooling.

The environmental chamber has the dimensions of 3.2 m $\times 4.2$ m $\times 2.8$ m and is equipped with two independent systems for controlling the air temperature and relative humidity. The precision in the set conditions of the environmental chamber is ± 0.5°C for temperature and $\pm 2\%$ for relative humidity. The test bed (width: 1 m, length: 1 m, and height: 0.65 m, see Fig. 4) placed inside the chamber is made of a 2 cm thick layer of plywood and is filled to the top with a homogeneous soil that is typically found in Lebanon and is composed of clay silty sand: 80% sand (fine), 12% silt, and 8% clay. The bed size was chosen based on preliminary numerical calculations to make sure that the boundary conditions along the sides of the bed do not affect the solution around the mine. The soil was sifted and cleaned from clutter and pebbles and its surface was carefully leveled. The measured soil density and specific heat were found to be $\rho_s = 1430$ kg/m^3, and $C_s = 750$ J/kg K, respectively. The soil thermal conductivity, measured using a Hilton Thermal Conductivity Unit TCU 100 of Heat Technology that does the analysis according to ISO 8301 [18], was found to be $k_s = 0.30 \pm 0.003$ W/m K. On the other hand, at the porous surface layer, the soil thermal conductivity was measured to be $k_s = 0.25 \pm 0.003$ W/m K. These measurements were performed on soil samples that were initially dried in a furnace.

Figure 4 shows the physical dimensions of the soil bed, the embedded mine, and the radiation source. The soil surface is exposed to radiant heat flux for a short period and then thermal signatures are observed while cooling takes place. The intention of the experiment is to understand the mechanism by which the thermal signature is induced and to develop and validate a numerical model capable of accurately predicting the mine's signature rather than simulate the actual diurnal heating and cooling cycle. The radiant heating source is composed of a set of six halogen lamps rated at 1000 W each (1 m $\times$ 1 m) placed horizontally above the soil bed at a height of 1 m and backed with parabolic reflectors. The power input to the lamp is monitored for stable nonfluctuating operation. The arrangement of the radiant lamps resulted in a nonuniform incident radiation on the soil surface. A special CM3 Campbell Scientific Pyranometer of spectral range 305–2800 nm is used to measure the radiative heat flux from the Halogen lamps at different locations on the soil surface using a grid of 0.05 m $\times$ 0.05 m resulting in 400 readings. The spectral selectivity of the pyranometer is $\pm 5\%$ (350–1500 nm), with a sensitivity of 10 μV/Wm^{-2} to 35 μV/Wm^{-2} and impedance of 60 Ω to 200 Ω.The measured reflected flux from the soil surface amounted to about 20% of the incident flux. The radiant heat flux at the surface ranged from 2052 W/m^2 to 2187 W/m^2 in the middle of the test bed region of area 0.3 m $\times$ 0.3 m. The unifor-

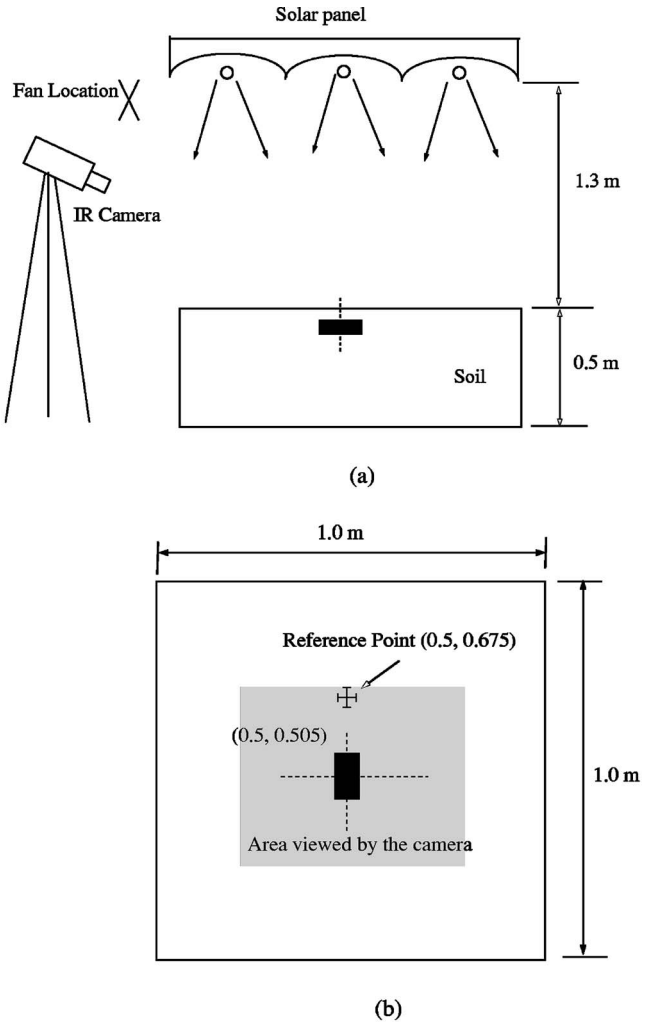

Fig. 4 A schematic of (*a*) the side view of the experimental setup and (*b*) the top view of the soil bed

mity of the radiation intensity at the soil surface is dependent on the height of the source lamps above the bed. A height of 1 m was found to give reasonable spatial uniformity on the surface above the buried mine and sufficient intensity of the radiant flux to generate realistic temperature changes on the surface and in the soil layer above the mine. Surface drying of the soil was not a problem since the thermal signature was observed during the cooling period when surface temperatures of the soil was less than 35°C. In addition, the variation of the relative humidity in the chamber was monitored to remain at 50% ± 2%. The continuous renewal of the air during cooling in the chamber maintained steady temperature above the soil bed.

The mine is embedded in the soil at a distance $x=0.5$ m and $y=0.505$ m from the origin of the bed, located on the lower left-hand corner. This location is selected so that the surface of soil above the mine is well within the view of the IR camera and is exposed to spatially uniform radiative flux during the heating period. A common type of antipersonnel mine of rectangular shape (13.9 cm × 5.4 cm × 6.7 cm) is used. The mine is filled with (RTV) material that has properties similar to TNT (specific heat $c_m=1500$ J/kg K, thermal conductivity $k_m=0.2$ W/m K, and density $\rho_m=1170$ kg/m^3) and is buried in the soil. The plastic cover of the mine has a thickness of 0.3 cm, specific heat $c_p=1260$ J/kg K, thermal conductivity $k_p=0.5$ W/m K, and density $\rho_p=1760$ kg/m^3. The burial depth is an experimental parameter and is varied from 0.5 cm to 2.5 cm.

Two measurement methods are used in this work. The main measurement instrument is the IR ThermaCAM S60 camera (7.5–13 μm spectral range), which has a temperature sensitivity of 0.08°C at 30°C and accuracy of ±2% of reading. The camera is air-cooled and tower mounted horizontally at a height of 0.6–1 m from the soil surface. A tripod mounted IR camera, at a lens-to-soil distance of 1 m angled at 45° from the horizontal, is utilized to capture images of the soil surface at the peak, when a significant variation in temperature is noted. The capture card employing the ThermaCam Professional 2.8 [19] software stores images (joint photographic experts group (JPEG) and Microsoft bitmap format (bmp)) and videos taken by the camera. The surrounding air temperature (level temperature) and the distance between the lens and the object are adjusted in the camera and autozoom is used. A major challenge in the work is processing the acquired images with a high degree of accuracy. Because IR sensors are passive sensors that quantify emitted infrared radiation from a body surface, the radiation measured by the camera is not only dependent on the temperature of the body, but it is also a function of the emissivity of the surface. This is why the emissivity setting of the camera significantly affects the accuracy of the measured temperature differences. To minimize error, the soil emissivity was carefully measured following two different procedures and was found to be equal to 0.92. Another input parameter was the reflected temperature, which was equal to the ambient temperature in an outdoor environment and takes into consideration the radiation from the surroundings reflected via the object surface to the camera. When reflected temperature input to the camera increased, the absolute temperatures decreased, but the difference in temperature between any points on the surface remained unchanged. The surrounding objects in the climatic chamber were all set at the ambient temperature with the exception of the halogen lamps panel. Since the solar panel is highly reflective and has a very low emissivity, the camera reflected temperature was put equal to the chamber air temperature. The camera resolution is 320 × 240 pixels capable of registering data at 76 800 pixel locations on the surface.

The second technique involves using K-type thermocouples to measure soil temperature with an accuracy of ±0.5°C. Thermocouples, mounted on a glass rod at the reference location ($x=0.675$ m, $y=0.505$ m) were positioned at depths of 0 mm, 4.5 mm, 10.5 mm, 18 mm, and 45 mm. The thermocouples tips were not bonded to the rod, but were stuck out at a distance of at least 10 mm from the rod surface into the desired soil locations to eliminate the effect of the glass rod conductivity on the readings. Additional thermocouples were located at the center of the mine's top surface and the soil's surface above the mine center. The soil surface temperature was monitored at the sensors reference location using a special temperature probe Model 108 Campbell Scientific with a resolution of ±0.3°C over the range −3°C to 90°C. In addition, a precision infrared temperature sensor (IRTS-P) is positioned 0.5 m above the bed corner directed toward the soil surfaces above the center of the buried mine. The IRTS-P sensor has a silicon lens whose field of view is a circle of 1 m diameter when the sensor is 3 m away from the target. To accurately process infrared images, the air temperature and relative humidity above the soil bed were monitored. All thermocouples were calibrated before the start of the tests and were connected to a Campbell Scientific CR23X logger capable of recording one set of readings per second. Sampling of the temperature readings was done every 10 s. A small fan was placed parallel to the heater and away from the soil bed, at the heating panel level of 1 m, to accelerate cooling by increasing convection heat transfer. The air speed at a height of 1 m was measured using a handheld airflow meter and was found to be equal to 4.5 m/s ± 0.1 m/s.

The soil bed was conditioned inside the environmental chamber at an air temperature of 25°C and relative humidity of 50% for at least 48 h for steady state to be reached. Following this conditioning period, the soil surface was heated for five minutes, after

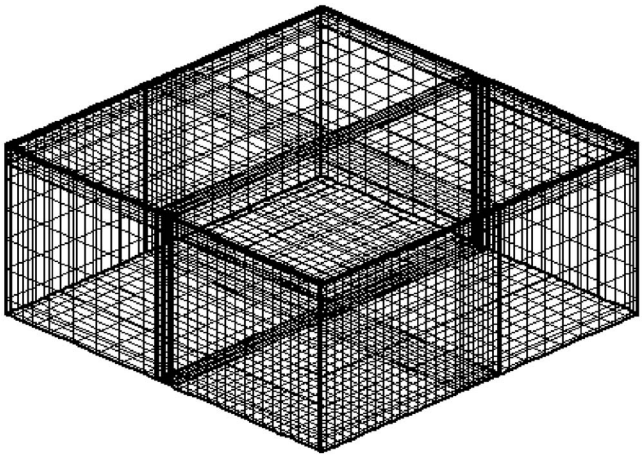

Fig. 5 The computational domain

which the heat source was stopped and images of the soil surface were taken at one-minute intervals to monitor the surface temperature changes during the cooling period. The tests were performed with the fan either on or off to study both forced and natural convection cooling, respectively. The experiments were carried out with a mine buried at predetermined depths to examine the surface signature changes during cooling using the IR camera and while recording temperature readings at the surface above the mine and at the reference point location and in depth. The air temperature in the environmental chamber was monitored at four different locations.

For natural cooling, the air temperature above the soil increases by about 5°C from its initial value (the heating period is 5 min), but cools quickly to the chamber temperature within the first five minutes after shutting off the heat source. When repeating the test with the fan turned on, the temperature of the air above the soil increases by 2.5°C only for the same heating period. The interval between any two experiments is at least 48 hours to allow the soil and the environmental chamber air to reach thermal equilibrium as this condition is important for the numerical simulation.

5 Result and Discussions

5.1 Experimental Results and Validation of the Numerical Thermal Model. The use of a three-dimensional conduction model was dictated by the non-uniform heating of the soil surface in the experiments, the geometry of the mine, and the willingness to validate such as model as it will be used for developing an IR-based tool for detecting buried landmines.

Before comparing numerical results to measured values, the grid and time step were adjusted until a grid and time step independent solution was obtained. This was accomplished with an $80\times80\times54$ grid network with the grid points nonuniformly distributed as shown in Fig. 5 using a time step of 10 s. All results presented here were generated using the aforementioned grid system and time step for the physical domain described in the experimental section and using the measured thermal properties of the soil, mine and RTV filling material ($\rho_s=1430$ kg/m^3, $c_s=770$ J/kg K, $c_m=1500$ J/kg K, $k_m=0.2$ W/m K, density $\rho_m=1170$ kg/m^3). The spatially varying heat flux on the soil surface, needed as a boundary condition in the numerical simulations, was calculated at the center of each control volume by interpolating between the nearest two or four experimentally measured incident heat flux values. These interpolated estimates were assumed to prevail over the entire control volume face. The initial temperature of the soil was set equal to the temperature of the ambient air in the environmental chamber. Results are presented for the two methods of cooling by forced and natural convection. Tests were carried out using a rectangular shaped mine filled with RTV material buried at depths of $z=0.5$ cm, 0.75 cm, and 1 cm from the surface at $x=0.5$ m and $y=0.505$ m. The reference point at which temperature values arerecorded corresponds to the location $x=0.675$ m and $y=0.505$ m. The environmental chamber is set to 25°C and 50% relative humidity.

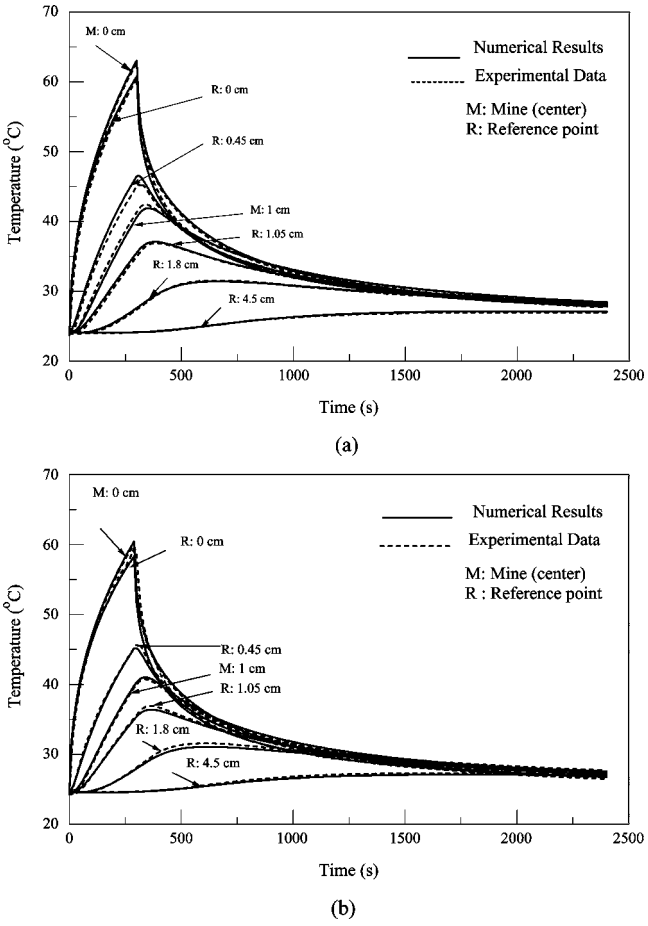

Fig. 6 The variation in time of the predicted and measured temperatures at the center of the mine surface at $z=0.01$ m, and the soil surface at the reference point at depths of 0.45 cm, 1.05 cm, 1.8 cm, and 4.5 cm for a test conducted in the environmental chamber while heating the soil bed for a period of 5 min and then cooling by (*a*) radiation and forced convection with the fan turned on and (*b*) radiation and natural convection with the fan turned off

Figure 6 shows the temporal variation of the predicted and measured temperatures at the center of the top surface of the mine ($z=1$ cm), the soil surface above the center of the mine, and the reference point at depths of 0.45 cm, 1.05 cm, 1.8 cm, and 4.5 cm for two test cases. Heating of the soil surface in both configurations took place over a period of 5 m. The difference between the two situations is in the cooling method, which occurred either with the fan turned on (Fig. 6(*a*)) or off (Fig. 6(*b*)). As shown in Figs. 6(*a*) and 6(*b*), the soil surface temperature is less sensitive to changes in the convection heat transfer coefficient during the heating period since the heat gain by radiation in that time interval is at least one order of magnitude higher than the convection heat loss. After turning off the lamps, the surface cooling rate shows a steep gradient indicating immediate response with its temperature dropping sharply. Comparing profiles in Figs. 6(*a*) and 6(*b*) it is noticed that the value of the convection heat transfer coefficient affects the cooling rate, but does not affect the time of peak at any depth z in the soil. Due to storage effects, the time at which the temperature peaks, for both methods of cooling, increases with

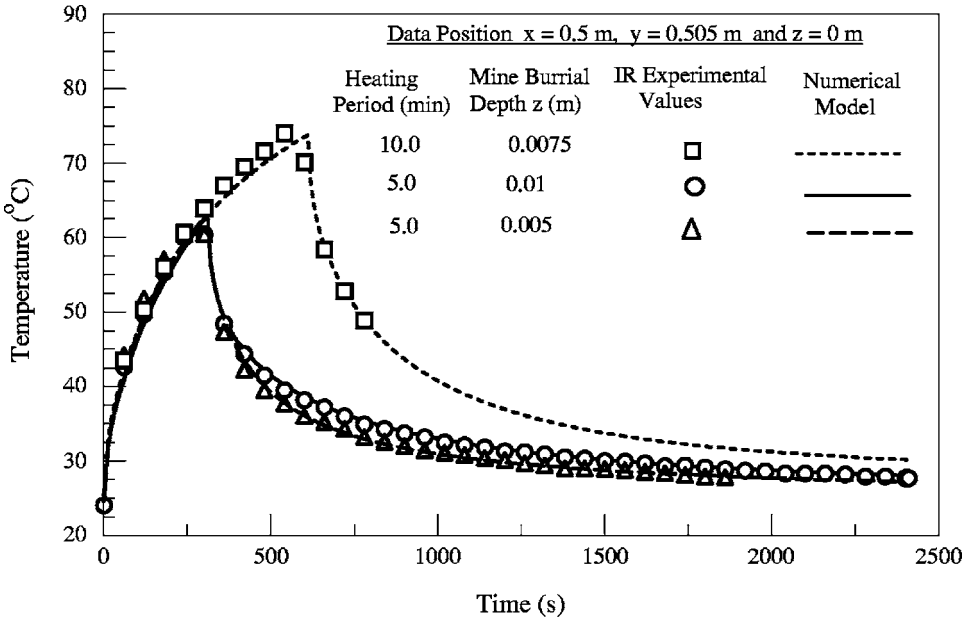

Fig. 7 The test results of the soil surface temperature above the mine center predicted by the numerical model and measured by the infrared camera at 1 min intervals for a mine burial depths of 0.005 m, and 0.01 m with a heating period of 5 min and a burial depth of 0.0075 m with a heating period of 10 min

depth. The numerical model is able to reproduce the actual thermal processes that take place in the soil since temporal temperature profiles obtained near the surface and inside the soil are in excellent agreement with measurements. The maximum error is less than 4% between the measured and numerically predicted values. This agreement was achieved after rigorous experimentation and sensitivity analysis of the effect of the various physical parameters on the predicted response. Initially, even though solutions were close to measurements below the surface, it was not possible to match it at the surface. The extensive analysis performed identified the soil thermal conductivity in the layer close to the surface to be the cause. Due to continuously disturbing the soil while setting up the experiment, the soil in the layer close to the surface has more air void than deeper soil. Therefore, the thermal conductivity of the surface layer is different from the measured soil value and has to be calculated as a weighted average of the thermal conductivities of the soil and air. This conclusion was verified experimentally using a portable Quicktime30 Thermal Properties Analyzer (the device has an accuracy of 5% or ± 0.001 W/m K for thermal conductivity in the range of 0.05–0.7 W/m K). The same situation would be faced with a newly buried landmine. For the conditions of the experiment, the value measured by the device helped developing the following equation for the soil thermal conductivity, which was used within the top 1 cm of the soil bed:

$$k_{s,\text{surface}} = k_s\left(1 - \frac{e^{-3z}}{6}\right) \tag{16}$$

where $k_{s,\text{surface}}$ is the soil thermal conductivity at depth z (expressed in centimeters) and k_s is the soil thermal conductivity. As depicted in Figs. 6(*a*) and 6(*b*), the use of Eq. (16) allowed accurate numerical predictions of the soil surface response while also predicting accurately the soil thermal response in depth. Moreover, the interface of the plastic layer surface of the mine box is not ideal due to the porous characteristics of the soil. A thin interface air layer of 0.03 mm thickness was used between the plastic cover of the mine, which has a thickness of 0.1 mm, and the soil. The thin interface layer introduced in the solution represents a physical effect resembling the contact resistance between the sand and the plastic rigid surface and is different than the top air gap region within the mine cover in the work of Khanafer and Vafai [12] of 10 mm thickness compared to the interface layer outside the plastic cover of 0.3 mm used in this work. The predicted soil surface temperature above the mine and on the mine center agrees well with experimentally measured values using thermocouples.

Figure 7 presents a comparison between numerical predictions and measurements taken by the infrared camera at 1 min intervals for the soil surface temperature above the mine center for burial depths of 0.005 m and 0.01 m when the heating period is 5 min and of 0.0075 m when the heating period is 10 min. Good agreement is observed where differences between readings and predictions is less than 0.3°C. The longer heating period results in higher surface temperatures and a faster cooling rate of the soil. The experiments have been limited to shallow burial depths due to the limitations imposed by the heating source strength and the type of soil which has a close thermal conductivity (0.25–0.3 W/m K)to the buried RTV material in the mine (0.2 W/m K). Typical soil conductivities that appeared in other studies ranged from 0.5–0.75 W/m K and have shown ability to detect signatures up to 2–5 cm depth in outdoor tests [12,14]. Further processing of surface images taken by the infrared camera will assess the thermal contrast between the surface temperature measured above the mine and at a point away from the mine.

6 Analysis of Thermographic Results and Image Processing

The output of the IR camera is a JPEG image with its temperature palette. An algorithm was developed to map the captured pixels' attributes to absolute temperatures. The input for this algorithm is the IR image and its color temperature palette, while the output is a set of temperature values. Figure 8(*a*) shows the reference spatial extent of the camera image, an actual image showing the mine signature, and the temperature distribution along a line on the surface of the soil for the experiment whose data are presented in Fig. 6(*a*). Figure 8(*b*) shows the three-dimensional temperature distribution on the surface as generated by the mapping algorithm from the IR images at 5 min and 10 min from the

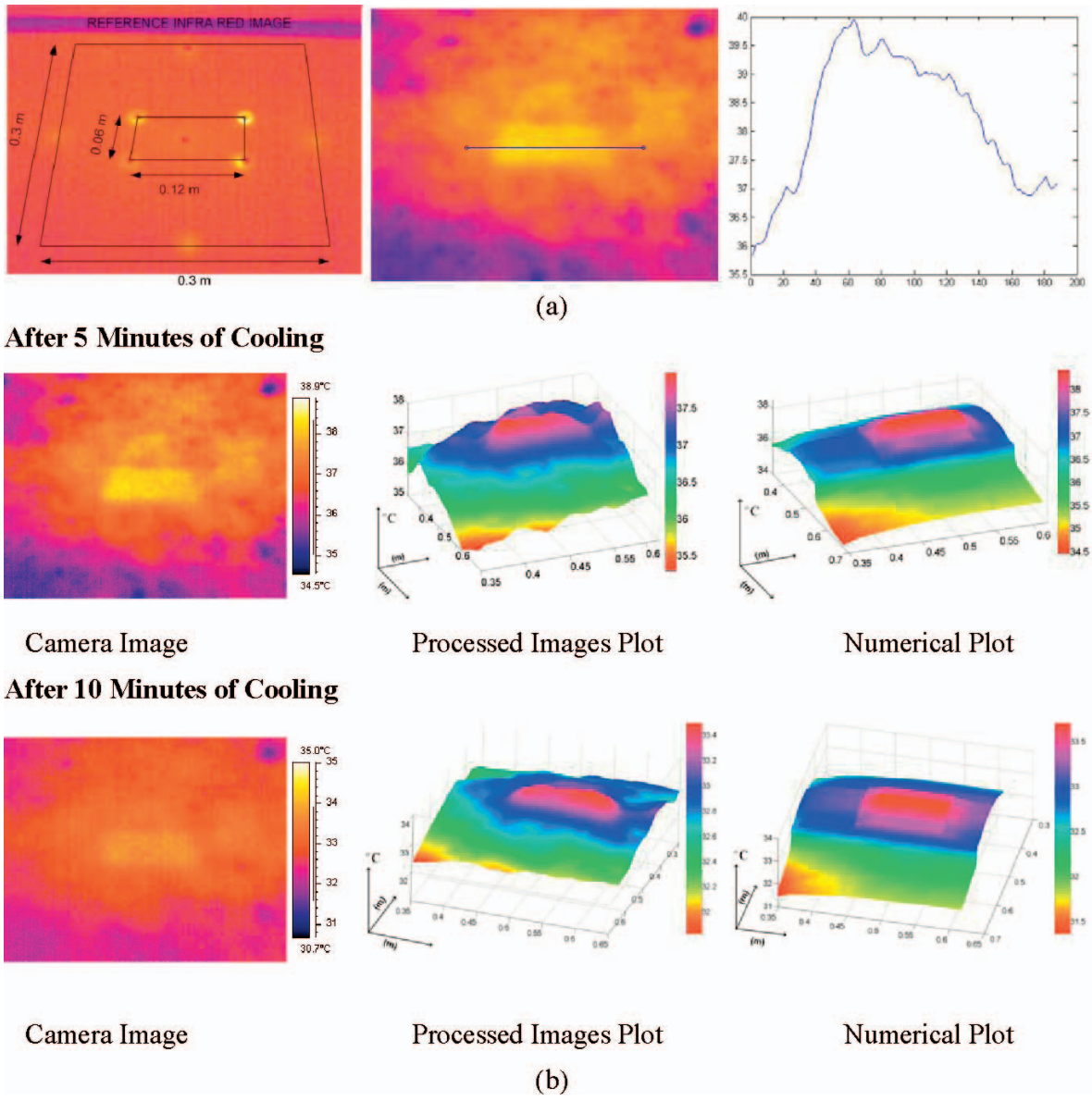

Fig. 8 (*a*) **The soil bed reference image at steady conditions of the environmental chamber, and the IR camera image during the cooling period, and the temperature distribution plot along a line on the surface of the soil for the experiment whose data were discussed and shown in Fig. 6(*a*); (*b*) the IR camera image, the 3-D temperature distribution of the surface as generated by the mapping algorithm from the IR images at 5 min and 10 min from the onset of cooling, and the corresponding surface images generated by the numerical model. (Heating period =5 min, mine depth=0.01 m, T_∞=25°C, RH=50%.)**

onset of cooling and the corresponding surface images generated by the numerical model. The mean difference in temperature values between the camera images and those produced by the numerical code is less than 0.2°C while the maximum difference is 0.3°C. The spatial nonuniformity in the camera image is due to the incident nonuniform flux from the heating lamps during heating.

The thermal signature or contrast is defined in this work as the temperature difference between the point on the soil surface above the mine center and the reference point. For the results discussed earlier, the numerical and experimental thermal contrasts were calculated and their values, denoted by TC'_{max}, were found to represent the maximum possible temperature difference on the soil surface. Figure 9 shows the predicted thermal contrast, and the measured thermal contrast using the IR images and the thermocouples' readings as a function of time for (*a*) mine burial depth of 0.005 m (5 min heating), and 0.0075 m (10 min heating) and (*b*) mine burial depth of 0.01 m (5 min heating). The first is for a mine buried at 0.005 m under the surface and exposed to 5 min of heating and the other is for a mine buried at 0.0075 m and exposed to 10 min of heating. The shallower mine has given a peak contrast of about 4°C after one minute from the start of the cooling process, while the deeper mine has given a maximum contrast of 3.5°C directly at the end of the heating period. The time of occurrence of the peak contrast depends on both the mine depth and the heating period. The difference in temperature between the numerical and experimental readings is less than ±0.3°C during cooling, while during heating the error is slightly higher (±0.5°C) due to the sensitivity of the camera to the surface temperature and the need to adjust its range for temperatures above 60°C. The camera images produce more accurate readings of the surface

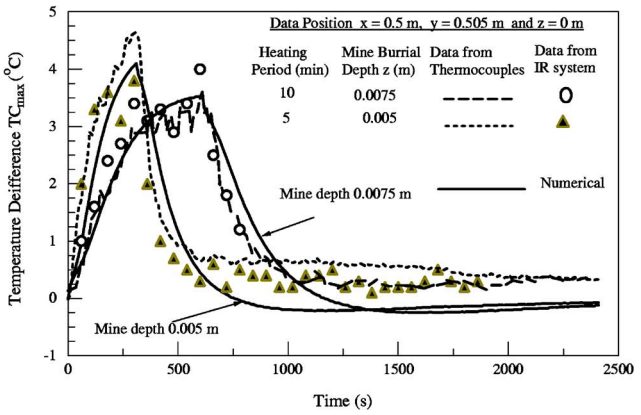

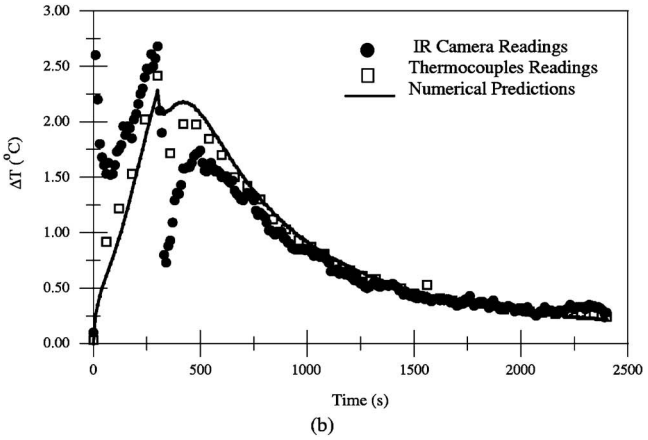

Fig. 9 A plot of the predicted thermal contrast, and the measured thermal contrast using the IR images and the thermocouples' readings as a function of time for (*a*) burial depth of 0.005 m (5 min heating), and 0.0075 m (10 min heating) and (*b*) burial depth of 0.01 m (5 min heating)

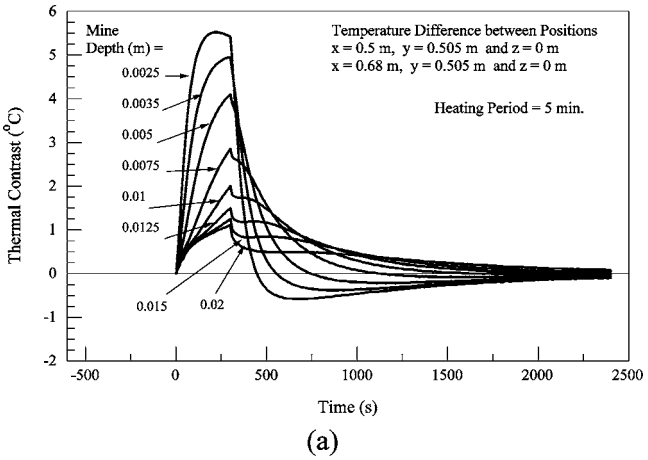

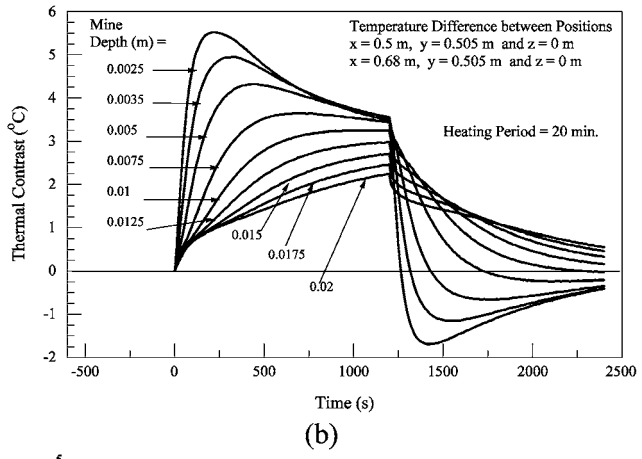

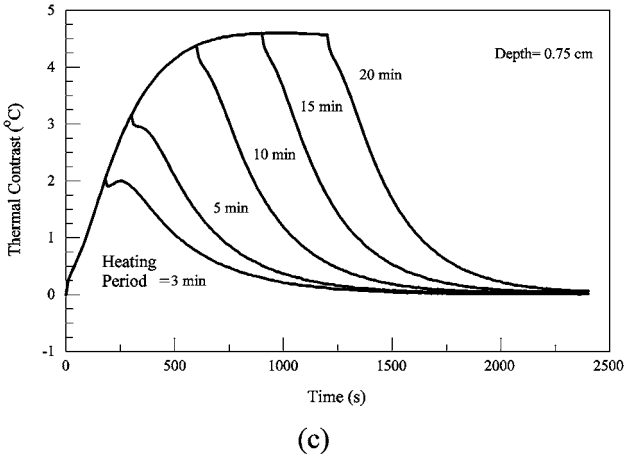

Fig. 10 A plot of the thermal contrast as a function of time for (*a*) a heating period of 5 min, (*b*) a heating period of 20 min at different mine depths, and (*c*) different heating periods at fixed mine depth for the same climatic conditions of the indoor experiments considered in this work

temperature than the thermocouple particularly in the period when heating source is turned off. The surface of the soil is rough and the tip of the thermocouple is in touch with the air and the soil grain. At the end of the heating period, the soil temperature is not in equilibrium with the air temperature in the void space of the soil. This causes a drop in the measured temperature at that instant given an error of about 0.7°C due to the sudden change from heating to cooling at the surface.

For fixed thermal properties of soil and mine material, the dependence of the peak thermal contrast on time, depth, and heating period was investigated numerically. Figure 10 shows plots of the thermal contrast as a function of time for (*a*) a heating period of 5 min. (*b*) a heating period of 20 min at different mine depths, and (*c*) different heating periods at fixed mine depth. Plots in Figs. 10(*a*) and 10(*b*) indicate that the thermal contrast decreases with increasing mine's burial depth. On the other hand, Fig. 10(*c*) reveals that the peak thermal contrast does not change when the heating period increases beyond 10 min. Figure 11 presents the variation with depth of (*a*) the peak thermal contrast and (*b*) the time of the peak occurrence for heating periods of 5 and 20 min. As shown in Fig. 11(*a*), the value of the peak thermal contrast increases with the heating period due to the larger amount of energy stored in the soil during heating. However, Fig. 11(*b*) indicates that the time of occurrence of the peak thermal contrast increases with depth and approaches the end of the heating period.

The numerical method has predicted well the transient thermal response of the soil surface and the resulting thermal signature. Integrating the model with an IR imaging system will help identifying potential target objects. In the real situation, the mine location is not known a priori. Moreover, relying on the experimental data is not enough neither to identify the targets nor to determine their depths if classified as mines. However, using the numerical model it is possible to generate a database of solutions against which real images can be compared. The thermal signature maps of the database at the different periods can then be used to aid classifying the target. Among other objectives, future work will be directed toward developing a criterion that transforms the

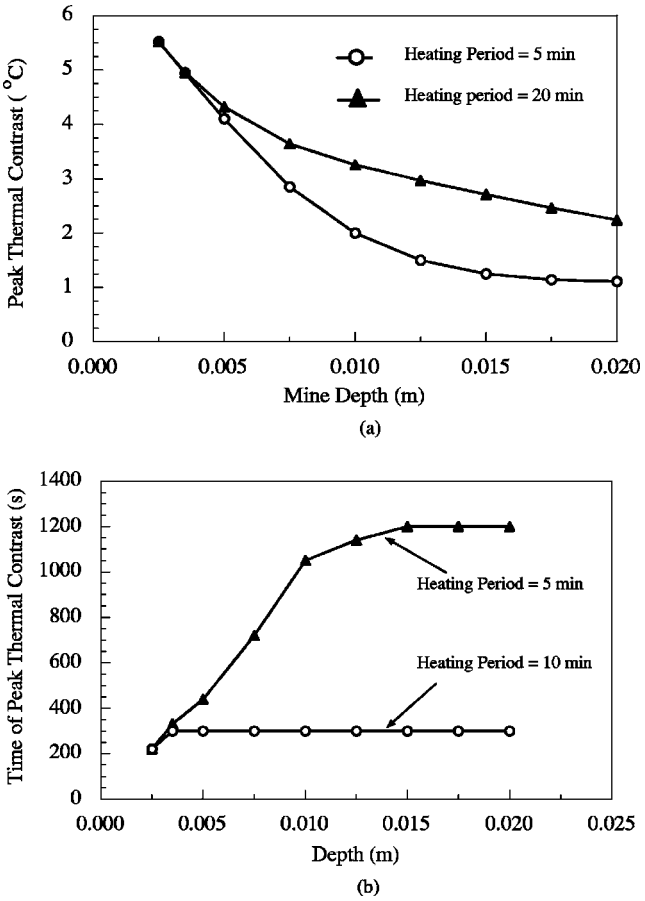

Fig. 11 The variation with depth of (*a*) the peak thermal contrast and (*b*) the time of the peak occurrence

information contained in the thermal contrast maps into decision indices that help identifying targets with precision and reduce false alarms.

7 Conclusion

A three-dimensional finite volume simulation tool for the prediction of buried landmines in dry soil has been developed. The numerical model was validated by comparison with published data and by experimentation. The model predicts the expected soil thermal signatures evolving due to the presence of buried objects. The generated numerical results match with high accuracy the experimentally generated IR images of the soil surface when subjected to heating and cooling. The key element in matching experimental and numerical images stems from the consideration of the change in thermal conductivity of the soil from surface and shallow surface values to higher value at more depth. The thermographic analysis of the model and IR images will further be developed to produce additional information that can help in classifying the detected objects.

Acknowledgment

The authors acknowledge the support of the Lebanese National Council for Scientific Research Grant No. LCR-11304-002208. In addition, the authors would like to acknowledge the support of Youssef Jameel Grant for acquisition of the IR camera, sensors, and support to graduate students. The environmental chamber lab facility is supported by the American School and Hospital Aid (ASHA) Grant No. AUB-FEA-793. The help of the research engineer, Samir Berjaoui in performing the sensitivity analysis, calibrating the sensors, and conducting the experiments is highly appreciated.

Nomenclature

$a_P, ..$ = coefficients in the discretized equation
b_P = source term in the discretized equation
k = thermal conductivity (W/m K)
urf = under-relaxation factor
$\mathbf{S}_f$ = surface vector
t = time (s)
T = temperature (°C)
$\mathbf{n}$ = outward unit vector normal to cell face
$\mathbf{d}_{PF}$ = vector joining the grid point P and F
$\mathbf{E}$ = vector collinear with $\mathbf{d}_{PF}$
$\mathbf{T}$ = vector equals to $\mathbf{S}-\mathbf{E}$
C = specific heat (J/kg K)
V = volume of control cell
h = heat transfer coefficient (W/m^2 K)
A = surface area of soil (m^2)
q = heat flux (W/m^2)
x,y,z = rectangular coordinate system

Greek Symbols

ρ = density (kg/m^3)
Δt = time step (s).
σ = Stefan-Boltzmann constant ($W/m^2 K^4$).
ε = emissivity.

Subscripts

f = refers to control volume face f
P = refers to the P grid point
F = refers to the neighbor of the P grid point
∞ = refers to ambient conditions
s = refers to soil
m = refers to mine
net = refers to net heat flux at soil surface
conv = refers to convection heat flux at soil surface
rhs = refers to incident radiation heat flux on soil surface
emis = refers to emitted heat flux from soil surface
NB = refers to the neighbors of the P grid point
nb = refers to faces surrounding the P grid point

Superscripts

o = refers to values from previous time step
n = refers to values from previous iteration
t = refers to transient contribution
D = refers to diffusion contribution

References

[1] Lopez, P., Sahli, H., Vilarino, D. L., and Cabello, D., 2003, "A Target Identification Procedure for the Detection and Classification of Landmines from IR images," *Proceedings of EUDEM2-SCOT-2003: International Conference on Requirements and Technologies for the Detection, Removal, and Neutralization of Landmines and UXO*, September 15–18, Brussels, Belgium, **5046**, pp. 242–252.
[2] Simard, J. R., 1996, "Improved Landmine Detection Capability (ILDC): Systematic Approach to the Detection of Buried Mines Using IR Imaging," Proc. SPIE, **2765**, pp. 489–500.
[3] Simard, J. R., 1997, "Theoretical and Experimental Characterizations of the IR Technology for the Detection of Low-Metal and Nonmetallic Buried Landmines," Centre de Recherches pour la Defense Valcartier, Quebec.
[4] Russell, K. L., McFee, J. E., and Sirovyak, W., 1996, "Remote Performance Prediction for Infra-Red Imaging of Buried Mines," Proc. SPIE, **2933**, pp. 762–769.
[5] Agrawal, S., Sriram, P., and Mitchell, R., 2001, "Algorithms for IR Imagery Based Airborne Landmine and Minefield Detection," Proc. SPIE, Remediation Technologies for Mines and Minelike Targets VI, **4394**, pp. 284–295.
[6] Ngan, P., 1995, "Development of Automatic Target Recognition for Infra-Red Sensor-Based Close Range Land Mine Detector," Proc. SPIE, **2496**, pp. 881–889.
[7] Bruschini, C., and Gros, B., 1998, "A Survey of Current Sensor Technology

Research for the Detection of Landmines," *Sustainable Humanitarian Demining: Trends*, Mid Valley Press, Verona, VA, pp. 314–325.
[8] Deans, J., Schmithalis, G., and Carter, L. J., 2001, "An Analysis of a Thermal Imaging Method for Landmine Detection Using Microwave Heating," J. Appl. Geophys., **47**, pp. 334–352.
[9] Hermann, J., and Ian, C., 1999, "Microwave Enhancement of Thermal Landmine Signatures," Proc. SPIE, **3710**, Part I, pp. 154–166.
[10] Mitchell, R., Srinivasa, S., and Agarwal, S., 1999, "Detection of Antipersonnel Landmines Based on Waterjet Induced Thermal Images," Proc. SPIE, **3710**, Part I, pp. 180–188.
[11] Depak, M., Agarwal, S., Ritech, G., and Swonger, C. W., 2004, "False-Alarm Mitigation and Feature-Based Discrimination for Airborne Mine Detection," Proc. SPIE, **5415**, pp. 1163–1173.
[12] Khanafer, K., and Vafai, K., 2002, "Thermal Analysis of Buried Land Mines over a Diurnal Cycle," IEEE Trans. Geosci. Remote Sens., **40**(2), pp. 461–473.
[13] Khanafer, K., Vafai, K., and Baertlein, B. A., 2003, "Effects of Thin Metal Outer Case and Top Air Gap on Thermal IR Images of Buried Antitank and Antipersonnel Land Mines," IEEE Trans. Geosci. Remote Sens., **41**(1), pp. 123–135.
[14] Lopez, P., Sahli, H., Vilarino, D. L., and Cabello, D., 2003, "Detection of Perturbations in Thermal IR Signatures: An Inverse Problem for Buried Land Mine Detection," *Proceedings of EUDEM2-SCOT-2003: International Conference on Requirements and Technologies for the Detection, Removal, and Neutralization of Landmines and UXO*, September 15–18, Brussels, Belgium, **1**, pp. 385–392.
[15] Sendur, I. K., and Baertlein, B. A., 2000, "Numerical Simulation of Thermal Signatures of Buried Mines Over a Diurnal Cycle," Proc. SPIE, Detection and Remediation Technologies for Mines and Minelike Targets V, **4038**, pp. 156–167.
[16] Patankar, S. V., 1980, *Numerical Heat Transfer and Fluid Flow*, Hemisphere Publishing, New York.
[17] Gordon, W. J., and Theil, L. C., 1982, "Transfinite Mappings and Their Applications to Grid Generation," J. F. Thopmson ed., *Numerical Grid Generation*, North Holland, New York, pp. 171–192.
[18] ISO 8301, 1991, Thermal Insulation, Determination of Steady-State Thermal Resistance and Related Properties," Heat Flow Meter Apparatus.
[19] Software 2004 "ThermaCamTM Researches Pro 2.8, Copyright©1997-2004, FLIR Systems AB.

Journal of Heat Transfer

Technical Briefs

Natural Convection From a Square Disk in the Intermediate Rayleigh Range

Arnout Willockx
Department of Fluid, Heat and Combustion Mechanics,
Ghent University-UGent,
Sint-Pietersnieuwstraat 41, 9000,
Ghent, Belgium
e-mail: arnout.willockx@ugent.be

Gilbert De Mey
Department of Electronic and Information Systems,
Ghent University-UGent,
Sint-Pietersnieuwstraat 41, 9000,
Ghent, Belgium

Christophe T'Joen

Hendrik-Jan Steeman

Michel De Paepe

Department of Fluid, Heat and Combustion Mechanics,
Ghent University-UGent,
Sint-Pietersnieuwstraat 41, 9000,
Ghent, Belgium

This technical brief reports on an experiment in which Ra is varied in an intermediate range. It is an interesting range because the values lie in a transition zone between laminar thin boundary layer dominated and conduction dominated natural convection. The experimental data are compared with existing correlations to check the accuracy and validity of these correlations for this transitional range of Ra. A new correlation that is only valid in this transitional zone is also proposed and compared with correlations of the same kind. [DOI: 10.1115/1.2190693]

Keywords: natural convection, square disk, transitional Rayleigh number

1 Introduction

Natural convection is found in many engineering applications. Natural convection from a heated object is particularly of interest for the cooling of electronic components. There are a lot of publications on natural convection from isothermal bodies [1–7]. Mainly, the goal in these studies is to develop correlations between the dimensionless Rayleigh number (Ra) and Nusselt number (Nu). Most of these studies propose a general correlation for natural convection from a body. These correlations vary from each other in different ways for a specific body: choice of the characteristic length L_{ref} [2,4,8], and the range of Ra for which they are valid (low Ra, laminar Ra, turbulent Ra or multiple ranges) [1,3–5]. The correlations are obtained from experiments. A common technique to obtain a wide range of Ra is varying the pressure and the temperature difference between body and ambient air [1,2]. In other experiments only the temperature difference is changed, but then only a small range of Ra is attained [3].

The correlation for laminar Ra can be derived analytically from the boundary layer equations for free convection [9] and is of the general form

$$\mathrm{Nu} = C_1(\mathrm{Pr}) \cdot \mathrm{Ra}^{1/4} \quad \text{for } 10^6 < \mathrm{Ra} < 10^8 \tag{1}$$

Equation (1) is invalid for high Ra ($\mathrm{Ra} > 10^8$) due to turbulent effects and the exponent becomes $1/3$ for fully turbulent regime. In between the turbulent and the laminar regime there is a transition zone. In this transition zone, the exponent changes from $1/4$ to $1/3$.

The exponent of $1/4$ also becomes incorrect for $\mathrm{Ra} < 10^6$. For $\mathrm{Ra} \to 0$, Nu is not zero but has a finite value because the boundary layer becomes too thick and conductive effects occur. The influence of this conductive effect becomes significant for $\mathrm{Ra} < 10^6$.

Therefore, correlations that are valid for a wide range of Ra have to be of another form than Eq. (1). For both small and laminar Ra numbers ($\mathrm{Ra} < 10^8$), two types of correlations exist

$$\mathrm{Nu} = C_2 + C_1(\mathrm{Pr}) \cdot \mathrm{Ra}^{1/4} \tag{2}$$

$$\mathrm{Nu} = [C_2^n + (C_1(\mathrm{Pr}) \cdot \mathrm{Ra}^{1/4})^n]^{1/n} \tag{3}$$

C_2 is the pure conduction limit at $\mathrm{Ra} = 0$ and the second term is the laminar boundary layer validity limit (cf. Eq. (1)). Both equations are certainly valid in the extreme cases of pure conduction and pure laminar natural convection. However, the question arises whether they also accurately describe natural convection in the transition zone. Equation (3) is an asymptotical correlation: it is an asymptotic approach of both modes and normally is more accurate in the transition zone. It is the objective of this technical brief to check the accuracy in the transitional zone of correlations developed for a wide range of Ra of the form of Eqs. (2) and (3). Also the value of the exponent of Ra is analyzed for equations of the form of Eq. (1) for the transitional zone.

Contributed by the Heat Transfer Division of ASME for publication in the JOURNAL OF HEAT TRANSFER. Manuscript received February 9, 2005; final manuscript received September 8, 2005. Review conducted by: Jay M. Khodadadi.

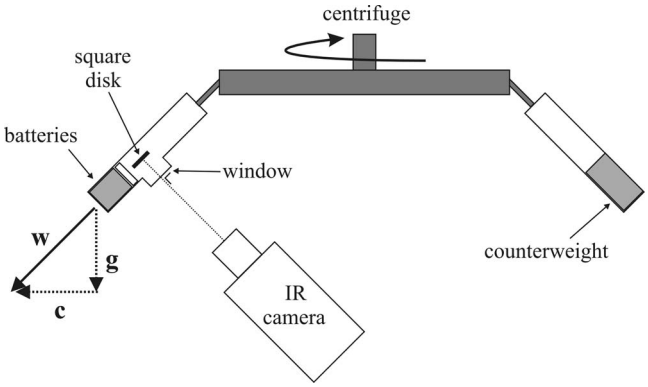

Fig. 1 Experimental setup

2 Experiment

The originality of the experiment lies in the fact that Ra is changed in another way than varying the pressure or the temperature difference. Since Ra is also determined by the gravitational acceleration g, it is also possible to vary Ra by varying the acceleration in a test section. A variable acceleration was realized with a centrifuge. A cylindrical enclosure hangs from an arm of the centrifuge. The acceleration inside the cylinder changes by rotating the centrifuge and the acceleration is directly determined by the rotational speed of the centrifuge. A resistor in the shape of a vertical square disk was put inside the cylinder. The properties of the square disk are an aspect ratio $L/D=0.03$ and a length of $L=0.0255$ m. The resistor dissipates power from batteries which are also placed inside the cylinder. The test section was separated from the batteries with an insulating layer. A sketch of the experimental setup is given in Fig. 1.

The power dissipated in the disk is transferred to the environment by natural convection, radiation, and conduction. The surface temperature of the disk is measured with a thermographic camera and the ambient temperature inside the cylinder with a thermocouple. Radiation and conduction are calculated from the measurements. Radiation was calculated with an accurate method keeping into account the transparency of the CaF_2 window (95%) and the emissivities of the disk, container, and window. The calculation was based on the method described in [10]. The conduction through the wires connecting the batteries with the disk is calculated with the one-dimensional conduction equation. The heat transferred by natural convection is then the dissipated power in the disk minus the heat transferred by radiation and conduction. This way the relation between Nu and Ra can be calculated [11]. The amount of radiative heat transfer and natural convection are of the same order of magnitude. A detailed description of the experiment and the measurement and calculation method is given in [11].

3 Results

The acceleration inside the cylinder can be varied from 9.81 to 53 m/s^2. The mean surface temperature of the disk varies from 84 to 72°C. The experimental data are plotted in a Nu-Ra graph for two characteristic lengths L_{ref}: the length of the disk L [8] and the square root of the surface area of the disk $\sqrt{A}$ [4] (Fig. 2). The values of Ra lie within a range of 1 decade (Fig. 2 and Eqs. (4) and (5))

A Nu-Ra correlation can be proposed from these experimental data for both characteristic lengths. Due to the small range of available data, only a correlation of the form $Nu=CRa^n$ is significant. This means that the correlation is only with certainty valid in the range of Ra of the experimental data. This gives the following correlations for both characteristic lengths

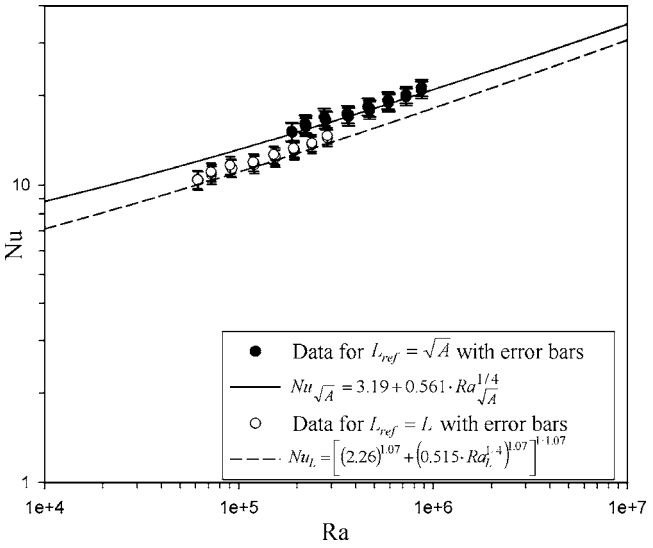

Fig. 2 Comparison between correlation of Yovanovich (Eq. (6)), asymptotic correlation (Eq. (7)) and the experimental data with error bars

$$\mathrm{Nu}_{\sqrt{A}}=1.314\mathrm{Ra}_{\sqrt{A}}^{0.202} \quad 10^5<\mathrm{Ra}_{\sqrt{A}}<10^6 \tag{4}$$

$$\mathrm{Nu}_L=1.134\mathrm{Ra}_L^{0.202} \quad 6\times10^4<\mathrm{Ra}_L<3\times10^5 \tag{5}$$

For both cases, the exponent $n=0.202$ is found, but another coefficient C was found. The exponent $n=0.202$ is smaller than 0.25. An error calculation gave a maximum error of 0.029 on the exponent n, so 0.25 is not in the error margin. This confirms that the experimental data lie in the transitional zone, which is the range of interest for this brief. So it is not necessary to have an experiment that attains higher Ra.

4 Discussion

4.1 Correlations for a Wide Range of Ra. The experimental data are compared with existing correlations for natural convection from a vertical square disk. This comparison gives information about the extent of accuracy of these correlations for the transitional zone. Two correlations are discussed. These correlations are developed for isothermal bodies. The thermographic images of the disk in the experiment show that it is not completely isothermal. The maximum difference between the highest temperature at the center of the disk and the lowest temperatures at the edges of the disk is 12% (if the difference is divided by the mean temperature). This can probably cause a small aberration, but generally a good estimation is expected for a near isothermal body by using correlations for isothermal bodies.

4.1.1 Correlation of Yovanovich. Yovanovich [4,7] uses $\sqrt{A}$ as characteristic length. He proposes a correlation of the form of Eq. (2). For a square disk it is

$$\mathrm{Nu}_{\sqrt{A}}=3.19+0.561\cdot\mathrm{Ra}_{\sqrt{A}}^{1/4} \tag{6}$$

Both constants in Eq. (6) depend on the shape and orientation of the disk and 0.561 depends also on the Prandtl number. This correlation is valid for all $\mathrm{Ra}<10^8$, thus not for turbulent Ra.

To make a comparison, both experimental data and Eq. (6) are plotted in Fig. 2. It seems that the equation of Yovanovich underestimates Nu and thus natural convection a bit. However, the largest deviation for Nu is 5.2%. The average deviation is 2.2%. If the error on the measurement data is taken into account, this error margin is always larger than the largest deviation (Fig. 2). The correlation of Yovanovich gives a very accurate prediction for the

experiment and as a result it is valid for the case of a small rectangular square disk in the transitional range of $10^5 < \mathrm{Ra}_{\sqrt{A}} < 10^6$.

4.1.2 Asymptotic Correlation. Most correlations for natural convection from bodies are of an asymptotical form like Eq. (3). The length L of the disk is used as characteristic length. The available values of thickness-to-length ratio in literature for which the constants are defined are 0 and 0.1 and higher. The aspect ratio of the disk of 0.03 is closer to zero than to 0.1. The following equation is given in [8] for an aspect ratio of 0

$$\mathrm{Nu}_L = [(2.26)^{1.07} + (0.515 \cdot \mathrm{Ra}_L^{1/4})^{1.07}]^{1/1.07} \quad (7)$$

The correlation for an aspect ratio of 0 is based on the approximate method of Raithby-Hollands [12]. The value 1.07 for the exponent was recommended by Hassani and Hollands [2]. Both experimental data and Eq. (7) are plotted in Fig. 2. The largest deviation is 7.2% and the average 4.4%. The error margin on the experimental data is also calculated and shown in Fig. 2. The predicted values of Nu with Eq. (7) lie within this error margin. Actually this is for a disk with a thickness to length ratio of 0, so very thin disks like a piece of paper. The disk used in the experiment has a ratio of 0.03. Interpolation between the correlations for a ratio of 0 and 0.1 increases the largest deviation with 1% for the ratio of 0.03, but it still lies within the error margins. So this correlation seems less accurate than that of Yovanovich, but nevertheless also predicts the experiment well. Thus the asymptotic correlation is also valid in the transitional range of $6 \cdot 10^4 < \mathrm{Ra}_L < 3 \cdot 10^5$.

4.2 Discussion on Exponent n of $\mathrm{Nu} = C \cdot \mathrm{Ra}^n$. Kobus and Wedekind [3] proposed a correlation for natural convection from a vertical circular disk. Nevertheless, their research is interesting, because they also performed experiments in the transitional zone ($2 \times 10^2 < \mathrm{Ra} < 4 \times 10^4$). They attained smaller Ra and a larger range of Ra (2 decades) than our experiment. Their correlation has the form of Eq. (1) but the exponent for Ra is not 1/4 but had to be determined from the data

$$\mathrm{Nu} = 1.759(\mathrm{Ra})^{0.15} \quad (8)$$

The exponent for Ra is smaller than 1/4, namely 0.15. In our correlations (Eqs. (4) and (5)) the exponent was 0.202. Yovanovich [4] also reported a correlation of Sparrow and Ansari [6] for a vertical cylinder. They used the diameter D of the cylinder as characteristic length. Yovanovich recalculated their calculation for $\sqrt{A}$ as characteristic length. The two correlations are:

$$\mathrm{Nu}_{\sqrt{A}} = 1.037\mathrm{Ra}_{\sqrt{A}}^{0.208} \quad 1.4 \times 10^5 < \mathrm{Ra}_{\sqrt{A}} < 1.3 \times 10^6 \quad (9)$$

$$\mathrm{Nu}_D = 0.775\mathrm{Ra}_D^{0.208} \quad 1.4 \times 10^4 < \mathrm{Ra}_D < 1.3 \times 10^5 \quad (10)$$

These correlations are similar to our correlations (4) and (5) and are valid for almost the same range of Ra. The exponent of Ra is as good as the same for both correlations (0.208 lies within error margin of 0.202 ± 0.029). So an exponent of 0.2 seems acceptable for $10^5 < \mathrm{Ra}_{\sqrt{A}} < 10^6$. The coefficients of Ra depend on shape, dimensions and orientation of the body, so they are different for Eqs. (9), (10), (4), and (5). Nevertheless, Sparrow and Ansari's correlation confirms our correlations (4) and (5) and an exponent smaller than 0.25. Kobus and Wedekind [3] found an exponent of 0.15, because their experiments were executed at even lower Ra. This confirms the decrease of the exponent n for decreasing Ra in the zone $0 < \mathrm{Ra} < 10^6$.

This can be explained as follows. Once $\mathrm{Ra} < 10^6$, the conductive effect has more influence on the heat transfer, while the influence of pure natural convection diminishes for decreasing Ra. This causes the exponent of Ra to decrease gradually with Ra for equations of the form $\mathrm{Nu} = C\mathrm{Ra}^n$. When $\mathrm{Ra} \to 0$ there is only conduction and $n = 0$, thus $\mathrm{Nu} = \mathrm{Cte}$. This gradual decrease of the exponent n causes a bend in the curve that represents natural convection in a Nu-$\mathrm{Ra}^{1/4}$ graph. In the range $10^6 < \mathrm{Ra} < 10^8$ the curve is linear. Once $\mathrm{Ra} < 10^6$, the curve begins to bend upwards to the value of pure conduction (C_2 in Eqs. (2) and (3)). Because the exponent of Ra will decrease with decreasing Ra, correlations of the form $\mathrm{Nu} = C\mathrm{Ra}^n$ will only be valid in a narrow range of Ra in the transitional zone. Correlations valid for a wider range of Ra have to be of the form of Eq. (2) or Eq. (3). So correlation (8) of Kobus and Wedekind can only be valid with certainty in the range of the experimental Ra ($2 \times 10^2 < \mathrm{Ra} < 4 \times 10^4$). To extend the validity of the correlation to lower and higher Ra, extra experimental data are needed. However, Kobus and Wedekind [3] assume that their correlation is also valid for higher Ra. Therefore they compare it with data from Hassani and Hollands [2] for higher Ra. They state that their correlation (Eq. (8)) under predicts Nu a bit and that more experiments need to be done to detect the precise limits of the correlation. The authors state that their correlation could be valid up to $\mathrm{Ra} = 10^5$ but not further, because then the influence of the laminar boundary layer becomes bigger. This asks for a larger exponent n. This is shown in Eqs. (4), (5), (9), and (10). These correlations are for a square disk and a vertical cylinder and not a circular disk, nevertheless this has probably not too much influence on the exponent n. So their assumption that the correlation can be extrapolated to other Ra needs to be nuanced, because it can be only a very small extrapolation or maybe it cannot even be extrapolated.

This exponent is only valid till a certain Ra where turbulent effects start to occur ($\mathrm{Ra} \approx 10^8$). A same transitional zone is expected between the laminar boundary layer assumption zone and the fully turbulent zone. Then the exponent changes from 0.25 to 0.33.

5 Conclusion

An experiment was executed to obtain values of Ra for free convection from a square disk that lie in a transition zone between laminar boundary layer dominated and conduction dominated free convection.

The measurements confirm that the general correlation of Yovanovich [4,7] and the asymptotic correlation are accurate for these transitional values of Ra. Thus correlations of the simple form: $\mathrm{Nu} = C_2 + C_1(\mathrm{Pr}) \cdot \mathrm{Ra}^{1/4}$ are as accurate as asymptotic correlations: $\mathrm{Nu} = [C_2^n + (C_1(\mathrm{Pr}) \cdot \mathrm{Ra}^{1/4})^n]^{1/n}$ for the whole range of laminar Ra, even in the transition area as shown by the experiment.

It is explained why extrapolation of a correlation of the form $\mathrm{Nu} = C\mathrm{Ra}^n$ is not allowed in the transitional zone and how the exponent n varies in the transitional zone.

Acknowledgment

This research was funded by Ghent University-Ugent BOF/GOA 12051299.

Nomenclature

a = thermal diffusivity (m^2/s)
$C_1(\mathrm{Pr})$ = correlation coefficient dependent of Pr
C_2 = correlation coefficient
g = gravity acceleration (=9.81 m/s^2)
L_{ref} = characteristic length: either $\sqrt{A}$ or L (m)
n = correlation coefficient
Nu = average Nusselt number: $\mathrm{Nu} = h \cdot L_{\mathrm{ref}}/\lambda$
Pr = Prandtl number
Ra = average Rayleigh number: $\mathrm{Ra} = g \cdot \beta \cdot (T_w - T_a) \cdot L_{\mathrm{ref}}^3 / \nu \cdot a$
T_w = temperature of the resistor (K)
T_a = ambient temperature in the cylinder (K)

Greek Symbols

β = thermal expansion coefficient (1/K)
υ = kinematical viscosity (m^2/s)

Subscripts

$\sqrt{A}$ = characteristic length = square root of the surface area of the square disk (m)

L = characteristic length = length of the square disk (m)

References

[1] Chamberlain, M. J., Hollands, K. G. T., and Raithby, G. D., 1985, "Experiments and Theory on Natural Convection Heat Transfer From Bodies of Complex Shape," ASME J. Heat Transfer, **107**, pp. 624–629.

[2] Hassani, A. V., and Hollands, K. G. T., 1989, "On Natural Convection Heat Transfer From Three-Dimensional Bodies of Arbitrary Shape," ASME J. Heat Transfer, **111**, pp. 363–371

[3] Kobus, C. J., and Wedekind, G. L., 1995, "An Experimental Investigation Into Forced, Natural and Combined Forced and Natural Convective Heat Transfer From Stationary Isothermal Circular Disks," Int. J. Heat Mass Transfer, **38**(18), pp. 3329–3339.

[4] Yovanovich, M. M., 1987, "On the Effect of Shape, Aspect Ratio and Orientation Upon Natural Convection From Isothermal Bodies of Complex Shape," HTD (Am. Soc. Mech. Eng.), **82**, pp. 121–129.

[5] Hassani, A. V., and Hollands, K. G. T., 1989, "Prandtl Number Effect on External Natural Convection Heat Transfer From Irregular Three-dimensional Bodies," Int. J. Heat Mass Transfer, **32**(11), pp. 2075–2080.

[6] Sparrow, E. M., and Ansari, M. A., 1983, "A Refutation of King's Rule for Multidimensional External Natural Convection," Int. J. Heat Mass Transfer, **26**(9), pp. 1357–1364.

[7] Yovanovich, M. M., and Jafarpur, K., 1993, "Bounds on Laminar Natural Convection From Isothermal Disks and Infinite Plates of Arbitrary Shape for All Orientations and Prandtl Numbers," HTD (Am. Soc. Mech. Eng.), **264**, pp. 93–110.

[8] Rohsenow, M. W., Hartnett, J. P., and Cho, Y. I., 1998, *Handbook of Heat Transfer*, McGraw–Hill, New York, Chap. 4, pp. 4.25–4.32.

[9] Kays, W. M., and Crawford, M. E., 1993, *Convective Heat and Mass Transfer*, McGraw-Hill, New York, Chap. 17.

[10] Siegel, R., and Howell, J. R., 1992, *Thermal Radiation Heat Transfer*, 3rd ed., Hemisphere, Bristol, UK, Chap. 7, pp. 263–272 and 936–939.

[11] Willockx, A., Steeman, H., De Mey, G., and De Paepe, M., 2005, "Analysis of Natural Convection and Radiation by Using Thermography," 14th International Conference on Thermal Engineering and Thermogrammetry, June 22–24, Budapest, Hungary.

[12] Rohsenow, M. W., Hartnett, J. P., and Ganiç, E. N., 1985, *Handbook of Heat Transfer*, McGraw–Hill, New York, Chap. 6, pp. 6.9–6.16.

Least-Squares Finite Element Analysis for Transient Radiative Transfer in Absorbing and Scattering Media

W. An

L. M. Ruan
e-mail: ruanlm@hit.edu.on

H. P. Tan

H. Qi

School of Energy Science and Engineering,
Harbin Institute of Technology,
150001 Harbin, People's Republic of China

In some radiative transfer processes, the time scales are usually on the order of 10^{-9}–10^{-15} s, *so the transient effect of radiation should be considered. In present research, a finite element model, which is based on the discrete ordinates method and least-squares variational principle, is developed to simulate the transient radiative transfer in absorbing and scattering media. The numerical formulations and detailed steps are given. Moreover, two transient radiative transfer problems are investigated and the results are compared with those by integral method and finite volume method. It indicates that the present model can simulate the transient radiative transfer effectively and accurately.*
[DOI: 10.1115/1.2190694]

Keywords: transient radiative transfer, finite element, absorbing and scattering media, microscale, non-intrusive diagnostics

1 Introduction

In most of the radiative transfer studies, the temporal variation of radiative signal is not considered since the time scale of radiative transport is far smaller than the time scales of the observable properties. For these applications, radiative transfer can be taken as steady-state process. The transient term of radiative transfer equation (RTE) can be neglected. However, recent research on the propagation of ultrashort light pulse inside the absorbing and scattering media has led to some interesting applications such as material properties diagnostics, optical imaging, laser therapy, particle detection and sizing, remote sensing, etc. For these emerging applications, the transient effect of radiation should be considered, because the time scales of such processes are usually on the order of 10^{-9}–10^{-15} s. In these applications, the variation of radiative signals with time always needs be precisely computed. As pointed out by Tan [1], the accurate forward calculation is essentially important for inverse analysis and estimates. Therefore, the consideration of the transient term in the radiation transport equation is necessary. Besides these emerging technologies, in astrophysical radiation hydrodynamics, a better model of the transient radiative transport is also needed [2]. Over the past five years, transient radiative transfer in participating media has received considerable attention. Several numerical strategies have been developed, which include discrete ordinate method (DOM) [3,4], finite volume method (FVM) [5,6], integral equation (IE) models [1,7], and Monte Carlo method [8]. However, little information about finite element method (FEM) for transient radiative transfer was reported.

As a numerical method, finite element method has become a sophisticated technology in mechanics and thermal analyses. It has many advantages over other methods. For complex geometric shape, it shows considerable flexibility. Its complication does not increase with the complexity of geometric shape and boundary conditions. Besides, the approximation for the field variables in a volume or surface element can vary across the element, and the variation of field variables in the FEM can be specified to increase degrees of approximation. Therefore, the FEM of radiation heat transfer has been investigated by many researchers.

Early FEM for radiative transfer is based on integral form of RTE, as in the case of Burns [9], who developed a FEM to simulate radiative heat transfer in multidimensional media with nongray, non-homogeneous radiative properties. Furmanski and Bannaszek [10] studied the coupled conduction and radiation heat transfer in a semitransparent medium by FEM. Their finite element models need the complex integration and geometrical computation which may require too much calculation in multidimensional problems. Furthermore, it is difficult to deal with anisotropic scattering and obstacles in the media by their methods. Very recently, standard Galerkin finite element method (GFEM) has been developed and integrated with DOM to simulate the radiation transfer by Liu [11]. This model can solve anisotropic scattering conveniently and needs no complex integration and visibility judgment. The accuracy of this model in absorbing and anisotropic scattering media is investigated by An et al. [12]. The least-squares finite element method (LSFEM) [13] and discontinue finite element method [14] also are presented to simulate the radiative transfer. However, all of these finite element methods are used to simulate the steady radiative heat transfer. Further research should be devoted in the transient radiative transfer due to the hyperbolic wave equation coupled with the in-scattering integral term. As Tan [1] suggested, the simulation of transient radiative transfer is an important approach to verify the reliability of the model from the perspective of numerical simulation. For the model with considerable accuracy in steady simulation, some difficulties such as stability and unrealistic oscillation may be identified in transient simulation. It follows that, the objective of the present study is to verify the accuracy and stability of LSFEM for transient radiative transfer.

Due to hyperbolic wave characteristic of the transient radiative transfer equation (TRTE), the numerical computation based on GFEM has an unstable behavior leading to unrealistic oscillations for advection-dominated problems. To eliminate the unrealistic oscillations, some numerical techniques have been developed in the past decades. The successful representations in these numerical techniques are the Petrov-Galerkin method [15], Taylor-Galerkin method [16], and least-squares method [17]. The Taylor-Galerkin and Petrov-Galerkin method provide much stabilized numerical solutions by generating numerical diffusion, which is an artificial diffusion as an inherent upwind damping. But for the Petrov-Galerkin method, particularly the Streamline Upwind Petrov-Galerkin method [15], there is at least one free parameter to be tuned. The Taylor-Galerkin method is implemented by using a Taylor series for time discretization before applying space discretization. The high order derivatives of temporal variable need to be deduced and introduced into the discrete equation. Accordingly, the Taylor-Galerkin method is relatively complicated.

The reason for the success of the LSFEM for fluid flows and heat transfer problems can be justified as follows: in the first place, unlike the standard Galerkin and Petrov-Galerkin method, LSFEM leads to symmetric, positive-definite matrix systems for advection-dominating transfer equations. Only half of a sparse

Contributed by the Heat Transfer Division of ASME for publication in the JOURNAL OF HEAT TRANSFER. Manuscript received June 19, 2005; final manuscript received October 7, 2005. Review conducted by Walter W. Yuen.

matrix needs to be stored. Some highly-efficient matrix solvers such as the preconditioned conjugate gradient method, and the Cholesky decomposition method can be successfully used. Whereas the Galerkin or Petrov-Galerkin method results in a large, sparse and non-symmetric matrix system which requires a robust iterative solver and a prohibitive amount of memory storage and computing time for multidimensional problems. Further, there is no free parameter to be tuned in the LSFEM. The LSFEM can be applied in a straightforward manner, much in the same way as the Galerkin finite element method. The program for LSFEM can be realized by very little modification in the program of standard Galerkin finite element method. Compared with the Petrov-Galerkin method in which the tuning parameter may be different for high order interpolation element, in the LSFEM, higher order interpolation element without any modification for the weight function is used, which is more efficient and accurate for transient radiative simulation. Donea and Quartapelle [18] studied the convergence of LSFEM in the convection dominated transport problems compared with that of other FEMs.

As a pioneering and creative research, LSFEM is applied to analyze the one-dimensional (1D) steady radiative transfer problem by Pontaza and Reddy [13]. The space-angle coupled and decoupled least-squares finite element models were proposed to simulate the radiative transfer in one-dimensional absorbing and scattering media in the literature. However, the space-angle coupled model is difficult to extend to a multidimensional problem. Therefore, the present paper employs a space-angle decoupled model and extends this model to transient radiative transfer simulation in one-dimensional and two-dimensional (2D) participating media. In the following section of the present paper, the mathematic formulation and numerical process of LSFEM are proposed and two transient radiative transfer cases are simulated. The results produced by the present model are compared with those by IE and FVM, and the efficiency and accuracy of our model is verified.

2 Mathematic Formulation

2.1 Radiative Transfer Equation. For the participating media, the transient radiative transfer equation (TRTE) in the Cartesian coordinate system can be written as

$$\frac{\partial \mathbf{I}(\mathbf{r},\boldsymbol{\Omega},t)}{C\partial t}+\frac{\partial \mathbf{I}(\mathbf{r},\boldsymbol{\Omega},t)}{\partial s}=-(\boldsymbol{\kappa}_a+\boldsymbol{\sigma}_s)\mathbf{I}(\mathbf{r},\boldsymbol{\Omega},t)+\kappa_a\mathbf{I}_b(\mathbf{r},t)+\frac{\boldsymbol{\sigma}_s}{4\boldsymbol{\pi}}\int_{\boldsymbol{\Omega}'=4\boldsymbol{\pi}}\mathbf{I}(\mathbf{r},\boldsymbol{\Omega}',t)\Phi(\boldsymbol{\Omega}',\boldsymbol{\Omega})d\boldsymbol{\Omega}' \tag{1}$$

where $\mathbf{I}(\mathbf{r},\boldsymbol{\Omega},t)$ is radiative intensity, which is a function of position $\mathbf{r}$, direction $\boldsymbol{\Omega}$ and time t; $\mathbf{I}_b(\mathbf{r},t)$ is the blackbody radiative intensity of media, C is propagation speed of radiation transport in the medium, $\boldsymbol{\kappa}_a$ and $\boldsymbol{\sigma}_s$ are the absorption and scattering coefficient, respectively. The $\boldsymbol{\Phi}(\boldsymbol{\Omega}',\boldsymbol{\Omega})$ is the scattering phase function between incoming direction $\boldsymbol{\Omega}'$ and scattering direction $\boldsymbol{\Omega}$. The term on left side of the equation represents the gradient of radiative intensity in the direction $\boldsymbol{\Omega}$. The three terms on right side of equation represent the change in intensity due to absorption and outgoing scattering, emission and incoming scattering, respectively. When considered the gray and diffuse reflection boundary, the radiative boundary condition can be written as following form

$$\mathbf{I}(\mathbf{r}_w,\boldsymbol{\Omega},t)=\boldsymbol{\varepsilon}_w\mathbf{I}_b(\mathbf{r}_w,t)+\frac{1-\boldsymbol{\varepsilon}_w}{\boldsymbol{\pi}}\int_{n\cdot\Omega'<0}\mathbf{I}(\mathbf{r}_w,\boldsymbol{\Omega}',t)\times|\mathbf{n}\cdot\boldsymbol{\Omega}'|d\boldsymbol{\Omega}'\quad(\mathbf{n}\cdot\boldsymbol{\Omega}>0) \tag{2}$$

where $\mathbf{I}(\mathbf{r}_w,\boldsymbol{\Omega},t)$ is the leaving intensity on the boundary, $\mathbf{I}(\mathbf{r}_w,\boldsymbol{\Omega}',t)$ is the arriving intensity on the boundary. The term $\boldsymbol{\varepsilon}_w$ is the wall emissivity; $\mathbf{n}$ is the unit normal vector on the wall. To solve the TRTE numerically, the angular dependence has to be removed first. Similar to the conventional DOM, the angular integration over 4π solid angles is replaced by summing up the function on the discrete, a finite number of ordinates directions. For specific ordinate direction $\mathbf{m}$, its direction cosines along the coordinates x, y, and z can be denoted as μ_m, η_m and ξ_m. Then, the TRTE of $\mathbf{m}$ direction can be written as

$$\frac{\partial I^m}{C\partial t}+\mu_m\frac{\partial I^m}{\partial x}+\eta_m\frac{\partial I^m}{\partial y}+\xi_m\frac{\partial I^m}{\partial z}=-(\kappa_a+\sigma_s)I^m+\kappa_a I_b+\frac{\sigma_s}{4\pi}\sum_{m'=1}^{M}I^{m'}\boldsymbol{\Phi}^{m'm}w_{m'} \tag{3}$$

where M is the number of discrete directions; the boundary conditions can be written as

$$I_w^m=\varepsilon_w I_{bw}+\frac{1-\varepsilon_w}{\pi}\sum_{|n_w\cdot s_{m'}|<0}I_w^{m'}|\mathbf{n}_w\cdot\mathbf{s}_{m'}|w_{m'} \tag{4}$$

where $\mathbf{s}_{m'}$, $w_{m'}$ are the unit vector and the solid angle associated with the direction $\mathbf{m}'$; $\mathbf{n}_w$ is the unit normal vector on the wall. If the following simplified coefficients are defined

$$B=\kappa_a+\sigma_s-\frac{\sigma_s}{4\pi}\Phi^{mm}w_m \tag{5a}$$

$$S=\kappa_a I_b+\frac{\sigma_s}{4\pi}\sum_{m'=1,m'\neq m}^{M}I^{m'}\Phi^{m'm}w_{m'} \tag{5b}$$

Then Eq. (3) can be simplified as the form

$$\frac{\partial I^m}{C\partial t}+\mu_m\frac{\partial I^m}{\partial x}+\eta_m\frac{\partial I^m}{\partial y}+\xi_m\frac{\partial I^m}{\partial z}+BI^m=S \tag{6}$$

Equation (6) is a hyperbolic partial difference equation about I^m which can be solved numerically by using finite difference method or finite volume method, certainly by using finite element method too. The weighted residual method applied to Eq. (6) provides

$$\int_V\left(\frac{\partial I^m}{C\partial t}+\mu_m\frac{\partial I^m}{\partial x}+\eta_m\frac{\partial I^m}{\partial y}+\xi_m\frac{\partial I^m}{\partial z}+BI^m-S\right)W_l dV=0 \tag{7}$$

where V is the domain of solution. For FEM, different weighting function W_l will lead to different finite element methods. The unknown variable I^m and its derivative can be written as

$$I^m=\sum_{l=1}^{N}I_l^m\varphi_l \tag{8}$$

$$\frac{\partial I^m}{\partial x_i}=\sum_{l=1}^{N}\frac{\partial\varphi_l}{\partial x_i}I_l^m\quad(x_i=x,y,z) \tag{9}$$

where I_l^m is the radiative intensity at the node l and φ_l is the shape function. For standard Galerkin finite element approach, the weight function W_l is equal to the shape function φ_l, whereas in the least-squares finite element approach, the weight function can be expressed as

$$W_l=\varphi_l+\theta\cdot\Delta t^*\left(\mu_m\frac{\partial\varphi_l}{\partial x}+\eta_m\frac{\partial\varphi_l}{\partial y}+\xi_m\frac{\partial\varphi_l}{\partial z}+B\varphi_l\right) \tag{10}$$

where θ is the factor of time difference; its value can be 1, 0.5, 2/3, or 0, which represent implicit (Backward-Euler), Crank-Nicolson, Galerkin, and explicit (Forward-Euler), respectively. The time step $\Delta t^*=C\cdot\Delta t$. For the triangle isoparametric element, the shape function φ_l $(l=i,j,k)$ can be written as a function of x,y

$$\varphi_i = \frac{1}{2A}[(x_j y_k - x_k y_j) + (y_j - y_k)x + (x_k - x_j)y] \tag{11}$$

where A is the area of triangle element, x_l and y_l $(l=i,j,k)$ are the values of coordinates of three nodes in the triangle element. The values of x_l and y_l $(l=i,j,k)$ in φ_i are variable by turning i, j, k.

The Eq. (7) can be rewritten in matrix form as

$$[K][I_{n+1}^m] = [K'][I_n^m] + [R] \tag{12}$$

with

$$[K] = \sum_e \int_e \left[\varphi_i + \theta \cdot \Delta t^* \left(\mu_m \frac{\partial \varphi_i}{\partial x} + \eta_m \frac{\partial \varphi_i}{\partial y} + \xi_m \frac{\partial \varphi_i}{\partial z} + B\varphi_i\right)\right] \times \left[\varphi_j + \theta \cdot \Delta t^* \left(\mu_m \frac{\partial \varphi_j}{\partial x} + \eta_m \frac{\partial \varphi_j}{\partial y} + \xi_m \frac{\partial \varphi_j}{\partial z} + B\varphi_j\right)\right] dxdydz \tag{13}$$

$$[K'] = \sum_e \int_e \left[\varphi_i - (1-\theta) \cdot \Delta t^* \left(\mu_m \frac{\partial \varphi_i}{\partial x} + \eta_m \frac{\partial \varphi_i}{\partial y} + \xi_m \frac{\partial \varphi_i}{\partial z} + B\varphi_i\right)\right] \times \left[\varphi_j + \theta \cdot \Delta t^* \left(\mu_m \frac{\partial \varphi_j}{\partial x} + \eta_m \frac{\partial \varphi_j}{\partial y} + \xi_m \frac{\partial \varphi_j}{\partial z} + B\varphi_j\right)\right] dxdydz \tag{14}$$

$$[R] = \sum_e \int_e \theta \cdot \Delta t^* (S_{n+1} + S_n)\varphi_i \times \left[\varphi_j + \theta \cdot \Delta t^* \left(\mu_m \frac{\partial \varphi_j}{\partial x} + \eta_m \frac{\partial \varphi_j}{\partial y} + \xi_m \frac{\partial \varphi_j}{\partial z} + B\varphi_j\right)\right] dxdydz \tag{15}$$

where $[K]$ is the stiffness matrix, $[R]$ is the right side term. I_{n+1}^m is the radiative intensity in m direction at the $n+1$ moment. It can be solved through the value of I_n^m. The stiffness matrix generated from the LSFEM is symmetric and positive definite (SPD), whereas that generated from the Galerkin finite element method is unsymmetric. Consequently, storing of the stiffness matrix for the LSFEM is very inexpensive and some fast, robust iterative solutions for SPD matrix systems can be employed. By solving the Eq. (12), the radiative intensity in **m** direction can be acquired. Similarly, we can write out the equations and obtain the radiative intensity in each discrete direction.

2.2 Discretization. The present method involves not only spatial discretization but also angular discretization. For spatial discretization, FEM is highly flexible. Spatial grid can be polygonal unstructured element, which is more convenient and easier to use than structured grid in the application of complex geometry.

The 4π angular domain at any spatial location is divided into a finite number of discrete, non-overlapping solid angle. Many angular discretization strategies have been developed in the last three decades. The Sn-type discretization and azimuthal discretization are two of the most widely used strategies. The former is always employed in the DOM and the latter is associated with the FVM. Theoretically, the Sn-type discretization is more rigorous than azimuthal discretization. The DOM adopts a numerical quadrature method to evaluate the solid angle integrals. These quadrature sets are constructed to be invariant under any 90 deg rotation and to satisfy a number of key moments of the radiative intensity. The FVM treats directional discretization by analytical integration. In our previous study, in spite of the numerical results predicted by these two directional discretization strategies, the results of Sn-type discretization are more accurate than that of azimuthal discretization. Hence, the Sn-type discretization is employed in the following numerical test. However, as pointed out by Raithby [19], the azimuthal discretization could be necessary in some radiative problem such as collimated radiation problem, because it allows the angular grid to be adapted to resolve sharp changes in the intensity with direction.

2.3 Solution Method. The spatial discretization and computational processes in each discrete direction are the same, and the radiative intensity in each direction is solved independently. The boundary condition expressed in Eq. (4) should be imposed upon Eq. (12) as the inflow boundary condition. Due to the dependence of both source terms and boundary conditions on the intensities, global iterations are necessary at each time step. At the outset, the source terms S in Eq. (5*b*) and irradiation should be computed by the initial intensity. Then the stiffness matrix K, K' and right hand term R in Eqs. (13)–(15) are computed. The matrix expressed in Eq. (12) is solved for each direction. At each time step, the computational results replace the previous ones and the iterative procedure will continue until the convergence is met. The processes above are repeated until the end time. The solver of the discretized equations is based on preconditioned conjugate gradients arithmetic.

3 Results and Discussion

Based on the above theories, a computer code is implemented. Two transient cases are used to evaluate the accuracy of our model. In these cases, the numerical solution was considered to be convergent when the relative error of radiative intensity is less than 0.01%. All computation is realized in a PC with AMD2100 +CPU. The grid-independent checks for all results have already been verified in our research.

In the first case of a one-dimensional problem, we compared the results of FEM with those of IE [1], which is considered as precise one. The walls are black and at a cold temperature (0 K). At initial time $t=0$, the temperature of the left boundary is suddenly raised to provide an unit radiative intensity I_0 for all subsequent time. Considering the absorbing and isotropic scattering media, the optical thickness is 1.0 and the albedo is 0.5. The solid angular discretization adopts S_{20} and the spatial domain is discretized into 100 uniform linear elements. With Crank-Nicolson scheme as the time difference scheme, the time step is taken as $\Delta t^* = 0.02$. The time t^* is defined as $t^* = Ct$. The dimensionless radiative heat flux Q and incident radiation G are, respectively, defined as

$$Q(\mathbf{x},t) = \frac{1}{I_0}\int_{4\pi} \mathbf{I}(\mathbf{x},\mathbf{\Omega},t)\cos(\mathbf{s},\mathbf{n})d\mathbf{\Omega} \tag{16}$$

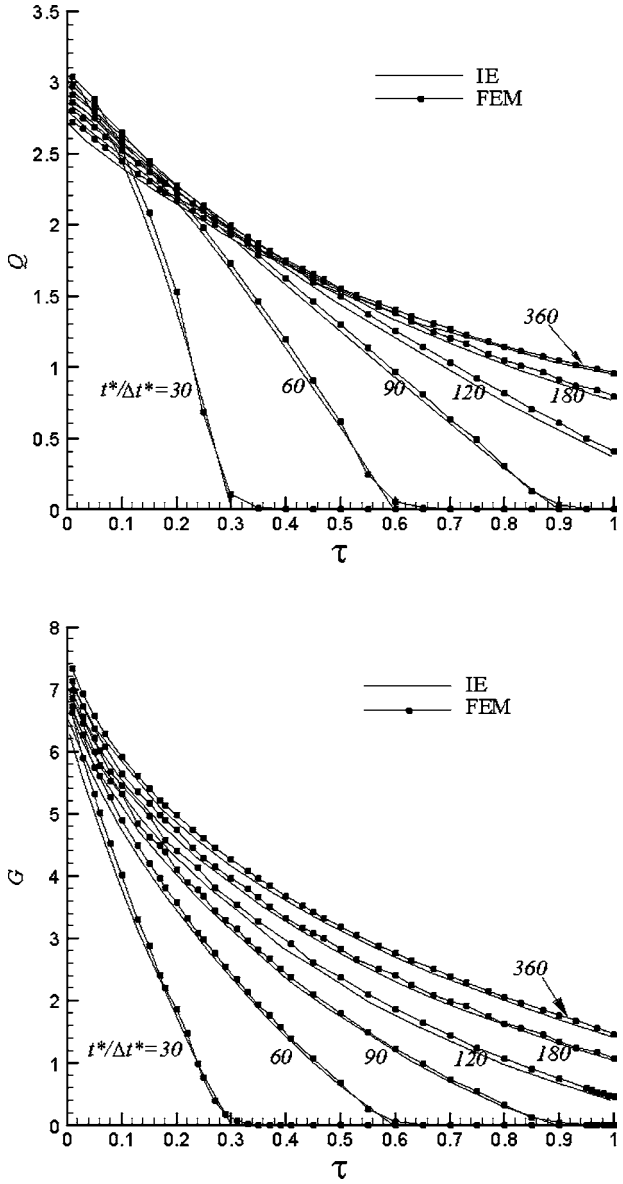

Fig. 1 The heat flux and incident radiation in one-dimensional slab at different time: (a) the heat flux in the media at different time; (b) the incident radiation in the media at different time

$$G(\mathbf{x},t)=\frac{1}{I_0}\int_{4\pi}\mathbf{I}(\mathbf{x},\boldsymbol{\Omega},t)d\boldsymbol{\Omega}$$

where **s** present the direction of the radiative intensity **I**; **n** is the direction of coordinate axis **x**.

As shown in Fig. 1, the results of FEM and IE have a desired agreement. The maximum relative error is less 4.0%. With the time elapsing, the incident radiation increases, however the radiative flux near the hot surface decreases due to the backscattering of radiant energy.

In the second case, a two-dimensional transient radiative transfer problem is studied. As shown in Fig. 2, an irregular quadrilateral enclosure is filled with an absorbing-emitting medium maintained at a constant temperature of T_g. The wall is black and cold $T_w=0$ K. The absorption coefficient is 1.0 m^{-1}. The solid angular discretization adopts S_8. The spatial domain is discretized into 40×40 quadrangular bilinear elements. The Crank-Nicolson scheme is also employed in the time difference scheme. The time step is taken as $\Delta t^*=0.025$. Figure 3 shows the radiative flux on the bottom wall at the different time. This case has been investigated by using the FVM [6]. As shown in Fig. 3, the results of FEM and FVM are very close. The maximum relative error is less 6.5%.

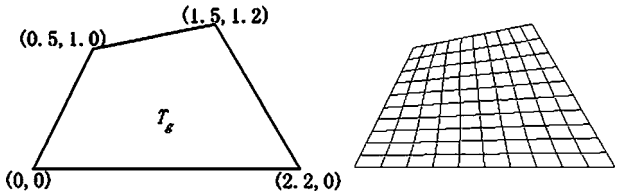

Fig. 2 Schematic diagram and quadrangle-element grid (10×10) in 2D irregular quadrilateral enclosure

4 Conclusion

In the present study, a finite element model has been developed and applied to simulate transient radiative transfer in one-dimensional and two-dimensional enclosure. The simulation is based on least-squares variational principles and DOM. It leads to a symmetric positive definite coefficient matrix which can be stored inexpensively and solved efficiently. This model could produce smooth result even for a longer time step. Compared with the other oscillation-eliminate numerical techniques, the LSFEM contains the implicit upwind component and does not need to tune any parameter. The discretization strategy for angular domain could use either the Sn-type discretization or the azimuthal discretization. The results of LSFEM show a good agreement with that of IE and FVM. Therefore, the present model is a promising approach for the transient radiative transfer, and can easily be expanded to a three-dimensional problem. Just as the present model has been developed in a 1D and 2D transient radiative problem, it is would seem especially fruitful to promote the study of transient radiative transfer with collimated light irradiation by LSFEM. In summary, the present model might realize its potential and make a difference in the transient radiative research.

Acknowledgment

The support of this work by the National Natural Science Foundation of China (No. 50276014) is gratefully acknowledged.

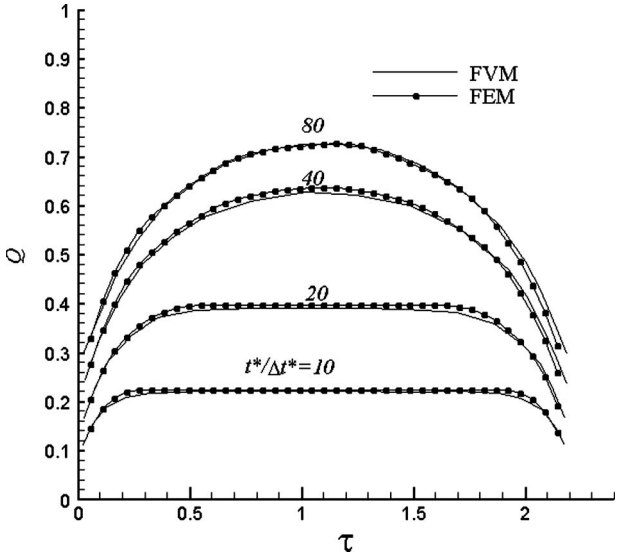

Fig. 3 The heat flux on the bottom wall in 2D irregular quadrilateral enclosure at different time

Nomenclature

A = area of element
B = modified extinction coefficient, Eq. (5*a*)
C = propagation speed of radiation transport in the medium
G = dimensionless incident radiation, Eq. (16)
I = radiative intensity, $W/(m^2\,sr)$
K, K' = stiffness matrix of finite element
M = number of discrete directions
Q = dimensionless radiative heat flux, Eq. (16)
S = modified source function, Eq. (5*b*)
R = right side term of finite element
V = the domain of solution
W_l = the weight function
$\mathbf{n}_w$ = unit normal vector of boundary surface
q = radiative heat fluxes, W/m^2
$\mathbf{r}$ = the location
$\mathbf{s}_{m'}$ = unit vector in the direction $\mathbf{m}'$
t = the time
$w_{m'}$ = angular weight
x, y, z = coordinate directions
Ω = solid angle, sr
Φ = scattering phase function
ε = emissivity
κ_a = absorption coefficient, m^{-1}
σ_s = scattering coefficient, m^{-1}
ω = scattering albedo
φ_l = shape function
τ = optical thickness
μ, η, ξ = direction cosines

Subscripts

b = blackbody
e = element
i, j, k, l = node
n = time step
w = wall
θ = zenith angle
φ = round angle

Superscripts

m, m' = indices for ordinate directions

References

[1] Tan, Z. M., and Hsu, P. F., 2001, "An Integral Formulation of Transient Radiative Transfer," ASME J. Heat Transfer, **123**, pp. 466–475.

[2] Balsara, D. W., 1999, "An Analysis of the Hyperbolic Nature of the Equations of Radiation Hydrodynamics," J. Quant. Spectrosc. Radiat. Transf., **61**(5), pp. 617–627.

[3] Guo, Z., and Kumar, S., 2000, "Discrete-Ordinates Solution of Short-Pulsed Laser Transport in Two-Dimensional Turbid Media," Appl. Opt., **39**(24), pp. 4411–4417.

[4] Sakami, M., Mitra, K., and Vo-Dinh, T., 2002, "Analysis of Short-Pulse Laser Photon Transport Through Tissues for Optical Tomography," Opt. Lett., **27**(5), pp. 336–338.

[5] Chai, J. C., 2003, "One-Dimensional Transient Radiation Heat Transfer Modeling Using a Finite-Volume Method," Nat. Biotechnol., **44**, pp. 187–208.

[6] Chai, J. C., 2004, "Transient Radiative Transfer in Irregular Two-Dimensional Geometries," J. Quant. Spectrosc. Radiat. Transf., **84**, pp. 281–294.

[7] Wu, C. Y., 2000, "Propagation of Scattered Radiation in a Participating Planar Medium With Pulse Irradiation," J. Quant. Spectrosc. Radiat. Transf., **64**, pp. 537–548.

[8] Hsu, P. F., 2001, "Effects of Multiple Scattering and Reflective Boundary on the Transient Radiative Transfer Process," Int. J. Therm. Sci., **40**, pp. 539–549.

[9] Burns, S. P., Howell, J. R., and Klein, D. R., 1995, "Finite Element Solution for Radiative Heat Transfer With Nongray, Nonhomogeneous Radiative Properties," *ASME National Heat Transfer Conference*, Vol. 13, pp. 3–10.

[10] Furmanski, P., and Bannaszek, J., 2004, "Finite Element Analysis of Concurrent Radiation and Conduction in Participating Media," J. Quant. Spectrosc. Radiat. Transf., **84**, pp. 563–573.

[11] Liu, L. H., 2004, "Finite Element Simulation of Radiative Heat Transfer in Absorbing and Scattering Media," J. Thermophys. Heat Transfer, **18**(4), pp. 555–557.

[12] An, W., Ruan, L. M., Qi, H., and Liu, L. H., 2005, "Finite Element Method for Radiative Heat Transfer in Absorbing and Anisotropic Scattering Media," J. Quant. Spectrosc. Radiat. Transf., **96**(3–4), pp. 409–422.

[13] Pontaza, J. P., and Reddy, J. N., 2005, "Least-Squares Finite Element Formulations for One-Dimensional Radiative Transfer," J. Quant. Spectrosc. Radiat. Transf., **95**(3), pp. 387–406.

[14] Cui, X., and Li, B. Q., 2005, "Discontinuous Finite Element Solution of 2D Radiative Transfer With and Without Axisymmetry," J. Quant. Spectrosc. Radiat. Transf., **96**(3–4), pp. 383–407.

[15] Hughes, T. J. R., and Brooks, A., 1982, "Streamline Upwind/Petrov-Galerkin Formulation for Convection Dominated Flows With Particular Emphasis on the Incompressible Navier-Stokes Equations," Comput. Methods Appl. Mech. Eng., **32**, pp. 199–259.

[16] Donea, J., 1984, "A Taylor-Galerkin Method for Convective Transport Problems," Int. J. Numer. Methods Eng., **20**, pp. 101–119.

[17] Jiang, B. N., and Povinelli, L. A., 1990, "Least-Squares Finite Element Method for Fluid Dynamics," Comput. Methods Appl. Mech. Eng., **81**, pp. 13–37.

[18] Donea, J., and Quartapelle, L., 1992, "An Introduction to Finite Element Methods for Transient Advection Problems," Comput. Methods Appl. Mech. Eng., **95**, pp. 169–203.

[19] Raithby, G. D., 1999, "Discussion of the Finite Volume Method for Radiation and its Application Using 3D Unstructured Meshes," Numer. Heat Transfer, Part B, **35**, pp. 389–405.

On the Entropy Generation Formula of Radiation Heat Transfer Processes

L. H. Liu[1]
e-mail: lhliu@hit.edu.cn

S. X. Chu

School of Energy Science and Engineering,
Harbin Institute of Technology,
92 West Dazhi Street,
Harbin 150001,
People's Republic of China

Because thermal radiation is a long-range phenomenon, the local radiative heat flux is dependent on the temperature distribution of the entire enclosure under consideration and is not determined by the local temperature gradient. In the community of heat transfer, traditionally, the conduction-type formula of entropy generation rate is used to calculate the entropy generation rate of radiation heat transfer. In the present study, three counterexamples are considered. The discrete ordinates method is employed to solve the radiative transfer equation and then solve the radiative entropy generation rate. The results show that the traditional formulas of entropy generation rate for heat transfer generally cannot be used to calculate the local entropy generation rate of radiation heat transfer. Only in optically extremely thick situations, the traditional formula of entropy generation rate for heat transfer can be approximately used to calculate the local entropy generation rate of radiation heat transfer. [DOI: 10.1115/1.2190695]

Keywords: entropy generation rate, radiative heat transfer, semitransparent medium, calculation formula

1 Introduction

Entropy generation is associated with thermodynamic irreversibility, which is present in all heat transfer processes and results in the loss of available work. The contemporary trend in the field of heat transfer and thermal design is to apply the second law analysis of thermodynamics and its design-related concept of entropy generation minimization. The entropy generation and its minimization were investigated extensively by Bejan [1–3], who presented systematically the concept and the optimization method of entropy generation minimization.

Thermal radiation is an important factor in the thermodynamic analysis of many high-temperature systems, such as solar collectors, boilers, and furnaces. The correct evaluation of radiation entropy generation is important when determining the second-law performance of these energy conversion devices. Planck [4] was the first to investigate the interaction between light and matter with respect to its irreversibility. Thermodynamic aspects of radiative transfer processes were later studied by Wildt [5] who was mainly interested in atmospheres in radiative equilibrium. Wildt derived a number of inequalities for the radiative entropy that follow from macroscopic considerations alone, and was the first to formulate the transfer equation for the radiative entropy. Starting from basic statistical relations, Kroll [6] analyzed the general form of the entropy production and discussed the sign of its time derivative. It is shown that the entropy production due to emission, absorption, and scattering of radiation is a form bilinear in generalized thermodynamic fluxes and forces. Arpaci [7–10], and Arpaci and Esmaeeli [11] studied the radiative deformation and radiation entropy generation. Recently, Caldas and Semiao [12] presented a numerical simulation method of radiative entropy generation in semitransparent participating media. This method is completely compatible with standard radiative transfer calculation like the discrete ordinate ordinates method.

In the community of heat transfer, traditionally, the formula of entropy generation rate per unit volume for heat transfer, including conduction or radiation, is written as

$$\dot{S}'''_{\text{gen}}(\mathbf{r}) = -\mathbf{q}(\mathbf{r}) \cdot \frac{\nabla T_M(\mathbf{r})}{T_M^2(\mathbf{r})} \tag{1}$$

where T_M is the medium temperature, and $\mathbf{q}$ is the total heat flux vector. According to Eq. (1), the entropy generation rate per unit volume for radiation heat transfer is often written as (see, for example, Arpaci [7–10], and Arpaci and Esmaeeli [11])

$$\dot{S}'''_{R,V}(\mathbf{r}) = -\mathbf{q}^R(\mathbf{r}) \cdot \frac{\nabla T_M(\mathbf{r})}{T_M^2(\mathbf{r})} \tag{2}$$

where $\mathbf{q}^R$ is the radiative heat flux vector. Equation (2) is similar to the formula of entropy generation rate of heat conduction. However, as shown in the next section, careful examination of Eq. (2) reveals that this equation is incorrect in a thermodynamics sense. The processes of radiation heat transfer differ from those of conduction heat transfer. One distinguishing feature between conduction and radiation is the difference in their temperature dependencies. Conduction heat transfer is well described by Fourier's law, and the local heat flux of conduction is linearly proportional to the local temperature gradient. In the view of irreversible thermodynamics, the heat flux of conduction is driven by the local temperature gradient. Therefore, the conductive entropy generation rate per unit volume can be calculated using Eq. (1). However, thermal radiation is generally a long-range phenomenon, therefore the local radiative heat flux is dependent on the temperature distribution of the entire enclosure under consideration and is not determined by the local temperature gradient. Only in optically extremely thick situations, radiation heat transfer processes can be described by the diffusion approximation and the local heat flux of radiation is approximately proportional to the local temperature gradient.

In this paper, we take three counterexamples to show that the traditional formula (Eq. (2)) of entropy generation rate for heat transfer cannot be used to calculate the local entropy generation rate of radiation heat transfer.

2 Counterexamples

To show the incorrectness of a traditional formula (Eq. (2)) of radiation entropy generation, as shown in Fig. 1, we consider a one-dimensional absorbing, emitting, and isotropic scattering gray medium bounded by two blackbody walls. The thickness of the semitransparent slab is $L=1.0$ m. The optical thickness based on the slab thickness is denoted as τ_L. The temperatures of the left and the right walls are imposed as T_{W_1} and T_{W_2}, respectively. The distribution of medium temperature T_M is prescribed. In this study, we mainly check the correctness of the traditional formula (Eq. (2)) for radiative entropy generation rate, therefore no conduction entropy generation is considered. For the following numerical analysis, the semitransparent slab is uniformly divided into 1000 parts, and the discrete ordinates method (S_8) [13] is employed to solve the radiative transfer equation and then solve the radiative entropy generation rate.

2.1 Example 1. We first consider the radiative heat transfer and the radiative entropy generation in the case of $\omega=0.0, \tau_L$

Contributed by the Heat Transfer Division of ASME for publication in the JOURNAL OF HEAT TRANSFER. Manuscript received July 30, 2005; final manuscript received October 21, 2005. Review conducted by Walter W. Yuen.

[1]Corresponding author.

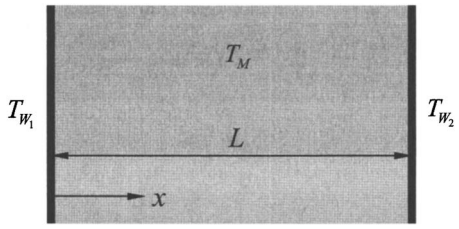

Fig. 1 One-dimensional semitransparent slab system

$=1.0$, $T_{W_1}=1000$ K, and $T_M=T_{W_2}=500$ K. In the view of irreversible thermodynamics, for the example under consideration, the one-dimensional system shown in Fig. 1 is equivalent to a system in which heat is transported from a high-temperature heat source (1000 K) to a low-temperature heat source (500 K) by radiation, but from which no work has been obtained. Therefore, theoretically, the total radiative entropy generation of the system is

$$S^R_{\text{gen}} = q^R_{W_1}\left(\frac{1}{T_M} - \frac{1}{T_{W_1}}\right) > 0 \tag{3}$$

In this example, the temperature of semitransparent medium is uniform, therefore the temperature gradient is $\partial T_M/\partial x=0$. Because T_{W_1} is greater than T_M and T_{W_2}, as shown in Fig. 2, the axial radiative heat flux is greater than zero. The radiative heat transfer process is irreversible, but the local radiative entropy generation rate calculated using Eq. (2) is $\dot{S}'''_{R,V}(\mathbf{r})=0$. This conflicts with the thermodynamics analysis of the system.

2.2 Example 2. In this example, we consider the radiative heat transfer and the radiative entropy generation in the case of $\omega=0.0, \tau_L=1.0$, $T_{W_1}=1000$ K, $T_{W_2}=500$ K, and $T_M=300+200x/L$, K. The temperature gradient is $\partial T_M/\partial x=200/L>0$. As shown in Fig. 3, the axial radiative heat flux is greater than zero. The local radiative entropy generation rate calculated using Eq. (2) is shown in Fig. 4. The local radiative entropy generation rate calculated using Eq. (1) is $\dot{S}'''_{R,V}(\mathbf{r})<0$. This conflicts with the second law of thermodynamics.

2.3 Example 3. In this example, we consider the radiative entropy generation in the case of $\omega=0.5$, $T_{W_1}=T_{W_2}=1000$ K, and $T_M=1000+500\sin(2\pi x/L)$, K. The axial radiative heat flux and the local radiative entropy generation rate calculated using Eq. (2) are shown in Figs. 5 and 6 for the cases of $\tau_L=2$ and $\tau_L=40$, respectively. In the case of $\tau_L=2$, both the temperature gradient and the axial radiative heat flux within the region of $x/L \in [0.75, 0.95]$ are greater than zero. This leads to the result that the local radiative entropy generation rate calculated using Eq. (2) is less than zero within the region under consideration. Similar to Examples 1 and 2, this also conflicts with the second law of thermodynamics. Therefore, Eq. (2) is incorrect, and the traditional formula (Eq. (2)) of entropy generation rate for heat transfer cannot be used to calculate the local entropy generation rate of radiation heat transfer.

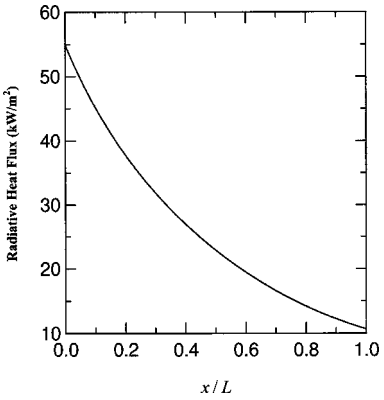

Fig. 3 Radiative heat flux for Example 2

The local radiative entropy generation rate calculated using the formulas of Caldas and Semiao in Ref. [12] is also shown in Fig. 6 for Example 3. By comparison with the results calculated using Eq. (2), it is shown that, even if both the temperature gradient and the axial radiative heat flux within the region of $x/L \in [0.75, 0.95]$ are greater than zero for the case of $\tau_L=2$, the local radiative entropy generation rate calculated using the formulas of Caldas and Semiao [12] is greater than zero. This is consistent with the Second Law of Thermodynamics. For the case of $\tau_L=40$, the local radiative entropy generation rate calculated using Eq. (2) is close to that calculated using the formulas of Caldas and Semiao [12]. In optically extremely thick situations, the traditional formulas (Eq. (2)) of entropy generation rate for heat transfer can be approximately used to calculate the local entropy generation rate of radiation heat transfer.

3 Conclusions

The processes of radiation heat transfer differ from those of conduction heat transfer. One distinguishing feature between conduction and radiation is the difference in their temperature dependencies. Thermal radiation is a long-range phenomenon. Therefore, the local heat flux is dependent on the temperature distribution of the entire enclosure under consideration and is not determined by the local temperature gradient. In the present study, three counterexamples are considered. The results show that the

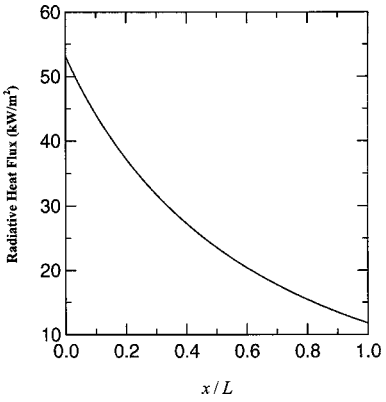

Fig. 2 Radiative heat flux for Example 1

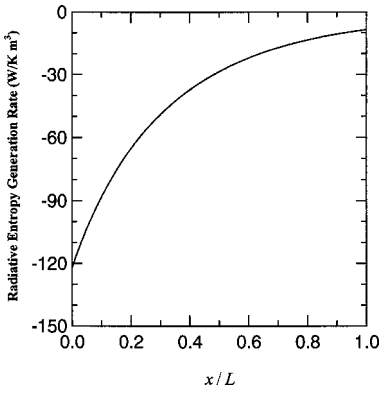

Fig. 4 Radiative entropy generation rate computed using Eq. (2) for Example 2

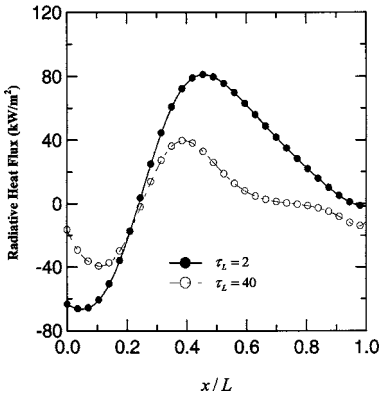

Fig. 5 Radiative heat flux for Example 3

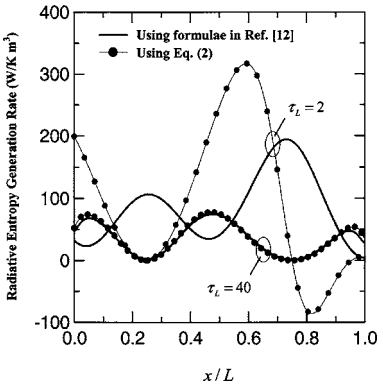

Fig. 6 Comparison of radiative entropy generation rates for Example 3

traditional formulas of entropy generation rate for heat transfer generally cannot be used to calculate the local entropy generation rate of radiation heat transfer. Only in optically extremely thick situations, can the traditional formula of entropy generation rate for heat transfer be approximately used to calculate the local entropy generation rate of radiation heat transfer.

Acknowledgment

The supports of this work by the National Natural Science Foundation of China (50425619) and the Science Fund of Heilongjiang Province for Distinguished Young Scholars (No. JC04-03) are gratefully acknowledged.

Nomenclature

L = thickness of semitransparent slab, m
$\mathbf{q}$ = heat flux vector
$\mathbf{q}^R$ = radiative heat flux vector
$\mathbf{r}$ = position vector
$\dot{S}'''_{\text{gen}}$ = entropy generation rate of heat transfer per unit volume, W/K m^3
S^R_{gen} = total radiative entropy generation of slab system, W/K m^2
$\dot{S}'''_{R,V}$ = radiative entropy generation rate per unit volume, W/K m^3
T_M = medium temperature, K
T_{W_1}, T_{W_2} = temperature at walls, K
τ_L = optical thickness
ω = single scattering albedo

References

[1] Bejan, A., 1982, *Entropy Generation Through Heat and Fluid Flow*, Wiley, New York.
[2] Bejan, A., 1996, *Entropy Generation Minimization*, CRC Press, New York.
[3] Bejan, A., 1997, *Advanced Engineering Thermodynamics*, 2nd ed., Wiley, New York.
[4] Planck, M., 1959, *The Theory of Heat Radiation*, Dover, New York.
[5] Wildt, R., 1956, "Radiative Transfer and Thermodynamics," Astrophys. J., **123**, pp. 107–116.
[6] Kroll, W., 1967, "Properties of the Entropy Production due to Radiative Transfer," J. Quant. Spectrosc. Radiat. Transf., **7**, pp. 715–723.
[7] Arpaci, V. S., 1986, "Radiative Entropy Production," AIAA J., **24**, pp. 1859–1860.
[8] Arpaci, V. S., 1987, "Radiative Entropy Production—Lost Heat into Entropy," Int. J. Heat Mass Transfer, **30**, pp. 2115–2123.
[9] Arpaci, V. S., 1991, "Radiative Entropy Production—Heat Loss into Entropy," in *Advances in Heat Transfer*, J. P. Hartnett and T. F. Irvine, eds., **21**, Academic, New York, pp. 239–276.
[10] Arpaci, V. S., 2001, "Thermal Deformation: From Thermodynamics to Heat Transfer," ASME J. Heat Transfer, **123**, pp. 821–826.
[11] Arpaci, V. S., Esmaeeli, A., 2000, "Radiative Deformation," J. Appl. Phys., **87**, pp. 3093–3100.
[12] Caldas, F., Semiao, V., 2005, "Entropy Generation Through Radiative Transfer in Participating Media: Analysis and Numerical Computation," J. Quant. Spectrosc. Radiat. Transf., **96**, pp. 423–437.
[13] Modest, M. F., 2003, *Radiative Heat Transfer*, 2nd ed., Academic, New York.